AN ABSTRACT OF THE THESIS OF

Richard D. Romea for the degree of Doctor of Philosophy

in Oceanography presented on June 10, 1982

Title: On Coastal Trapped Waves at Low Latitudes in a Stratified Ocean

Abstract approved: Redacted for privacy

J. S. Allen / R. L. Smith

The response on the continental shelf of a baroclinic ocean to driving by an alongshore coastal wind stress and by barotropic and baroclinic wind forced interior motions is studied as a function of latitude. The relative excitation of continental shelf waves and internal Kelvin waves is studied.

The response of a rotating stratified ocean with a vertical boundary, forced at the surface by an alongshore coastal wind stress, shows vertically propagating subinertial motions. Several examples which illustrate the basic properties of the response are presented. Changes in amplitude and frequency with depth are predicted. Components that decay with depth from the surface and components

that represent coastal internal Kelvin waves with negative vertical group velocity and upward phase propagation are forced.

The effect of bottom Ekman layer friction and slope topography on free internal Kelvin waves is examined, using both a steep and weak slope model. The steep slope represents the low latitude case while the weak slope represents the mid-latitude case. There are substantial differences between the results from the two models. Free waves are frictionally damped and offshore and vertical phase shifts are induced by friction, as well as an onshore flow. Topography induces changes to the wave frequency and alongshore phase speed. The modal amplitude is altered and an onshore flow is induced.

Sea level and current velocity data from the equator to 17°S on the west coast of South America show that low frequency (0.1-0.2 cpd) fluctuations propagate poleward with phase speeds similar to those predicted for first mode baroclinic Kelvin waves. The sea level and currents are coherent and approximately 180° out of phase. The waves do not appear to be the result of local atmospheric forcing. Empirical orthogonal functions show that the alongshore and vertical structure of alongshore velocity is consistent with first mode internal Kelvin waves.

ON COASTAL TRAPPED WAVES AT LOW LATITUDES IN A STRATIFIED OCEAN

by

Richard Dennis Romea

A THESIS

submitted to

Oregon State University

in partial fulfillment of
the requirements for the
degree of
Doctor of Philosophy

Completed June 10, 1982

Commencement June 1983

APPROVED:

Redacted for privacy

Professor of Oceanography in charge of major

Redacted for privacy

Professor of Oceanography in charge of major

Redacted for privacy

Dean of the School of Oceanography

Redacted for privacy

Dean of Graduate School

Date thesis is presented June 10, 1982

Typed by Pam Wegner and Laina Hardenburger for Richard Romea

ACKNOWLEDGEMENTS

This research was supported by the Oceanography Section of the National Science Foundation under Grants DES 7515202, OCE 7803382, OCE 8024116, OCE 7826820, OCE 8017929, and OCE 7803380.

TABLE OF CONTENTS

LIST OF FIGURES

LIST OF TABLES

ON COASTAL TRAPPED WAVES AT LOW LATITUDES IN A STRATIFIED OCEAN

Chapter I

INTRODUCTION

ON COASTAL TRAPPED WAVES AT LOW LATITUDES IN A STRATIFIED OCEAN

I. Introduction

During 1876-1977 an extensive oceanographic field program called JOINT-2 was conducted off the central Peru coast between 10° and 15°S latitude as part of the Coastal Upwelling Ecosystems Analysis Program. The ESACAN (Estudio del Sistema de Afloramiento Costero en el Area Norte) field experiment during 1977 near 5°S off the Peru coast supplemented the JOINT-2 observations and the combined data set provides us with observations along the Peru coast between 5° and 15°S.

Using a subset of this data, Smith (1978) found propagation of fluctuations in sea level and currents between 10° and 15°S at about 200 km day^{-1} in the poleward direction. These fluctuations were in the 0.1-0.2 cpd frequency band and did not appear well correlated with the local winds. While coastally trapped waves have been observed at mid-latitudes (e.g., Hammon, 1966; Cutchin and Smith, 1973; Kundu and Allen, 1976; Brooks and Mooers, 1977), the Peru observations are of particular interest because they are low latitude measurements.

At mid-latitudes, barotropic continental shelf waves are observed, whose structure and dynamics are governed by shelf-slope topography with only small effects due to stratification. These waves have been well studied theoretically (e.g., Reid, 1958; Robinson, 1964; Mysak,

1967; Buchwald and Adams, 1968; Adams and Buchwald, 1969; Gill and Schumann, 1974; Huthnance, 1975). In addition, perturbation effects on continental shelf waves due to bottom friction, and variations in Coriolis parameter, coastline curvature, and bottom topography have been studied (e.g., Allen, 1976; Buchwald, 1977; Clarke, 1977; Grimshaw, 1977; Brink and Allen, 1978; Brink, 1980).

Allen and Romea (1980) have shown theoretically that, at low latitudes, coastal trapped waves are not barotropic and internal Kelvin waves may play an important role in shelf dynamics. Analysis of the structure of the current fluctuations and the dynamic balances from the JOINT-2 data (Smith, 1978; Brink, et. al., 1978; Brink, et. al., 1980; Allen and Smith, 1981) suggests that the waves near 15°S are internal Kelvin wave-like.

This thesis is motivated by a desire to better understand the Peru observations. In order to model low latitude coastal wave dynamics, both the effects of stratification and topography should be included. This is relatively difficult and, in the past, investigators have appealed to two-layer models (e.g., Allen, 1975; Allen, 1976; Gill and Clarke, 1974; Allen and Romea, 1980) and numerical models with realistic stratification (e.g., Huthnance, 1978; Brink, 1982 a,b) in order to obtain results. However, two-layer models can be difficult to relate to observations, and numerical models have difficulties at low latitudes (Brink, private communication). In addition, numerical models generally solve for pressure and it is computationally difficult to obtain an accurate solution for velocity (see, e.g., Brink, 1982b).

Analytical models for low latitude shelf dynamics with continuous stratification are needed.

This study is composed of four parts, each of which addresses a particular aspect of coastal trapped wave dynamics at low latitudes. The first three parts are theoretical in nature, and were motivated by a desire to fill a gap in the existing theory. In Chapter II, the response on the continental shelf and slope to driving by an alongshore wind stress at the coast and by barotropic and baroclinic wind forced interior motions is studied as a function of latitude. A two layer model is utilized. The observations off the coast of Peru indicate that the wave-like fluctuations are typically not well correlated with the local component of the alongshore wind stress (Brink, et. al., 1978). Motivated by these observations, we are particularly interested in interior oceanic motions as a possible source for the observed propagating energy.

Offshore and vertical phase lags are observed in the velocity data from the Peru coast (see, e.g., Brink, 1982a). Propagation in the offshore or vertical directions or frictional effects may be responsible for these phase lags. In Chapter III the dynamics of vertically propagating internal Kelvin waves at low latitudes is studied and conditions are defined where phase lags due to vertically propagating waves would be observed in the ocean. The perturbation effects of both friction and topography on internal Kelvin waves in a contiuously stratified ocean are studied in Chapter IV, and predicted phase lags due to frictional effects are derived and compared to observations.

In Chapter V, the data from the JOINT-2 and ESACAN experiments is used to document the existence of propagating fluctuations and to elucidate their structure. The longer and more extensive data set is used to revisit the analysis of Smith (1978), and the behavior of the fluctuations is compared to theories of coastal trapped waves at low latitudes.

Chapter II

ON FORCED COASTAL TRAPPED WAVES AT LOW LATITUDES IN A STRATIFIED OCEAN

Introduction

The response on a continental shelf and slope to forcing by wind stress and by interior oceanic motion will vary with latitude. This response will also depend on the stratification, the shelf-slope topography, and the nature of the motion in the interior ocean.

Recent observations from the Coastal Upwelling Ecosystems Analysis (CUEA) experiment on the continental shelf and slope off the coast of Peru (Brink et al., 1978; Smith, 1978) at 10°-15°S indicate strong poleward propagating wavelike motions in the alongshore component of the currents which are typically not well correlated with the local alongshore component of the wind stress. Motivated by these observations, we study the characteristics of forced long waves trapped over a continental shelf and slope as a function of latitude and we investigate the interior oceanic motion as a possible source for the observed propagating energy. We consider a linear inviscid two layer ocean with a continental shelf and slope along the eastern boundary. A response may be forced on the shelf by the wind directly through the alongshore component of the wind stress at the coast and indirectly through the interaction with the shelf of motions forced in the interior ocean by the wind stress curl.

We first solve the forced problem in terms of cross-shelf eigenfunctions of the unforced problem, using an f-plane. With this approach, a first order wave equation may be obtained for the alongshore and time-dependent behavior of each wave mode. This method is particularly well-suited for initial-value problems where it shows how the forced flow on the shelf develops as each wave mode responds to the forcing. Since the phase velocities vary and the eigenfunctions change structure as a function of latitude, the mid-latitude forced response, aspects of which

have been discussed by Gill and Schumann (1974) and Allen (1976a), will differ from the low latitude forced response.

The problem is also approached in another way. For an idealized wind stress forcing, with sinusoidal dependence on time and on the horizontal spatial coordinates (e.g., a traveling wave), the onshore-offshore structure of the solutions on the shelf may be obtained directly. These solutions are particularly well suited for determining the relative importance of the various mechanisms for forcing shelf circulations. For example, the offshore dependence of the solutions forced by the alongshore component of the wind stress at the coast and by the interior wind forced barotropic and baroclinic motions may be compared as a function of latitude, forcing frequency and wavenumber. Since the solutions change character for forcing at very low frequency (Section 5b), the β-effect is included in the anlaysis to establish the validity of the f-plane solutions presented in Sections 3-5.

2) Formulation

We consider a north-south oriented boundary on the eastern side of a two layer β-plane ocean, where Cartesian coordinates (x', y', z'), are utilized[1], with x' positive in the offshore direction (the coastline is at x' = 0), y' positive southward, and z' positive vertically upward. Stratification is modelled by two layers of homogeneous fluid of different density, with the heavier fluid on the bottom. The top surface is bounded by a rigid lid. The upper layer fluid has density ρ_1, and a constant undisturbed depth H_1'. The lower layer fluid has density ρ_2 and a variable undisturbed depth $H_2' = H_2'(x', y')$. The total depth is $H' = H_1' + H_2'$. The difference in density $\Delta\rho = \rho_2 - \rho_1$ is assumed to be small, $\Delta\rho/\rho_2 << 1$. Along the boundary there is a continental shelf and slope topography which is confined to the region $0 \leq x' \leq L_s$. In the interior ($x' \geq L_s$), the depth is constant, $H' = H_0' = H_1' + H_{20}'$.

Dimensionless variables are formed in the following manner:

$$(x, y) = (x', y')/L,\quad z = z'/H_0',\quad t = t'f_0,$$

$$(u_i, v_i) = (u_i', v_i')/U,\quad w_i = w_i'L/(H_0'U),$$

$$p_1 = [p_1' + \rho_1 g(z' - H_0')]/(\rho_1 U f_0 L),$$

$$p_2 = [p_2' + \rho_2 g(z' - H_{20}') - \rho_1 g H_1']/(\rho_2 U f_0 L),$$

$$h = h' g\Delta\rho/(\rho_2 U f_0 L),$$

$$(H_1, H_2, H) = (H_1', H_2', H')/H_0',$$

$$\underset{\sim}{\tau} = \underset{\sim}{\tau}'/(U\rho_2 f_0 H_1),$$

$$f = (f_0 - \beta' y')/f_0 = 1 - \beta y, \qquad (2.1)$$

[1] In this and the following sections, dimensional variables for which a nondimensional counterpart will be defined are denoted with primes.

where i = 1, 2 refers to the upper and lower layer, respectively. The variables (u', v', w') are the velocity components in the (x', y', z') directions, p' is the pressure, t' is time, L is a characteristic horizontal alongshore scale (the dimensional alongshore wavelength $\lambda' = 2\pi L$), U is a characteristic horizontal velocity [$U = \tau_0'/(\rho_2 f_0 H_1)$, where τ_0' is a characteristic wind stress], g is the acceleration of gravity, τ' is the surface wind stress vector with (x', y') components $(\tau^{(x')'}, \tau^{(y')'})$, f_0 is the value of the Coriolis parameter at a reference latitude and $\beta = \beta' L/f_0$. $h = p_2 - p_1$ is the dimensionless perturbation interface height.

The resulting linear, depth integrated continuity and momentum equations for each layer are (subscripts x, y, t denote partial differentiation)

$$(H_1 u_1)_x + (H_1 v_1)_y = S^{-1} h_t, \tag{2.2a}$$

$$u_{1t} - f v_1 = -p_{1x} + \tau^{(x)}, \tag{2.2b}$$

$$v_{1t} + f u_1 = -p_{1y} + \tau^{(y)}, \tag{2.2c}$$

$$(H_2 u_2)_x + (H_2 v_2)_y = -S^{-1} h_t, \tag{2.2d}$$

$$u_{2t} - f v_2 = -p_{2x}, \tag{2.2e}$$

$$v_{2t} + f u_2 = -p_{2y}, \tag{2.2f}$$

where $S = (N H_0'/f_0 L)^2$ is the stratification parameter and $N^2 = g\Delta\rho/(\rho_2 H_0')$ is the square of the Brunt-Väisälä frequency.

If (2.2a) and (2.2d) are combined, a streamfunction may be defined, such that

$$\psi_y = u_1 + (H_2/H_1)\, u_2, \tag{2.3a}$$

$$-\psi_x = v_1 + (H_2/H_1) v_2. \tag{2.3b}$$

The general governing equations for the perturbation interface height h and the mass transport streamfunction ψ may be obtained from (2.2) (Allen, 1975) and are:

$$[\psi_{xx} + \psi_{yy} - (H_x/H)\psi_x - (H_y/H)\psi_y]_t - \beta\psi_x$$

$$= (H_x/H)(h_y - f\psi_y + \tau^{(y)}) - (H_y/H)(h_x - f\psi_x + \tau^{(x)})$$

$$- (\tau_x^{(y)} - \tau_y^{(x)}), \qquad (2.4a)$$

$$[h_{xx} + h_{yy} + a(H_x/H)h_x + a(H_y/H)h_y - (SH)^{-1}\mathcal{L}h$$

$$-(\beta/f)(h_x - h_y)]_t - \beta h_x$$

$$= -a(H_x/H)\,[fh_y - \mathcal{L}\psi_y + f\tau^{(y)} + \tau_t^{(x)}]$$

$$-a(H_y/H)\,[fh_x - \mathcal{L}\psi_x + f\tau^{(x)} - \tau_t^{(y)}]$$

$$+ \beta\tau^{(x)} - f(\tau_x^{(y)} - \tau_y^{(x)}) - (\tau_x^{(x)} + \tau_y^{(y)})_t, \qquad (2.4b)$$

where $\mathcal{L} = f^2 + (\partial^2/\partial t^2)$, $a = H_1/H_2$.

The following assumptions are utilized:

1) restrict the topography to have no alongshore variations, so that $H = H(x)$ only;

2) assume $\beta << 1$;

3) restrict attention to motions on a time scale δ_t large compared with an inertial period, i.e., $\delta_t >> f^{-1}$;

4) assume the scale of the wind stress and therefore the scale of the interior motion and the alongshore scale of the motion on the shelf is O(1);

5) assume the interior Rossby radius of deformation [defined in (2.8)] is much smaller than the O(1) alongshore scale,

$$\delta_{R(1)} << 1; \tag{2.5a}$$

6) assume the dimensionless width of the shelf-slope region δ is also much smaller than the O(1) alongshore scale,

$$\delta << 1. \tag{2.5b}$$

7) assume that the small parameters δ, $\delta_{R(1)}$, and β are, in general, of the same order-of-magnitude, i.e.,

$$O(\delta) = O(\delta_R) = O(\beta). \tag{2.5c}$$

It is convenient to define a new cross-shelf variable

$$\xi = x/\delta, \tag{2.6a}$$

and an associated time scale

$$\bar{t} = t\delta. \tag{2.6b}$$

With the above assumptions the equations for the interior, where $H_x = 0$, are

$$\delta(\tilde{\psi}_{xx} + \tilde{\psi}_{yy})_{\bar{t}} - \beta\tilde{\psi}_x = -(\tau_x^{(y)} - \tau_y^{(x)}), \tag{2.7a}$$

$$\delta(\tilde{h}_{xx} + \tilde{h}_{yy} - \delta_{R(1)}^{-2}\tilde{h})_{\bar{t}} - \beta\tilde{h}_x = -f(\tau_x^{(y)} - \tau_y^{(x)}), \tag{2.7b}$$

where a tilda superscript denotes an interior variable. The interior Rossby radius, which is the natural offshore decay scale for baroclinic disturbances, is given by

$$\delta_R^2(\xi = 1) = \delta_{R(1)}^2 = f^{-2}S\bar{H}_{(1)}, \tag{2.8a}$$

where

$$\bar{H}(\xi) = H_1H_2(\xi)/H(\xi) \text{ and } \bar{H}_{(1)} = \bar{H}(\xi = 1). \tag{2.8b,c}$$

Equations (2.7a) for the barotropic interior motion and (2.7b) for the baroclinic interior motion are uncoupled and may be solved separately, subject to the proper boundary conditions.

At $x = \delta$, the junction of the interior and the shelf-slope region, the matching conditions, which follow from the continuity of mass flux and pressure, are

$$\tilde{h}(x = \delta) = h(\xi = 1), \tag{2.9a}$$

$$\tilde{h}_{x\bar{t}}(x = \delta) = \delta^{-1} h_{\xi\bar{t}}(\xi = 1), \tag{2.9b}$$

$$\tilde{\psi}_y(x = \delta) = \psi_y(\xi = 1), \tag{2.9c}$$

$$\tilde{\psi}_{x\bar{t}}(x = \delta) = \delta^{-1} \psi_{\xi\bar{t}}(\xi = 1). \tag{2.9d}$$

We expand $\tilde{\psi}$ in an asymptotic series, i.e.,

$$\tilde{\psi} = \delta^{-1}(\tilde{\psi}_0 + \delta\tilde{\psi}_1 + \ldots), \tag{2.10}$$

where the leading order is suggested by (2.7a). With this representation, (2.7a) is

$$(\tilde{\psi}_{0xx} + \tilde{\psi}_{0yy})_{\bar{t}} - \beta\delta^{-1}\,\tilde{\psi}_{0x} = -(\tau_x^{(y)} - \tau_y^{(x)}). \tag{2.11}$$

The interior variable $\tilde{h}$ is conveniently written as two terms,

$$\tilde{h} = \tilde{h}_I + \tilde{h}_B, \tag{2.12}$$

where, from (2.7b) and with assumption (2.5a),

$$\delta\delta_{R(1)}^{-2}\,\tilde{h}_{I\bar{t}} + \beta\tilde{h}_{Ix} = f(\tau_x^{(y)} - \tau_y^{(x)}), \tag{2.13}$$

and

$$(\tilde{h}_{Bxx} - \delta_{R(1)}^{-2}\tilde{h}_B)_{\bar{t}} - \delta^{-1}\,\beta\tilde{h}_{Bx} = 0. \tag{2.14}$$

The variable $\tilde{h}_I$ is an approximate particular solution for the interior baroclinic field forced by a wind stress curl with $\delta_{R(1)} \ll 1$, whereas $\tilde{h}_B$ is an approximate homogeneous solution which is added to $\tilde{h}_I$ so that $\tilde{h}$ satisfies the boundary conditions. Except for very low frequency motion, $\omega \ll \frac{1}{2}\beta\delta_{R(1)}/\delta$, the second term in (2.13) and the last term in (2.14) are small with respect to the other terms, and $\tilde{h}_B$ in (2.14)

represents the interior extension of a coastally trapped internal Kelvin wave. For very low frequency forcing, the third term in (2.11) and the second term in (2.13) balance the wind stress curl, resulting in an interior Sverdrup balance.

Expansions of the form

$$\psi = \psi_0 + \delta\psi_1 + \ldots, \tag{2.15a}$$

$$h = h_0 + \delta h_1 + \ldots, \tag{2.15b}$$

are assumed for the shelf. Since the interface perturbation h over the shelf due to the interior solution will consist of the interior interface deformation at x = 0, $\tilde{h}_{I(0)}$, with a boundary layer correction to satisfy the boundary condition at $\xi = 0$, it is convenient to define a new shelf variable $\hat{h}$, where

$$h = \tilde{h}_{I(0)} + \hat{h}. \tag{2.16}$$

Using (2.5a,b), (2.6a,b), and (2.16), the lowest order equations for the shelf variables become

$$(\psi_{0\xi\xi} - \delta_B^{-1}\psi_{0\xi})_{\bar{t}} - \delta_B^{-1}(\hat{h}_y - f\psi_{0y}) = \delta_B^{-1}(\tau^{(y)}_{(0)} + \tilde{h}_{Iy(0)}) - \delta(\tau^{(y)}_{x(0)} - \tau^{(x)}_{y(0)}) + \beta\psi_{0\xi}, \tag{2.17a}$$

$$(\hat{h}_{\xi\xi} + a\delta_B^{-1}\hat{h}_\xi - (\delta/\delta_R)^{-2}\hat{h})_{\bar{t}} + a\delta_B^{-1}f(\hat{h}_y - f\psi_{0y}) = -a\delta_B^{-1}f(\tau^{(y)}_{(0)} + \tilde{h}_{Iy(0)}) - f\delta(\tau^{(y)}_{x(0)} - \tau^{(y)}_{x(0)}) + \beta\hat{h}_\xi, \tag{2.17b}$$

where $\delta_B^{-1}(\xi) = (H_\xi/H)$ and where $\delta_R^2(\xi) = f^{-2}\,\bar{SH}(\xi)$. The last two terms in (2.17a,b) are $O(\delta/\omega)$ and $O(\beta/\omega)$ with respect to terms on the left hand sides and are neglected in general, except in the limit $\omega \to 0$.

The velocities on the shelf may be obtained for each layer from ψ_0 and $\hat{h}$. They are

$$u_1 = H^{-1} H_1[\psi_{0y} + f^{-2}a^{-1}(f\hat{h}_y + \hat{h}_{\xi\bar{t}}) + (af)^{-1}(\tau^{(y)}_{(0)} + \tilde{h}_{I(0)y})], \quad (2.18a)$$

$$u_2 = H^{-1} H_1[\psi_{0y} - f^{-2}(f\hat{h}_y + \hat{h}_{\xi\bar{t}}) - f^{-1}(\tau^{(y)}_{(0)} + \tilde{h}_{I(0)y})], \quad (2.18b)$$

$$v_1 = (\delta H)^{-1} H_1[-\psi_{0\xi} - (af)^{-1}\hat{h}_{\xi}], \quad (2.18c)$$

$$v_2 = (\delta H)^{-1} H_1[-\psi_{0\xi} + f^{-1}\hat{h}_{\xi}], \quad (2.18d)$$

where (2.5b) has been used in the derivation of (2.18c,d). Eqs. (2.18c,d) imply that the alongshore component of the velocity is in geostrophic balance.

The boundary conditions at the coast ($\xi = 0$), which follow from the requirement that $u_1(\xi = 0) = u_2(\xi = 0) = 0$ and (2.18) are

$$\psi_{0y} = 0 \quad \text{at} \quad \xi = 0, \quad (2.19a)$$

$$f\hat{h}_y + \hat{h}_{\xi\bar{t}} = -f(\tau^{(y)}_{(0)} + \tilde{h}_{I(0)y}) \quad \text{at} \quad \xi = 0. \quad (2.19b)$$

If a Taylor series expansion around $x = 0$ is used for $\tilde{\psi}$, (2.10) and (2.15) may be substituted into the matching conditions (2.9c,d) and terms of the same order may be collected to yield (Allen, 1976b):

$$\tilde{\psi}_{0y}(x = 0) = 0, \quad (2.20a)$$

$$\tilde{\psi}_{0x\bar{t}}(x = 0) = \psi_{0\xi\bar{t}}(\xi = 1), \quad (2.20b)$$

Assuming that a boundary condition for $\tilde{\psi}_0$, similar to (2.20a), holds on the other boundaries of the interior region, the lowest order barotropic motion in the interior may be determined from (2.11), (2.20a), and that condition, and is uncoupled from the shelf motion.

The relations (2.12), (2.15b), and (2.16) are substituted for $\tilde{h}$ and h in (2.9a,b) and a Taylor series expansion around $x = 0$ is utilized for $\tilde{h}_I$ to yield the matching conditions for the perturbation interface, i.e.,

$$\tilde{h}_B(x = \delta) = \hat{h}(\xi = 1), \tag{2.21a}$$

$$\tilde{h}_{Ix}(x = 0) + \tilde{h}_{Bx}(x = \delta) = \delta^{-1}\, \hat{h}_\xi(\xi = 1). \tag{2.21b}$$

The two terms on the left hand side of (2.21b) are retained with the anticipation that, over the total frequency range, either one may be important in balancing the right hand side.

3) The Free Wave Solutions

Before proceeding to the forced problem, it is useful to have an understanding of the unforced or free wave problem. The detailed solutions to (2.17a,b) for the free waves are discussed in Allen and Romea (1980) (henceforth denoted as AR), and only a brief summary will be presented here.

We adopt an f-plane analysis ($\beta = 0$, f = constant), and choose the exponential shelf profile of Buchwald and Adams (1968), i.e.,

$$H = \exp\,[(\xi - 1)/\delta_B]. \tag{3.1}$$

In this case, $H_\xi/H = \delta_B^{-1}$ is a constant. This depth profile, while still highly idealized, is not an unreasonable approximation to actual shelf slope topography.

The equation for the free waves may be written

$$(\psi_{0\xi}/H)_{\xi\bar{t}} + (H_\xi/H^2)(f\psi_{0y} - \hat{h}_y) = 0, \tag{3.2a}$$

$$(\hat{h}_\xi/aH)_{\xi\bar{t}} - (\delta/\delta_R)^2(\hat{h}_{\bar{t}}/H_1) - f(H_\xi/H^2)(f\psi_{0y} - \hat{h}_y) = 0, \tag{3.2b}$$

$$\psi_{0y} = 0, \quad f\hat{h}_y + \hat{h}_{\xi\bar{t}} = 0 \quad \text{at } \xi = 0, \tag{3.3a,b}$$

$$\psi_{0\xi\bar{t}} = 0, \quad \hat{h}_\xi + (\delta/\delta_{R(1)})\hat{h} = 0 \quad \text{at } \xi = 1. \tag{3.4a,b}$$

By multiplying (3.2a) and (3.2b) by, repectively, ψ_0 and $\hat{h}$, integrating the two equations over ξ from 0 to 1, assuming periodicity in y and integrating over a period in y, we obtain an equation for the total energy density:

$$E = \frac{1}{2}\{\int_0^1 [H^{-1}\,\psi_{0\xi}{}^2 + (af^2H)^{-1}\,\hat{h}_\xi{}^2 + (f^2\delta_R^2H_1)^{-1}\,\delta^2\hat{h}^2]d\xi$$

$$+ (\delta_{R(1)}\,a_{(1)}\,H_{(1)}f^2)^{-1}\,\delta\hat{h}(1)^2\}. \tag{3.5}$$

As a result of assumptions (2.5b), all of the coastal trapped waves in the present model are nondispersive. Accordingly, free wave solutions are sought in the form

$$(\psi_0, \hat{h}) = \mathrm{Re}\{\exp[-i\omega(\bar{t} + c^{-1}y)]\ (\phi(\xi), g(\xi))\}, \tag{3.6}$$

where ω is the radian frequency, c is the phase velocity, and Re denotes the real part.

The equations and boundary conditions for the eigenfunctions (ϕ_n, g_n) with corresponding eigenvalues c_n are

$$\phi_{n\xi\xi} - \delta_B^{-1}\phi_{n\xi} + (\delta_B c_n)^{-1}(f\phi_n - g_n) = 0, \tag{3.7a}$$

$$g_{n\xi\xi} + a\delta_B^{-1} g_{n\xi} - (\delta/\delta_R)^2 g_n - a(\delta_B c_n)^{-1} f(f\phi_n - g_n) = 0, \tag{3.7b}$$

$$\phi_n = 0, \quad g_{n\xi} + (f/c_n)g_n = 0 \quad \text{at } \xi = 0, \tag{3.8a,b}$$

$$\phi_{n\xi} = 0, \quad g_{n\xi} + (\delta/\delta_R)g_n = 0 \quad \text{at } \xi = 1. \tag{3.9a,b}$$

The orthogonality relation for the eigenfunctions is

$$f^{-1}\left[\int_0^1 (\delta_B H)^{-1}(f\phi_n - g_n)(f\phi_m - g_m)d\xi + (a_{(0)}H_{(0)})^{-1} g_n(0)\, g_m(0)\right] = \delta_{mn} c_n E_n, \tag{3.10a}$$

where, from (3.5), the energy density for each mode is

$$E_n = \frac{1}{2}\left\{\int_0^1 [H^{-1}\phi_{n\xi}^2 + (af^2H)^{-1} g_{n\xi}^2 + (f^2\delta_R^2 H_1)^{-1}\delta^2 g_n^2]d\xi + (\delta_{R(1)}a_{(1)}H_{(1)}f^2)^{-1}\delta g_{n(1)}^2\right\} \tag{3.10b}$$

The factor on the right hand side of (3.10a) follows from multiplying (3.7a,b) for (ϕ_n, g_n) by, respectively, ϕ_n and g_n, integrating over ξ from 0 to 1 and combining. The result is

$$c_n E_n = H_n = \frac{1}{2} f^{-1}\left[\int_0^1 (\delta_B H)^{-1}(f\phi_n - g_n)^2 d\xi + (a_{(0)}H_{(0)})^{-1} g_{n(0)}^2\right]. \tag{3.11}$$

We may rewrite (3.11) as

$$c_n^{-1} = E_n/H_n. \tag{3.12}$$

Eq. (3.12) represents a variational formulation of (3.7) and (3.8) in the sense that the admissible functions (ϕ_0,g_0) which minimize the quotient E_n/H_n are eigenfunctions for the problem defined by (3.7) and (3.8), and the minimum value is the associated eigenfunction c_0^{-1}. If the orthogonality condition (3.10a) is imposed, the variational formulation results in an increasing sequence of values for c^{-1}, e.g., c_1^{-1} is the minimum of E_n/H_n among functions orthogonal to (ϕ_0,g_0). In addition,

$$\lim_{n \to \infty} c_n^{-1} = \infty, \tag{3.13}$$

and the eigenfunctions (ϕ_n,g_n) form a complete set (Courant and Hilbert, Vol. 1, pp. 412, 424-426). The result (3.13) was demonstrated explicitly in Appendix B of Allen (1975).

Similar variational principles are obtained by Clarke (1976) and Huthnance (1978) in connection with the eigenvalue problem for coastal trapped waves in a continuously stratified fluid. One additional consequence of (3.12) (also reported by Clarke and Huthnance) is that for monotonic H, the right hand side of (3.12) is positive definite and all free waves propagate poleward (toward -y).

While (3.7b) and (3.9b) have non-constant coefficients, if we assume that

$$a_{(0)} = H_1/H_{2(0)} << 1, \tag{3.14}$$

(3.7a,b), (3.8a,b), and (3.9a,b) may be solved by perturbation methods, as in AR. The eigenfunctions consist of an infinite set of "shelf wave" (SW) solutions (ϕ_n,g_n), $(n = 1,2,\ldots)$, and a single internal Kelvin

wave (IKW) solution (ϕ_0, g_0). At mid-latitudes, $\delta_R/\delta \ll 1$, the SW modes are barotropic and have offshore structures which are essentially those found for barotropic continental shelf waves in an unstratified ocean. For $\delta_R/\delta \gg 1$, the SW modes are "bottom trapped," i.e., all their motion is confined to the lower layer. The IKW mode is baroclinic and has an offshore structure and wave speed similar to that obtained for a flat bottom internal Kelvin wave. In this case, however, there is a barotropic contribution to the onshore velocities from ϕ_0.

The phase speed c_0 of the IKW mode is independent of f while the SW mode phase speeds depend on f. Estimates of c_0 and c_1 (the first SW mode) are calculated in Appendix B of AR for the Pacific coast of South America. For latitudes less than 5°S, $c_0 \gg c_1$, i.e., the IKW mode travels faster than the first SW mode, while for mid-latitudes, $c_0 \ll c_1$, i.e., the first SW mode travels faster than the IKW mode. The two wave modes have the same phase speeds at a latitude of about 10°S.

For parameter values where the wave speeds of the IKW mode and a SW mode are nearly equal, i.e., where $c_0 \approx c_n$, there is a coupling between the two types of wave modes. A plot of the phase speeds for the first three eigenfunctions as a function of δ_R/δ is shown in Figure 1. As is indicated by the behavior of the wave speeds as a function of δ_R/δ, the mode which is originally an IKW becomes a first SW mode, and vice versa. At a larger value of δ_R/δ, a similar behavior occurs for the IKW and second SW modes.

Note that, while the parameter δ_R/δ varies strongly with latitude, it is also a function of shelf width, so it is possible, for example, for δ_R/δ to be small at low latitudes for a very wide shelf.

4) Solutions via a Cross Shelf Modal Analysis

Solutions to the shelf equations (2.17a,b), with the boundary conditions (2.19a,b), (2.20b), and (2.21a,b) may be obtained for a coastal wind stress with a general $(y, \bar{t})$ structure by expanding the shelf variables in terms of the cross shelf eigenfunctions of the unforced equations.

As in Section 3, an f-plane analysis is employed here and the assumptions in Section 2 (2.5a,b) are retained.

In a manner similar to (2.16) for h_0, we define

$$\psi_0 = \hat{\psi} + \tilde{\psi}_{x(0)} \int_0^{\xi} H(\xi')d\xi'. \tag{4.1}$$

The last term in (4.1) represents the extension of the interior alongshore velocity at $x = \delta$ onto the shelf topography.[1]

With (4.1), the governing equations for the shelf variables (2.17a,b) are

$$(\hat{\psi}_{\xi\xi} - \delta_B^{-1}\hat{\psi}_{\xi})_{\bar{t}} - \delta_B^{-1}(\hat{h}_y - f\hat{\psi}_y) = \delta_B^{-1}F, \tag{4.2a}$$

$$(\hat{h}_{\xi\xi} + a\delta_B^{-1}\hat{h}_{\xi} - (\delta/\delta_R)^2\hat{h})_{\bar{t}} + fa\delta_B^{-1}(\hat{h}_y - f\hat{\psi}_y) = -a\delta_B^{-1}fF, \tag{4.2b}$$

where

$$F(\xi,y,\bar{t}) = \tau^{(y)}_{(0)} + \tilde{h}_{I(0)y} + f\tilde{\psi}_{x(0)y} \int_0^{\xi} H(\xi')d\xi'. \tag{4.2c}$$

The boundary conditions at the coast are

$$\hat{\psi}_y = 0 \quad \text{at} \quad \xi = 0, \tag{4.3a}$$

$$\hat{h}_{\xi\bar{t}} + f\hat{h}_y = -fF_{(0)} \quad \text{at} \quad \xi = 0. \tag{4.3b}$$

[1] In Allen (1976b) the substitution $\psi_0 = \hat{\psi} + \xi\tilde{\psi}_{x(0)}$ was used. This represents an extension of the interior alongshore transport onto the shelf. The definition (4.1) turns out to be more appropriate.

The solution to (2.14) (with $\beta = 0$) is:

$$\tilde{h}_B(x,y,\bar{t}) = C_0(y,\bar{t}) \exp(-x/\delta_{R(1)}). \tag{4.4}$$

This solution may be used in (2.21a,b) to derive the boundary condition on $\hat{h}$ at $\xi = 1$. The boundary condition at $\xi = 1$ for $\hat{\psi}$ may be derived by introducing (4.1) into (2.20b). These conditions are

$$\hat{\psi}_{\xi\bar{t}} = 0 \quad \text{at} \quad \xi = 1, \tag{4.5a}$$

$$\hat{h}_\xi + (\delta/\delta_{R(1)})\hat{h} = 0 \quad \text{at} \quad \xi = 1, \tag{4.5b}$$

where the term $\tilde{h}_{Ix(0)}$ is neglected relative to $\delta_{R(1)}^{-1}\tilde{h}_{Bx}(x = 0)$ and $\delta^{-1}\hat{h}_\xi(x = 0)$ in (2.21b), and where we use, from (2.21a),

$$\hat{h}(\xi = 1) = \tilde{h}_B(x = \delta) = C_0 \exp(-\delta/\delta_{R(1)}). \tag{4.6}$$

This relation may be used to calculate C_0 and hence $\tilde{h}_B$, after a solution is obtained for $\hat{h}$.

We now expand the shelf variables in terms of the eigenfunctions of the unforced problem, i.e.,

$$[\hat{\psi}(\xi,y,\bar{t}),\ \hat{h}(\xi,y,\bar{t})] = \sum_{m=0}^{\infty} [\phi_m(\xi),\ g_m(\xi)]Y_m(y,\bar{t}). \tag{4.7}$$

The series in (4.7) is summed over the single IKW pair $(\phi_0,\ g_0)$ and all the SW pairs $(\phi_n,\ g_n)$, $(n = 1,2,\ldots)$. The expansions (4.7) for $\hat{\psi}$ and $\hat{h}$ are substituted into the shelf equations (4.2a,b) and the forced boundary condition at $\xi = 0$ (4.3b). If (4.2a,b) are multiplied by $(\phi_m,\ g_m)$ respectively, integrated with respect to ξ from 0 to 1, and are combined in a suitable manner with (4.3b) and the orthogonality relation (3.6), a forced first order wave equation is obtained for the $(y,\bar{t})$ structure of each mode (Gill and Clarke, 1974; Clarke, 1977), i.e.,

$$c_m^{-1}Y_{m\bar{t}} - Y_{my} = -T_m(y,\bar{t}), \tag{4.8}$$

where

$$T_m(y,\bar{t}) = f^{-1}\Big[\int_0^1 (\delta_B H)^{-1}\,(f\phi_m - g_m)F d\xi$$

$$- (a_{(0)}H_{(0)})^{-1}\, g_{m(0)}F_{(0)}\Big], \qquad (4.9)$$

$T_m(y,\bar{t})$ contains two terms; one is integrated over the shelf and one is evaluated at the coast.

Two separate types of forcing contribute to F, i.e.,

$$F(\xi,y,\bar{t}), = \Phi + \hat{\tau}, \qquad (4.10)$$

where

$$\Phi(\xi,y,\bar{t}) = f\tilde{\psi}_{xy(0)} \int_0^{\xi} H(\xi')d\xi', \qquad (4.11a)$$

$$\hat{\tau}(y,\bar{t}) = \tau_{(0)}^{(y)} + \tilde{h}_{I(0)y}. \qquad (4.11b)$$

The alongshore component of the wind stress at the coast and the baroclinic interior flow force motion on the shelf through the boundary condition at $\xi = 0$ and always appear together, while Φ, the effect of the interior barotropic flow, depends on ξ and vanishes at the coast ($\Phi(0) = 0$; $F(0) = \hat{\tau}$). For $(\delta_R/\delta) \ll 1$, $\hat{\tau}$ forces the IKW response mainly through the boundary term in (4.9), since g_0 decays rapidly from the coast and the contribution from the integral in (4.9) is small. The SW response arises predominantly from the integrated term in (4.9) which represents the cross-shelf bottom velocity u_2. For $(\delta_R/\delta) \ll 1$, an offshore barotropic flow interacting with a shelf-slope topography can force a SW response in this manner.

In order to examine the relative efficiency of excitation of the various modes by both $\tau_{(0)}^{(y)}$ and Φ we use (3.5), (3.10), (4.8) and (4.9) to calculate the total energy density E_m of the lower modes. Approximate

expressions for Y_m may be obtained for short time by solving (4.8) as an initial value problem with initial condition

$$Y_m\ (y,\bar{t} = 0) = 0. \tag{4.12}$$

For this case, the balance in (4.8) is $Y_{m\bar{t}} \approx - c_m T_m$, and

$$E_m \approx \frac{1}{2} \{ \int_0^1 [H^{-2}\ \phi_{m\xi}{}^2 + (f^2 aH)^{-1}\ g_{m\xi}{}^2 + (\delta/\delta_R)^2\ H_1^{-1}\ g_m{}^2] d\xi$$

$$+ (\delta/\delta_R)(a_{(1)}H_{(1)}f)^{-1}\ g_{m(1)}{}^2 \}\ T_m{}^2 c_m{}^2 \bar{t}^2. \tag{4.13}$$

Figures 2 and 3 show the energy density (divided by $\bar{t}^2$) of the first several modes, forced by $\hat{\tau}$ and Φ, respectively, as a function of δ_R/δ. As in Fig. 1, we use the solutions derived in AR for $a_{(0)} << 1$. The mode which, for $\delta_R/\delta << 1$ is an IKW, is labelled E_1, while the mode which is a first mode SW is labelled E_2. The interaction (see Fig. 1) between E_1 and E_2 occurs at $\delta_R/\delta = 0.43$. For $\delta_R/\delta << 1$, E_1 is a first mode SW. E_2 interacts at $\delta_R/\delta = 0.11$ with E_3 (the second mode SW). Poleward of this interaction, E_3 is an IKW and E_2 is a second mode SW.

Without solving the interior problem for $h_{I(0)y}$ and $\tilde{\psi}_{x(0)}$, the relative importance of driving by $\hat{\tau}$ and Φ cannot be deduced, and we defer a discussion of this subject until Section 5. However, several points can be made from Figs. 2 and 3, together with our understanding of the eigenfunctions discussed in Section 3.

Forcing by $\hat{\tau}$ for $\delta_R/\delta << 1$ results in an IKW response which is confined within δ_R/δ of the coast and a set of barotropic SW modes which extend over the shelf. This implies that it is possible for interior baroclinic motions to drive barotropic motions on the shelf, although estimates using typical parameter values give $|\tau^{(y)}_{(0)}| >> |\tilde{h}_{I(0)y}|$. For $\delta_R/\delta >> 1$ the response to $\hat{\tau}$ consists of a baroclinic IKW mode which decays slowly into the interior and a set of "bottom trapped" SW modes.

Hence, forcing by a surface wind stress or interior baroclinic motion yields a SW response on the shelf which is bottom intensified.

Fig. 2 shows that, for $\delta_R/\delta >> 1$ and forcing by $\hat{\tau}$, E_1 (the IKW) is very efficiently excited, while E_2 (the bottom trapped first mode SW) is not very energetic. For latitudes less than 5°, the SW response is negligible. For $\delta_R/\delta << 1$, E_3 (the IKW) and E_1 (the first mode SW) are both excited, with the IKW more energetically forced than the SW. If kinetic energy density (not shown in Fig. 2) is considered instead of total energy density, the IKW mode, with $a_{(0)} = 0.3$, is less energetic than the first mode SW for $\delta_R/\delta > 0.15$, i.e., for latitudes >40°.

Note that, for a completely two-dimensional response, the dependence of h and ψ on y vanishes and (4.2a,b) uncouple. Forced solutions may be directly obtained and may be used in (4.13) to derive the total energy density which is also shown in Fig. 2. The response will consist of an infinite sum of modes and the total energy of the response, of course, will be higher than that of the first two modes alone. Note, however, that the first two modes contain most of the energy.

The barotropic interior forcing excites an IKW response and a SW response on the shelf. Fig. 3 shows that both the IKW and the SW responses are not forced efficiently for $\delta_R/\delta >> 1$. For mid-latitudes, the IKW response (E_2) is not forced efficiently, while the first mode (barotropic) SW is relatively energetic.

Examples

It is useful to consider some simple solutions to (4.8). We focus only on driving by the alongshore component of the wind stress at the coast ($F = \tau^{(y)}_{(0)}(y,\bar{t})$), so that (4.8), (4.9) and (4.12) are

$$c_m^{-1} Y_{m\bar{t}} - Y_{my} = -b_m \tau, \tag{4.14a}$$

$$b_m = f^{-1} \int_0^1 (\delta_B h)^{-1} (f\phi_m - g_m) d\xi - (afH_{(0)})^{-1} g_{m(0)}, \tag{4.14b}$$

$$\sum_{m=0}^{\infty} (f\phi_m - g_m) b_m = 1, \tag{4.14c}$$

$$Y_m(y, \bar{t} = 0) = 0. \tag{4.14d}$$

In the following examples, we concentrate on the qualitative differences between the results at mid and low latitudes. (Examples at mid-latitude have been discussed by Allen [1976a].)

We first examine a simple impulsive wind stress with a limited alongshore extent, i.e.,

$$\tau(y, \bar{t}) = \delta(\bar{t}) T(y), \tag{4.15}$$

where, e.g.,

$$T(y) = \tau_0 \exp(-y^2/2). \tag{4.16}$$

The solution to (4.14a) with a wind stress given by (4.15) and (4.16) is

$$Y_m = -c_m b_m T(y - c_m \bar{t}). \tag{4.17}$$

This solution corresponds to a response of limited extent propagating in the negative y direction (poleward) with speed c_m, for each mode. At low latitudes, the IKW response propagates relatively quickly away from the forcing region, while the bottom trapped SW modes, whose phase speeds c_n are small compared with c_0, remain behind. This behavior can result in bottom intensified undercurrents over the continental slope.

We now consider an alongshore wind stress of the form

$$\tau(y, \bar{t}) = H(\bar{t}) T(y), \tag{4.18a}$$

where $H(\bar{t})$ is the Heaviside unit function. Here, for simplicity in

illustrating the features of the solution (Allen, 1976a) we use the "top hat" function

$$T(y) = \begin{cases} 0 & 0 < y, \\ \tau_0 & -|y_0| < y < 0 \\ 0 & y < -|y_0| \end{cases} \qquad (4.18b)$$

The solution for Y_m as a function of y for various times is shown in Fig. 4. This solution is obtained by the method of characteristics in Allen (1976a). For the purely baroclinic problem, Y_0 is the interface height at the coast, while for the purely barotropic problem Y_n gives the (y,t) structure in the expansion of the mass transport streamfunction in terms of the free shelf wave eigenfunctions.

The initial response, for $-|y_0| < y < -c_m\bar{t}$, is time dependent and two-dimensional ($Y_{my} = 0$). The three-dimensional flow pattern develops as a free IKW front and a set of SW fronts are generated and propagate poleward (toward negative y). For $c_m\bar{t} > |y_0|$, a region where Y_m is constant and where the alongshore velocity associated with a particular mode m is in steady geostrophic balance exists between the time dependent free wave front and the location of forcing, i.e., in $-c_m\bar{t} < y < -|y_0|$. A steady state is achieved at a given y as $\bar{t} \to \infty$ after the free wave fronts associated with every mode have propagated past that location.

The two-dimensional flow pattern which results from the impulsive application of τ_0 in the region $-|y_0| < y < 0$ consists of an offshore flow u_E in the surface Ekman layer which is balanced by an inviscid onshore flow u_I toward the coast in the same cross-shelf plane. For the mid-latitude case $\delta_R/\delta \ll 1$, the onshore flow u_I is depth independent over most of the shelf. Within a distance δ_R/δ from the coast the flow also has a baroclinic component and the interface rises. At $\xi = 0$, a

mass flux equal to the offshore Ekman transport is fed into the surface Ekman layer from the upper layer interior and the lower layer onshore flux is zero.

For $\delta_R/\delta >> 1$, the two-dimensional picture is much the same except that the baroclinic component of the flow becomes important farther offshore and the flow is surface intensified over the shelf with a weak onshore velocity component in the lower layer. As a result the bottom trapped shelf waves are not efficiently excited, as is evident in Fig. 2.

In order to describe the three-dimensional flow field, we utilize (4.7) in (2.18a-d) to obtain expressions for the velocities. In particular,

$$fu_1 = (H_1/H)a^{-1}\{\tau_0 + \sum_{m=0}^{\infty}[(af\phi_m + g_m)Y_{my} + f^{-1}g_{m\xi}Y_{m\bar{t}}]\}, \qquad (4.19a)$$

$$fu_2 = (H_1/H)\{-\tau_0 + \sum_{m=0}^{\infty}[(f\phi_m - g_m)Y_{my} - f^{-1}g_{m\xi}Y_{m\bar{t}}]\}. \qquad (4.19b)$$

The steady solution, with $Y_{m\bar{t}} = 0$, $Y_{my} = b_m\tau_0$ and with (4.14c), is

$$fu_1 = (H_1/H)(1 + a)a^{-1}\sum_{m=0}^{\infty} f\phi_m b_m \tau_0, \qquad (4.20a)$$

$$fu_2 = 0. \qquad (4.20b)$$

When $Y_{m\bar{t}} = 0$, we may write

$$Y_m = b_m \int_0^y \tau dy. \qquad (4.21)$$

Utilization of (4.14c), (4.21), and (4.7) in (2.18d) yields the result that $v_2 = 0$. Hence for all δ_R/δ the final steady solution over the slope has no motion in the lower layer.

The cross-shelf eigenfunctions obtained in AR and discussed in Section 3 of this paper may be used to examine the steady flow field in the upper layer. With $a_{(0)} << 1$, the IKW solution for g is

$$g_0 \simeq \exp(-\delta\xi/\delta_R), \tag{4.22}$$

while, for the SW modes

$$g_n = O(a_{(0)}). \tag{4.23}$$

From (2.18), (4.7), (4.14), (4.22), and (4.23), u_1 and v_1 may be expressed as

$$fu_1 \simeq \tau_0[1 - \exp(-\delta\xi/\delta_R)] + O(a), \tag{4.24}$$

$$fv_1 \simeq \delta^{-1} \exp(-\delta\xi/\delta_R) \int_0^y \tau dy + O(a). \tag{4.25}$$

Eqns. (4.24) and (4.25) show that baroclinic processes bring u_1 to zero at $\xi = 0$ within a scale of δ_R/δ, and that the final steady alongshore flow in the upper layer is confined to a region with an offshore scale of the Rossby radius (this result and the limiting behavior $u_2, v_2 \to 0$ was not pointed out in Allen [1976a]).

The flow pattern that develops at mid-latitudes is different from that at low latitudes and we will briefly discuss each case. The qualitative discussion given here can be easily verified using the approximate solution for the eigenfunctions given in AR for a "weak slope" and with the assumption $a_{(0)} << 1$.

For mid-latitudes, the Rossby radius is a fraction of the shelf width. The SW modes are barotropic and the first several modes, which represent a dominant portion of the total SW response (see Fig. 2), have phase speeds which are faster than the IKW mode phase speed. For simplicity, we assume that all the SW modes move faster than the IKW mode.

Fluid is drawn onshore in a region near each SW front and the region of onshore flow to the shelf-slope region propagates poleward with the SW phase speed. (The region of dominant onshore flow occurs in connection with the first mode SW and propagates poleward with the first mode SW phase speed.) The solution for increasing $\bar{t}$, as the first several SW modes achieve a steady balance but before the IKW front has propagated away from the forcing region, consists of an equatorward barotropic alongshore current which is asymptotically confined to a distance δ_R/δ of the coast as $\bar{t} \to \infty$. This is shown schematically in Fig. 5. The current connects the locations where fluid is drawn onto the slope to the region of forcing. The IKW front propagates into this barotropic current, leaving behind a final steady solution having velocities in the lower layer equal to zero and an upper layer flow confined within a baroclinic radius of deformation of the coast. This upper layer flow is turned in the region of forcing and is fed horizontally to the coast to satisfy the boundary condition at $\xi = 0$.

At low latitudes, the IKW mode has a large offshore scale with respect to the shelf width and propagates poleward with a much faster speed than the SW modes which are bottom trapped. A schematic of the flow field for low latitudes is shown in Fig. 6. When the IKW mode has propagated away from the forcing region, the onshore flow in the bottom layer turns poleward in a broad region within δ_R/δ of the coast. The velocity in the bottom layer is poleward up to the location of an IKW front, where the density interface moves vertically upward (Allen, 1976a). The corresponding return flow in the top layer, from the location of the wave front to the region where the stress acts, is turned and fed horizontally to the coast, and, together with a component of the flow

which comes directly onshore in the upper layer, is fed into the surface Ekman layer at $\xi = 0$. The SW modes are forced by the stress driven onshore flow in the lower layer and respond such that the location of the onshore flow to the slope in the lower layer propagates poleward. The velocities in the lower layer behind the region of onshore flow for all the modes are zero. This implies that, for steady forcing of limited extent at low latitudes, the upper layer will assume a steady flow relatively quickly, while the lower layer will be time dependent, adjusting slowly toward a steady state with zero motion in the lower layer over the slope as each bottom-trapped SW mode propagates away from the region of forcing. In addition, Fig. 6 shows that, as the flow field develops, water is drawn onto the slope at different alongshore locations in the upper and lower layers.

As a final example, we examine forcing by a standing wave, given by

$$\tau = \tau_0 \cos \ell y \cos \omega \bar{t}, \tag{4.26}$$

where τ_0 is a constant. For $c_m >> (\omega/\ell)$, the balance in (4.14a) is approximately steady, i.e.,

$$Y_{my} = b_m \tau, \tag{4.27}$$

while for $c_m << (\omega/\ell)$, the balance is time dependent and locally two-dimensional, i.e.,

$$-c_m^{-1} Y_{m\bar{t}} = b_m \tau. \tag{4.28}$$

For (ω/ℓ) in the range $c_0 >> (\omega/\ell) >> c_n$ the balance in (4.28) applies to the time dependent solutions Y_n for the SW modes at low latitudes, while (4.27) is the approximate balance for the more rapidly propagating IKW mode.

These solutions are

$$Y_0 = b_0 \ell^{-1} \tau_0 \cos(\ell y - \tfrac{1}{2}\pi) \cos\omega\bar{t}, \qquad (4.29a)$$

$$Y_n = -b_n (c_n/\omega) \tau_0 \cos\ell y \cos(\omega\bar{t} - \tfrac{1}{2}\pi). \qquad (4.29b)$$

Since the shelf wave modes are bottom trapped, the (y,t) behavior of v_1 will be governed by Y_0 whereas that of v_2 will depend on a sum involving Y_0 and Y_n. This will lead to phase differences between v_1 and v_2 and therefore the flow will have a depth dependent phase relation with τ.

With an IKW speed $c_0 \approx 200$ km/day (Smith, 1978), an estimated first mode wave speed $c_1 \approx 25$ km/day (AR), and wind stress forcing with wavelength $\approx$1000 km, the solutions (4.29a,b) are valid for wind stress forcing with period in the range 5 days < T < 40 days.

5) Sinusoidal Forcing

We now consider solutions for the interior and shelf motion when the wind stress has a sinusoidal dependence on time and on the horizontal spatial coordinates, i.e.,

$$(\tau^{(x)}, \tau^{(y)}) = \mathrm{Re}\{T_0 \exp[-i(\omega\bar{t} - kx - \ell y)]\}, \tag{5.1}$$

so that the wind stress curl becomes

$$\tau_x^{(y)} - \tau_y^{(x)} = \mathrm{Re}\{imT_0 \exp[-i(\omega\bar{t} - kx - \ell y)]\}, \tag{5.2}$$

where

$$m = k - \ell, \quad \omega > 0. \tag{5.3a,b}$$

We look for interior and shelf solutions of the form

$$(\tilde{\psi}_0, \tilde{h}_0, \psi_0, \hat{h}) = \mathrm{Re}\{[\tilde{\phi}(x), \tilde{g}(x), \phi(\xi), \hat{g}(\xi)] \exp[-i(\omega\bar{t} - \ell y)]\}. \tag{5.4}$$

Equations for $\tilde{\phi}$ and $\tilde{g}$ may be obtained by substituting (5.4) in (2.11), (2.13) and (2.14) while equations for the shelf variables may be obtained by utilizing (5.4) in (2.17a,b) (Appendix A). As in Section 4, the shelf equations are forced at the boundary $\xi = 0$ by $\tau_{(0)}^{(y)}$ and by interior baroclinic wind forced motions. In addition, interior wind forced barotropic motion $\tilde{\phi}$ drives a flow on the shelf through the boundary condition at $\xi = 1$ (A13c). Expressions for the interior motions are presented in Appendix A (A1-A4), and $\tilde{\phi}_{x(0)}$, the relevant expression for interior barotropic forcing at $\xi = 1$ is given by (A7). In general, $\tilde{\phi}_{x(0)}$ is complex and the shelf circulation due to $\tilde{\phi}$ will have components both in phase and out of phase with $\tau_{(0)}^{(y)}$. Examination of the forcing terms in (A12a,b) and (A13b) indicates that the response over the shelf due to $\tau_{(0)}^{(y)}$ is $\frac{\pi}{2}$ out of phase with the wind.

Fig. 7 shows the absolute value of $\tilde{\phi}_{x(0)}$ scaled by T_0/ω for various k/ℓ as a function of inverse frequency scaled as $\beta(2\omega\delta\ell)^{-1}$. Fig. 8

shows the phase of $\tilde{\phi}_{x(0)}$. For $\ell >> k$ (alongshore traveling wind) the phase relation between components driven by $\tilde{\phi}_{x(0)}$ and $\tau^{(y)}_{(0)}$ changes considerably as a function of ω, with these components being $\frac{\pi}{2}$ out of phase for $\beta(2\omega\delta\ell)^{-1} << 1$ and in phase for $\beta(2\omega\delta\ell)^{-1} \simeq 1$. For $k >> \ell$ (onshore traveling wind) the phase difference is $\simeq\frac{\pi}{2}$. Therefore, motions on the shelf driven by $\tilde{\phi}$ and $\tau^{(y)}_{(0)}$ will exhibit a phase relation which is dependent on the frequency and wavenumbers of the wind.

a) Forced coastally trapped waves

In Appendix A it is shown that for forcing at moderate frequency (A5a,b) (e.g., $T' < 60$ days for oceanic parameters at 6° latitude off the west coast of South America) the interior baroclinic forcing term is negligible compared to T_0 (A15) and hence is neglected in the calculated examples below. Also, the interior barotropic forcing is given by the approximate form (A8a)

$$\tilde{\phi}_{x(0)} \simeq T_0/\omega. \tag{5.5}$$

The validity of this approximation for forcing at moderate frequencies is also discussed in Appendix A.

With (A5a,b), the equations for the shelf variables are given by (A12a,b) and solutions which represent coastally trapped waves may be obtained by perturbation methods for $a_{(0)} << 1$ using an exponential slope topography (Appendix B). These solutions are presented in Figs. 9-11 with $T_0 = 1$, where the figures show the contributions of forcing by the wind stress at $\xi = 0$ and by interior barotropic motions at $\xi = 1$. The parameters we vary are δ_B, δ_R/δ, and ℓ/ω. Figs. 9 and 10 represent solutions for $\ell > 0$. We choose $a_{(0)} = 0.3$ (the results are relatively insensitive to the value of $a_{(0)}$ in the range $0.05 < a_{(0)} < 0.3$). As

indicated above, the forcing in (A12a,b) and (A13b,c) appears as T_0/ω, if ℓ/ω is regarded as a parameter. Accordingly, the velocities in Figs. 9-11 have been rescaled with ω, i.e.,

$$V_i = v_i\omega, \quad i = 1,2. \tag{5.6}$$

Note that, in comparing solutions at different latitudes (i.e., different δ_R/δ), ℓ/ω contains a factor of f_0, and ℓ/ω corresponding to a wave with a certain period and wavelength will vary with f_0 (e.g., in Figs. 9a,b a wave with period $T' = 10$ days and wavelength $\lambda' = 1000$ km corresponds to $\ell/\omega \simeq 16$ for $\delta_R/\delta = 0.05$ and $\ell/\omega \simeq 0.4$ for $\delta_R/\delta = 2.0$).

Figs. 9a and 9b show V_1 and V_2 on the shelf ($0 \leq \xi \leq 1$) for $\delta_R/\delta = 0.05$ and $\delta_R/\delta = 2.0$ respectively. The subscripts τ and Φ refer to forcing by $\tau^{(y)}_{(0)}$ and interior barotropic motions, respectively. The phase relation between $V_{(\Phi)}$ and τ may be obtained from Fig. 8 with $\beta = 0$. Fig. 9a is the mid-latitude case and, except on the inner shelf, the flow is barotropic. The highly baroclinic region near $\xi = 0$ is due to the forced internal Kelvin wave which decays rapidly away from the coast. The interior motion forces a non-negligible barotropic shelf response, which is confined to the outer slope. This behavior is evident in the approximate solutions (B10a,b) given in Appendix B for $\delta_R/\delta \ll 1$.

Fig. 9b shows V_1 and V_2 for the low latitude case ($V_{1(\tau)}$ is rescaled for ease in plotting). These solutions are qualitatively very different from the mid-latitude response, due to the increased decay scale for baroclinic motions at low latitudes, and to the increased coupling between the equations (A12a,b) for the shelf variables. For low latitudes, the response over the entire shelf-slope region is highly baroclinic. V_1 is dominated by the forced internal Kelvin wave. This is evident in Fig. 9b, where V_1 decays with $\exp(-\xi\delta/\delta_R)$ with only a slight

modification due to other terms. This behavior may be seen in the approximate solution (B11a,b) given in Appendix B for $\delta_R/\delta >> 1$, where the contribution to the alongshore velocity in the upper layer due to $\hat{\phi}_0$ is cancelled by the O(a) correction to $\hat{g}$. This is equivalent to bottom trapping of the modal SW forced response at low latitudes. Similar qualitative behavior was obtained by Clarke (1976) with a step shelf topography. For $\delta_R/\delta >> 1$, $V_{2(\Phi)} \geq V_{2(\tau)}$ over the whole shelf region. Similar behavior is evident in the low latitude approximate solution (B11b), where $v_{2(\tau)}$ is $O(\delta_R/\delta)$ while $v_{2(\Phi)}$ is O(1). Note also that $v_{2(\tau)}$ is relatively large near the shelf edge and decreases toward mid-shelf.

A dependence on latitude is also evident in Figs. 10a-d where solutions have been plotted for $\delta_R/\delta << 1$ (10a,c) and $\delta_R/\delta >> 1$ (10b,d) for various (ω/ℓ). $V_{1(\tau)}$ decays away from $\xi = 0$ with $\exp(-\xi\delta/\delta_R)$ in all cases. For $\delta_R/\delta = 0.1$, the decay is rapid, and the response is confined to the near-shore region. As δ_R/δ becomes larger, the baroclinic decay scale increases, and the response extends across the entire shelf-slope region into the interior.

Figs. 10b,d illustrate the growing importance of $V_{2(\Phi)}$ with respect to $V_{2(\tau)}$ as δ_R/δ increases. Near $\xi = 1$, $V_{2(\Phi)}$ dominates for all δ_R/δ. For $\delta_R/\delta << 1$, the wind forced motion is the dominant response for $\xi < 0.5$. For $\delta_R/\delta = 2.0$, $|V_{2(\Phi)}| > |V_{2(\tau)}|$ over the entire shelf-slope region.

We may examine the behavior of the exponential slope solutions given in Appendix B as a function of ω, keeping in mind the conditions (A5a,b) required to preserve their validity. In particular, for $\gamma^2 \approx \ell(\omega\delta_B)^{-1} >> 1$, $\gamma >> \delta/\delta_R$, approximate solutions for the shelf velocities

with low frequency forcing are given in Appendix B (B12a-c). The contribution to v_1 due to $\hat{\phi}$ is cancelled by part of the O(a) correction to $\hat{g}$, which is equivalent to bottom trapping of the modal SW solutions when their cross-shelf scale is much less than the Rossby radius. The contribution to v_2 due to $\hat{g}_0$ is cancelled by part of $\hat{\phi}$, which implies that the IKW response becomes surface trapped for forcing at low frequency. V_1 is due entirely to the IKW response with offshore Rossby radius scale and $v_{2(\tau)}$ and $v_{2(\Phi)}$ are confined within boundary layers of width $\gamma^{-1}(<<\delta_R/\delta)$ and decay rapidly away from $\xi = 0$ and $\xi = 1$, respectively. Wind forced and interior barotropic motions penetrate less effectively onto the shelf in the lower layer as ω becomes small, reflecting the reluctance of low frequency motions to cross contours of constant depth.

Several of the qualitative features of (B12a-c) are evident in Figs. 10b,d. For both $\delta_R/\delta >> 1$ and $\delta_R/\delta << 1$, $V_{2(\phi)}$ exhibits a decreased penetration onto the shelf, and becomes more important with respect to $V_{2(\tau)}$, as ω/ℓ decreases.

It is evident from (B12a-c) that as $\omega \to 0$, interior barotropic motions do not penetrate onto the slope and $v_{2(\tau)} \to 0$, which implies that for nearly steady forcing there is no motion in the lower layer. This corresponds to the limiting steady solution as $\bar{t} \to \infty$ for "top hat" forcing (4.18), given in the modal analysis of Section 4.

The case $\ell < 0$ is more difficult to interpret due to the fact that the wind forcing can resonate with the free wave solutions. Fig. 11 is a plot of $V_1(0)$ for $\ell > 0$ and $\ell < 0$ as a function of $\ell/\omega(\delta_R/\delta = 0.1)$, and clearly shows the resonance with the free internal Kelvin wave mode for $\ell/\omega = \delta/\delta_R = 10$. There is a π phase shift as ℓ/ω passes through the resonance.

In addition to the above resonance, free barotropic continental shelf waves over an exponential shelf will resonate with the wind forcing ($\ell < 0$) when γ satisfies (see Appendix B)

$$\tan\gamma = -2\delta_B\gamma \tag{5.7}$$

where γ is given by (B5e). With $\delta_B = 0.33$, $a = 0.1$, the first three resonance points are $(\ell/\omega)_1 \simeq 2.33$, $(\ell/\omega)_2 \simeq 9.04$, and $(\ell/\omega)_3 \simeq 22.09$.

b) Very low frequency behavior

The cases (A6a,b) and (A10a) where $\tilde{g}_I$ and $\tilde{g}_B$ are given by (A6c,d) respectively, and where $\tilde{\phi}_{x(0)}$ is given by (A10b) correspond to forcing at very low frequency ($T' > 60$ days). The approximate O(1) motion in the interior consists of a Sverdrup balance in the upper layer which extends onto the shelf and no motion in the lower layer.

The alongshore coastal wind stress and interior baroclinic motions force an internal Rossby wave which propagates into the interior (Anderson and Gill, 1975).

The transition from a coastally trapped internal Kelvin wave to a westward propagating internal Rossby wave as the forcing frequency is lowered may be seen in the expression for R in (A4b). For $(\delta/\delta_R)^2 > (\frac{1}{2}\beta/\omega)^2$, the solution is coastally trapped with an oscillatory character. As $(\frac{1}{2}\beta/\omega)^2 \to (\delta/\delta_R)^2$ the trapping scale grows, until $(\frac{1}{2}\beta/\omega)^2 \geq (\delta/\delta_R)^2$ and the solution is no longer coastally trapped.

6) Summary

The main question we pose in the introduction is: what is the response on a continental shelf and slope to direct wind stress forcing and to forcing by interior motions, and how does this response vary with latitude? The simple theory presented here provides some answers to this question, and gives some insight for further observational and theoretical work.

In Section 2, it was shown that motions in the shelf-slope region are coupled to those in the interior ocean. The cross-shelf modal analysis of Section 4 clearly shows forcing of shelf circulations by interior barotropic and baroclinic flow. The modal solutions of Section 4 exhibit a dependence of the cross-shelf and vertical structure on latitude. At mid-latitudes, the barotropic (shelf wave) response extends over the shelf, while the baroclinic (internal Kelvin wave) response is confined to a region of width $\delta_R/\delta << 1$ near the coast. At low latitudes, the response is highly baroclinic over the entire shelf, reflecting the relatively large size of the baroclinic boundary layer. The shelf wave response is bottom intensified for low latitudes. This depth dependence, coupled with the fact that, for low latitudes, the internal Kelvin wave speed is larger than the $n = 1$ shelf wave speed, yields a different qualitative time dependent response to wind stress forcing than that obtained for mid-latitudes. With a constant wind stress forcing which is switched on at $t = 0$ and which has a limited extent in y (i.e., a "top hat" function), the upper layer assumes a steady flow relatively quickly with an offshore scale given by δ_R/δ, while the lower layer remains time dependent, adjusting slowly toward a steady state of no motion.

Using the modal solutions of Section 4 and the energy density of each forced mode, we obtain an understanding of the relative efficiency of energy transfer into each mode. At low latitudes, $\hat{\tau}^{(y)}_{(0)}$, the alongshore wind stress at the coast, forces a very energetic internal Kelvin wave, but is inefficient in forcing shelf waves. For driving by $\tau^{(y)}_{(0)}$ at mid-latitudes, the IKW and n = 1 SW modes have energy densities of the same order. However, the kinetic energy of the n = 1 SW mode is greater than that of the IKW mode at mid-latitudes. Interior barotropic motions do not efficiently excite the IKW or the SW modes at low latitudes. The n = 1 SW mode is efficiently excited, however, for mid-latitude offshore barotropic forcing.

A simple solution obtained with forcing by a traveling wave wind disturbance enables us to compare the relative effects of forcing by $\tau^{(y)}_{(0)}$ and by $\tilde{\phi}_{Ix(0)}$, offshore generated barotropic motions. With the assumptions of the present model, interior baroclinic motions are unimportant except for very low frequency driving.

Coastal wind stress forcing is an important effect for all latitudes. For mid-latitudes, interior driving mechanisms force motions on the shelf and slope which, for $\xi > 0.5$, are as large or larger than the coastal wind stress forced motion. The mid-latitude forced response over most of the inner shelf and slope ($\xi < 0.5$) is predominantly due to the local alongshore wind stress. However, the effect of interior forcing on the velocity in the lower layer grows with respect to the direct wind forced effect as δ_R/δ becomes larger, and the low latitude forced response to interior barotropic motions $v_{2(\phi)}$ can be comparable to or greater than the wind forced response $v_{2(\tau)}$.

For low frequency driving $[\frac{1}{2}\delta_{R(1)}(\beta/\delta) << \omega << |\ell|/\delta_B$, (20 days < T' < 60 days at 6° latitude)], interior motions penetrate less effectively onto the shelf, reflecting the topographic constraint on low frequency circulations. The coastal wind forced response is also inhibited from crossing contours of constant depth, so that, for low frequency driving, the circulation over the outer shelf and slope is controlled predominently by the interaction of the interior flow with the shelf. In cases where $V_{(\tau)}$ is concentrated near the coast and $V_{(\Phi)}$ is concentrated near the outer shelf, cross-shelf phase shifts of $\frac{\pi}{2}$ are predicted for driving by a wind which is traveling predominantly in the alongshore direction. In the general case, predicted cross shelf phase lags may be estimated using Fig. 8. For forcing at very low frequency $[\omega << \frac{1}{2}(\delta_{R(1)}\beta/\delta)$, (T' > 60 days at 6° latitude)], an interior Sverdrup flow in the upper layer extends onto the shelf and represents the dominant shelf response. Wave motions on the shelf are not coastally trapped, but propagate into the interior in the form of westward traveling long internal Rossby waves.

Finally, we point out that the ability of interior motion to contribute significantly to shelf-slope circulation is limited for this model by assumptions of a linear interior ocean driven locally by a wind stress curl. Strong nonlinear offshore baroclinic currents, for example, or free Rossby waves that propagate toward the shelf might drive appreciable baroclinic shelf motion at low latitudes. This problem remains to be investigated.

Figure Captions

Figure 1: Variation of wave speeds as a function of δ_R/δ for the 3 eigenfunctions E_1, E_2, and E_3, which, for $\delta_R/\delta < 0.43$, represent the internal Kelvin wave, the n = 1 and the n = 2 shelf waves, respectively. The values $a_{(0)} = 0.3$ and $\delta_B = 0.33$ have been utilized. Dimensionless f ($f = f'/f_c'$, where f_c' is the dimensional latitude for the interaction between the internal Kelvin wave and the n = 1 shelf wave) is plotted along the top axis. With dimensional values of shelf width $L_s = 90$ km and internal Kelvin wave phase speed $c_0' = 100$ cm s^{-1}, $\delta_R/\delta = c_0'/(f'L_s)$ is plotted along the bottom axis, where $\delta_R/\delta = 0.43$ at the critical latitude $f' = f_c'$. Corresponding latitudes for f = 1, 2, 3, 4, 5 are 10°, 21°, 32°, 45°, and 63°, respectively.

Figure 2: Energy density E_m (4.13) divided by $\bar{t}^2$ as a function of δ_R/δ for the 3 eigenfunctions E_1, E_2, and E_3, forced by $\hat{\tau}$ ($\hat{\tau} = 1$). The dashed line represents the total energy density. The parameters used are the same as in Fig. 1.

Figure 3: Energy density E_m (4.13) divided by $\bar{t}^2$ as a function of δ_R/δ for the 3 eigenfunctions E_1, E_2, and E_3, forced by Φ, ($\tilde{\psi}_{xy(0)} = 1$). The parameters used are the same as in Fig. 1.

Figure 4: Y_m as a function of y for four values of $\bar{t}$ ($\bar{t}_{i+1} > \bar{t}_i$) [from Allen (1976a)].

Figure 5: A schematic of the flow pattern that develops at mid-latitudes in the upper and lower layers for a constant wind stress which is switched on at $\bar{t} = 0$ in the region $-|y_0| < y < 0$. The flow pattern is shown for two times ($\bar{t}_2 > \bar{t}_1$) <u>after</u> the SW modes have achieved a steady balance. Regions where the density interface moves vertically

upward are shaded. The upper layer flow pattern does not include the offshore flow due to the surface Ekman layer.

Figure 6: A schematic of the flow pattern that develops at low-latitudes. For simplicity, the effects of all the SW modes are represented by one SW front. The notation is the same as for Fig. 5.

Figure 7: Scaled interior barotropic forcing $|\hat{\phi}_{x(0)}|/(T_0/\omega)$ as a function of scaled inverse frequency $\beta(2\omega\delta\ell)^{-1}$ for various values of (k/ℓ).

Figure 8: Phase difference θ between $\tilde{\phi}_{x(0)}$ and $\tau^{(y)}_{(0)}$ as a function of $\beta(2\omega\delta\ell)^{-1}$ for various values of (k/ℓ).

Figure 9: (a) Scaled alongshore velocity V_1 (in the upper layer) and V_2 (in the lower layer) over the shelf ($0 \leq \xi \leq 1$), for $\delta_R/\delta = 0.05$, $\ell/\omega = 16$, $\delta_B = 0.33$, and $a_{(0)} = 0.3$ ($V_i = v_i\omega$, $i = 1,2$). The solid line represents $V_{(\tau)}$ forced only by $\tau^{(y)}_{(0)}$, with $\tilde{\phi}_{x(0)} = 0$. The dashed line represents $V_{(\Phi)}$, forced only by $\tilde{\phi}_{x(0)}$, with $\tau^{(y)}_{(0)} = 0$. $V_{1(\tau)}$ near $\xi = 0$ goes off scale ($V_{1(0)} = 0.51$). (b) V_1 and V_2 for $\delta_R/\delta = 2$, $\ell/\omega = 0.4$. $V_{1(\tau)}$ has been rescaled.

Figure 10: (a) $V_{1(\tau)}$; $\delta_R/\delta = 0.1$, (b) $V_{2(\tau)}$ and $V_{2(\Phi)}$; $\delta_R/\delta = 0.1$, (c) $V_{1(\tau)}$; $\delta_R/\delta = 2$, (d) $V_{2(\tau)}$ and $V_{2(\Phi)}$; $\delta_R/\delta = 2$, for various values of ℓ/ω, with $\delta_B = 0.33$ and $a_{(0)} = 0.3$. $V_{1(\Phi)} << V_{1(\tau)}$ in both cases (a) and (c) and has not been plotted.

Figure 11: $V_{1(\tau)(0)}$ ($V_{1(\tau)}$ at $\xi = 0$) vs. ℓ/ω for $\ell < 0$ (forcing traveling poleward) and $\ell > 0$ (forcing traveling equatorward), with $\delta_R/\delta = 0.1$, $\delta_B = 0.33$, and $a_{(0)} = 0.1$. A resonance at $|\ell/\omega| = 10$ occurs for the case $\ell < 0$. This corresponds to the atmospheric forcing resonating with the free internal Kelvin wave.

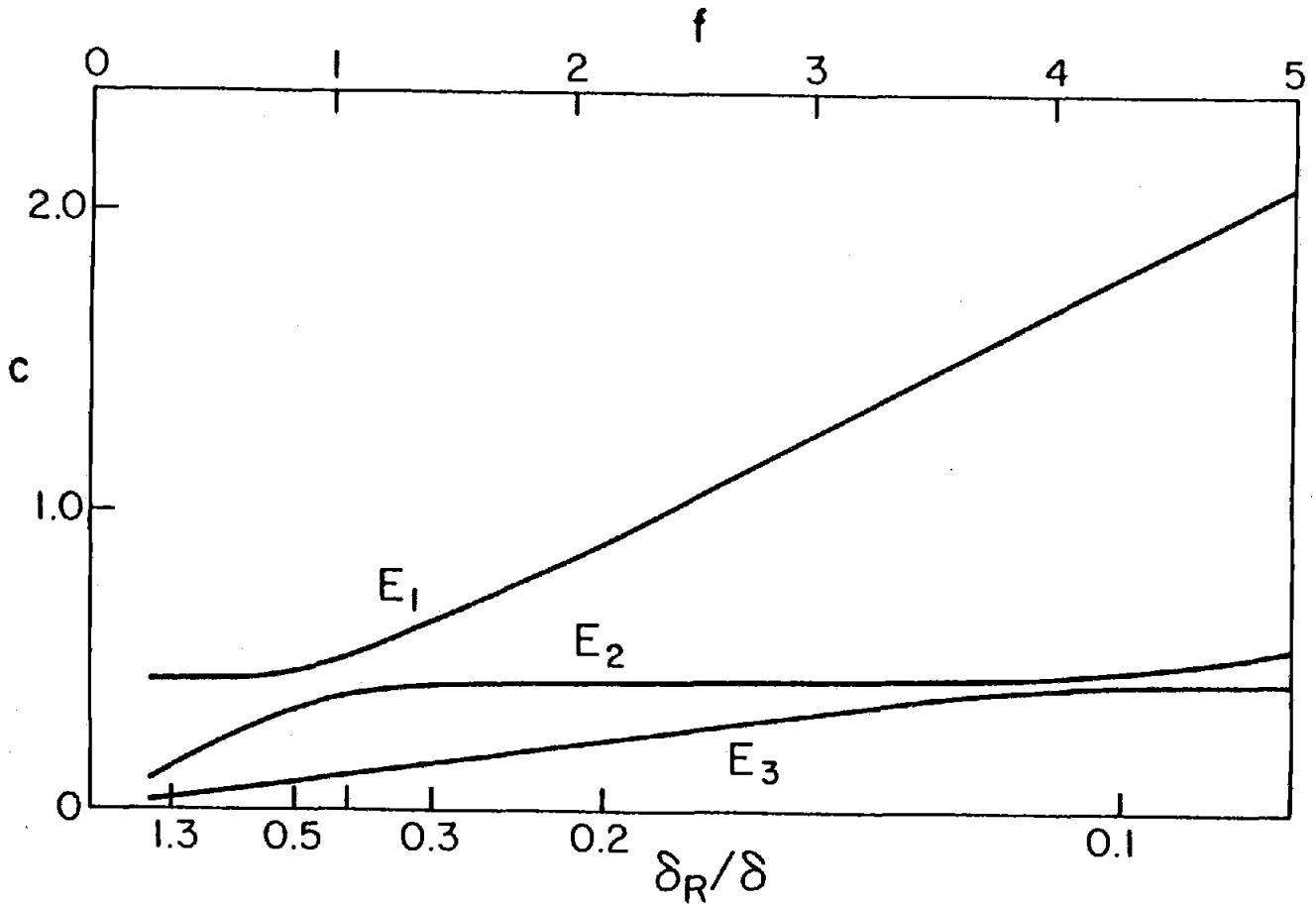

Figure II-1

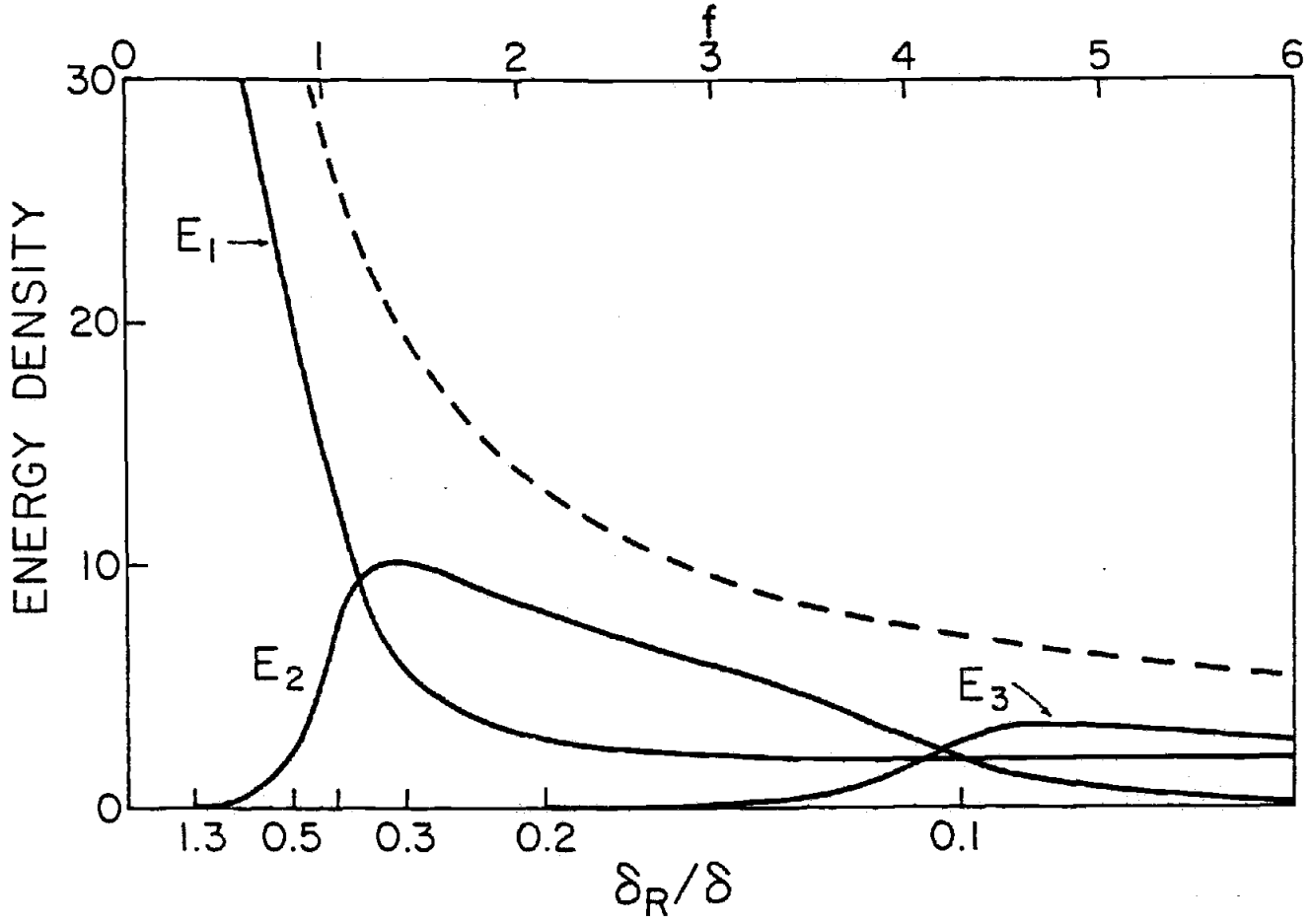

Figure II - 2

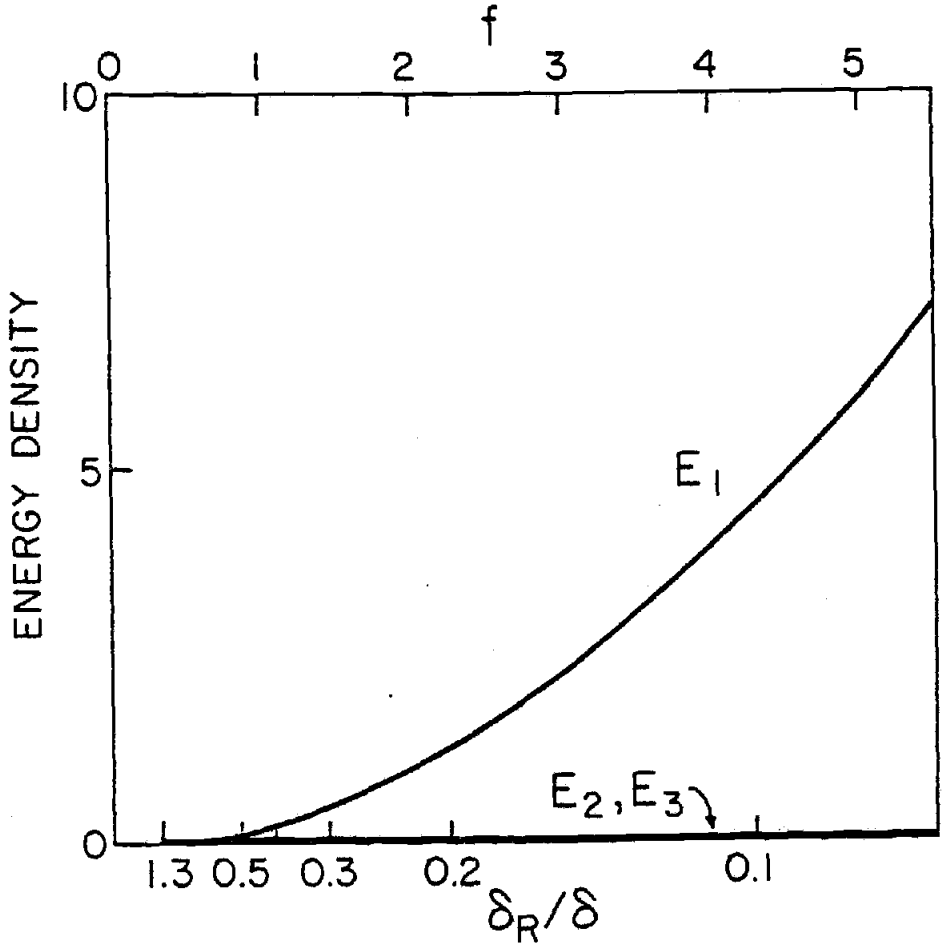
f
0
1
2
3
4
5
10
5
0
ENERGY DENSITY
E_1
E_2, E_3
1.3
0.5
0.3
0.2
0.1
δ_R/δ

Figure II - 3

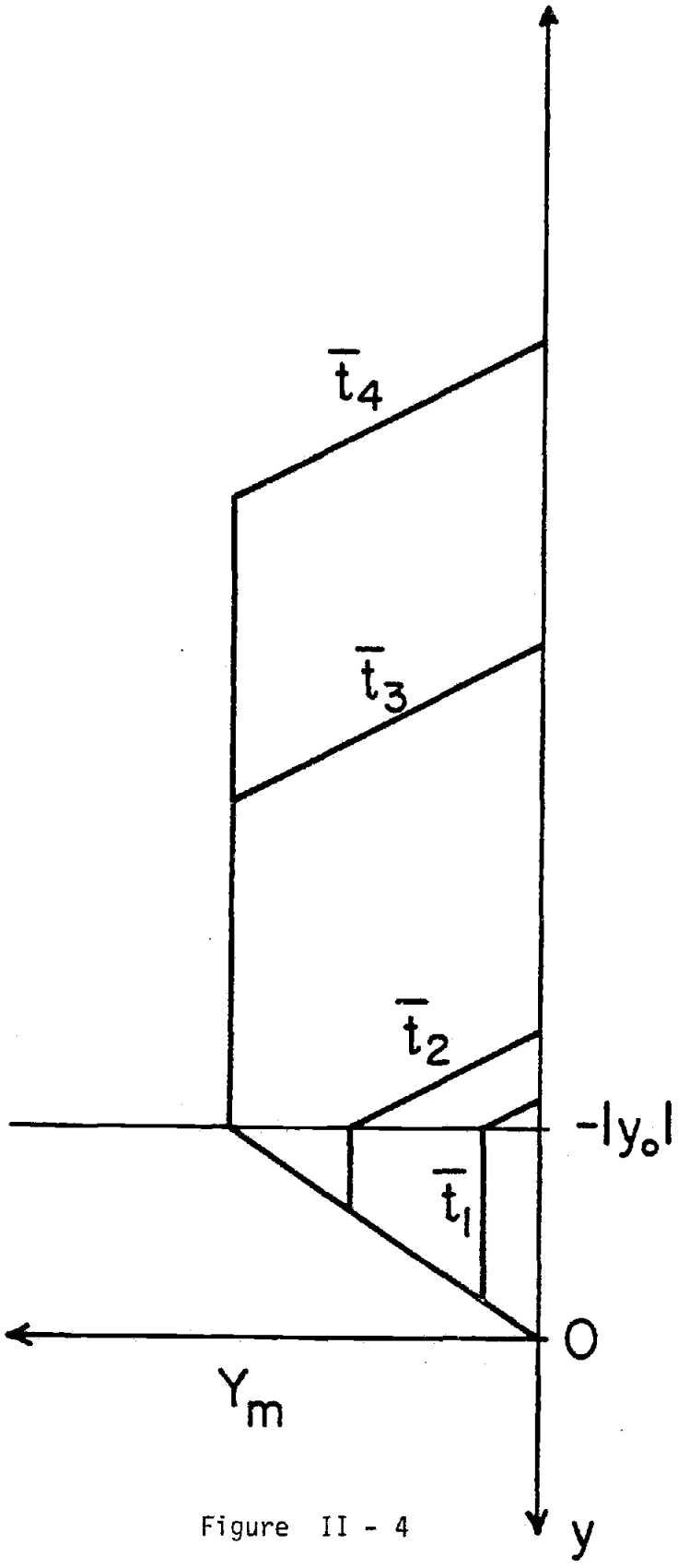

Figure II - 4

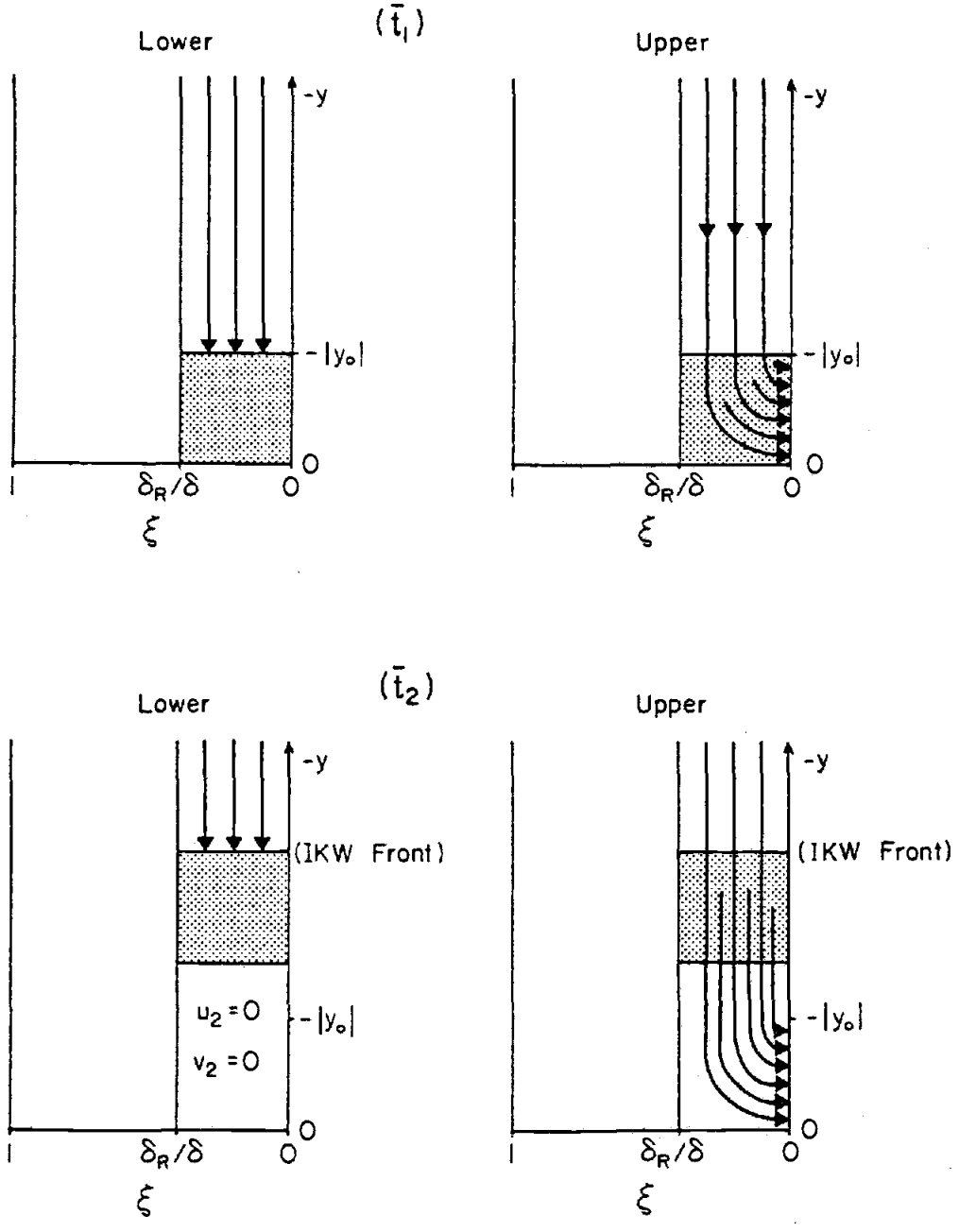
($\bar{t}_1$)
Lower
Upper
-y
$-|y_o|$
0
1
δ_R/δ
ξ
($\bar{t}_2$)
(IKW Front)
$u_2 = 0$
$v_2 = 0$

Figure II - 5

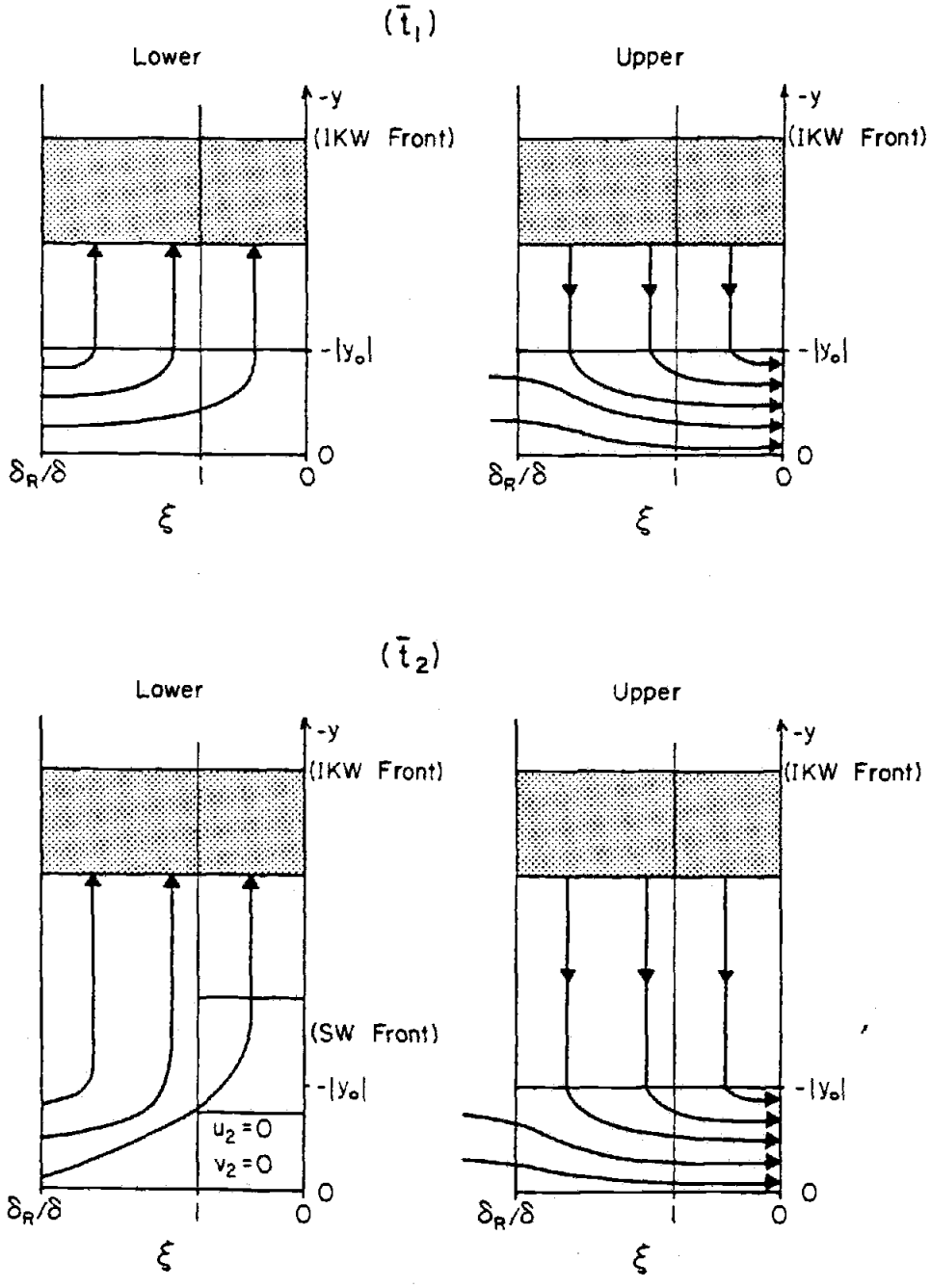
$(\bar{t}_1)$
Lower
Upper
-y
(IKW Front)
$-|y_o|$
0
δ_R/δ
1
0
ξ
$(\bar{t}_2)$
(SW Front)
$u_2 = 0$
$v_2 = 0$

Figure II - 6

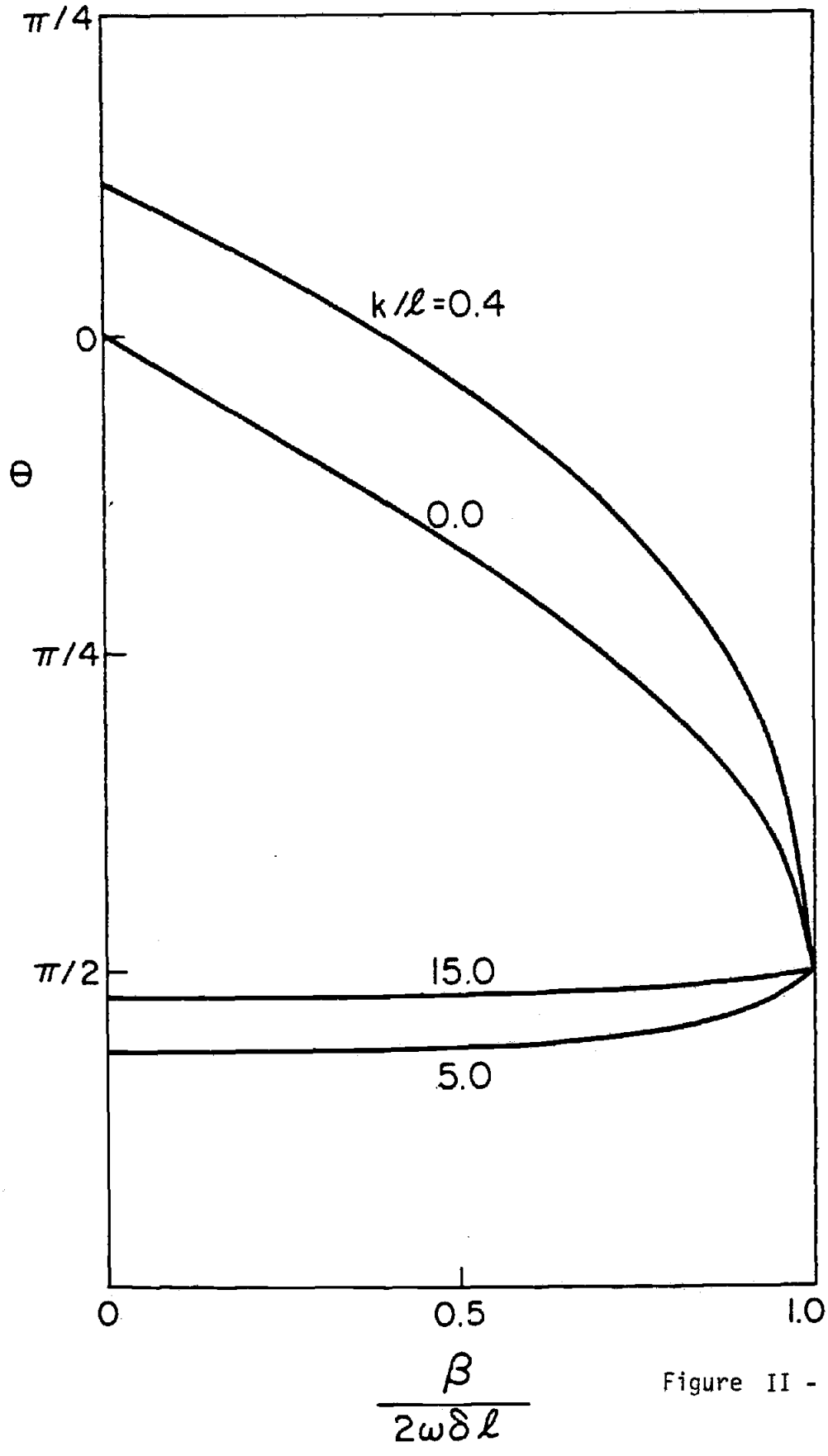

Figure II - 7

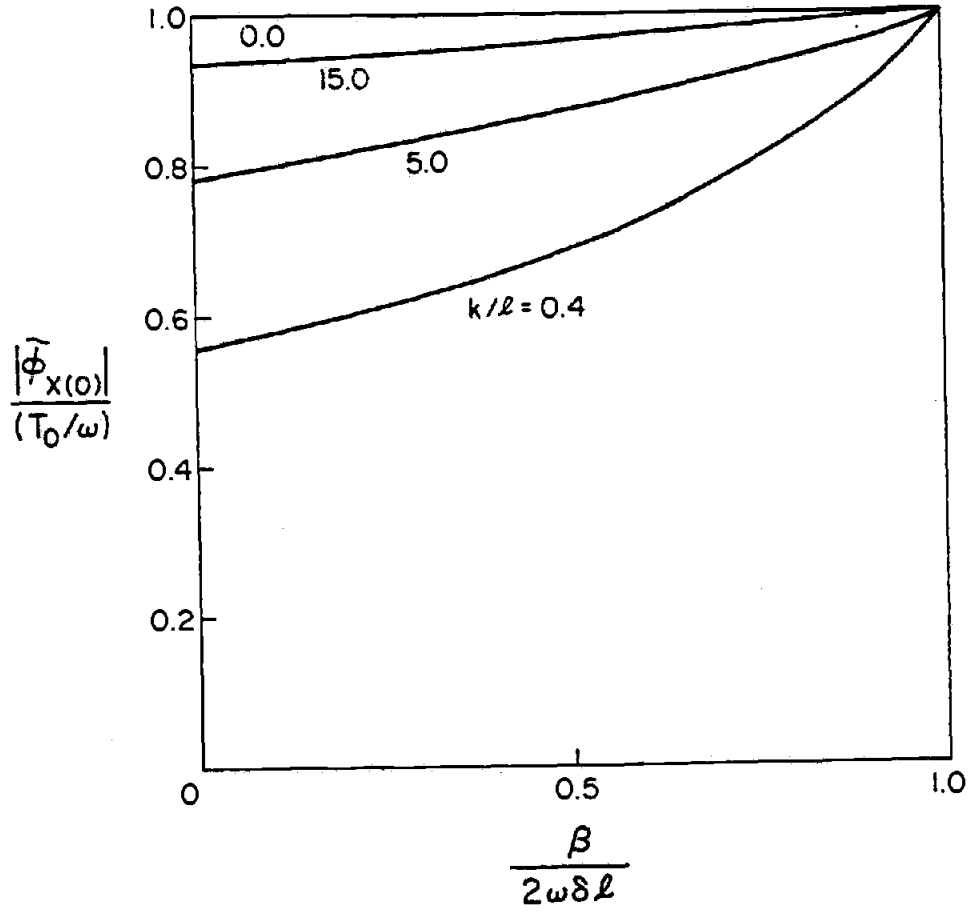
1.0
0.8
0.6
0.4
0.2
0
0.5
1.0
0.0
15.0
5.0
k/ℓ = 0.4
$\frac{|\tilde{\Phi}_{x(0)}|}{(T_0/\omega)}$
$\frac{\beta}{2\omega\delta\ell}$

Figure II - 8

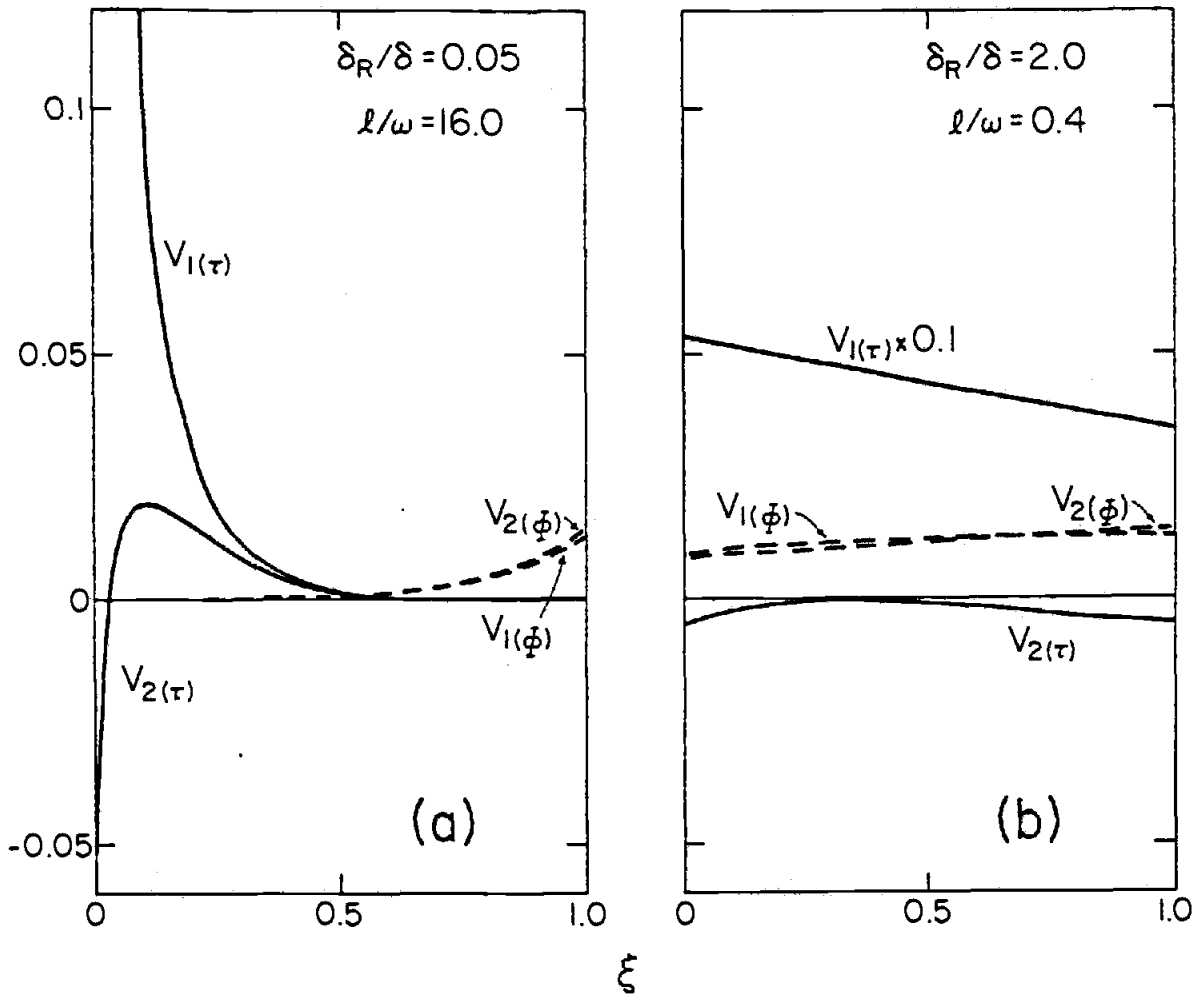
δR/δ = 0.05
ℓ/ω = 16.0
V1(τ)
V2(φ)
V1(φ)
V2(τ)
(a)
δR/δ = 2.0
ℓ/ω = 0.4
V1(τ)×0.1
V1(φ)
V2(φ)
V2(τ)
(b)
0.1
0.05
0
-0.05
0
0.5
1.0
ξ

Figure II - 9

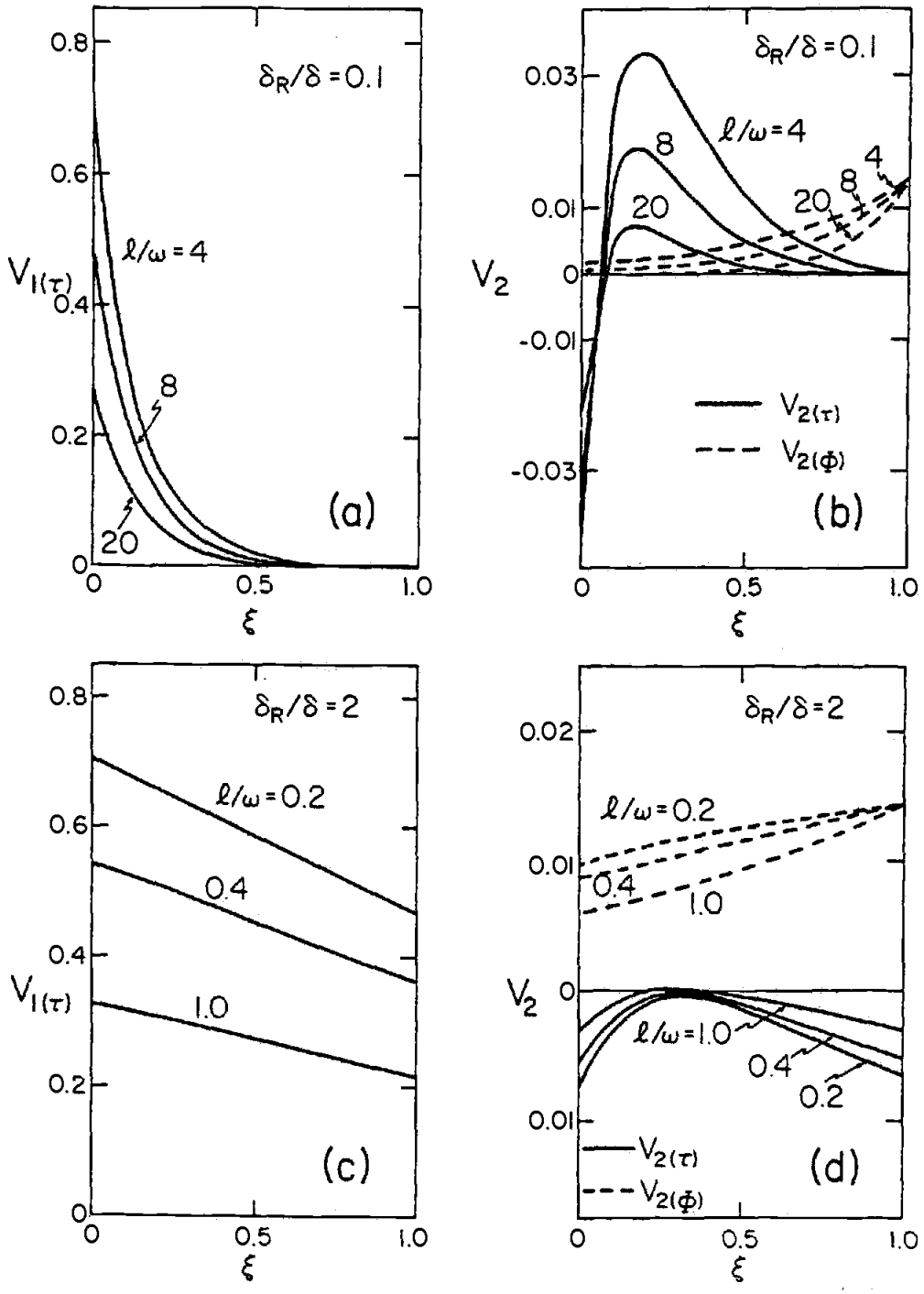
δR/δ = 0.1
ℓ/ω = 4
8
20
(a)
V1(τ)
ξ
δR/δ = 0.1
ℓ/ω = 4
8
20
4
8
20
V2(τ)
V2(Φ)
(b)
V2
ξ
δR/δ = 2
ℓ/ω = 0.2
0.4
1.0
(c)
V1(τ)
ξ
δR/δ = 2
ℓ/ω = 0.2
0.4
1.0
ℓ/ω = 1.0
0.4
0.2
V2(τ)
V2(Φ)
(d)
V2
ξ

Figure II - 10

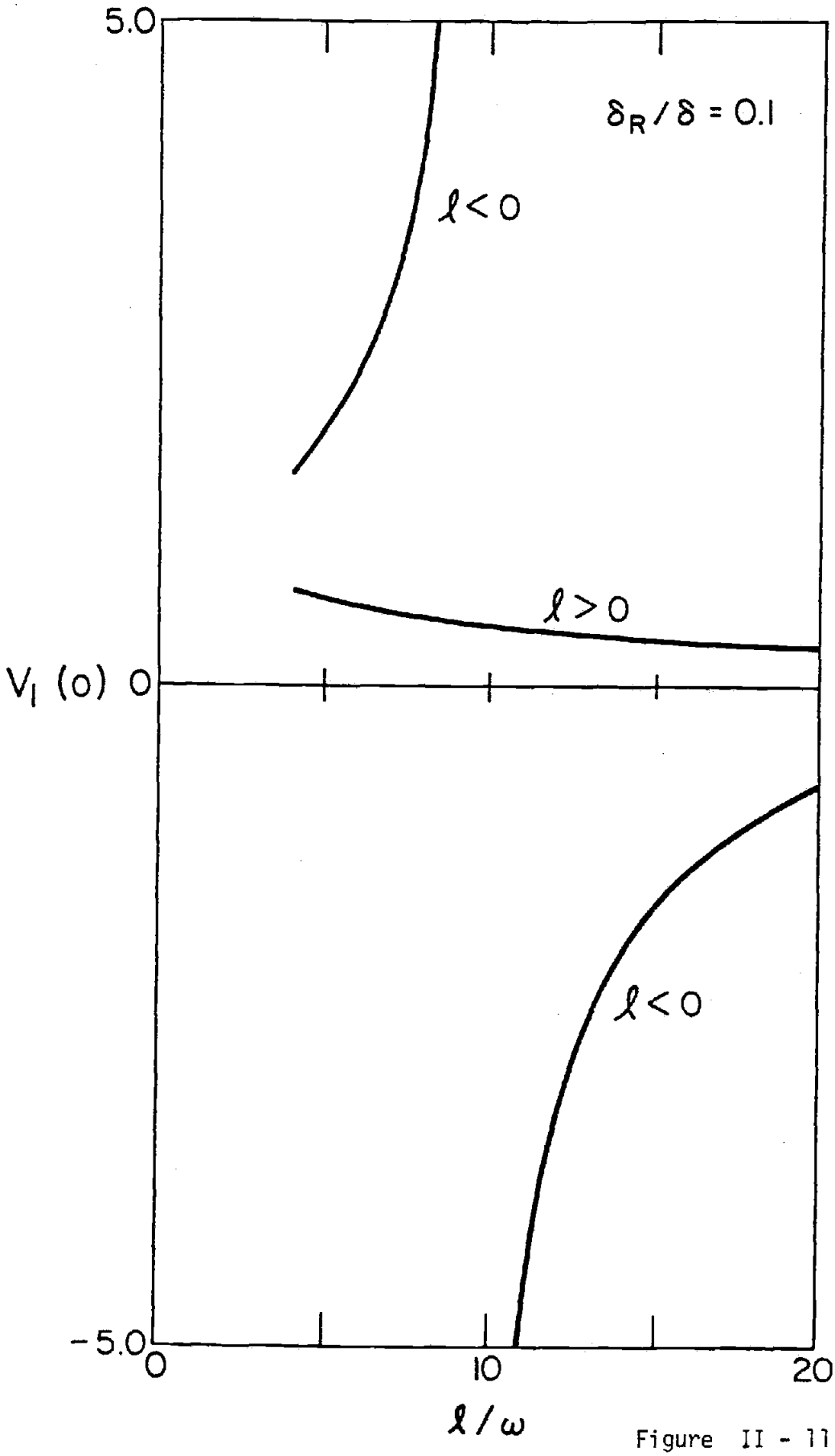

Figure II - 11

REFERENCES

Allen, J. S., 1975: Coastal trapped waves in a stratified ocean. J. Phys. Oceanogr., 5,300-325.

_____, 1976a: Some aspects of the forced wave response of stratified coastal regions. J. Phys. Oceanogr., 6,113-119.

_____, 1976b: On forced, long continental shelf waves on an f-plane. J. Phys. Oceanogr., 6,426-431.

_____, and R. D. Romea, 1980: On coastal trapped waves at low latitudes in a stratified ocean. J. Fluid Mech., 98,555-585.

Anderson, D. L. T. and A. E. Gill, 1975: Spin up of a stratified ocean, with applications to upwelling. Deep-Sea Res., 22,583-596.

Brink, K. H., J. S. Allen, and R. L. Smith, 1978: A study of low frequency fluctuations near the Peru coast. Submitted to J. Phys. Oceanogr.

Buchwald, V. T., and J. K. Adams, 1968: The propagation of continental shelf waves. Proc. Roy. Soc. London, A305,235-250.

Clarke, A. J., 1976: Coastal upwelling and coastally trapped long waves. Ph.D. thesis, Cambridge University, 178 pp.

Clarke, A. J., 1977: Observational and numerical evidence for wind-forced coastal trapped long waves. J. Phys. Oceangr., 7,231-247.

Gill, A. E.,and A. J. Clarke, 1974: Wind induced upwelling, coastal currents, and sea level changes. Deep-Sea Res., 21,325-345.

_____, and E. H. Schumann, 1974: The generation of long shelf waves by the wind. J. Phys. Oceanogr., 4,83-90.

Huthnance, J. M., 1978: On coastal trapped waves: analysis and numerical calculation by inverse iteration. J. Phys. Oceanogr., 8,74-92.

Smith, R. L., 1978: Poleward propagating perturbations in sea level and currents along the Peru coast. J. Geophys. Res., 83,6083-6092.

Chapter III

ON VERTICALLY PROPAGATING COASTAL KELVIN WAVES AT LOW LATITUDES

1. INTRODUCTION

Vertically propagating internal waves in the ocean are generally constrained such that $f < \omega < N$, where ω is the radian frequency, f is the Coriolis parameter, and N is the Brunt Väisälä frequency. For $\omega < f$, vertical propagation is possible when one of the horizontal wavenumbers is imaginary, a condition that is satisfied for equatorially trapped waves with meridional modal structure or for coastally trapped waves that propagate along a boundary and that decay exponentially with distance from the coast (internal Kelvin waves). Such low frequency vertically propagating waves have been observed near the equator, e.g., by Weisberg et al. (1978) who find that equatorially trapped motions in the Gulf of Guinea are downward propagating, not vertically standing modes. Also, from observations on the continental slope in the Gulf of Guinea, Picaut (1981) reports an upward phase propagation of temperature associated with the seasonal upwelling cycle, which he interprets as the signature of a coastal Kelvin wave that propagates westward and vertically.

Recent observations on the Peru continental shelf and slope during ESACAN (Estudio del Sistema de Afloramiento Costero en el Area Norte), the joint German-Peruvian experiment at 5°S latitude, and during the CUEA (Coastal Upwelling Ecosystems Analysis) JOINT-2 experiment at 15°S latitude indicate that vertically propagating waves exist over the slope at low frequencies (period $T = 2\pi/\omega >$ 20 days). For example, Figure 1 shows low-pass filtered alongshore velocity and temperature, from the ESACAN C2 mooring which is on the continental slope in 1360 m of water. The velocity data shows a low frequency pulse-like event that amplifies between 86 m and 560 m

depth, and that propagates vertically downward between 86 and 560 m. The relationship between velocity and temperature at 560 and 860 m suggests that there is a phase propagation upward of both signals with velocity and temperature $\pi/2$ out of phase.

In this study we analyze the dynamics of the second class of subinertial vertically propagating waves described above, namely coastally trapped internal Kelvin waves (hereafter referred to as IKWs). We focus on low latitude dynamics, where the Rossby radius scale, which is the natural offshore length scale for baroclinic motions, is much larger than the shelf-slope width. For this case, the shelf-slope region appears like a vertical wall, and we adopt a model with a vertical coastal boundary.

We pay particular attention to the low frequency behavior ($T \simeq 20$-40 days) but specify that the waves are still coastally trapped. The condition on coastal trapping is $\omega^2 > (\frac{1}{2}\beta/\ell)^2$, where ℓ is alongshore wavenumber and β is a measure of the variation of the Coriolis parameter with latitude, and is satisfied for $\omega \gtrsim 1.8 \times 10^{-6}$ s^{-1} ($T \lesssim 40$ days) with an alongshore wavelength $\lambda_y \simeq 1000$ km (see Allen and Romea, 1980, for an additional discussion of this point).

Typically, oceanic problems are solved with the bottom boundary condition $w = 0$. Recently it has been suggested that the ocean might be better modelled in some frequency-wavenumber regimes by neglecting the effects of a bottom boundary and assuming that the ocean is infinitely deep (Wunsch, 1977; Philander, 1978). We utilize a model of this type in Sections 2 and 3, where we consider the response of a

rotating stratified f-plane ocean with a rigid lid, forced by an alongshore wind stress at the coast. The forced response for several different types of wind stress is calculated and shows components that are trapped near the surface and components that propagate vertically.

The assumption of infinite depth is justified if the bottom is highly dissipative, and scatters energy rather than reflecting it uniformly, or if internal motions generated at the surface dissipate before the energy can reflect off the bottom and travel back toward the surface (Wunsch, 1978). In order to assess the frequency-wavenumber regimes where frictional processes justify the neglect of a bottom boundary, the effect of internal dissipation is included in Section 4 and the dissipation time scale is compared to the time required for initial disturbances to propagate vertically from the surface to the bottom. The forced response with a bottom boundary is calculated in Section 5 and compared to the results of Sections 2 and 3 in order to assess further the space and time scales where the analyses of Sections 2 and 3 are valid. Finally, in order to generalize the f-plane results, the Coriolis parameter is regarded in Appendix A as a slowly varying function on the alongshore scale of the waves. The forced response is obtained with a variable f and is compared to the f-plane results.

2. THEORETICAL FORMULATION

We consider a continuously stratified ocean which rotates on an f-plane in the Northern hemisphere. Cartesian coordinates (x,y,z) are utilized with x positive westward, y positive southward, and z positive vertically upward. There is a rigid lid on top (z = 0), a straight north-south coastline at x = 0, and the fluid is unbounded for $x \to \infty$, $z \to -\infty$. The problem is linearized by the assumption that the motion results in negligible nonlinear fluid accelerations and in small departures from an equilibrium stable density distribution $\bar{\rho}(z)$. The hydrostatic approximation is utilized and we consider interior motions away from frictional boundary layers. The long wave assumptions for coastal trapped waves are made, i.e., we assume that $\omega \ll f$ and that the characteristic alongshore scale L is large relative to the internal Rossby radius of deformation.

With the above assumptions, the governing equations are

$$- fv = -p_x/\rho_0, \tag{2.1a}$$

$$v_t + fu = -p_y/\rho_0, \tag{2.1b}$$

$$0 = -p_z - g\rho, \tag{2.1c}$$

$$u_x + v_y + w_z = 0, \tag{2.1d}$$

$$\rho_t + w\,\bar{\rho}_z = 0, \tag{2.1e}$$

where subscripts denote partial differentiation. The variables (u,v,w) are the velocity components in the (x,y,z) directions, t is

time, p is pressure, and g is the acceleration of gravity. The total density is given by

$$\rho_T(x,y,z,t) = \rho(x,y,z,t) + \bar{\rho}(z) + \rho_0, \tag{2.2}$$

where ρ_0 is a constant.

Eqs. (2.1 a-e) may be combined into a single equation for the pressure:

$$[p_{xx} + f^2 (p_z/N^2)_z]_t = 0, \tag{2.3}$$

where

$$\rho_0 f^2 u = -p_{xt} - f p_y, \tag{2.4}$$

$$\rho_0 w = -N^{-2} p_{zt}, \tag{2.5}$$

and where $N^2 = -g\bar{\rho}_z/\rho_0$ is the square of the Brunt-Väisälä frequency.

We assume, consistent with the long wave approximation, that only the alongshore component of the wind stress is important and that it is approximately constant over the scale of the Rossby radius. The alongshore wind stress acts as a driving mechanism through suction of fluid into the surface Ekman layer at the coast. An offshore or onshore mass flux in the upper Ekman layer produces the equivalent of a sink or source-like flow below the Ekman layer at the coast. The vertical extent of the region is sufficiently small so that the corner acts very nearly as a point sink or source for the flow below the Ekman layer (e.g., Pedlosky, 1969; Allen, 1973; Pedlosky, 1974). Consequently, we specify a forced boundary condition at the

surface which represents an Ekman suction in the upper coastal corner at $x = 0$, $z = 0$ and no flow through the vertical boundary at $z = 0$, i.e.,

$$p_{xt} + fp_y = f\,\tau(y,t)\,\delta(z), \qquad \text{at } x = 0, \tag{2.6}$$

where $\delta(z) = 0$, $z \neq 0$, and

$$\int_{-H}^{0} \delta(z)\,dz = 1. \tag{2.7}$$

The remaining boundary conditions are

$$p_{zt} = 0, \qquad \text{at } z = 0, \tag{2.8}$$

$$p_x, p_y, p_z < \infty, \qquad \text{as } x \to \infty, \tag{2.9a}$$

$$z \to -\infty. \tag{2.9b}$$

Condition (2.8) specifies no normal flow through the top, while (2.9a,b) follow from (2.1a), (2.4), (2.5) and the requirement that the energy be finite as $x \to \infty$ or $z \to -\infty$. In addition, we impose a radiation condition which restricts the solution to have energy propagating away from the source at $x = 0$, $z = 0$.

We consider initial value problems where

$$\tau = 0,\ p = 0, \qquad \text{for } t < 0. \tag{2.10}$$

(a) Free waves

Before solving the forced problem, it is useful to obtain the free wave solution to (2.3) for a vertically unbounded fluid governed

by a homogeneous version of (2.6) and without condition (2.8).

We assume N^2 is a constant and seek a free wave solution of the form

$$p(x,y,z,t) = \phi(x)\ \mathrm{Re}\{\exp[-i\ (\omega t - \ell y - mz)]\}, \qquad (2.11)$$

where ℓ and m are wavenumbers, and Re denotes the real part. Substituting (2.11) in (2.3), (2.6) (with $\tau = 0$), and (2.9a), we obtain

$$\phi_{xx} - (fm/N)^2\ \phi = 0, \qquad (2.12)$$

$$\phi_x - (f\ell/\omega)\ \phi = 0, \qquad \text{at } x = 0, \qquad (2.13a)$$

$$\phi,\ \phi_x < \infty, \qquad \text{as } x \to \infty. \qquad (2.13b)$$

The solution to (2.12) subject to (2.13a,b) is

$$\phi = \exp\ (f\ell x/\omega), \qquad (2.14)$$

where the dispersion relation is

$$\omega = N\ell/m. \qquad (2.15)$$

The condition (2.13b) imposes the familiar restriction,

$$\ell/\omega < 0, \qquad (2.16)$$

i.e., free coastally trapped subinertial waves propagate with the boundary on their right side (poleward toward -y with our mode). The dispersion relation (2.15) gives a phase velocity with vertical component $\omega/m = \omega^2(N\ell)^{-1}$ and a group velocity with vertical component

$\partial\omega/\partial m = -\omega/m$. The group and phase velocities are oppositely directed, e.g., for $\omega/m > 0$, the vertical component of the phase velocity is directed upward while the vertical group velocity is downward.

(b) Solution to the forced problem

The solution to (2.3) subject to (2.6)-(2.10) and the radiation condition may be conveniently represented in terms of its Fourier cosine transform in z:

$$\hat{p}(x,y,m,t) = \int_0^\infty p(x,y,z,t) \cos mz \, dz, \tag{2.17a}$$

$$p(x,y,z,t) = (2/\pi) \int_0^\infty \hat{p}(x,y,m,t) \cos mz \, dm. \tag{2.17b}$$

Multiplying (2.3), (2.6) and (2.9a) by cos(mz) and integrating over z from 0 to ∞, we obtain

$$\hat{p}_{xx} - (mf/N)^2 \hat{p} = 0, \tag{2.18a}$$

$$\hat{p}_{xt} + f\hat{p}_y = f\,\tau(y,t), \quad \text{at } x = 0, \tag{2.18b}$$

$$\hat{p}_y, \hat{p}_x < \infty, \quad \text{as } x \to \infty. \tag{2.18c}$$

Eqs. (2.18a-c) have a solution

$$\hat{p} = \hat{Y}(y,m,t) \exp(-fmx/N), \tag{2.19}$$

where

$$-(m/N) \hat{Y}_t + \hat{Y}_y = \tau(y,t). \tag{2.20}$$

Eq. (2.20) is a forced first order wave equation for the (y,t) structure of the response and may be easily solved for various $\tau(y,t)$. In particular, we may obtain a formal solution for general $\tau = \tilde{F}(y)\,\tilde{T}(t)$ by first considering the solution to (2.20) for a wind stress of the form

$$\tau(y,t) = \tilde{F}(y)\,\delta(t), \tag{2.21}$$

where $\delta(t)$ is the Dirac delta function and where the initial condition corresponding to (2.10) is

$$\hat{Y}(0) = 0. \tag{2.22}$$

With (2.21) and (2.22), the solution to (2.20) is

$$\hat{Y} = -(N/m)\,\tilde{F}(y + Nt/m), \tag{2.23}$$

which, together with (2.17b) and (2.19), gives

$$p = p_D = -(2N/\pi)\int_0^\infty \tilde{F}(y + Nt/m)\exp(-fmx/N)\,m^{-1}\cos(mz)\,dm. \tag{2.24}$$

The subscript D identifies (2.24) as the response to forcing by a wind stress whose time dependence is given by a delta function. p_D represents a Green's function for a wind stress concentrated in time. If now a wind stress with general time dependence $\tilde{T}(t)$ is applied, the pressure is given by

$$p = \int_0^t p_D(x,y,z,t-\alpha)\,\tilde{T}(\alpha)\,d\alpha. \tag{2.25}$$

3. EXAMPLES

To gain an appreciation for some of the features of the solutions, we examine three idealized situations for the y and t variation of τ.

Example A

We first choose a wind stress of the form

$$\tau(y,t) = \delta(y)\ \delta(t)\ \tau_0. \tag{3.1}$$

The solution, which may be obtained directly from (2.24), is

$$p = (2/\pi)\ (N\tau_0/y)\ \cos(Ntz/y)\ \exp(fxt/y), \qquad y < 0. \tag{3.2}$$

The disturbance at $y = 0$ acts like a source that emits waves of all frequencies and wavelengths. The pressure exhibits an exponential decay in x for fixed y and decays like $|y|^{-1}$ in the alongshore direction. In Figure 2, v obtained from (3.2) is plotted as a function of t for various values of z in terms of scaled variables defined in the Figure Caption. We show v rather than p because velocity may be directly compared with current observations. Frequency variations with depth are evident. The envelope $t\ \exp(fxt/|y|)$, which is the response at $z = 0$, governs the initial growth of v at all depths to some maximum value and its subsequent decay with time.

For $|Ntz/y| \gg 1$, the waves behave locally like simple harmonic waves of a certain fixed period and wavelength which move in accordance with the relation

$$\theta = Ntz/y = \text{constant}, \tag{3.3}$$

where θ is the phase and both $z, y < 0$. The local frequency and

wavenumbers are given by

$$\omega_0 = -(\partial\theta/\partial t) = -Nz/y, \tag{3.4}$$

$$m_0 = \partial\theta/\partial z = Nt/y, \tag{3.5}$$

$$\ell_0 = \partial\theta/\partial y = -Ntz/y^2, \tag{3.6}$$

where variations in frequency or wavenumber are small over a frequency or wavenumber interval, i.e., $\omega_0^{-1}\Delta\omega$, $m_0^{-1}\Delta m$, $\ell_0^{-1}\Delta\ell \ll 1$ (Bretherton, 1970). Thus the frequency varies as a function of position while the wavenumbers change with both position and time. For fixed time, waves farther in y from the source have longer wavelengths.

The alongshore and vertical components of the local phase velocity may also be computed. These are

$$c_{p0}^{(z)} = -(\partial\theta/\partial t)/(\partial\theta/\partial z) = \omega_0/m_0 = -z/t, \tag{3.7a}$$

$$c_{p0}^{(y)} = -(\partial\theta/\partial t)/(\partial\theta/\partial y) = \omega_0/\ell_0 = y/t, \tag{3.7b}$$

and the phase velocity is directed upward and poleward. For fixed y or z, the phase move more slowly as time increases, but for fixed t more rapidly as $|y|$ or $|z|$ increase.

We may express the local frequency in terms of the local wavenumbers, which gives

$$\omega_0 = N\ell_0/m_0. \tag{3.8}$$

Local group velocity components are

$$c_{g0}^{(z)} = \partial\omega_0/\partial m_0 = -N\ell_0/m_0^2 = z/t, \tag{3.9}$$

$$c_{g0}^{(y)} = \partial\omega_0/\partial \ell_0 = N/m_0 = y/t. \tag{3.10}$$

The local group velocity vector associated with waves of fixed wavenumbers ℓ_0 and m_0 at time t is directed downward and poleward. Comparison of (3.8), (3.9), and (3.10) with the corresponding expressions obtained from (2.15) for the free wave example in Section 2 shows, as expected, that for $|Ntz/y| \gg 1$, the response behaves locally like free waves with fixed frequency and wavenumbers in a vertically unbounded ocean. With $y/t = N/m_0$ from (3.5), the condition $|Ntz/y| \gg 1$ is $|m_0 z| \gg 1$, which specifies that the disturbance must be much more than a local wavelength away from the surface.

Example B

We next consider

$$\tau(y,t) = \delta(y)\, H(t)\, T(t)\, \tau_0, \tag{3.11}$$

where H(t) is the Heaviside function $H(t) = 0$, $t < 0$; $H(t) = 1$, $t > 0$. This example represents forcing by a wind stress that is localized in space and that has a general time behavior initiated at $t = 0$. Substitution of (3.11) in (2.25) gives

$$p = -(2/\pi)(N/|y|)\exp(-fxt/|y|)\int_0^t \cos[Nz(t-\alpha)/|y|]\exp(fx\alpha/|y|)T(\alpha)d\alpha. \tag{3.12}$$

The special case $T(t) = \delta(t)$ corresponds to Example A and yields the same answer.

If we assume

$$T(t) = \mathrm{Re}\{\exp(-i\sigma t)\}, \tag{3.13a}$$

and scale the variables as

$$x' = x(\sigma'|y|)^{-1},\ z' = (N/\sigma)(z/|y|),\ t' = \sigma t,\ \sigma' = \sigma/f,$$

$$p' = p/[(2/\pi)(N/\sigma)\tau_0], v' = v[(2/\pi)(N/\sigma)\tau_0(\rho_0 f|y|)^{-1}]^{-1}, \tag{3.13b}$$

the evaluation of (3.12) gives, with (3.1),

$$p' = \mathrm{Re}(-y^{-1}(B^2 + z'^2)^{-1}\ \{B\exp(-it') -$$
$$[B\cos(t'z') - z'\sin(t'z')]\exp(-x't')\}), \quad y < 0, \tag{3.14a}$$

where

$$B = x' - i. \tag{3.14b}$$

The first term in the curly brackets represents a response at the forcing frequency σ. The remaining two terms are transients which, for fixed y and $x > 0$, decay exponentially with t and are coastally trapped.

The initial response for $t' < 10$ where the transients are still important is illustrated in Figure 3. The phase propagation is upward, consistent with a downward propagation of energy from the surface, while a maximum in v propagates from the surface downward. Examination of (3.14) for $x't' \gg 1$, when the transient terms have decayed, shows a subsurface maximum of v at $z' = -1$. From (2.15),

this is the ray path $dy/dz = (\partial\omega/\partial m)/(\partial\omega/\partial \ell)$ that passes through $y = 0$, $z = 0$ for a freely propagating IKW of frequency $\omega = \sigma$. Figure 3 shows the maximum in v propagating downward from the surface to $z' = -1$, where it intersects the IKW free wave ray path. Subsequently, the maximum in v remains at $z' = -1$.

Example C

Finally, we examine a more general wind stress,

$$\tau(y,t) = H(t)\, H(-y)\, F(y)\, T(t)\, \tau_0, \tag{3.15}$$

where the wind has a general y structure for $y < 0$.

The substitution of (3.15) in (2.24) and (2.25) gives

$$p = -(2/\pi)N\tau_0 \int_0^t T(\alpha)\, d\alpha \int_0^{|y|} F(\beta-|y|)\exp[-fx(t-\alpha)/\beta]\cos[N(t-\alpha)z/\beta]\, \beta^{-1} d\beta,$$

$$y < 0. \tag{3.16}$$

A special case of interest is

$$F(y)\, T(t) = \mathrm{Re}\{\exp[-i(\sigma t - \ell y)]\}. \tag{3.17}$$

The substitution of (3.17) in (3.16) and the subsequent evaluation of the integral over α yields

$$p = \mathrm{Re}\{-(2/\pi)N\tau_0 \exp(i\ell y) \int_0^{|y|} \exp[i\ell\beta - fxt/\beta][K \exp(Kt) - K \cos(Ntz/\beta) +$$

$$(Nz/\beta) \sin(Ntz/\beta)]\, [Nz/\beta)^2 + K^2]^{-1}\, \beta^{-1}\, d\beta\}, \quad y < 0, \tag{3.18}$$

where

$$K = fx/\beta - i\sigma. \tag{3.19}$$

We first examine (3.18) for small y, i.e., $|\ell y| \ll 1$, or equivalently $|y| \ll \lambda_y/(2\pi)$, where $\lambda_y = 2\pi/\ell$ is the alongshore wavelength of the wind. Evaluation of (3.18) with $|\ell y| \ll 1$ gives

$$v' \sim \sigma'^{-1} \quad \mathrm{Re} \quad (x'^2 + z'^2)^{-1}(B^2 + z'^2)^{-1}$$

$$\times \{\exp(-it')\, E + \exp(-x't')[-E \cos(z't') - z'(B + x') \sin(z't')]\}\,, \qquad y < 0, \tag{3.20a}$$

where

$$E = -Bx' + z'^2, \tag{3.20b}$$

and where B is given by (3.14b).

Figure 4 shows v' from (3.20) as a function of z' and t'. A subsurface maximum of v' travels downward to z' = -1 where it remains. In Example B this behavior was found for $F(y) = \delta(y)$, while here a similar behavior is observed, which is evidently associated with the step function at y = 0.

For large time ($x't' \gg 1$) when the transient terms have decayed, (3.20) is asymptotically equal to

$$v' \sim \tfrac{1}{2}\,[\sin(t')\, x'\, (2/I - I_-^{-1} - I_+^{-1})$$

$$- \cos(t')\, (\mu_+/I_+ - \mu_-/I_-)], \qquad y < 0, \tag{3.21a}$$

where

$$I = x'^2 + z'^2, \tag{3.21b}$$

$$I_\pm = x'^2 + \mu_\pm^2, \tag{3.21c}$$

$$\mu_{\pm} = z' \pm 1. \qquad (3.21d)$$

Note that (3.21a) corresponds to the solution that may be obtained directly by solving (2.26) and (2.27) with $\tau(y,t) = H(-y)\exp(-i\sigma t)$. For $x' \ll 1$, a maximum in v' occurs at the surface and near the line $\mu_+ = 0$, that is the ray path passing through $y = 0$, $z = 0$ for a free IKW. The maximum at the surface is associated with the local forcing while the maximum near $\mu_+ = 0$ is associated with the step function at $y = 0$. This behavior is illustrated in Figures 5 a-d, which show the magnitude and phase of V, where $v' = V\exp(-it')$ (from (3.20) with $x't' \gg 1$) as a function of y and z' and as a function of x' and z'. The subsurface maximum along the free IKW ray path is evident in Figure 5a. Figure 5c shows that the subsurface maximum is strongest near the coast and weakens with increasing x'. The maximum of v' near the surface is also evident on Figures 5a,c. The phase plots shown on Figures 5b,d indicate that there is a 180° phase difference from the surface to below the subsurface maximum, with an upward phase propagation. The phase plot shown in Figure 5d indicates relatively small offshore phase differences for $|z'| < 1$ and shows nearshore motions leading for $|z'| > 1$.

For large $|y|$ and large t, i.e., for $|\ell y| \gg 1$ and $fxt/|y| \gg 1$, an approximate expression for (3.18) is

$$p \sim \mathrm{Re}\{(2/\pi)N\tau_0 \exp[-i(\sigma t - \ell y)] \int_0^{\infty} K[(Nz/\alpha)^2 + K^2]^{-1} \exp(i\ell\alpha)\alpha^{-1} d\alpha,$$

$$y < 0. \qquad (3.22)$$

This limit gives p far from the region influenced by the step function in y and after the transient components have decayed. Evaluation of the integral in (3.22) yields

$$p \sim \mathrm{Re}((\pi\sigma)^{-1} N\tau_0 \exp[-i(\sigma t - \ell y)] \exp(f\ell x/\sigma)$$

$$\times \{-i[\exp(iN\ell z/\sigma)\, Ei(-f\ell x/\sigma - iN\ell z/\sigma) + \exp(-iN\ell z/\sigma)\, Ei(-f\ell x/\sigma + iN\ell z/\sigma)]$$

$$+ H(-\ell/\sigma)\pi \exp(-iN\ell z/\sigma)\}), \quad y < 0, \qquad (3.23)$$

where Ei is the exponential integral function (Gradshteyn and Ryshik, 1980, p. 925) and where $H(-\ell/\sigma) = 1$ for $\ell/\sigma < 0$ and 0 for $\ell/\sigma > 0$.

The response is composed of two parts, one of which (the last term in curly brackets) is forced only for $\ell/\sigma < 0$ and represents a coastally trapped IKW with vertical wavenumber $m = N\ell/\sigma$ and negative vertical group velocity $c_{gz} = -\sigma/m$. The offshore trapping scale (Rossby radius scale) is $\sigma/f\ell$. The remaining two terms in (3.23) represent a forced response which decay as $|z|^{-2}$ for $|z|$ large and which exhibit the proper behavior at $x = 0$, $z = 0$ to satisfy (2.6).

In Appendix B, we derive a solution for forcing by a traveling plane wave wind stress with a generalized integral transform in x, in a manner similar to that utilized by Huppert and Stern (1974). That procedure gives the same result as the asymptotic solution (3.23) obtained with a cosine transform in z and provides an alternative computationally convenient representation of the solution.

The magnitude of the alongshore velocity associated with the surface trapped response (calculated numerically from the integral in (B21)) is plotted for several depths as a function of $f|\ell/\sigma|x$ in Figure 6 for both poleward ($\ell/\sigma < 0$) and equatorward ($\ell/\sigma > 0$)

traveling wind. For $\ell/\sigma < 0$, the magnitude of the downward propagating IKW is also plotted for comparison, and the propagating component may be seen to be the dominant contribution to the forced response for $N|\ell/\sigma|\ z < -0.5$. The offshore structure of the surface trapped response is depth dependent and also differs for $\ell/\sigma \gtrless 0$. In both cases, near the surface the magnitude of the response grows as a function of x to some maximum near $f|\ell/\sigma| = 0.2$ and decays with a Rossby radius scale for $f|\ell/\sigma|x > 0.2$.

Figure 7 shows v at x = 0 for various z as a function of $\theta = \sigma t - \ell y$ with $\ell/\sigma < 0$. The outstanding feature is the reversal of phase with depth, where the signal at $N|\ell/\sigma|z = -0.2$ lags the signal above and leads the signal below. The phase behavior near the surface reflects the superposition in time of the vertically propagating and the surface trapped components, while for $N|\ell/\sigma|z < -0.5$, the vertically propagating component dominates the response and the phase lag is consistent with a downward propagating IKW (the dashed line in Figure 7 represents the phase lag expected for a free downward propagating IKW).

4. INTERNAL DISSIPATION

The theory presented in Sections 2 and 3 is limited by the neglect of bottom topography. For forcing at the surface, an initial disturbance must propagate from the surface to the bottom and back to a subsurface point z before the effect of the bottom is felt at z. Figure 8 shows the scaled time $t^* = f^2 L T_t/(N H_0)$ it takes for an internal Kelvin wave with frequency ω and horizontal wavenumber ℓ to propagate at its group velocity from the surface to the bottom $z = -H_0$, as a function of $\omega' = \omega/f$ and $\ell' = L\ell$ ($T_t = H_0/c_{gz}$). The figure indicates that waves with lower frequency or larger wavenumber ℓ travel more slowly. With L = 1000 km, H_0 = 2 km, $f = 1.3 \times 10^{-5}$ s^{-1} (5°S latitude) and $N = 4 \times 10^{-3}$ s^{-1}, a wave with λ_y = 1000 km, $T = 2\pi/\omega$ = 5.7 days takes approximately 3 days to reach the bottom while a wave with T = 25 days takes about 30 days.

Internal dissipation, which causes an energy decay with time, may prevent the energy that is reflected at the bottom from affecting the response near the surface. For such cases, the response obtained with an infinitely deep ocean may be valid near the surface for much longer times than indicated on Figure 8. We next examine this point, using a model which allows the vertical mixing of heat and momentum in the deep ocean.

The linearized equations are (2.1a), (2.1c), (2.1d) and

$$v_t + fu = -p_y + \nu v_{zz}, \tag{4.1a}$$

$$\rho_t + \bar{\rho}_z w = \kappa \rho_{zz}, \tag{4.1b}$$

where ν and κ are coefficients of vertical eddy viscosity and diffusivity, respectively, assumed constant.

Eqs. (2.1a,c,d) and (4.1a,b) may be combined to form a single equation for p, given by

$$[p_{xx} + (f/N)^2 p_{zz}]_t - \nu[p_{xx} + (f/N)^2 Pr^{-1} p_{zz}]_{zz} = 0, \qquad (4.2)$$

where $Pr = \nu/\kappa$ is the Prandtl number and where for simplicity we assume that N = constant. Regularity conditions as $x \to \infty$ and $z \to -\infty$ are given by (2.9a,b) and the remaining boundary conditions are

$$p_{xt} + f p_y - \nu p_{zz} = f\tau(y,t)\, \delta(z), \qquad \text{at } x = 0, \qquad (4.3a)$$

$$p_{zt} = (\kappa/N^2)\, p_{zz}, \qquad \text{at } z = 0. \qquad (4.3b)$$

Eq. (4.2) and conditions (4.3a,b) are analagous to (2.3), (2.6) and (2.8) for the inviscid case.

(a) Free wave solution

Before solving the forced problem, we obtain the free wave solution to (4.2) for a vertically unbounded ocean subject to a homogeneous version of (4.3a) with condition (4.3b) dropped. The assumed form of the free wave is given by (2.11). The x structure and the dispersion relation are derived in a manner similar to that in Section 2a and are given by

$$\phi = \exp[-(fm/N)\, (1 + im^2\kappa/\omega)^{\frac{1}{2}}\, (1 + im^2\nu/\omega)^{-\frac{1}{2}} x], \qquad (4.4a)$$

$$\omega = (N\ell/m)\, (1 + im^2\kappa/\omega)^{\frac{1}{2}}\, (1 + im^2\nu/\omega)^{-\frac{1}{2}}. \qquad (4.4b)$$

These reduce to (2.14) and (2.15) when $\nu = \kappa = 0$. For the general case $Pr \neq 1$, there is an offshore phase shift induced by internal dissipation, as well as a correction to the offshore structure. The frequency and hence the phase speed is modified and ω has a negative imaginary part which corresponds to a decay with time.

The special case $Pr = 1$ yields

$$\phi = \exp(-fmx/N), \tag{4.5a}$$

$$\omega = N\ell/m - im^2\nu, \tag{4.5b}$$

i.e., the phase speed and offshore structure are unaffected by dissipation (see (2.14) and (2.15)), but a decay with time is still present.

We may estimate a dissipation decay time,

$$T_d = (m^2\nu)^{-1} = (\omega^2/\nu)\ (N\ell)^{-2}, \tag{4.6a}$$

from (4.5b) with (2.11) for the free vertically propagating waves. The ratio,

$$T_d/T_t = \omega(m^3\nu H_0)^{-1} = \omega^4(\nu H_0)^{-1}\ (N\ell)^{-3}, \tag{4.6b}$$

gives a measure of the effectiveness of dissipation in damping the wave before a reflection occurs at the bottom. For $T_d/T_t \gg 1$, the wave reflects many times at the surface and the bottom before it decays, while for $T_d/T_t \ll 1$ dissipation damps the wave before a single reflection takes place.

Figure 9 shows $(\nu H_0 N^3 f^{-4} L^{-3})(T_d/T_t)$ plotted as a function of ω and ℓ. The waves are damped more effectively for shorter wavelength

or lower frequency. The dependence on the dimensional magnitude of ν is shown in Figure 10, where T_d/T_t is plotted as a function of ω and ν, with λ_y = 1000 km, N = 4 x 10^{-3} s^{-1}, f = 1.3 x 10^{-5} s^{-1}, and H_0 = 2 km.

(b) Forced problem

As in Section 2b, we represent the solution to (4.2) subject to (4.3a,b), (2.8) and (2.9) in terms of its Fourier cosine transform in z, given by (2.17a,b). In doing this, we assume that each side of (4.3b) is zero independently, i.e., that both w = 0 and the perturbation density ρ = 0 at the ocean surface. This requirement on ρ implies that the basic state density or temperature at the surface is fixed. A more appropriate condition would specify a relationship between heat flux and other parameters. However, we are concerned mainly with the velocity structure of the forced response and the condition on ρ invoked above has been commonly utilized (Pedlosky, 1974; Allen, 1973; McCreary, 1981).

With Pr = 1, the transformed equation and boundary conditions have a solution given by (2.19) where

$$-(m/N)\,\hat{Y}_t + \hat{Y}_y - (\nu m^3/N)\hat{Y} = \tau(y,t). \qquad (4.7)$$

Eq. (4.7) is a forced first order wave equation similar to (2.20) for the inviscid case but which contains an additional term due to internal friction. The general solution for $\tau(y,t) = \tilde{F}(y)\,\tilde{T}(t)$ is (2.27), where

$$p_D = -(2n/\pi)\int_0^\infty \tilde{F}(y + Nt/m)\exp(-fmx/N - \nu m^2 t)\, m^{-1} \cos mz\, dm. \qquad (4.8)$$

With the wind stress τ given by (3.2a) (Example A from Section 3),

$$p = (2/\pi)\ (N\tau_0/y)\ \cos(Ntz/y)\ \exp(fxt/y - \nu N^2 t^3/y^2), \qquad y < 0. \quad (4.9)$$

This response is similar to the inviscid response (3.1b) except that there is a decay in time due to the effect of dissipation. At a fixed location the damping behaves like $\exp(-\nu t^3)$, which with (3.5), may also be expressed as $\exp(-\nu m_0^2 t)$, where m_0 is the local vertical wavenumber. Thus, locally the forced response decays on the same time scale as the free waves of Section 4a.

5. EFFECT OF A BOTTOM BOUNDARY

(a) Inviscid case

In order to examine the effects of a bottom boundary at $z = -H_0$, the radiation and regularity conditions that apply to the unbounded ocean are replaced by the boundary condition $w = 0$ at $z = -H_0$. In terms of pressure, (2.5) implies that (2.8) holds also at $z = -H_0$. The remaining equations are (2.3), (2.6), and (2.9a), where again N is assumed constant for simplicity.

In this section it is useful to define variables $\hat{x}$ and $\hat{z}$, where we scale x with the internal Rossby radius scale and z with the depth, i.e.,

$$\hat{x} = f \pi (NH_0)^{-1} x, \qquad \hat{z} = z/H_0. \tag{5.1a}$$

In addition, we define

$$\hat{y} = \sigma \pi (NH_0)^{-1} |y|, \qquad \hat{t} = t. \tag{5.1b}$$

The solution is conveniently represented by expanding the pressure in terms of vertical modes. This gives

$$p = \sum_{m=0}^{\infty} \phi_m(x,y,t) \cos(m\pi\hat{z}). \tag{5.2}$$

Substitution of (5.2) in (2.3) and utilization of the orthogonality of the vertical eigenfunctions gives

$$\phi_{mxx} - (fm\pi)^2 (NH_0)^{-2} \phi_m = 0. \tag{5.3}$$

Solving (5.3) subject to (2.9a), we obtain

$$\phi_n = \exp(-n\hat{x})\ Y_n(y,t), \qquad n = 1, 2... \tag{5.4}$$

Substitution of (5.4) and (5.2) in (2.6) yields

$$-\ n\pi(NH_0)^{-1}Y_{nt} + Y_{ny} = (2/H_0)\ \tau(y,t). \tag{5.5}$$

The $n = 0$ term is $\phi_0 = Y_0(y,t)$ and it corresponds to the representation, within $x \leq O[NH_0(f\pi)^{-1}]$, of the barotropic response that varies on the larger scale $L_x >> NH_0(f\pi)^{-1}$.

For

$$\tau(y,t) = H(-y)\ H(t)\ \mathrm{Re}\{\exp(-i\sigma t)\}, \tag{5.6}$$

we obtain

$$v = p_x(\rho_0 f)^{-1} = 2i\tau_0(\rho_0 H_0 \sigma)^{-1}\ \exp(-i\hat{t})$$

$$\times \{ \sum_{n=1}^{\infty} \exp(-n\hat{x})\ \cos(n\pi\hat{z})$$

$$+ \sum_{n=1}^{J} \exp[-n\hat{x} + in\hat{y}]\ \cos(n\pi\hat{z}) , \qquad y < 0, \tag{5.7a}$$

where

$$J = [\hat{t}/\hat{y}] \tag{5.7b}$$

is the largest integer less than $\hat{t}/\hat{y}$. The first sum is the particular solution to (5.5) while the partial sum is required to satisfy $v = 0$ for $y = 0$.

The series in (5.7a) may be summed to yield

$$v = 2i\tau_0(\rho_0 H_0 \sigma)^{-1} \exp(-i\hat{t})$$
$$\times \{\tfrac{1}{2} + \tfrac{1}{2} \sinh \hat{x}(\cosh \hat{x} - \cos\pi\hat{z})^{-1} - q^J \cos(J\pi\hat{z})$$
$$- [1 - q\cos(\pi\hat{z}) - q^J \cos(J\pi\hat{z}) + q^{J+1} \cos((J-1)\pi\hat{z})]$$
$$\times [1 - 2q\cos(\pi\hat{z}) + q^2]^{-1}\}, \quad y < 0, \tag{5.8a}$$

where

$$q = \exp[-\hat{x} + i\hat{y}]. \tag{5.8b}$$

Figure 11 shows v from (5.8) as a function of $\hat{z}$ and $\hat{t}$ for $\hat{y} = \pi/2$, and illustrates the adjustment toward the long time solution. The behavior is similar to that shown in Figure 4, which is the response of an infinitely deep ocean that is obtained with (3.15), (3.17), and $|\ell y| << 1$. At an alongshore location y, the response is entirely due to the periodic forcing at the surface until the effect of the step function at y = 0 propagates past y. This occurs at $t = f\pi(N_0 H)^{-1}|y|c_1^{-1}$ when the first mode, which travels the fastest, passes y. The response shown in Figure 11 develops as the higher mode propagate past y.

The limiting solution for v as $J \to \infty$, which corresponds to long time after transients have dispersed may be obtained from (5.7a) and is given by

$$v = \tfrac{1}{2}\tau_0(\rho_0 H_0 \sigma)^{-1} \{\sin\hat{t} \sinh\hat{x} [2(\cosh\hat{x} - \cos\pi\hat{z})^{-1} - (\cosh\hat{x} - \cos\mu_-)^{-1}$$
$$- (\cosh\hat{x} - \cos\mu_+)^{-1} - \cos\hat{t}[\sin\mu_+(\cosh\hat{x} - \cos\mu_+)^{-1}$$
$$- \sin\mu_-(\cosh\hat{x} - \cos\mu_-)^{-1}]\}, \quad y < 0, \tag{5.9}$$

where

$$\mu_{\pm} = \pi\hat{z} \pm \hat{y}. \tag{5.10}$$

The long time response (5.9) is periodic in $\hat{y}$ and $\hat{t}$ with a maximum in v for z = 0 and near $\mu_{\pm} = 2k\pi$, k = 0, 1, 2..... Figures 12a,b show the magnitude and phase of v, where $v = 2i\tau_0 \ (\rho_0 H_0 \sigma)^{-1} V \exp(-i\hat{t})$, from (5.8a) with J >> 1, as a function of $\hat{y}$ and $\hat{z}$. The subsurface maximum along $\mu_{\pm} = 0$ (Figure 12a) is associated with the ray path for a free vertically propagating IKW with frequency $\omega = \sigma$ that passes through $\hat{y} = 0$, $\hat{z} = 0$ and travels to the bottom, while the maximum along $\mu_{-} = 2\pi$ is associated with the ray path of the reflected wave that propagates from the bottom to the surface. Subsequent reflections at $\hat{z} = 0$ and $\hat{z} = -1$ occur periodically in $\hat{y}$. In regions where the ray path implies downward (upward) propagation of energy, the phase velocity is directed upward (downward). This is illustrated in Figure 12b, which shows the phase of V.

The adjustment toward the long time solution (Figure 11) shows that a maximum in v propagates from the surface to a depth where it intersects the ray path shown in Figure 12a. The maximum subsequently remains at the location of the ray path.

With the conditions

$$\pi\hat{z} << 1, \qquad \hat{x} << 1, \qquad \hat{y} << 1, \tag{5.11}$$

(5.8) may be shown to be asymptotically equal to (3.20), the response of an infinitely deep ocean which is obtained in Section 3c with (3.15), (3.17), and $|\ell y| << 1$. Similarly, with (5.11), the long time solution (5.9) is asymptotically equal to (3.21a). Hence,

for forcing given by (5.6), (5.11) establishes limits on the validity of the analysis in Sections 2 and 3. For example, with the parameters chosen above, the effect of a bottom may be neglected for $|z| \ll 0.64$ km, $x \ll 196$ km, and $|y| \ll 875$ km.

(b) Internal friction

The inviscid analysis of the previous section predicts an infinite number of reflections at $\hat{z} = 0$ and $\hat{z} = -1$, periodic in $\hat{y}$. The effect of internal dissipation modifies this behavior. Equations and boundary conditions for this problem with friction are (4.2), (4.3a), and (4.3b).

The response to a wind stress $(y,t) = \tilde{F}(y)\,\tilde{T}(t)$, derived as in Section 5a, with Pr = 1, is given by

$$p = -(2n/\pi)\int_{t_0}^{t} \sum_{n=1}^{\infty} n^{-1}\exp[-n\hat{x} - \nu(n\pi/H_0)^2(t-\alpha)]\cos(n\pi\hat{z})\tilde{F}[y+NH_0(n\pi)^{-1}(t-\alpha)] \times \tilde{T}(\alpha)\,d\alpha, \qquad y < 0. \tag{5.12}$$

The form of (5.12) is similar to the inviscid solution, with an additional term which corresponds to an exponential damping due to dissipation. The effect of dissipation is greater for higher mode number n. With the forcing (5.6),

$$\begin{aligned} v = 2\tau_0(\rho_0 H_0)^{-1} \sum_{n=1}^{\infty} &\exp(-n\hat{x})\cos(n\pi\hat{z})\,(\sigma^2 + r^2n^4)^{-1} \\ &\times \{rn^2\cos\hat{t} + \sigma\sin\hat{t} \\ &- H(\hat{t} - \hat{y})[rn^2\cos(\hat{t} - n\hat{y}) + \sigma\sin(\hat{t} - n\hat{y})]\exp(-r\hat{y}\,n^3/\sigma) \\ &- H(\hat{y} - \hat{t})\,rn^2\exp(-rn^2t)\}, \qquad y < 0, \end{aligned} \tag{5.13a}$$

where

$$r = \nu(\pi/H_0)^2. \tag{5.13b}$$

The first two terms in the curly brackets represent a particular solution while the remaining terms are required to satisfy $v = 0$ for $y = 0$, and represent the effect of the step function at $y = 0$.

The long time behavior, which may be obtained from (5.13a) by letting $t \to \infty$ is no longer periodic in y. The effect of the step function decays rapidly with y for high mode number, and only the effect due to the lowest several modes remains. The beam pattern which results from the inviscid analysis only exists near $y = 0$, and far from the origin the response exhibits no vertical phase propagation.

6. DISCUSSION

Utilizing a simple f-plane model with a vertical boundary, we have shown that under certain conditions vertically propagating sub-inertial motions may be forced by the alongshore component of the wind at the coast. Several examples which illustrate the basic properties of the forced flow are presented in Section 3. A Green's function for impulsive forcing at a point on the surface (Example A) is shown to result in vertically propagating free coastally trapped internal Kelvin waves. The waves propagate poleward on an eastern boundary and the group velocity vector is directed downward while the phase propagation is upward. When the local vertical wavelength is much less than the distance to the surface, the disturbance appears like a free wave with local frequency and wavenumbers.

With $N = 4 \times 10^{-3}\ s^{-1}$ and $\lambda_y \simeq 1000$ km, the dispersion relation (2.15) gives $\lambda_z \simeq 0.7$ km and $c_z \simeq -30$ m day^{-1} for $T = 25$ days. This estimate for λ_z indicates that it is unlikely that the low frequency signal in Figure 1, which is measured at depths $|z| < 0.8$ km, i.e., $|z| \leq \lambda_z$, may be explained in terms of a single wave with fixed frequency or wavenumbers.

Example B illustrates the effect of forcing that is initiated at $t = 0$ and that is oscillatory in time and localized in space. Changes in amplitude and frequency content with depth are predicted, as well as an upward propagation of phase. Both a transient component and a response at the forcing frequency ω are generated. Initially, when the transients are still important, a maximum in v propagates downward until it intersects the ray path, which passes

through $y = 0$, $z = 0$, of a free vertically propagating IKW with frequency $\omega = \sigma$. The maximum subsequentially remains on the ray path and, for long time, after the transients have decayed, the forced response exhibits a subsurface maximum in the y-z plane associated with this free IKW ray path.

In Example C, the wind stress is modelled by a traveling wave with step functions in y and t. The step function in y is an approximate model for low latitudes, where the presence of the equator introduces an effective step function behavior to the forcing, since a wind stress applied at a location is felt only poleward of that location. With the forcing given in Example C, the response has a very different qualitative behavior in two limiting cases. For $|y| << \lambda_y$, the solution resembles that of Example B, with a maximum in v which initially amplifies and propagates downward and with a subsurface maximum associated with the free IKW ray path for long time. This behavior reflects the presence of the step function at $y = 0$.

The limits $fxt/|y| >> 1$ and $|y| >> \lambda_y$, which corresponds to long time so that the transients have vanished and an alongshore location far from the influence of the step function at $y = 0$, yield a different response. A standing component that decays with depth from the surface and that is trapped within a Rossby radius of the coast is forced for $\sigma/\ell < 0$ (poleward traveling wind) and $\sigma/\ell > 0$ (equatorward traveling wind). For $\sigma/\ell < 0$, an additional propagating component is forced, which represents a coastally trapped IKW with negative vertical group velocity and upward phase propagation. The response to forcing by a wind stress that is standing in the

alongshore direction may be obtained by summing the effects of traveling waves with $\sigma/\ell > 0$ and $\sigma/\ell < 0$. For this case, downward propagating waves will be generated by the poleward propagating component of the wind while a surface trapped response will be generated by both poleward and equatorward traveling components of the wind. For $|z| > |\sigma/N\ell|$, the surface trapped component is small compared to the vertically propagating component. With the parameters chosen above, the vertically propagating IKW is the dominant response for $z \leq -115$ m, i.e., below 115 m one would expect to see an upward propagation of phase associated with downward propagating IKWs, while above 115 m the surface trapped component of the forced response will be important and a more complicated phase dependence with depth would be expected.

These examples illustrate how the coastal response is sensitive to the exact nature of the wind forcing. The response to an initial disturbance is very different from the flow due to a steady forcing, and the behavior near the origin of a step function in y (i.e., near the equator) differs considerably from the behavior far from the origin. The examples also indicate the dependence of the oceanic response on the frequency-wavenumber structure of the wind forcing. Based on these examples, together with the analysis of Sections 4 and 5, we may make some general statements about the conditions for which vertically propagating coastally trapped waves would be observed in the ocean.

For an initial disturbance at the surface, with a general frequency-wavenumber spectrum and large alongshore scale, downward propagating energy would be observed for those frequency-wavenumber

components of the forced response that have not reflected from the bottom. Those components that have reflected from the bottom will exhibit a more complicated vertical phase dependence due to the superposition of downward and upward propagating energy. Figure 8 shows the time required for an IKW to reach the bottom as a function of ω and ℓ. Waves with higher frequencies and longer wavelengths travel faster.

The energy of the disturbance may dissipate before a round trip from the surface to the bottom to the surface is completed and hence internal dissipation may prevent the interference of reflected energy with downward propagating energy, even for longer time. With these conditions, one would expect to see vertically propagating waves near the surface for those frequencies and wavenumbers where they are damped effectively by internal dissipation. The ratio of dissipation decay time to travel time (T_d/T_t) is shown in Figures 9 and 10. Internal dissipation damps the waves more effectively for shorter wavelength or lower frequency. For λ_y = 1000 km and with $\nu \simeq 10$ cm^2 s^{-1}, $T_d/T_t < 1$ for $\omega/f < 0.2$, i.e., free waves are damped considerably before a reflected wave reaches the surface. At 5° latitude, $\omega/f = 0.2$ corresponds to T = 28.5 days.

These simple calculations may explain why vertically standing coastally trapped waves are observed along the Peru coast in the 5-10 day band (Smith, 1978; Brink, Allen, and Smith, 1978; Romea and Smith, 1982) while relatively large phase lags are observed in the vertical for perturbations in velocity for T > 25 days (Figure 1).

For cases where dissipation or long travel times may not be invoked in order to neglect the effects of reflection from the ocean

bottom, the calculations of Section 5 suggest that, near the equator, where the wind forcing may be approximated with a step function behavior in y, the results of Example C, with $|y| \ll \lambda_y$, apply for $|z| \ll H_0/\pi$ and $|y| \ll (NH_0/f\pi)(f/\sigma)$. An example in Section 5 with $T \simeq 25$ days, at 5° latitude and with $H_0 \simeq 2$ km shows that the effect of the bottom may be ignored for $|z| \ll 0.64$ km, $|y| \ll 875$ km. For an initial forcing at the surface, an upward propagation of phase would be expected associated with the propagation of a subsurface maximum in v downward. For longer time, the response to steady forcing at a frequency σ has a maximum along a line $z = \sigma y/N$ which is associated with the IKW ray path, with an upward propagation of phase in the vicinity of the ray path. Since the ray path is a function of σ, the response to a wind with a general frequency spectrum and a step function at $y = 0$ will consist of many rays emanating from $y = 0$, $z = 0$, and an upward propagation of phase will be observed near $y = 0$ over much of the depth.

At 5°S latitude, with $|y| \simeq 550$ km (the approximate distance near the equator to the ESACAN array), $T \simeq 25$ days and $N \simeq 4 \times 10^{-3}$ s^{-1}, the subsurface maximum propagates downward at about 40 m day^{-1} and intersects the IKW ray path at about 400 m depth. This is in qualitative agreement with the observations shown in Figure 1, although more extensive measurements for longer times are needed to obtain an accurate description of low frequency phenomena along the Peru coast at low latitudes.

Finally, we point out several interesting questions: (1) Do low frequency waves that are forced along the equator and that propagate vertically turn at the intersection of the equator with the

Peru-Equador coast and travel north and south as vertically propagating IKWs? (2) Can vertically propagating IKWs transfer momentum downward and interact with the mean flow? These questions suggest avenues for further theoretical studies.

FIGURE CAPTIONS

Figure 1. Time series of low-pass filtered alongshore wind from Talara (top plot) and of alongshore current v (solid line) and temperature T (dashed line) from the ESACAN C2 mooring, which was on the continental slope in 1360 m of water at 5°S latitude. The low pass filter has a half power point of 8.5 days.

Figure 2. Scaled alongshore velocity $v^* = [(2/\pi)\ N\tau_0\ (\rho_0|y|fx)^{-1}]^{-1}v$ as a function of $t' = fxt/|y|$ and $z' = Nz(fx)^{-1}$ for Example A $[\tau(y,t) = \delta(y)\ \delta(t)\ \tau_0]$.

Figure 3. Scaled alongshore velocity $v^* = [(2/\pi)\ N\tau_0(\rho_0\sigma' f^2|y|)^{-1}v|y|]$ as a function of $t' = \sigma t$ and $z' = (N/\sigma)(z/|y|)$ with $x = x/(\sigma'|y|) = 0.04$, for Example B $[\tau(y,t) = \delta(y)\ H(t)\ \tau_0\ \exp(-i\sigma t)]$.

Figure 4. Scaled alongshore velocity $v^* = [(2/\pi)\ N\tau_0\ (\rho_0\sigma'^2 f^2|y|)^{-1}]^{-1}v$ as a function of $t' = \sigma t$ and $z' = (N/\sigma)(z/|y|)$ with $x' = x/(\sigma'|y|) = 0.04$, from Example C $[\tau(y,t) = H(-y)\ H(t)\ \tau_0\ \exp\{-i(\sigma t - \ell y)\}]$ for the limiting case $|\ell y| \ll 1$. Dark lines: contours of $v^* = 0$; light lines: $v^* > 0$; dashed lines $v^* < 0$; contour interval: 1.

Figure 5. Magnitude (a,c) and phase θ(b,d) of V for Example C as a function of $y' = y/L$ and z' (a,b) (with $x' = 0.04$) and as a function of x' and z' (c,d), where $v' = V\exp(-it')$. Limiting case $|\ell y| \ll 1$, $x't' \gg 1$. Scaling the same as in Figure 4. $\theta_1 > \theta_2$ implies 2 leads 1.

Figure 6. Scaled alongshore velocity $V^* = V/[(2/\pi)\ N\tau_0\ell(\rho_0\sigma^2)^{-1}]$

for Example C, obtained for the limiting cast $fxt/|y| \gg 1$ and $|\ell y| \gg 1$, as a function of $x^* = f\ell x/\sigma$ for various $z^* = N\ell z/\sigma$, where $v = V \exp[-i(\sigma t - \ell y)]$. The response is plotted for $\ell/\sigma > 0$ and $\ell/\sigma < 0$. The scale for V^* at $z^* = -0.2$ applies to V^* at all depths. The solid line represents the vertically trapped response while the dotted line represents the magnitude of the vertically propagating IKW. The two components are $\pi/2$ out of phase in time and are plotted on the same figure in order to compare magnitudes. The offshore distance $x^* = 1$ corresponds to the Rossby radius scale.

Figure 7. Scaled alongshore velocity $v^* = v/[2N\tau_0\ell(\rho_0\sigma^2)^{-1}]$ at $x = 0$ for Example C obtained with the limits $fxt/|y| \gg 1$ and $|\ell y| \gg 1$ as a function of $\theta = \sigma t - \ell y$ for various $z^* = N\ell z/\sigma$, with $\ell/\sigma < 0$. The straight lines connect the local maxima of v^* and indicate the vertical phase structure while the dashed line represents the vertical phase lag predicted for a free IKW with positive vertical phase velocity.

Figure 8. Scaled travel time $t^* = f^2Lt(NH_0)^{-1}$ for a free IKW with scaled frequency $\omega' = \omega/f$ and horizontal wavenumber $\ell' = \ell L$ to propagate at its group velocity from the surface to the bottom ($z = -H_0$), as a function of ω' and ℓ'.

Figure 9. Scaled ratio of dissipation decay time to travel time $(T_d/T_t)(\nu H_0 N^3 f^{-4} L^{-3})$ as a function of $\omega' = \omega f$ and $\ell' = \ell L$.

Figure 10. Ratio of dissipation decay time to travel time T_d/T_t as a function of $\omega' = \omega/f$ and ν, with $\lambda_y = 1000$ km, $N = 4 \times 10^{-3}$ s^{-1}, $f = 1.3 \times 10^{-4}$ s^{-1} and $H_0 = 2$ km.

Figure 11. Scaled alongshore velocity $v^* = v/[2\tau_0(\rho_0 H_0 \sigma)^{-1}]$ as a function of $\hat{z} = z/H_0$ and $\hat{t} = \sigma t$ for $\hat{y} = \sigma\pi(NH_0)^{-1}|y| = \pi/2$ and $\hat{x} = f\pi(NH_0)^{-1}\, x = 0.2$. Flat bottom at $z = -H_0$. Dark line: contour of $v^* = 0$; light line; contour of $v^* = 1$; dashed line: contour of $v^* = -1$.

Figure 12. Magnitude (a) and phase θ (b) of V as a function of $\hat{y}$ and $\hat{z}$, with $\hat{x} = 0.02$ and $\hat{t}/\hat{y} \gg 1$, where $v^* = iV \exp(-i\hat{t})$. Flat bottom at $z = -H_0$. Same scaling as in Figure 11. $\theta_1 > \theta_2$ implies 2 leads 1.

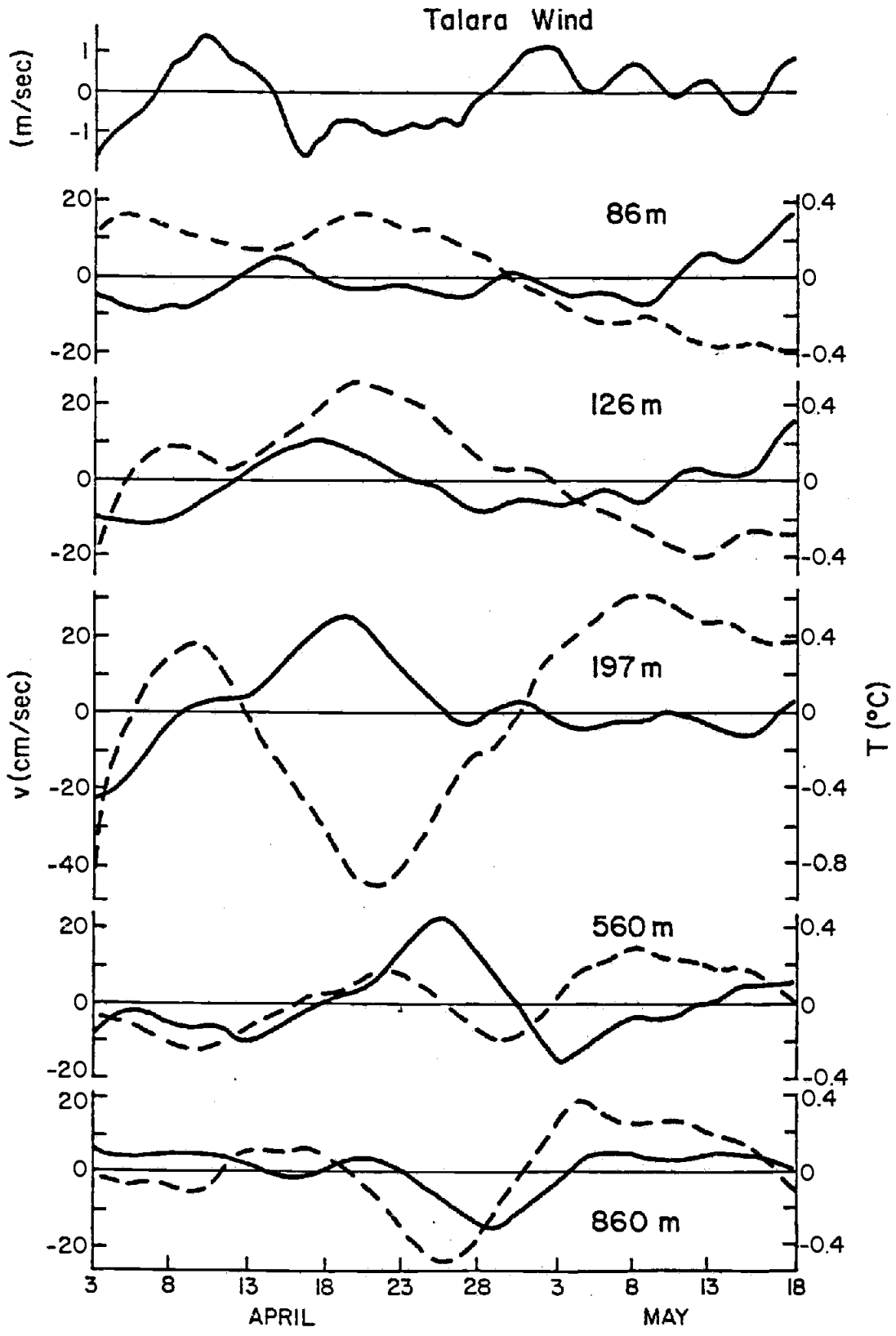
Talara Wind
(m/sec)
1
0
-1
86m
126 m
197 m
560 m
860 m
20
0
-20
0.4
0
-0.4
-40
-0.8
v (cm/sec)
T (°C)
3
8
13
18
23
28
3
8
13
18
APRIL
MAY

Figure III-1

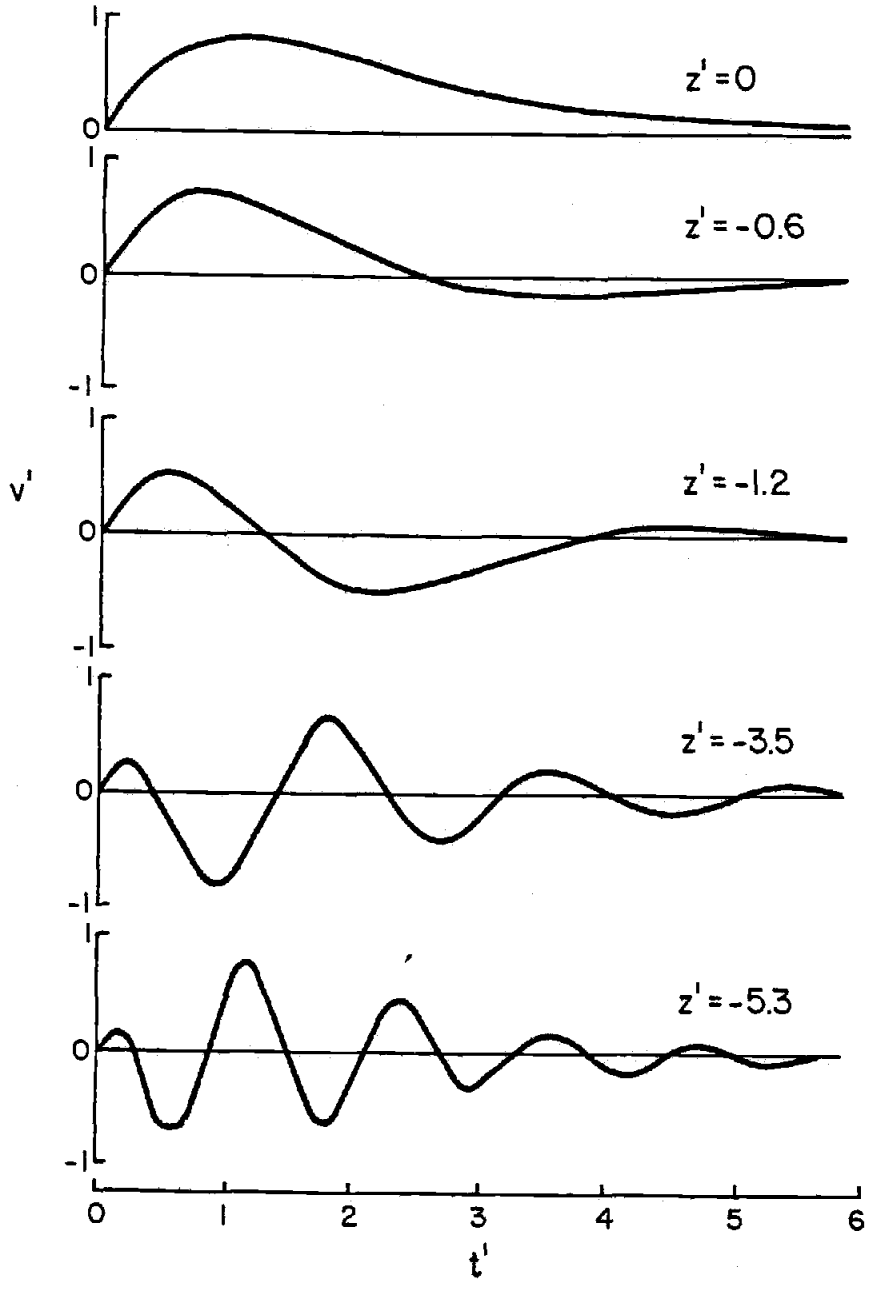

Figure III-2

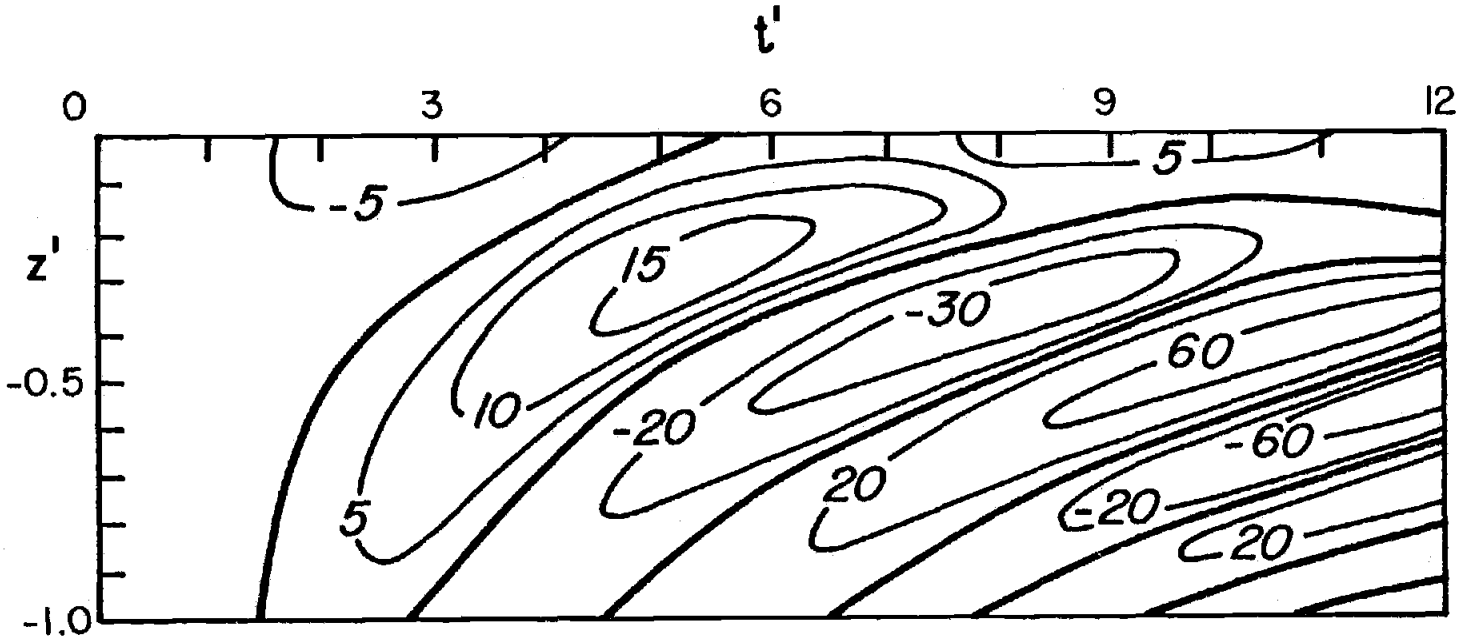

Figure III-3

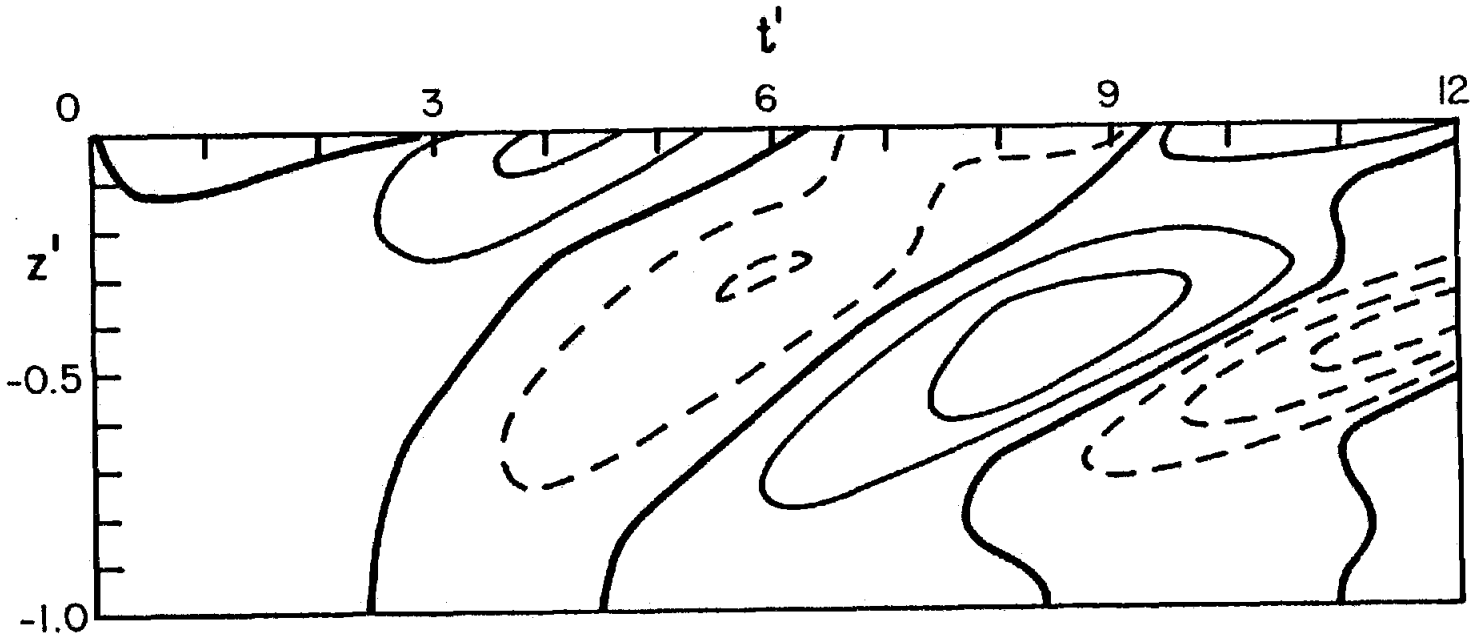

Figure III-4

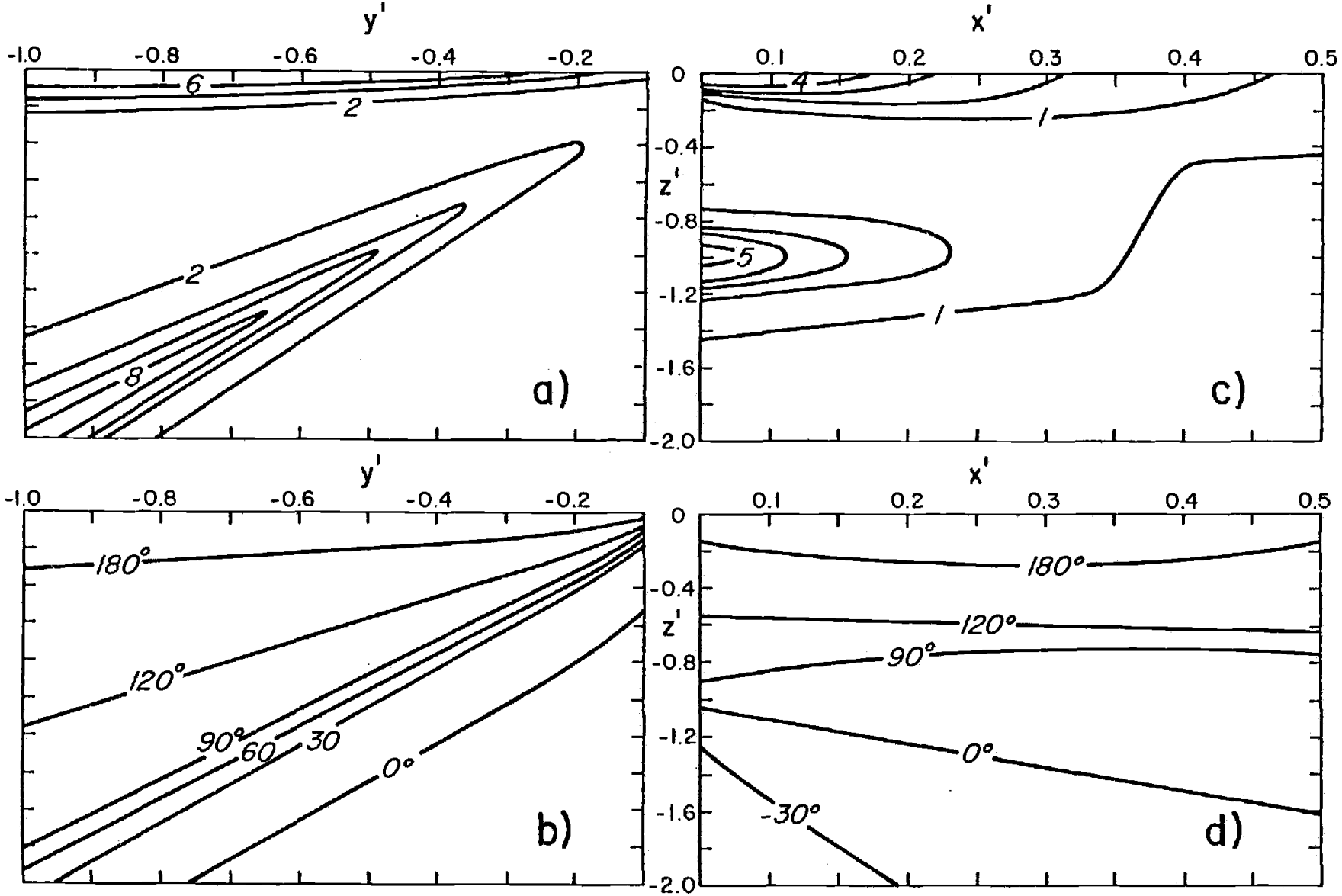
y'
-1.0
-0.8
-0.6
-0.4
-0.2
6
2
2
8
a)
x'
0.1
0.2
0.3
0.4
0.5
0
-0.4
z'
-0.8
-1.2
-1.6
-2.0
4
1
5
1
c)
y'
-1.0
-0.8
-0.6
-0.4
-0.2
180°
120°
90°
60
30
0°
b)
x'
0.1
0.2
0.3
0.4
0.5
0
-0.4
z'
-0.8
-1.2
-1.6
-2.0
180°
120°
90°
0°
-30°
d)

Figure III-5

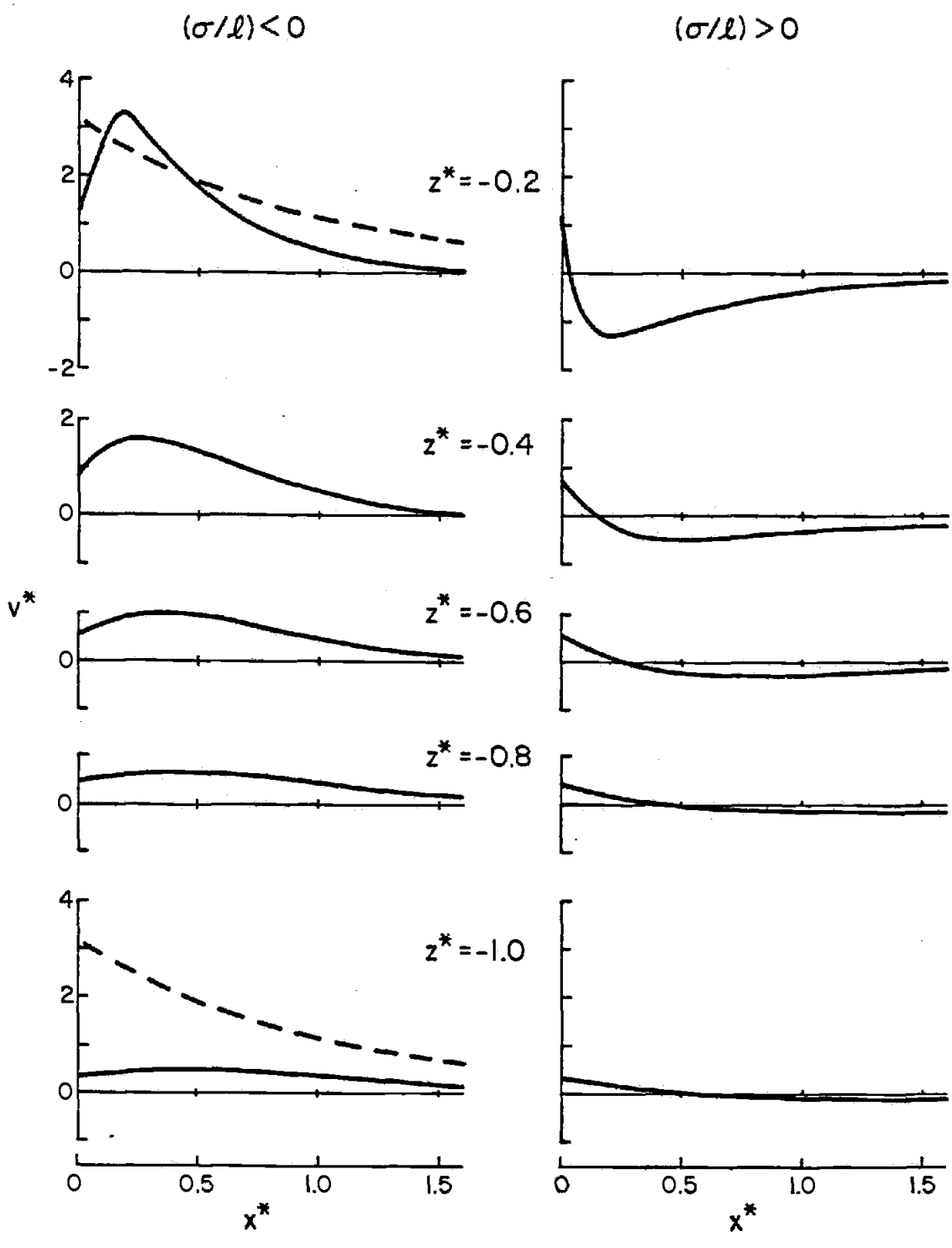

Figure III-6

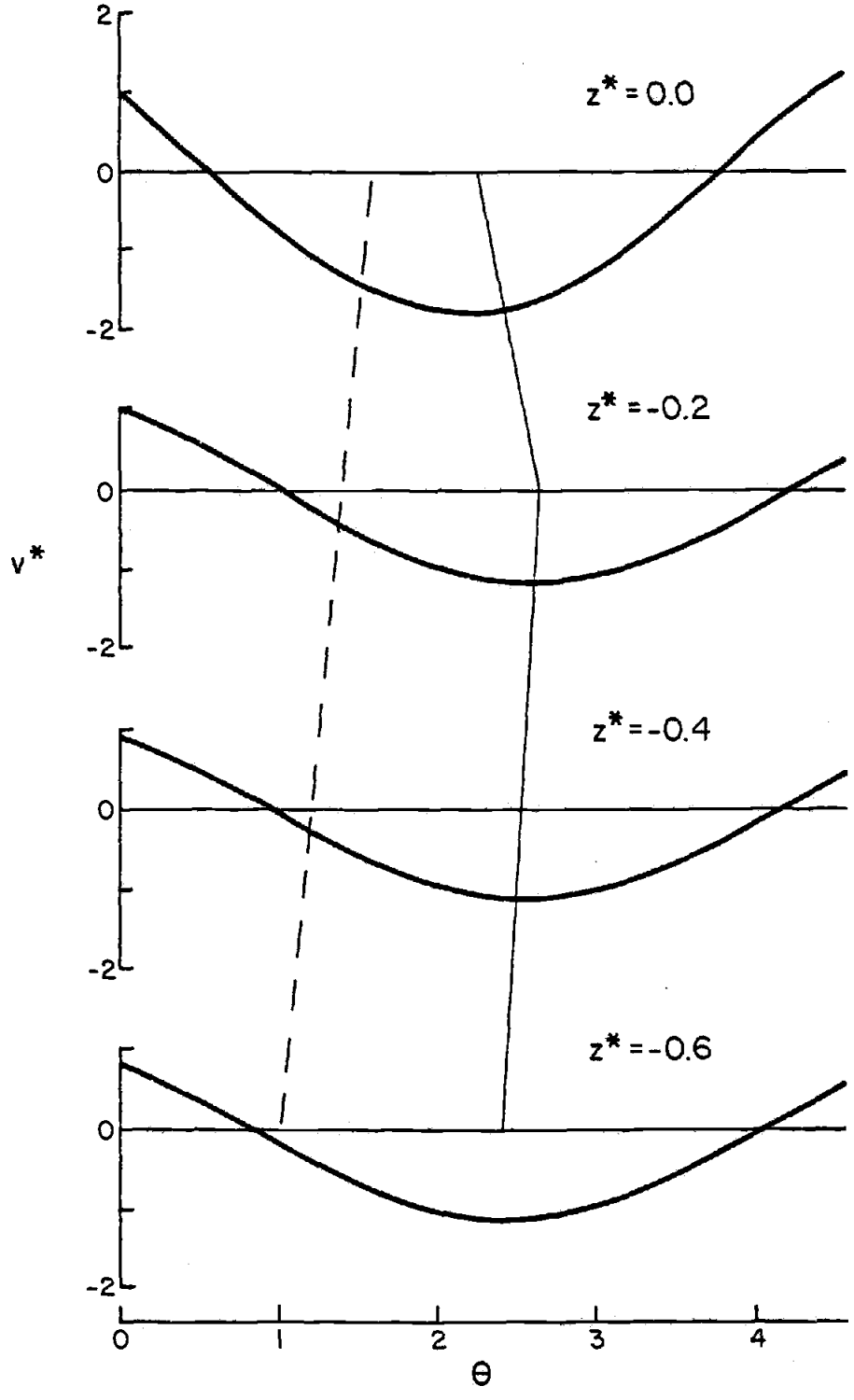

Figure III-7

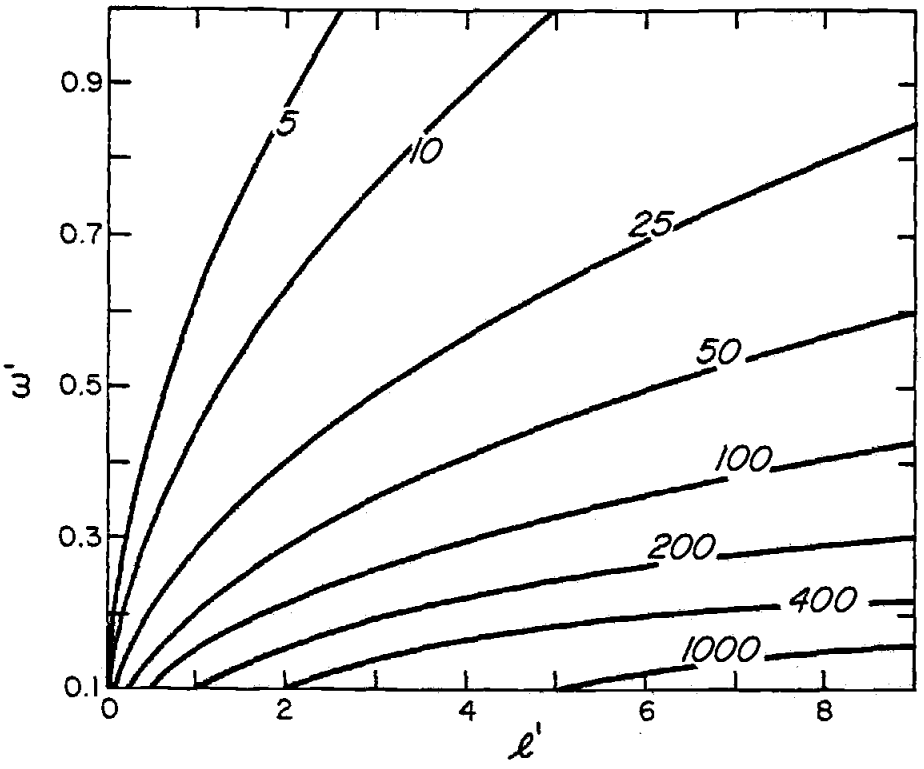

Figure III-8

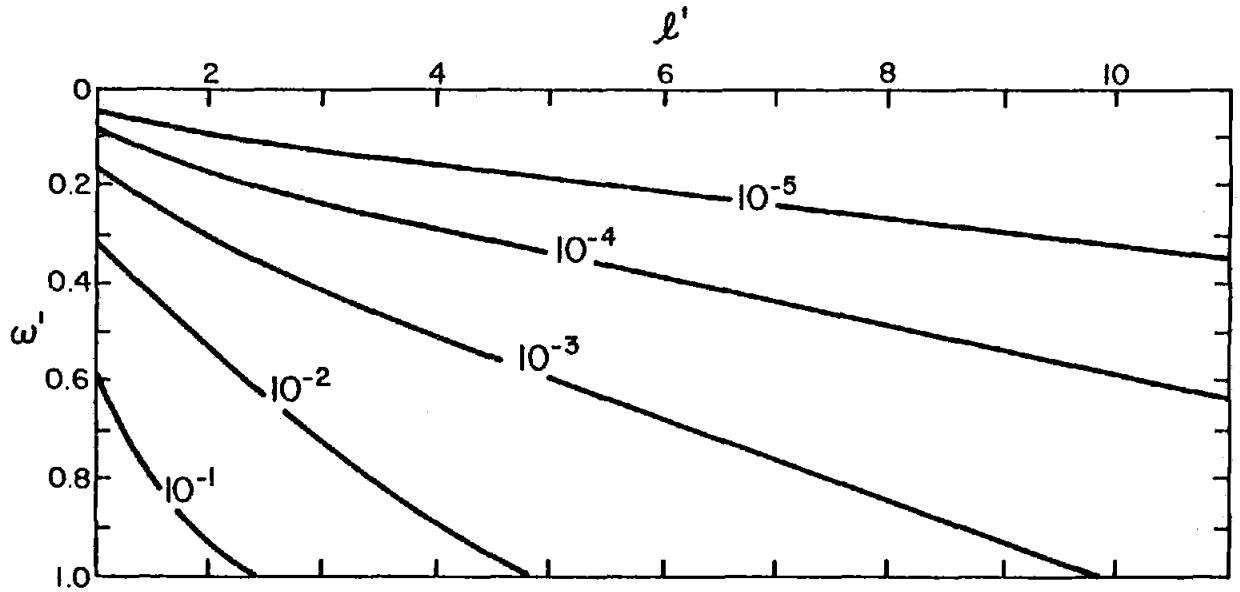

Figure III-9

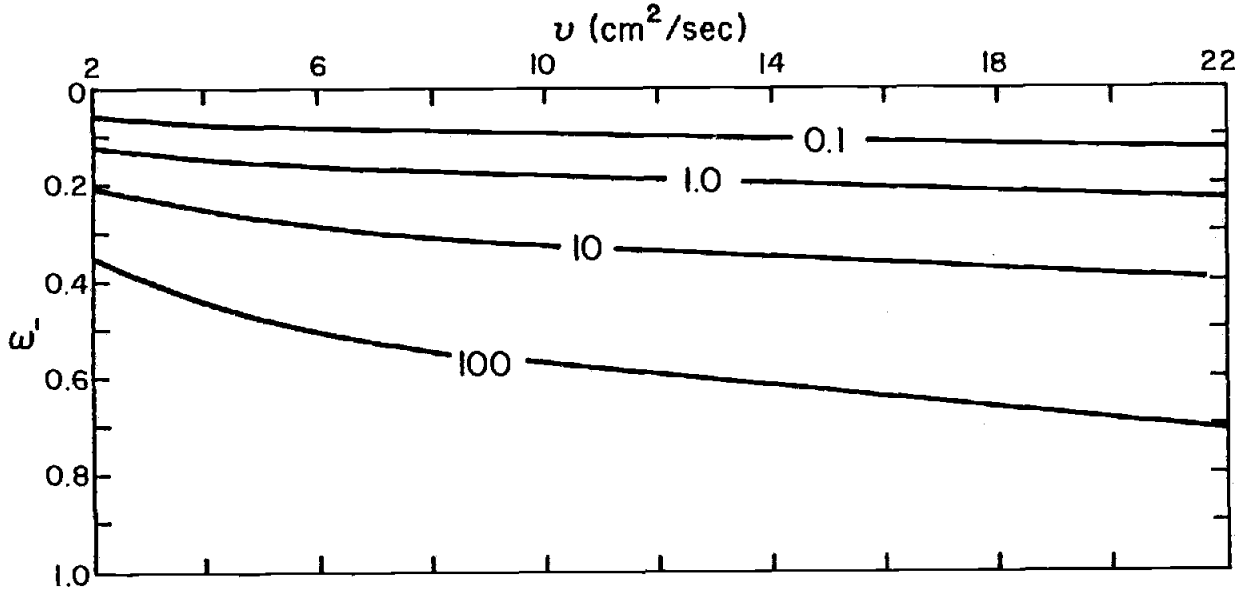

Figure III-10

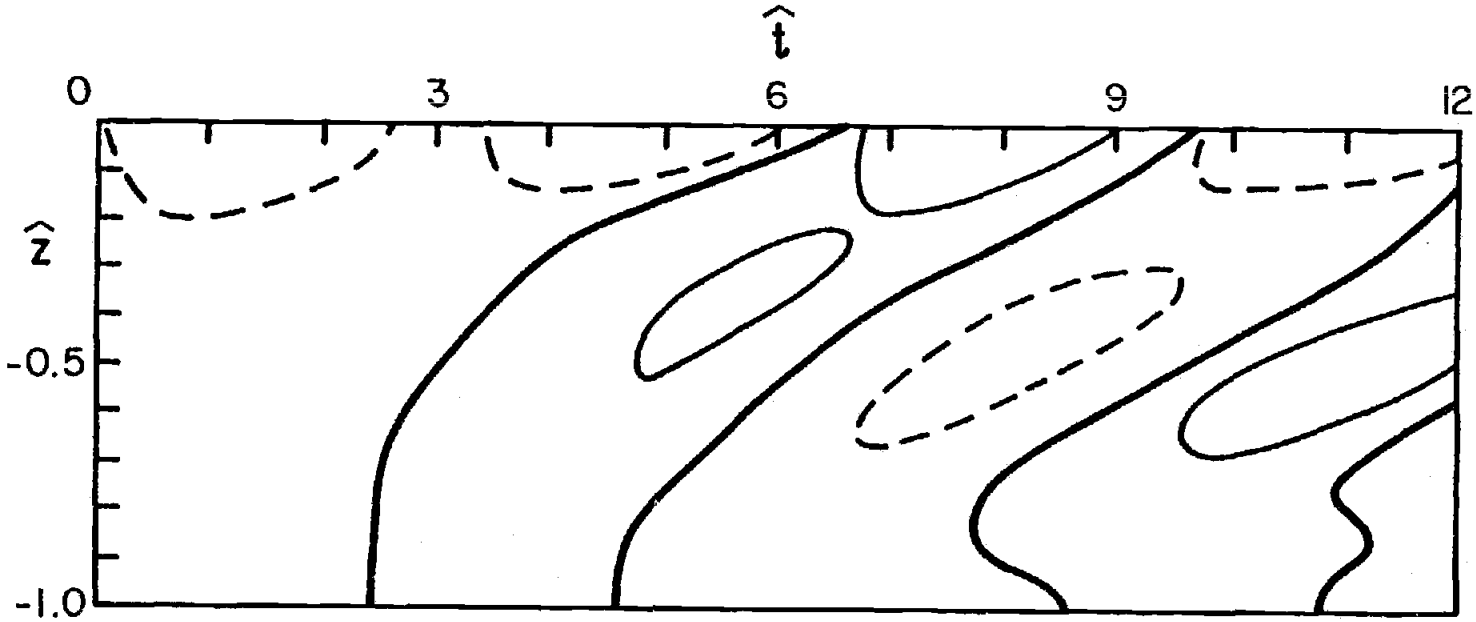

Figure III-11

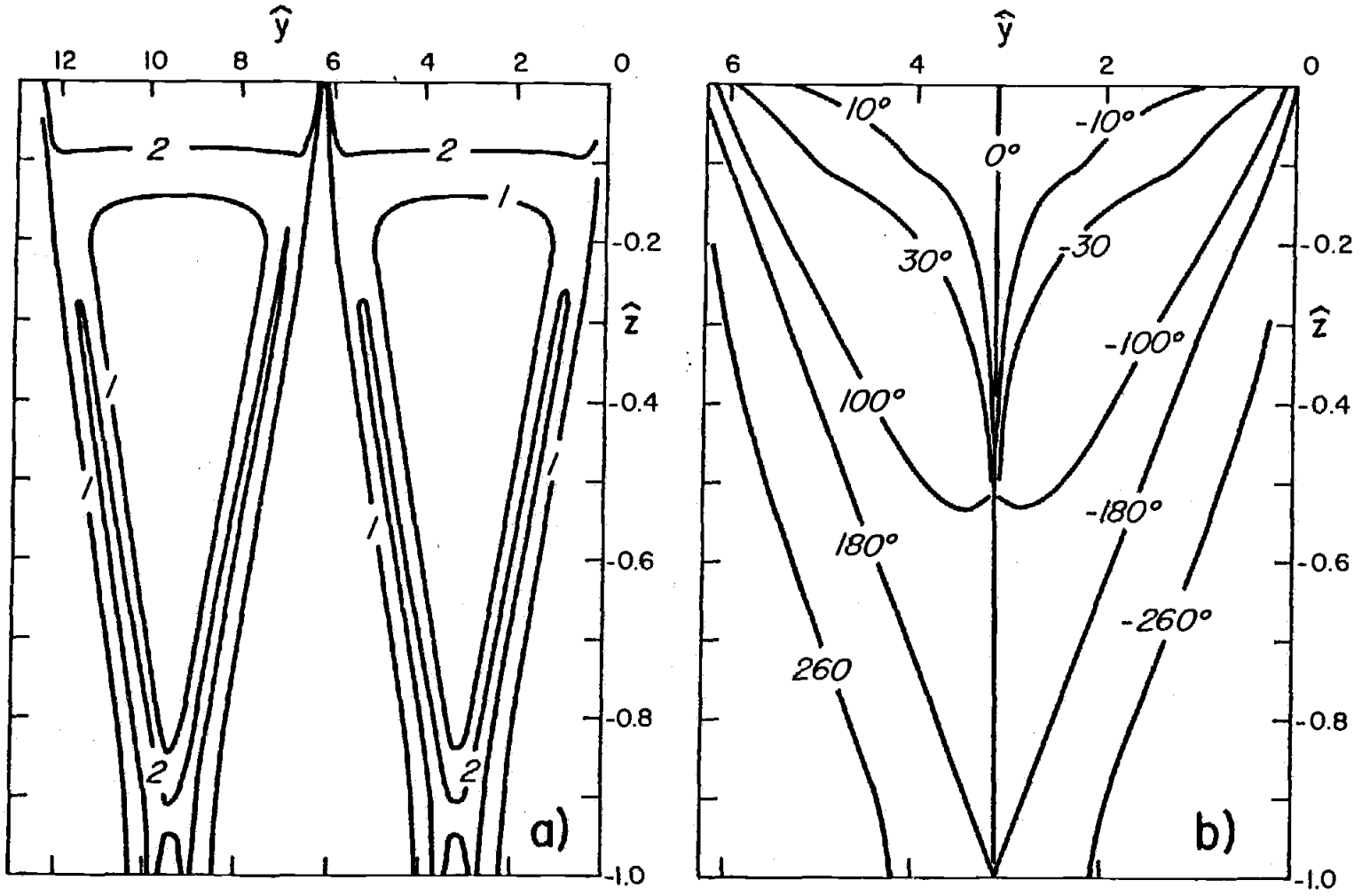

Figure III-12

REFERENCES

Allen, J. S., 1973. Upwelling and coastal jets in a continuously stratified ocean. J. Phys. Oceanogr., 3:245-257.

Allen, J. S., and Romea, R. D., 1980. On coastal waves trapped at low latitudes. J. Fluid Mech., 98:555-585.

Bretherton, F. P., 1970. The general linearized theory of wave propagation. Mathematical Problems in the Geophysical Sciences, Am. Math. Soc., Providence, R. I., W. H. Reid, ed., 13:61-102.

Brink, K. H., Allen, J. S., and Smith, R. L., 1978. A study of low-frequency fluctuations near the Peru coast. J. Phys. Oceanogr., 8:1025-1041.

Gradshteyn, I. S. and Ryzhik, I. M., 1980. Tables of Integrals, Series, and Products, Academic Press, New York, 1160 pp.

Huppert, H. E. and Stern, M. E., 1974. Ageostrophic effects in rotating stratified flows. J. Fluid Mech., 62:369-385.

McCreary, J. P., 1981. A linear stratified ocean model of the coastal undercurrent. Philos. Trans. R. Soc. London, Ser. A., 298:603-635.

Miles, J. W., 1972. Kelvin waves on oceanic boundaries. J. Fluid Mech., 55:113-127.

Pedlosky, J., 1969. Linear theory of the circulation of a stratified ocean. J. Fluid Mech., 35:185-205.

Pedlosky, J., 1974. On coastal jets and upwelling in bounded basins. J. Phys. Oceanogr., 4:3-18.

Philander, S. G. H., 1978. Forced oceanic waves. Rev. Geophys. and Space Phys., 16:15-46.

Picaut, J., 1981. Seasonal coastal upwelling in the eastern Atlantic. Unpublished Manuscript. Tropical Ocean-Atmosphere Newsletter, 5:2-3.

Romea, R. D., and Smith, R. L., 1982. The compilation of evidence for coastal trapped waves along the Peru coast. In preparation.

Smith, R. L., 1978. Poleward propagating perturbations in sea level and currents along the Peru coast. J. Geophys. Res., 83: 6083-6092.

Weisberg, R. H., Horigan, A., and Colin, C., 1978. Equatorially trapped Rossby-gravity wave propagation in the Gulf of Guinea. J. Mar. Res., 37:66-86.

Wunsch, C., 1977. Response of an equatorial ocean to a periodic monsoon. J. Phys. Oceanogr., 7:497-511.

Wunsch, C., 1978. Observations of equatorially trapped waves in the ocean: a review prepared for equatorial workshop, July 1977. Review papers of Equatorial Oceanography, FINE Workshop Proceedings.

Chapter IV

THE EFFECT OF FRICTION AND TOPOGRAPHY ON COASTAL INTERNAL KELVIN WAVES AT LOW LATITUDES

1. INTRODUCTION

Evidence has been presented for the existence of coastally trapped waves along the central Peru coast (Smith, 1978), where observations indicate poleward propagation between 10° and 15°S of fluctuations in sea level, alongshore currents and temperature in the 0.1-0.2 cpd frequency band with phase speeds of about 200 km day^{-1}. Although the frequency range of the propagating fluctuations is similar to that of weather events, they are found to be uncorrelated with the local winds measured at 12°S or 15°30'S (Brink, et al., 1978). The analysis has recently been extended equatorward and poleward by Romea and Smith (1982), and free waves are found to propagate poleward between 2° and 17°S.

In general, free coastally trapped waves have modal structures and phase speeds that are dependent on shelf topography, stratification, and latitude (see, e.g., Allen and Romea, 1980, for a detailed discussion of this point). The structure of the current fluctuations and the nature of the dynamical balances suggest that the waves observed along the Peru coast are internal Kelvin wave-like (Smith, 1978; Brink, et al., 1978; Brink, et al., 1980; Allen and Smith, 1981; Brink, 1982a; and Romea and Smith, 1982), i.e., that the density stratification is the dominant mechanism for the waves, with the bottom topography inducing only a minor modification to their structure and dynamics. This observational result agrees with the conceptual model that the effect of the continental margin should be much like a vertical wall for low latitudes where the

Rossby radius of deformation, δ_R, which is the natural baroclinic offshore length scale, is greater than the shelf-slope width L_s. Estimating the Rossby radius scale by $\delta_R = c/f$, where c is an alongshore phase speed and f is the Coriolis parameter, we find, at 5°S latitude, with $f \simeq 1.3 \times 10^{-5}$ s^{-1} and $c \simeq 200$ km day^{-1}, that $\delta_R \simeq$ 180 km, whereas $L_s \simeq$ 80-100 km.

Phase shifts in the offshore and vertical directions have been observed in the velocity data from the Peru coast (Brink et al., 1978). For barotropic motions, Brink and Allen (1978) have shown that cross-shelf phase lags may be induced by the effect of bottom Ekman layer friction, and Brink, et al. (1980) report an observed mean bottom Ekman layer thickness of 10-20 m based on the Peru data from March-May 1977. Thus, the observed phase shifts may be due to the effects of bottom friction. To investigate this possibility for conditions near the Peru coast, we present a simple analysis of the effect of bottom friction and shelf slope topography on free internal Kelvin waves in a continuously stratified ocean. Models with continuous stratification and realistic bottom topography are the most useful for direct comparison with coastal trapped wave observations at low latitudes. These models are generally intractable analytically and a numerical approach has been adopted in the past (e.g., Huthnance, 1978; Brink, 1982a). However, there are difficulties with numerical models for low latitudes where $L_s/\delta_R \ll 1$ (Brink, personal communication). In addition, if bottom friction effects are included, it is difficult to numerically calculate the structure of alongshore velocity accurately (Brink, 1982b).

We concentrate primarily on the low latitude case with weak bottom friction effects and derive analytical results with a perturbation analysis for $L_s/\delta_R \ll 1$ and for $T_f/T \ll 1$, where T_f is the frictional time scale and T is the wave period. The limit $L_s/\delta_R \to 0$ corresponds to the flat bottom vertical wall case. As will be discussed, the formulation including the effect of bottom friction at low latitudes depends conceptually on taking the limit $T_f/T \to 0$ before the limit $L_s/\delta_R \to 0$.

For comparison to the low latitude case $L_s/\delta_R \ll 1$, we also include results for an idealized mid-latitude case $L_s/\delta_R \gg 1$, with a vertical wall and a weak slope. Phase lags induced by bottom friction are qualitatively different in this case and it is of interest to contrast these results with those from the low latitude case.

2. FORMULATION

We consider a continuously stratified ocean on an f-plane in the northern hemisphere. Cartesian coordinates are utilized with x' positive westward, y' positive southward, and z' positive vertically upward. Primes denote dimensional quantities for which a non-dimensional counterpart will later be defined. The ocean is bounded on top by a rigid lid and on the bottom by a boundary at z' = -H. There is a straight north-south oriented coastline at x' = 0. The problem is linearized by the assumption that the motion results in negligible nonlinear fluid accelerations and in small departures ρ' from an equilibrium stable density distribution $\bar{\rho}(z')$. The hydrostatic approximation is utilized, and we consider interior motions away from frictional boundary layers. The long wave assumptions for coastally trapped waves are made, i.e., the frequency ω of the wave motions is small compared to f, and the alongshore scale L_y of the waves is large compared to their offshore scale L.

Dimensionless variables are formed in the following manner:

$$(x,y) = (x',y')/L,\ z = z'/H,\ t = t'f,$$

$$(u,v) = (u',v')/U,\ w = w'L/(HU), \tag{2.1}$$

$$p = p'/(\rho_0 UfL),\ \rho = (\rho' gH)/(\rho_0 UfL).$$

The variables (u',v',w') are the velocity components in the (x',y',z') directions, t' is time, p' is the pressure, U is a characteristic horizontal velocity, and the total density is given by

$$\rho_T'(x',y',z',t') = \rho'(x',y',z',t') + \bar{\rho}(z') + \rho_0, \qquad (2.2)$$

where ρ_0 is a constant.

With the above assumptions and scaling, the governing equations are

$$v = p_x, \qquad (2.3a)$$

$$v_t + fu = -p_y \qquad (2.3b)$$

$$0 = -p_z - \rho, \qquad (2.3c)$$

$$\rho_t - R^2 w = 0, \qquad (2.3d)$$

$$u_x + v_y + w_z = 0, \qquad (2.3e)$$

where

$$R(z) = NH/(fL), \qquad (2.4a)$$

$$N^2(z) = -g\bar{\rho}_z/\rho_0, \qquad (2.4b)$$

and where the subscripts denote partial differentiation. $N^2(z)$ is the square of the Brunt-Väisälä frequency, and R(z) is a stratification parameter that represents the ratio of the Rossby radius scale to L.

Eqs. (2.3a-e) may be combined into a single equation for the pressure given by

$$\{p_{xx} + [R^{-2}(z)p_z]_z\}_t = 0. \qquad (2.5)$$

Boundary conditions for p, resulting from the assumption that the surface is a rigid lid and a regularity condition that specifies coastal trapping, are respectively

$$p_{zt} = 0, \quad \text{at } z = 0, \tag{2.6a}$$

$$p_x, p_y \to 0, \quad \text{as } x \to \infty. \tag{2.6b}$$

The remaining boundary conditions depend on the specific bottom topography chosen, and will be introduced later.

3. STEEP SLOPE

The geometry of the steep slope model is shown in Figure 1. The side wall, located at $x' = \epsilon'(z)$, intersects the surface at $x' = 0$, $z' = 0$. We assume that the offshore scale of the slope topography is small compared to a characteristic offshore scale L, i.e., $\epsilon = \epsilon'/L \ll 1$, and that the slope intersects the bottom at $x = \epsilon_0 \ll 1$, $z = -1$.

We introduce friction in the problem by assuming there are quasi-steady Ekman layers on the bottom at $z = -1$ and on the slope $x = \epsilon(z)$. The boundary condition at $z = -1$, which represents the Ekman compatibility condition (Pedlosky, 1979, p. 198) on the interior flow, is given by

$$p_{zt} = -\tfrac{1}{2}R^2 E_v^{\frac{1}{2}} p_{xx}, \text{ at } z = -1, \tag{3.1a}$$

where

$$E_v^{\frac{1}{2}} = H^{-1}(\tfrac{1}{2}\nu_v/f)^{\frac{1}{2}}. \tag{3.1b}$$

E_v is the vertical Ekman number and ν_v is a constant vertical eddy coefficient.

A standard boundary layer analysis (e.g., Pedlosky, 1979, p. 208-215) for a constant sloping boundary, which will be valid for general slope topography as long as the radius of curvature is large compared to the boundary layer thickness, gives a normal layer thickness of $E_v^{\frac{1}{2}}(\cos\alpha')^{\frac{1}{2}}$, where α' is the dimensional slope angle. The normal velocity w_N at the top of the layer and the transport T_E parallel to the slope in the layer are given by

$$w_N = \tfrac{1}{2}E_v^{\frac{1}{2}}\, v_{\hat{z}}(\cos\alpha')^{-\frac{1}{2}}, \tag{3.2a}$$

$$T_E = -\tfrac{1}{2}E_v^{\frac{1}{2}}\, v(\cos\alpha')^{-\frac{1}{2}}, \tag{3.2b}$$

where $\hat{z}$ measures distance along the slope downward from the surface. The results (3.2a,b) are derived with the assumption that L is large enough that $E_v/E_h = (\nu_v/\nu_h)(L/H)^2 \gg 1$, where ν_h is a constant horizontal eddy coefficient. This assumption has been discussed by Allen (1973) and Pedlosky (1974), and is equivalent to the statement that the offshore scale is large compared to the horizontal diffusion scale.

With the scaling given in (2.1) and with $\varepsilon \ll 1$, the magnitude of the slope angle α in the nondimensional system is

$$\tan\alpha = O(\varepsilon_0^{-1}) \gg 1. \tag{3.3a}$$

However, the problem is formulated such that $NH(f\pi)^{-1} \gg L \gg H$, i.e., that the shelf-slope width is much greater than the deep ocean depth but much less than the internal Rossby radius scale associated with the first baroclinic mode. Therefore the magnitude of α' is

$$\tan\alpha' = O(H/L) \ll 1. \tag{3.3b}$$

In terms of variables in x and z,

$$w_N = u \sin\alpha + w \cos\alpha \tag{3.3c}$$

and

$$\partial/\partial\hat{z} = \cos\alpha\,(\partial/\partial x) - \sin\alpha\,(\partial/\partial z). \qquad (3.3d)$$

With (3.3a,c,d), (3.2a) is

$$u = -\varepsilon w - \tfrac{1}{2}E_v^{\frac{1}{2}}(\cos\alpha')^{-\frac{1}{2}}v_z + O(\varepsilon_0) + O(E_v). \qquad (3.4a)$$

Typical values ($H \simeq 4$ km, $L \simeq 100$ km) give $\alpha' \simeq 2.3°$, so that the dimensional slope appears locally almost horizontal. Thus, we anticipate that the bottom Ekman layer will extend over the slope up to the surface. With $\cos\alpha' \simeq 1$ and at $x = \varepsilon(-1)$, the Ekman layer transport (3.2b) on the slope is approximately equal to the Ekman layer transport on the flat bottom. Since the fluxes approximately match where the slope meets the bottom, there will be negligible flux into the interior due directly to the change in slope although there will be a discontinuity in normal velocity. With no wind stress forcing, and hence no flux in the surface Ekman layer, any net flux into the Ekman layer along the flat bottom or along the slope must be pumped out at $x = 0$, $z = 0$. The approximate boundary condition along the sloping boundary from (3.4a) is thus

$$p_{xt} + p_y = \varepsilon_z R^{-2} p_{zt} + \tfrac{1}{2}E_v^{\frac{1}{2}}[p_{xz} - p_{x(0)}\delta(z)], \quad \text{at } x = \varepsilon(z), \qquad (3.4b)$$

where $p_{x(0)} = p_x(x = 0, z = 0)$. This condition specifies that the onshore flow in the interior is balanced by the inviscid vertical velocity produced by the slope plus the Ekman pumping along the slope. The last term on the right hand side of (3.4b) represents the flow out of the Ekman layer at $x = 0$, $z = 0$ and must be included so that the mass flux condition

$$\int_{\Gamma} w_N d\hat{s} = 0 \tag{3.4c}$$

is satisfied, where Γ is the lower boundary, and $\hat{s}$ is distance along the boundary (see comment after Eq. (3.27)). The function δ is defined here such that $\delta(z) = 0$ for $z \neq 0$ and

$$\int_{-1}^{0} \delta(z)dz = 1 \tag{3.4d}$$

We seek a free wave solution of the form

$$p(x,y,z,t) = \mathrm{Re}\{\phi(x,z)\exp[-i(\omega t + \ell y)]\}, \tag{3.5}$$

where ω and ℓ are radian frequency and alongshore wavenumber, respectively. Substituting (3.5) in (2.5), (2.6a,b), (3.1a) and (3.4b) we obtain

$$\phi_{xx} + (\phi_z/R^2)_z = 0, \tag{3.6}$$

$$\phi_z = 0, \text{ at } z = 0, \tag{3.7a}$$

$$\phi_z = -\tfrac{1}{2}i\lambda R^2\phi_{xx}, \text{ at } z = -1, \tag{3.7b}$$

$$\phi_x + (\ell/\omega)\phi = \varepsilon_z R^{-2}\phi_z + \tfrac{1}{2}i\lambda[\phi_{xz} - \phi_{x(0)}\delta(z)], \quad \text{at } x = \varepsilon(z), \tag{3.7c}$$

$$\phi_x \to 0, \text{ as } x \to \infty, \tag{3.7d}$$

where, as in (3.4b), the notation $\phi_{x(0)}$ implies $\phi_x(x = 0, z = 0)$, and where $\lambda = E_V^{\frac{1}{2}}/\omega$. Eqs. (3.6) and (3.7a-d) describe an eigenvalue

problem for ϕ with complex eigenvalue ω.

To proceed, we first transform the boundary conditions at $x = \epsilon(z)$ to hold on a constant surface $\xi = 0$ by defining a new coordinate system (ξ,y,z), where

$$\xi = x - \epsilon(z). \tag{3.8}$$

A similar transformation has been used by Huthnance (1978) to handle boundary conditions similar to (3.7c). The surfaces $z = 0, -1$ remain unaffected by the coordinate transformation.

The transformed equations and boundary conditions are

$$\phi_{\xi\xi} + (\phi_z/R^2)_z + (\epsilon_z/R)^2\phi_{\xi\xi} - 2\epsilon_z R^{-2}\phi_{\xi z} - (\epsilon_z/R^2)_z\phi_\xi = 0, \tag{3.9}$$

$$\phi_z - \epsilon_z\phi_\xi = 0, \text{ at } z = 0, \tag{3.10a}$$

$$\phi_z - \epsilon_z\phi_\xi = -\tfrac{1}{2}i\lambda R^2\phi_{\xi\xi}, \text{ at } z = -1 \tag{3.10b}$$

$$\phi_\xi + (\ell/\omega)\phi = \epsilon_z R^{-2}(\phi_z - \epsilon_z\phi_\xi) + \tfrac{1}{2}i\lambda\{\phi_{\xi z} - \epsilon_z\phi_{\xi\xi} - \phi_{\xi(0)}\delta(z)\},$$

$$\text{at } \xi = 0, \tag{3.10c}$$

$$\phi_\xi \to 0, \text{ as } \xi \to \infty. \tag{3.10d}$$

A relatively simple solution to (3.9) and (3.10) may be obtained by perturbation methods. We assume $\lambda = O(\epsilon_0) << 1$, which corresponds to limiting the wave period to be much less than the spin down time. In addition, it is important that the limits $\lambda \to 0$, $\epsilon \to 0$ be taken in that order, since if $\epsilon \to 0$, $\lambda \neq 0$, the Ekman layer on the slope would vanish and (3.10c) would be incorrect.

The variables are expanded as

$$\phi = \phi^{(0)} + \phi^{(1)} + \ldots, \tag{3.11a}$$

$$\omega = \omega^{(0)} + \omega^{(1)} + \ldots, \tag{3.11b}$$

where $\phi^{(0)}$ and $\omega^{(0)}$ are assumed to be $O(1)$ and $\phi^{(1)}$ and $\omega^{(1)}$ are assumed to be $O(\varepsilon_0)$. If (3.11a,b) are substituted in (3.9) and (3.10), the lowest order balance is the familar inviscid internal Kelvin wave problem, i.e.,

$$\phi_{\xi\xi}^{(0)} + (\phi_z^{(0)}/R^2)_z = 0, \tag{3.12}$$

$$\phi_z^{(0)} = 0, \text{ at } z = 0,-1, \tag{3.13a}$$

$$\phi_\xi^{(0)} + (\ell/\omega^{(0)})\phi^{(0)} = 0, \text{ at } \xi = 0, \tag{3.13b}$$

$$\phi_\xi^{(0)} \to 0, \text{ as } \xi \to \infty, \tag{3.13c}$$

with solutions

$$\phi_n^{(0)} = \exp(-\ell\xi/\omega_n^{(0)})P_n(z), \tag{3.14}$$

where

$$(P_{nz}/R^2)_z + (\ell/\omega_n^{(0)})^2 P_n = 0 \tag{3.15}$$

$$P_{nz} = 0, \text{ at } z = 0, -1. \tag{3.16}$$

Eqs. (3.15) and (3.16) form an eigenvalue problem with eigenfunctions P_n and real eigenvalues $\omega_n^{(0)}$. The eigenfunctions

form a complete set and are orthogonal over the domain (-1,0), subject to

$$\int_{-1}^{0} P_n P_m dz = \delta_{nm}, \tag{3.17}$$

where δ_{nm} is the Kronecker delta. An additional restriction due to (3.13c) is $\ell/\omega_n^{(0)} > 0$, which implies that the waves travel only poleward. These results have been obtained for general subinertial coastally trapped waves (see, e.g., Huthnance, 1975, and Clarke, 1977).

The equations describing the $O(\epsilon_0)$ correction to each mode n, where terms of $O(\epsilon_0^2)$, $O(\lambda^2)$, and $O(\lambda\epsilon)$ have been neglected, are

$$\phi_{n\xi\xi}^{(1)} + (\phi_{nz}^{(1)}/R^2)_z = 2\epsilon_z R^{-2}\phi_{n\xi z}^{(1)} + (\epsilon_z/R^2)_z \phi_{n\xi}^{(1)}, \tag{3.18}$$

$$\phi_{nz}^{(1)} = \epsilon_z \phi_{n\xi}^{(0)}, \text{ at } z = 0, \tag{3.19a}$$

$$\phi_{nz}^{(1)} = \epsilon_z \phi_{n\xi}^{(0)} - \tfrac{1}{2} i \lambda_n^{(0)} R^2 \phi_{n\xi\xi}^{(0)}, \text{ at } z = -1, \tag{3.19b}$$

$$\phi_{n\xi}^{(1)} + (\ell/\omega_n^{(0)})\phi_n^{(1)} = \ell(\omega_n^{(1)}/\omega_n^{(0)2})\phi_n^{(0)}$$
$$\epsilon_z R^{-2}\phi_{nz}^{(0)} + \tfrac{1}{2} i \lambda_n^{(0)}\{\phi_{n\xi z}^{(0)} - \phi_{n\xi(0)}^{(0)}\delta(z)\},$$
$$\text{at } \xi = 0, \tag{3.19c}$$

$$\phi_n^{(1)} \to 0, \text{ as } \xi \to \infty, \tag{3.19d}$$

where

$$\lambda_n^{(0)} = E^{\frac{1}{2}}/\omega_n^{(0)}. \tag{3.19e}$$

A compatibility condition for the solution of (3.19) may be found by multiplying (3.18) by $\phi_n^{(0)}$, integrating over ξ from 0 to ∞ and over z from -1 to 0, and utilizing the boundary conditions (3.13a,b,c), and (3.19a-d). This determines $\omega_n^{(1)}$ as

$$\omega_n^{(1)} = -\tfrac{1}{4}i\lambda_n^{(0)}[P_{n(0)}^2 + P_{n(-1)}^2 + R_{(-1)}^2(\omega_n^{(0)}/\ell)^2 I_{nn}] - (\omega_n^{(0)2}/\ell)\int_{-1}^{0}\epsilon_z R^{-2}P_{nz}P_m dz, \tag{3.20}$$

where

$$I_{nm} = \int_{-1}^{0}\{(P_{nz}/R^4)_z - (\ell/\omega_n^{(0)})^2(z/R^2)_z P_n\}\, P_m dz, \tag{3.21}$$

and where the P_n are determined by (3.15), (3.16) and (3.17). The solution to (3.18) and (3.19) is

$$\phi_n^{(1)} = \epsilon\phi_{n\xi}^{(0)} - \tfrac{1}{2}i\lambda_n^{(0)}(R_{(-1)}^2/R^2)z\phi_{nz}^{(0)} + \psi_n, \tag{3.22}$$

$$\psi_n = \sum_{m=0}^{\infty}\gamma_m(\xi)\, P_m(z), \tag{3.23a}$$

where, for $m \neq n$,

$$\gamma_m = A_m \exp(-\ell\xi/\omega_m^{(0)}) + B_m \exp(-\ell\xi/\omega_n^{(0)}), \tag{3.23b}$$

$$A_m = [(\ell/\omega_n^{(0)}) - (\ell/\omega_m^{(0)})]^{-1} \times \{\int_{-1}^{0}\epsilon_z R^{-2}P_{nz}P_m dz - \tfrac{1}{2}i\lambda_n^{(0)}(\ell/\omega_n^{(0)}) (\int_{-1}^{0} P_{nz}P_m dz - P_{n(0)}P_{m(0)})\}, \tag{3.23c}$$

$$B_m = \tfrac{1}{2}i\lambda_n^{(0)} R^2_{(-1)} \left[(\ell/\omega_n^{(0)})^2 - (\ell/\omega_m^{(0)})^2\right]^{-1} I_{nm}, \quad (3.23d)$$

while, for m = n,

$$\gamma_n = -\tfrac{1}{4}i\lambda_n^{(0)} (\omega_n^{(0)}/\ell) R^2_{(-1)} \int \xi \exp(-\ell\xi/\omega_n^{(0)}) I_{nn}. \quad (3.23e)$$

The coefficient of the homogeneous solution to (3.18) and (3.19) is arbitrary and the homogeneous solution may be absorbed in the O(1) solution.

Since the $\omega_n^{(0)}$ are ordered such that $\omega_n^{(0)} \to 0$ as $n \to \infty$, the perturbation procedure becomes invalid for high mode number, i.e., when $\lambda_n^{(0)} = E_v^{\frac{1}{2}}/\omega_n^{(0)} = O(1)$ and when $\delta_R/\varepsilon_0 = \omega_n^{(0)}(\ell\varepsilon_0)^{-1} = O(1)$. Therefore we must restrict our consideration to low modes where $\lambda^{(0)} \ll 1$ and $\delta_R/\varepsilon_0 \gg 1$. This restriction is not too severe, since we are generally only interested in the behavior of the first mode.

The frictional correction to the O(1) eigenfunction is $O(\lambda_n^{(0)})$ and is purely imaginary, while the topographic correction is $O(\varepsilon_0)$ and is real. To $O(\lambda_n^{(0)})$, $O(\varepsilon_0)$, the presence of bottom friction induces phase shifts in x and z but does not change the x,z structure of v or p, while the slope topography affects the x,z structure of v and p but not the phase. Both friction and topography induce corrections to the frequency. The $O(\lambda_n^{(0)})$ frictional correction (from the first three terms on the right hand side of (3.20)) is purely imaginary and represents a frictional decay or "spin-down" with time. The last term on the right hand side of (3.20) represents a correction to the real free wave speed

due to the slope topography. The contribution of that term may be seen by multiplying (3.15) by P_{nz}/R^2 and integrating over z from -1 to 0, to obtain, after integration by parts and the use of (3.16),

$$\int_{-1}^{0} R^{-2} P_{nz} P_n \, dz = 0. \tag{3.24}$$

Eq. (3.24) is a statement that the vertical velocity ($\simeq R^{-2}P_{nz}$) and the topographically induced onshore velocity ($\simeq P_n$) are orthogonal over the depth. This implies together with the last term in (3.20) that, for a linear slope, i.e., for

$$\varepsilon(z) = -\varepsilon_0 \, z, \tag{3.25}$$

where $\varepsilon_z = -\varepsilon_0 =$ constant, the interaction between u and w averaged over the slope is zero, so that the topographic correction to the phase speed is zero. There is still a distortion of the mode shape, however. For a non-linear slope, corrections to both modal structure and phase speed are induced.

For an arbitrary stratification, the eigenfunctions P_n and eigenvalues may be computed numerically from (3.15), (3.16), and (3.17). A simple case, for which eigenfunctions and eigenvalues may be obtained directly, is $R = R_0 =$ constant, which corresponds to a constant Brunt-Väisälä frequency. While this case is generally unrealistic (the modal amplitude for $z < -\frac{1}{2}$ tends to be over-estimated), it is useful for obtaining solutions that illustrate the essential physics. Solutions with a more realistic stratification are obtained in Appendix A and are discussed in Section 5.

With $R = R_0$, (3.14), (3.15), (3.16), and (3.17) give

$$\phi_n^{(0)} = 2\exp(-n\pi\xi/R)\cos(n\pi z), \tag{3.26a}$$

$$\omega_n^{(0)} = \ell R/(n\pi),\ n = 1, 2, 3, \ldots, \tag{3.26b}$$

and the correction to the frequency from (3.20), is

$$\omega_n^{(1)} = -\tfrac{1}{2}iE_v^{\frac{1}{2}} + 2(\omega_n^{(0)}/R)\int_{-1}^{0} \varepsilon_z \sin n\pi z \cos n\pi z\, dz. \tag{3.27}$$

Using (3.26a,b), the next order correction (3.22) may be calculated directly. Substitution of (3.27) in (3.5) shows that the $O(\lambda_n^{(0)})$ correction to the frequency represents a frictional decay with time, where the wave damping is given by $\exp(-\tfrac{1}{2}E_v^{\frac{1}{2}}t)$. This corresponds to the spin down time scale for homogeneous fluids (Greenspan, 1968, p. 34). Note that, if the first term in (3.20), which comes from the δ function in (3.4b), were not included, the frictional correction to ω would imply an exponential growth instead of decay.

We next examine the effect of bottom friction on the first vertical mode for the special case $R = R_0$ and $\varepsilon(z)$ given by (3.25) (A linear slope topography). The $n = 1$ eigenfunction may be written, to $O(\varepsilon_0)$ and $O(\lambda_n^{(0)})$, as

$$\phi_1 = |\phi_1| \exp(i\theta_1), \tag{3.28}$$

where

$$|\phi_1| = |\phi_1^{(0)}(1 - \varepsilon\pi z/R) - 2\varepsilon_0(\pi R)^{-1}(1 + 2S)|, \tag{3.29a}$$

$$\phi_1 = \tan^{-1}\{\tfrac{1}{2}\lambda_1^{(0)}[3 + \exp(-\pi\xi/R)(\pi z \sin \pi z + (\pi\xi/R)\cos \pi z) + 4S + D]/\phi_1^{(0)}\}, \quad (3.29b)$$

$$S = -\sum_{k=1}^{\infty} \phi_{2k}^{(0)} (1 - 2k)^{-1}(1 - 4k^2)^{-1} \cos(2k\pi z), \quad (3.29c)$$

$$D = \exp(-\pi\xi/R)\{\tfrac{1}{2}\cos(\pi z) \ln[1 - 2\exp(-\pi\xi/R)\cos \pi z + \exp(-2\pi\xi/R)] + \sin(\pi z) \tan^{-1}[\exp(-\pi\xi/R)\sin(\pi z)(1 - \exp(-\pi\xi/R)\cos(\pi z))^{-1}]\}. \quad (3.29d)$$

The polar representation for ϕ_1 ((3.28) and (3.29)) shows that there is an $O(\lambda_1^{(0)})$ phase shift in both the x and z directions. The dependence on λ indicates that the effect of friction is enhanced for higher latitude or lower frequency. Note that, if x and ε_0 are rescaled with R/π ($x^* = \pi x/R$, $\varepsilon_0^* = \pi\varepsilon_0/R$, $\xi^* = \pi\xi/R$), $\lambda_1^{(0)}$ and ε^* are the only parameters in (3.29).

The x,z structure of the correction to the alongshore velocity, computed using (2.3a) and (3.28), is given by

$$\phi_{1x} = (|\phi_{1x}| + i\theta_{1x}) \exp(i\theta_1). \quad (3.30)$$

The simple relationship between pressure and alongshore velocity for an inviscid internal Kelvin wave, i.e., $\phi_x = -(\pi/R)\phi$, is modified by the introduction of topographic and frictional effects. This behavior has been noted by Brink (1982b).

Figure 2 shows the frictionally induced phase shift in p and v for the first mode internal Kelvin wave in the x*-z plane for

$\lambda_1^{(0)} = 0.1$, topography given by (3.25) with $\varepsilon^* = \pi\varepsilon_0/R = 0.1$, and $R = R_0$. With (3.28) and (3.5), $\theta_1 > \theta_2$ implies 1 lags 2. Phase shifts for v and p are clearly different, however vertical phase shifts imply that both surface v and p lead those below. The 180° phase shift in the vertical is due to the structure of the first mode inviscid internal Kelvin wave, which has a zero crossing at $z = -\frac{1}{2}$, and would have an abrupt 180° phase shift at $z = -\frac{1}{2}$.

The offshore phase structure for both p and v is depth dependent. In the upper half (near surface), p offshore lags p at the coast, while the effect is reversed for the lower layer. For v, inshore motions lead for $-0.15 < z < 0$ (near the surface), while offshore motions lead those nearshore for $-0.15 > z > -0.5$. Phase shifts with x^* are small for $z < -0.5$, with a suggestion that nearshore motions lead except very near the bottom.

We next consider the effect of slope topography alone on the first mode internal Kelvin wave. Figure 3 shows the x^*-z structure of v for the n = 1 mode for $\lambda = 0$, (3.25) with $\varepsilon_0^* = 0.3$, and $R = R_0$. The alongshore velocity is not symmetric about the line $z = -\frac{1}{2}$, as would be expected with a vertical wall. Figure 4 shows several examples of shelf slope topographies and Table 1 lists the $O(\varepsilon_0)$ topographic corrections to the O(1) phase speed $c_n^{(0)}$ for each profile in Figure 4. For each case the shelf-slope width at $z = -1$ is ε_0^*, and $R = R_0$. The second term on the right hand side of (3.27), which represents the topographic correction to ω for $R = R_0$, yields the result that slope profiles that are concave downward (case (a), Figure 4) act to increase the free wave phase speed while profiles that are concave upward (case (b)) act to decrease the phase speed.

As expected, the special case ε_z = constant (case (c)) gives no correction to the phase speed at $O(\varepsilon_0)$. Most shelf-slope topographies in nature are concave downward.

The change of sign of the correction to $c_n^{(0)}$ for cases (d) and (e) may be explained in the following manner: For an internal Kelvin wave over a flat bottom with a vertical wall and with constant N, the phase speed is given by $c_n = NH(n\pi)^{-1}$. With a small shallow shelf which drops steeply to a deep ocean (case (d)), the wave "rides" on the bottom at $x > \varepsilon_0$ and the shelf acts as an additional fluid volume which augments the effective depth by an $O(\varepsilon_0)$ amount, thus increasing the phase speed. For case (e), the small topography near the bottom decreases the effective depth by an $O(\varepsilon_0)$ amount, thus decreasing the phase speed. Cases (d) and (e) may be regarded as limiting cases of (a) and (b), respectively.

For case (f), two linear slopes interrupted by a segment of vertical wall, the wave identifies the vertical segment as a coastal boundary; the additional fluid volume provided by the shelf for $0 > z > -|z_0|$ is cancelled by the decrease due to the shelf segment for $-|z_0| > z > -1$, and the phase speed is unaffected to $O(\varepsilon_0)$. For case (c), the linear slope, there is no equivalent vertical wall to provide a reference zero for the mode. Case (c) may be viewed as a limit of case (f) as the vertical segment shrinks to zero. The addition of fluid volume for $0 > z > -\frac{1}{2}$ is exactly cancelled by the decrease of fluid volume for $-\frac{1}{2} > z > -1$. The effective depth and hence the phase speed remain unchanged.

The onshore flow u may be obtained by solving (2.3a,b) with (3.5) for u in terms of ϕ. While there is no onshore flow associated

with an internal Kelvin wave over a flat bottom, the presence of a steep slope induces a u of $O(\varepsilon_0)$ while friction induces a u of $O(\lambda_n^{(0)})$. Figure 5 shows u/ε_o^* in the x^*-z plane with $\lambda_n^{(0)} = 0$, (3.25) with $\varepsilon_0^* = 0.1$, and $R = R_0$, i.e., this is the onshore flow induced by the topography alone. There is a maximum at $x^* = \varepsilon_0^*$, near $z = -\frac{1}{2}$, reflecting the interaction of the slope topography with the O(1) w which has a maximum near $z = -\frac{1}{2}$. Figure 6 shows the amplitude of u/ε_o^* in the x^*-z plane where we have chosen $\lambda_n^{(0)} = \varepsilon_0^* = 0.1$, and $R = R_0$, so that both topography and friction are important. A local maximum of u near $z = -\frac{1}{2}$, $x^* = \varepsilon_0^*$ is again evident, and is enhanced relative to u in Figure 5 due to the Ekman pumping along the sloping boundary. The relatively large u near $x^* = 0$, $z = 0$ is due to the mass flux out of the Ekman layer at that location required to satisfy (3.4).

4. WEAK SLOPE

The weak slope model shown in Figure 7 represents the case where the Rossby radius scale is much smaller than the shelf-slope width, appropriate for mid-latitudes or for very wide shelves. In the model, the continental shelf-slope region is represented by a linear bottom slope of small magnitude, i.e., by

$$H(x) = 1 + \varepsilon x, \tag{4.1}$$

where ε is a constant and $\varepsilon \ll 1$. While the vertical wall at $x = 0$ is unrealistic, such models are commonly utilized, therefore it is of interest to compare their results to the steep slope model of Section 3.

The analysis proceeds as in Section 3, with weak friction, i.e., where $\lambda = O(\varepsilon)$, except that here the limits $\varepsilon \to 0$, $\lambda \to 0$ may be taken independently. The governing equation (2.5) and the boundary conditions (2.6a,b) apply. The boundary condition on the lower boundary, which represents the Ekman compatibility on the interior flow plus the inviscid boundary condition appropriate for a sloping boundary, is

$$p_{zt} + R^2 H_x (p_{xt} + p_y) = -\tfrac{1}{2} R^2 E_v^{\frac{1}{2}} p_{xx}, \text{ at } z = -H(x). \tag{4.2}$$

The boundary condition that holds at $x = 0$ is

$$p_{xt} + p_y = -\tfrac{1}{2} E_v^{\frac{1}{2}} p_x(z = -1)\delta(z + 1), \text{ at } x = 0, \tag{4.3a}$$

where $\delta(z + 1)$ is equal to 0 for $z \neq -1$, and

$$\int_{-1}^{0} \delta(z + 1)\, dz = 1. \qquad (4.3b)$$

The term on the right hand side of (4.3a) is due to the flow out of the Ekman layer at $x = 0$ and must be included so that the mass flux condition

$$\int_{-1}^{0} w(z = -1)\, dx + u(z = -1) = 0 \qquad (4.4)$$

is satisfied. This is analagous to (3.4c) for the steep slope case, and, as in Section 3, neglect of this term leads to an exponential growth of the solution with time.

We seek a free wave solution given by (3.5). Substititing (3.5) in (2.5), (2.6a,b), (4.2) and (4.3a), we obtain (3.6), (3.7a), (3.7d) plus

$$\phi_x + (\ell/\omega)\phi = -\tfrac{1}{2}i\lambda\phi_x(z = -1)\delta(z + 1), \text{ at } x = 0, \qquad (4.5a)$$

$$\phi_z = -R^2 H_x[\phi_x + (\ell/\omega)\phi] - \tfrac{1}{2}iR^2\lambda\phi_{xx}, \text{ at } z = -H(x). \qquad (4.5b)$$

We define the new coordinate system (x, y, η), where

$$\eta = z/H(x), \qquad (4.6)$$

so that the lower boundary $z = -H(x)$ becomes $\eta = -1$ while the upper surface $z = 0$ becomes $\eta = 0$, i.e., the upper surface is unchanged. Transforming the equations and boundary conditions, we have

$$\phi_{xx} + 2\eta\varepsilon^2(1 - 2\varepsilon x + \ldots)\phi_\eta - 2\eta\varepsilon(1 - \varepsilon x + \ldots)\phi_{\eta x}$$
$$+ (\eta\varepsilon)^2(1 - 2\varepsilon x + \ldots)\phi_{\eta\eta} + (\phi_\eta/R^2)_\eta(1 - 2\varepsilon x + \ldots) = 0 \tag{4.7}$$

$$\phi_\eta = 0, \text{ at } \eta = 0, \tag{4.8a}$$

$$\phi_x - \eta\varepsilon(1 - \varepsilon x + \ldots)\phi_\eta + (\ell/\omega)\phi =$$
$$-\tfrac{1}{2}i\lambda[\phi_x + \eta\varepsilon(1 - \varepsilon x + \ldots)\phi_{\eta(-1)}\delta(\eta + 1)],$$
$$\text{at } x = 0, \tag{4.8b}$$

$$\phi_\eta = -R^2\varepsilon(1 + \varepsilon x)[\phi_x + (\ell/\omega)\phi - \eta\varepsilon(1 - \varepsilon x + \ldots)\phi_\eta]$$
$$-\tfrac{1}{2}i\lambda R^2[\phi_{xx} + 2\eta\varepsilon^2(1 - 2\varepsilon x + \ldots)\phi_\eta - 2\eta\varepsilon(1 - \varepsilon x + \ldots)\phi_{\eta x}$$
$$+ (\eta\varepsilon)^2(1 - 2\varepsilon x + \ldots)\phi_{\eta\eta}], \text{ at } \eta = -1, \tag{4.8c}$$

plus (3.7d) which is the coastal trapping condition. In (4.8b), $\phi_{\eta(-1)} = \phi_\eta(\eta = -1)$.

We expand ϕ and ω as in (3.11a,b), with the restrictions $\lambda \ll 1$, $x \leq O(1)$. The lowest order equations for $\phi^{(0)}$ give the inviscid internal Kelvin wave problem (3.12), (3.13a,b,c) with a sequence n of solutions given by (3.14), (3.15) and (3.16) (with z replaced by η), orthogonal subject to (3.17).

The $O(\varepsilon)$, $O(\lambda)$ balance, neglecting $O(\varepsilon^2)$, $O(\lambda^2)$, and $O(\varepsilon\lambda)$ is

$$\phi^{(1)}_{nxx} + (\phi^{(1)}_{n\eta}/R^2)_\eta = 2\varepsilon[\eta\phi^{(0)}_{nx\eta} + x(\phi^{(0)}_{n\eta}/R^2)_\eta], \tag{4.9}$$

$$\phi^{(1)}_{n\eta} = 0, \text{ at } \eta = 0, \tag{4.10a}$$

$$\phi_{nx}^{(1)} + (\ell/\omega_n^{(0)})\phi_n^{(1)} = \eta\epsilon\phi_{n\eta}^{(0)} + \ell(\omega_n^{(1)}/\omega_n^{(0)2})\phi_n^{(0)}$$

$$-\tfrac{1}{2}i\lambda_n^{(0)}\phi_{nx(-1)}^{(0)}\delta(\eta + 1), \text{ at } x = 0, \tag{4.10b}$$

$$\phi_{n\eta}^{(1)} = -\tfrac{1}{2}iR^2\lambda_n^{(0)}\phi_{nxx}^{(0)}, \text{ at } \eta = -1, \tag{4.10c}$$

$$\phi_{nx}^{(1)} \to 0, \text{ as } x \to \infty. \tag{4.10d}$$

The frequency correction is specified by the compatibility condition as in Section 3, and is

$$\omega_n^{(1)} = (\omega_n^{(0)2}/\ell)\{\tfrac{1}{2}\epsilon - \tfrac{1}{2}i\lambda_n^{(0)}[\tfrac{1}{2}(\omega_n^{(0)}/\ell)R^2{}_{(-1)}I_{nn}$$

$$+ (\ell/\omega_n^{(0)})P^2_{n(-1)}]\}, \tag{4.11}$$

where I_{nn} is given by (3.21) with z replaced by η.

The solution to (4.9) and (4.10) is

$$\phi_n^{(1)} = \tfrac{1}{2}i\lambda_n^{(0)}R^2{}_{(-1)}\phi_{nxx}^{(0)} + \psi_n, \tag{4.12}$$

$$\psi_n = \sum_{m=0}^{\infty} \gamma_m(x)P_m(\eta), \tag{4.13}$$

where

$$\gamma_m = A_m \exp(-\ell x/\omega_m^{(0)}) + B_m \exp(-\ell x/\omega_n^{(0)}), \; m \neq n, \tag{4.14a}$$

$$\gamma_n = (xD_n + x^2E_n)\exp(-\ell x/\omega_n^{(0)}), \tag{4.14b}$$

and

$$A_m = [(\ell/\omega_n^{(0)}) - (\ell/\omega_m^{(0)})]^{-1}$$

$$\times [\varepsilon J_{nm} + \tfrac{1}{2}i\lambda_n^{(0)}(\ell/\omega_n^{(0)})P_{n(-1)}P_{m(-1)}], \qquad (4.15a)$$

$$B_m = -[(\ell/\omega_n^{(0)})^2 - (\ell/\omega_m^{(0)})^2]^{-1}$$

$$\times [-\tfrac{1}{2}i\lambda_n^{(0)}R^2_{(-1)}I_{nm} + 2\varepsilon(\ell/\omega_n^{(0)})J_{nm}], \qquad (4.15b)$$

$$D_n = -\tfrac{1}{2}i\lambda_n^{(0)}R^2_{(-1)}(\omega_n^{(0)}/\ell)I_{nn}$$

$$+ \varepsilon[\tfrac{1}{2} + J_{nn}], \qquad (4.15c)$$

$$E_n = \tfrac{1}{2}\varepsilon(\ell/\omega_n^{(0)}), \qquad (4.15d)$$

$$J_{nm} = \int_{-1}^{0} \eta P_{n\eta} P_m \, d\eta. \qquad (4.15e)$$

As in Section 3, the topographic correction to ω is $O(\varepsilon)$ and real, representing an increase in the phase speed, while the frictional correction to ω is $O(\lambda_n^{(0)})$ and imaginary, representing a spin down with time. There is an $O(\varepsilon)$ correction to the structure of ϕ and an $O(\lambda_n^{(0)})$ correction to the phase of ϕ. The topographic correction to the phase speed is due to the depth variation from a flat bottom weighted with the Rossby radius scale, i.e.,

$$(\omega_n^{(1)}/\ell)_{Top} = \int_0^{\infty} \exp(-\ell x/\omega_n^{(0)})[1 - H(x)]dx. \qquad (4.16)$$

With (4.1), $\omega_n^{(1)}$ calculated with (4.16) is equal to the first term in (4.11). The weak slope topography increases the effective depth

(see Figure 7) relative to a flat bottom at z = -1, thus increasing the phase speed relative to the flat bottom case. A similar result was obtained by Allen (1975, Eq. (3.15c)) with a two layer model.

The m = 0 term in (4.13) represents a barotropic flow induced by both friction and topography. For $x \to \infty$, the baroclinic terms are exponentially small and $\phi_n^{(1)} \sim A_0$ which, with (3.5) and (2.3a,b), implies that far offshore a barotropic onshore flow remains. The matching of this barotropic flow to the outer shelf problem for x >> 1 is discussed in Appendix B.

With $R = R_0$, simple analytical solutions for ϕ are again obtained. In particular, the correction to the O(1) frequency is

$$\omega_n^{(1)} = \tfrac{1}{2}\varepsilon R\,(n\pi)^{-1} - \tfrac{1}{2}iE_v^{\frac{1}{2}} . \qquad (4.17)$$

Figure 8 shows the zero crossing for the first mode of v in the x*-z plane, where $x^* = \pi x/R$, $\lambda = 0$, $\varepsilon = 0.1$, and $R = R_0$. Except for $x^* < 0.15$, the zero crossing is deeper than the zero crossing (at z = -0.5) expected for an internal Kelvin wave with n = 1 and with a flat bottom at z = -1. Near $x^* = 0.5$, the zero crossing is near the predicted zero crossing for a flat bottom at an average depth of z = -1.05. This result again illustrates the increased effective depth due to the sloping bottom.

Figures 9a,b, show the frictionally induced phase shifts in p and v for the n = 1 mode internal Kelvin wave in the x*-z plane for $\lambda_n^{(0)} = 0.1$ and $\varepsilon = 0$. Phase shifts for v and p are clearly different, however vertical phase lags imply that both deeper v and p lead those above. In the upper half, p offshore leads p at the

coast, while the effect is reversed for the lower layer. For v, offshore motions lead those inshore for $-0.1 > z > -0.5$ while inshore motions lead for $-1.0 < z < -0.5$ and $-0.1 < z < 0$.

Figures 10 and 11 show the topographically induced scaled onshore velocity u_T/ε (with $\lambda_1^{(0)} = 0$ and $\varepsilon = 0.1$) and the frictionally induced scaled onshore velocity $u_F/\lambda_1^{(0)}$ (with $\varepsilon = 0$) for the $n = 1$ mode in the x^*-z plane with $R = R_0$. In each figure, $u \to 0$ as $x \to 0$, satisfying the boundary condition at $x = 0$. The flow u_F decreases offshore and upward, with a maximum at $x = 0$, $z = -1$, representing the mass flux out of the bottom Ekman layer required to satisfy (4.4). The flow u_T is largest directly over the slope and decreases upward and toward the coast.

5. DISCUSSION

We have examined the effects of bottom Ekman layer friction and slope topography on free internal Kelvin waves, using both steep and weak slope models. Frictional effects are assumed weak and specific slope topographies are chosen so that perturbation methods may be used to obtain solutions. There are substantial differences between the steep and weak slope models. The steep slope model represents the low latitude case where the Rossby radius scale is assumed large compared to the slope width. The slope topography is a small perturbation along the side wall and the remainder of the bottom is flat. The bottom Ekman layer is continuous along the flat bottom interior and along the slope and intersects the surface at the coast. As a result, the frictional effect depends on the geometry of the slope.

The weak slope model corresponds to the mid-latitude case where the Rossby radius scale is assumed to be much less than the slope width. The topography is assumed to be a small perturbation on a flat lower boundary, and a bottom Ekman layer intersects a vertical wall at $z = -H$, $x = 0$. For this case, we may examine frictional effects with a flat bottom or topographic effects in the absence of bottom friction.

The presence of bottom friction affects internal Kelvin waves in several ways. Free waves are damped with a dimensional time scale $T_f' = (\mu E_v^{1/2} f)^{-1}$ where $\mu = |\omega_n^{(1)}(\text{frictional})|/E_v^{1/2}$ is related to the frictional correction to the wave frequency. Phase shifts in x and z are induced as well as an onshore flow.

Table 2 shows estimates of the dimensional time scale T_f' for the first mode internal Kelvin wave for various s, where s is a measure of the exponential decay of N^2 with depth [see (A1) in Appendix A and Figure 12]. We choose $E_v^{1/2} = 0.02$ (Ekman depth = 40 m for H = 2 km) and $f = 1.3 \times 10^{-5} s^{-1}$ (5° latitude). In Appendix A we show that s = 3 yields a reasonable approximation to the modal structure for the Peru case (Figure 13). For the weak slope, where friction acts through the Ekman compatibility condition at z = -1, which involves the bottom velocity, we expect that a more realistic N^2 profile will yield a smaller bottom velocity and hence the effect of friction will be reduced. Table 2 shows that the correction to the frequency due to friction decreases and the spin down time increases for increasing s, which supports the above argument. In addition, Table 2 shows $\mu|v_{(-1)}/v_{(0)}|$ for the weak slope case and indicates that the spin down time is almost but not exactly proportional to the bottom velocity.

For the steep slope case, the effects of a more realistic N^2 profile is reversed, i.e., Table 2 shows that μ increases and T_f' decreases for increasing s. This is due to the fact that the mode interacts with the Ekman layer over the slope as well as on the bottom.

The expansion procedure used for both the weak and steep slope problems becomes invalid when the wave period is the same order as the spin down time. Table 2 shows that with $E_v^{1/2} = 0.02$, this restriction is satisfied for T < 15 days.

The estimates for decay time are relatively long compared to estimates given by Brink and Allen (1978) for barotropic continental shelf waves at mid-latitudes, reflecting both the dependence of spin down time on latitude and the inhibition of bottom friction effects by stratification. These long decay times may explain why free coastally trapped waves with T = 5-10 days are observed to propagate along the Peru coast between 2°S and 17°S latitude with little evidence of frictional decay (Smith, 1978; Romea and Smith, 1982).

Frictionally induced phase shifts are proportional to $\lambda = E_v^{1/2}/\omega$ and are stronger for higher latitudes or lower frequency. Plots of the x-z phase dependence of p and v for the n = 1 mode internal Kelvin wave (Figures 2a,b for the steep slope case and Figures 9a,b for the weak slope case) indicate substantial qualitative differences between the two cases. Phase shifts in v for the steep slope case are largest near the surface, with a phase lag in x of 30° over the Rossby radius scale with motions at the coast leading. Surface motions lead those below, and the vertical phase lags are greatest near the surface and the coast. In contrast, phase shifts predicted for the weak slope case are much smaller and motions at the bottom lead those above.

The onshore flow due to friction u_f also depends on the model used. For the steep slope (Figure 6), u_f is largest near x = 0, z = 0 due to the mass flux out of the Ekman layer at the point, while for the weak slope (Figure 10) u_f is strongest near x = 0, z = -1.

Slope topography affects free internal Kelvin waves directly in several ways: There is a change in wave frequency and alongshore

phase speed, the modal amplitude is altered, and an onshore flow is induced.

Changes in modal structure and phase speed due to topography for the weak slope case agree with arguments by Hogg (1980) that observations of baroclinic wave dynamics on a sloping bottom can be rationalized with internal modes on a flat bottom by defining an effective bottom depth as an average over the offshore decay scale. The expression (4.16), which is the modification to the wave speed due to a weak slope, is analagous to the result obtained by Miles (1972) for barotropic Kelvin waves with the assumption that the shelf width is small compared to the external Rossby radius scale.

For the steep slope case, corrections to the free wave speed are dependent on details of the slope geometry. A slope which is concave downward (Figure 4) acts to increase the speed while a slope which is concave upward decreases the speed. A linear slope induces a distortion to the x-z modal structure but does not affect the wave speed to first order. Most continental slopes are concave downward, therefore at low latitudes we may expect to see wave speeds that are augmented relative to the predicted flat bottom wave speed. These results are different from Miles' result for barotropic Kelvin waves that the addition of a narrow slope always slows the wave speed relative to the speed with a vertical wall.

The topographically induced onshore flow u_T for the weak slope is strongest directly over the slope and increases offshore, matching to an outer slope solution consisting of a topographic Rossby wave (see Appendix B). For the steep slope, u_T is strongest over the

slope near the zero crossing of v, reflecting the interaction of the O(1) w, which has a maximum near v = 0, with the slope.

Brink's (1982b, Figure 3) numerical calculation of free coastal trapped waves for $\frac{\omega}{f} = 0.15$ and near 15° latitude with bottom friction and realistic stratification and topography shows p at the bottom leading p above and p at the coast leading p offshore. These results agree with predictions from the weak slope model. An empirical orthogonal function (EOF) for the 0.1-0.2 cpd frequency band using alongshore velocity from the Lobivia and Lagarta moorings near 15°S over the slope off the Peru coast in 650 m of water (Romea and Smith, 1982, Figure 15a) shows v at 215 m leaving v at 58 m by 19°. On the shelf near 15°S, at the Mila mooring in 120 m of water, an EOF for the same frequency band as above shows v at 115 m leading v at 19 m by 30°. Both these observations and the numerical calculation suggest that, at 15°S, where $L_s/\delta_R \sim O(1)$, the predictions of the weak slope modes are more appropriate.

An EOF for the 0.1-0.2 cpd frequency band using alongshore velocity at 5°S off the Peru coast from the C2 mooring over the slope in 1360 m of water (Romea and Smith, 1982, Figure 15b) shows a phase shift from near the surface (86 m) to below the zero crossing for the EOF (860 m) of 190°, with the surface leading. This EOF and the EOF calculated for Lobivia and Lagarta are shown in Romea and Smith (1982) to represent first mode internal Kelvin waves. These observations at lower latitude where $L_s/\delta_R \ll 1$ are in qualitative agreement with predictions from the steep slope model (Figure 2).

Brink (1982a) also calculates free wave phase speeds for realistic stratification and topography using a numerical model and finds that, between 5° and 15° latitude, the wave speed is lower than the wave speed predicted with a vertical wall at the coast. This is in agreement with predictions from the weak slope model. Brink does not extend his analysis to lower latitude, however there is a hint (see Brink, 1982a, Figure 2) that the free wave phase speed begins to increase for latitudes less than 5°. This may reflect the increase in phase speed predicted with the steep slope model for $L_s/\delta_R << 1$ when the slope is concave downward.

CASE	$\varepsilon(z)$	$c_n^{(1)}$
(a)	$-2\varepsilon_0(z + \frac{1}{2} z^2)$	$c_n^{(0)}\varepsilon_0(n\pi R)^{-1}$
(b)	$\varepsilon_0 z^2$	$-c_n^{(0)}\varepsilon_0(n\pi R)^{-1}$
(c)	$-\varepsilon_0 z$	0
(d)	$-\varepsilon z/\lvert z_0\rvert$; $0 \geq z > -\lvert z_0\rvert$	$c_n^{(0)}\varepsilon_0[1-\cos(2n\pi\lvert z_0\rvert)](2n\pi R\lvert z_0\rvert)^{-1}$
	ε_0; $-\lvert z_0\rvert > z \geq -1$	
(e)	ε_0; $0 \geq z > (-1 + \lvert z_0\rvert)$	$-c_n^{(0)}\varepsilon_0[1-\cos(2n\pi\lvert z_0\rvert](2n\pi R\lvert z_0\rvert)^{-1}$
	$-\varepsilon_0(z + 1 - \lvert z_0\rvert)/\lvert z_0\rvert$;	
	$(-1 + \lvert z_0\rvert) > z \geq -1$	
(f)	$-\varepsilon_0 z/\lvert z_0\rvert$; $0 \geq z > -\lvert z_0\rvert$	0
	ε_0; $-\lvert z_0\rvert > z > (-1 + \lvert z_0\rvert)$	
	$-\varepsilon_0(z + 1 - \lvert z_0\rvert)/\lvert z_0\rvert$;	
	$(-1 + \lvert z_0\rvert) > z \geq -1$	

Chapter IV

TABLE 1: $O(\varepsilon_0)$ topographic corrections $c_n^{(1)}$ to the $O(1)$ phase speeds $c_n^{(0)}$ for each of the profiles $\varepsilon(z)$ shown in Figure 4. For each case, $\lambda = 0$, the shelf-slope width at $z = -1$ is ε_0, and $R = R_0$.

	WEAK SLOPE				STEEP SLOPE		
s	$\lvert v_{(-1)}/v_{(0)}\rvert$	μ	$\mu/\lvert v_{(-1)}/v_{(0)}\rvert$	T_f' (days)	μ	$\mu\lvert v_{(-1)}/v_{(0)}\rvert$	T_f' (days)
0	1	0.5	0.5	89	0.5	0.5	89
0.5	0.79	0.39	0.49	114	0.64	0.50	70
1	0.61	0.30	0.49	148	0.80	0.49	56
2	0.40	0.19	0.48	234	1.2	0.48	37
3	0.28	0.13	0.46	342	1.6	0.45	28
5	0.17	0.08	0.44	594	2.6	0.44	17

Chapter IV

TABLE 2: Ratio of bottom alongshore velocity $v_{(-1)}$ to surface alongshore velocity $v_{(0)}$ for the n = 1 internal Kelvin wave for various s, where the stratification is given by $R(z) = R_0 \exp(sz)$. Also shown are $\mu - |\omega_1^{(1)}(\text{frictional})|/E^{\frac{1}{2}}$ for the weak and steep slope models. The dimensional spin down time is listed and is given by $T_f' = (E^{\frac{1}{2}} f \mu)^{-1}$, with $E^{\frac{1}{2}} = 0.02$ and $f = 1.3 \times 10^{-5} s^{-1}$ (5° latitude).

FIGURE CAPTIONS

Figure 1: Steep slope model.

Figure 2: Frictionally induced phase shift θ (in degrees) in (a) p and (b) v for the n = 1 internal Kelvin wave in the x*-z plane for $\lambda_1^{(0)} = 0.1$, topography (3.25) with $\varepsilon_0^* = 0.1$, and $R = R_0$ = constant. $\theta_1 > \theta_2$ implies 1 lags 2. Steep slope model.

Figure 3: x*-z amplitude structure of v for the n = 1 internal Kelvin wave for $\lambda_1^{(0)} = 0$, topography (3.25) with $\varepsilon_0^* = 0.3$, and $R = R_0$. Steep slope model.

Figure 4: Various slope topographies. The letters correspond to the cases discussed in Section 3 and listed in Table 1; (a) slope profile which is concave downward, (b) slope profile which is concave upward, (c) linear slope.

Figure 5: Topographically induced scaled onshore first mode velocity u/ε_0 in the x*-z plane for $\lambda = 0$, topography (3.25) with $\varepsilon_0^* = 0.1$, and $R = R_0$. Steep slope model.

Figure 6: First mode u/ε^* in the x*-z plane for $\lambda_1^{(0)} = \varepsilon_0 = 0.1$, topography (3.25), and $R = R_0$. Steep slope model.

Figure 7: Weak slope model.

Figure 8: Zero crossing for the n = 1 internal Kelvin wave for v in the x*-z plane, with $\lambda = 0$, $\varepsilon = 0.1$, and $R = R_0$ (solid line). Dotted line: predicted zero crossing for corresponding flat bottom mode with bottom at z = -1. Dashed line: predicted zero crossing for corresponding flat bottom mode with bottom at z = -1.05. Weak slope model.

Figure 9: Frictionally induced phase shift θ (in degrees) in (a) p and (b) v for the first mode internal Kelvin wave in the x*-z plane for $\lambda_1^{(0)} = 0.1$, $\varepsilon = 0$, and $R = R_0$. $\theta_1 > \theta_2$ implies 1 lags 2. Weak slope model.

Figure 10: Topographically induced onshore flow u_T/ε in the x*-z plane with $\lambda = 0$, $\varepsilon = 0.1$, and $R = R_0$, for the first mode internal Kelvin wave. Weak slope model.

Figure 11: Frictionally induced onshore flow $u_F/\lambda_n^{(0)}$ in the x*-z plane with $\varepsilon = 0$ and $R = R_0$, for the first mode internal Kelvin wave. Weak slope model.

Figure 12: Profiles of $R(z)/R_0$ for various s, where $R(z) = R_0 \exp(sz)$, and R_0 = constant.

Figure 13: Vertical structure of v for the first mode internal Kelvin wave for various s. The modes are rescaled such that $v(x = 0, z = 0) = 1$. Also shown is the first dynamical mode (labelled R) calculated using the N^2 profile shown in Figure 14.

Figure 14: N^2 profile, smoothed with a three point moving average, calculated from CTD observations at 4°58.9'S, 81:33.0'W on May 22, 1977. The procedure used to obtain and process the CTD data is discussed by Huyer et al. (1978).

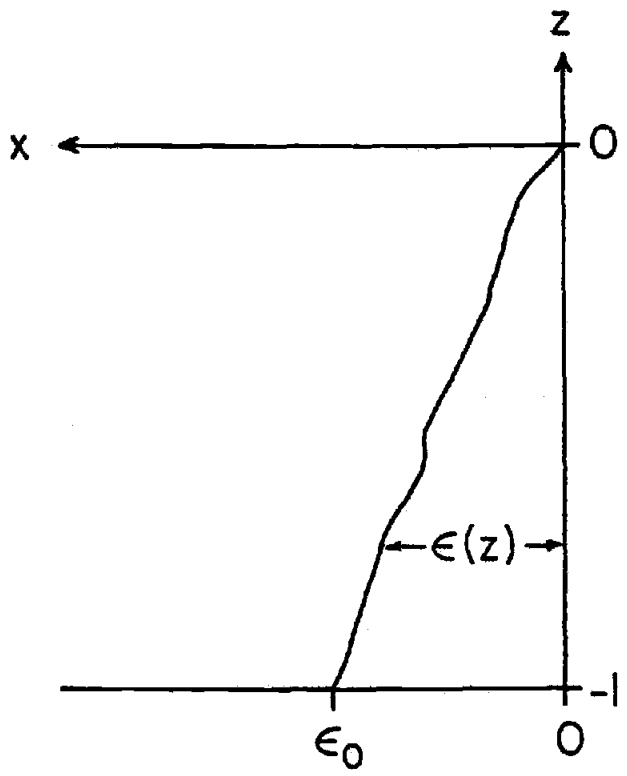

Figure IV-1

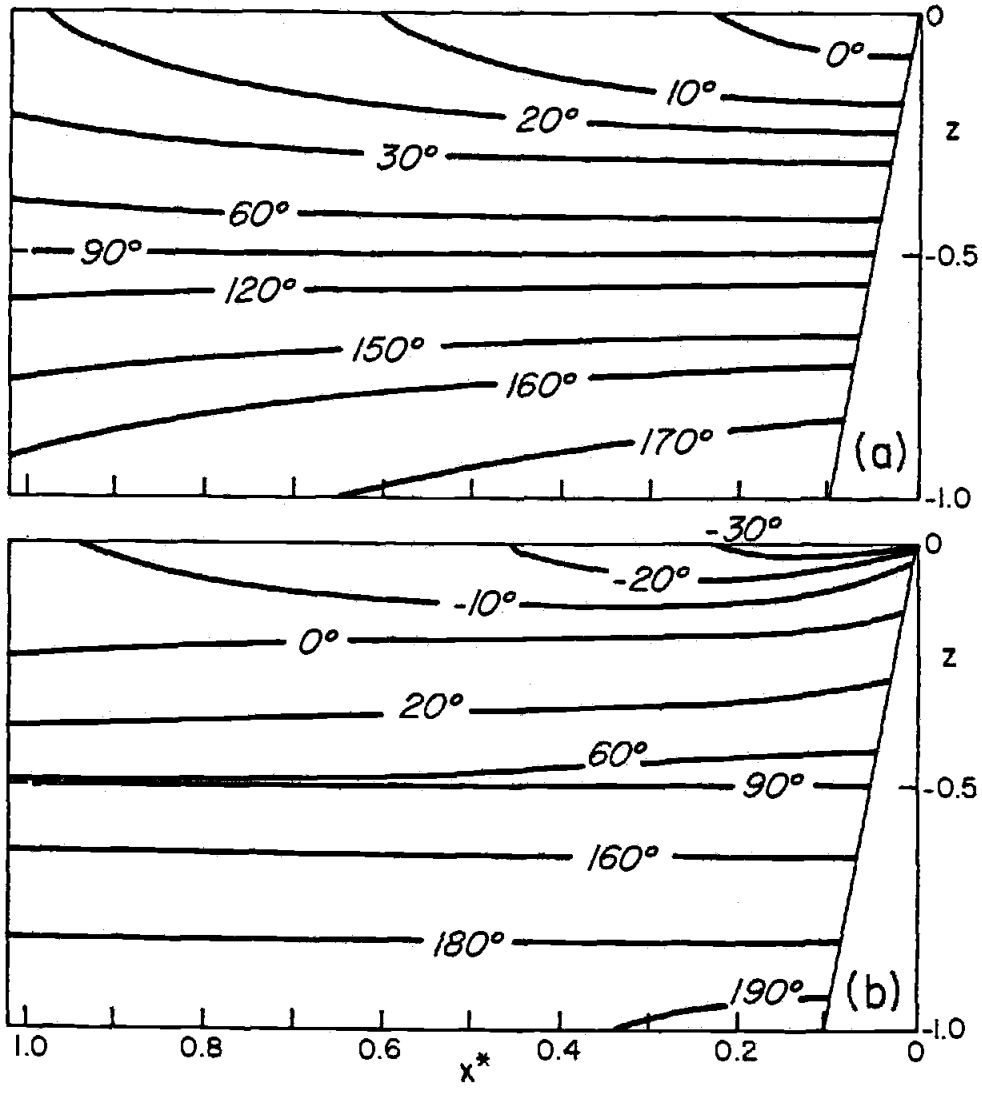
0°
10°
20°
30°
60°
90°
120°
150°
160°
170°
(a)
z
0
-0.5
-1.0
-30°
-20°
-10°
0°
20°
60°
90°
160°
180°
190°
(b)
1.0
0.8
0.6
0.4
0.2
0
x*

Figure IV-2

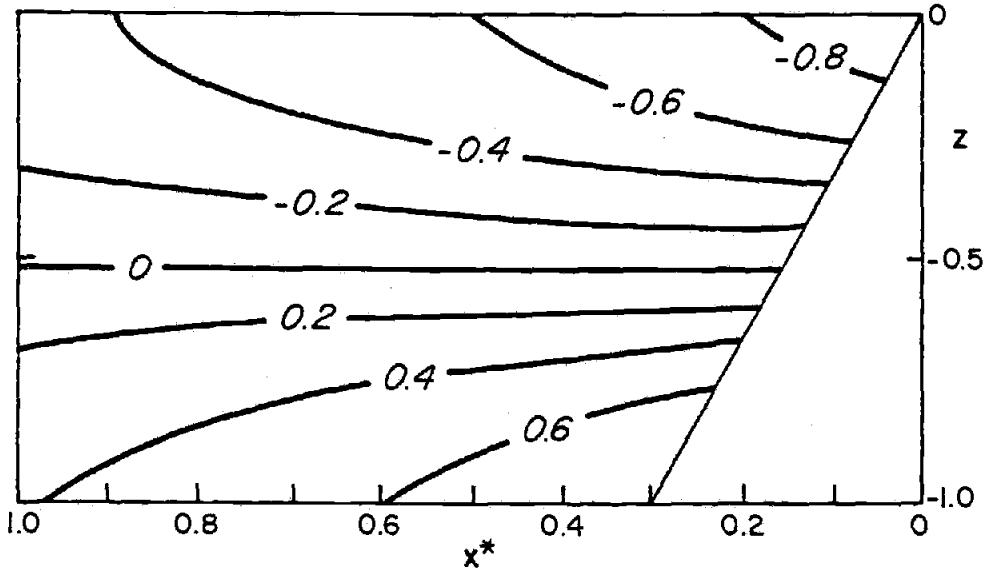

Figure IV-3

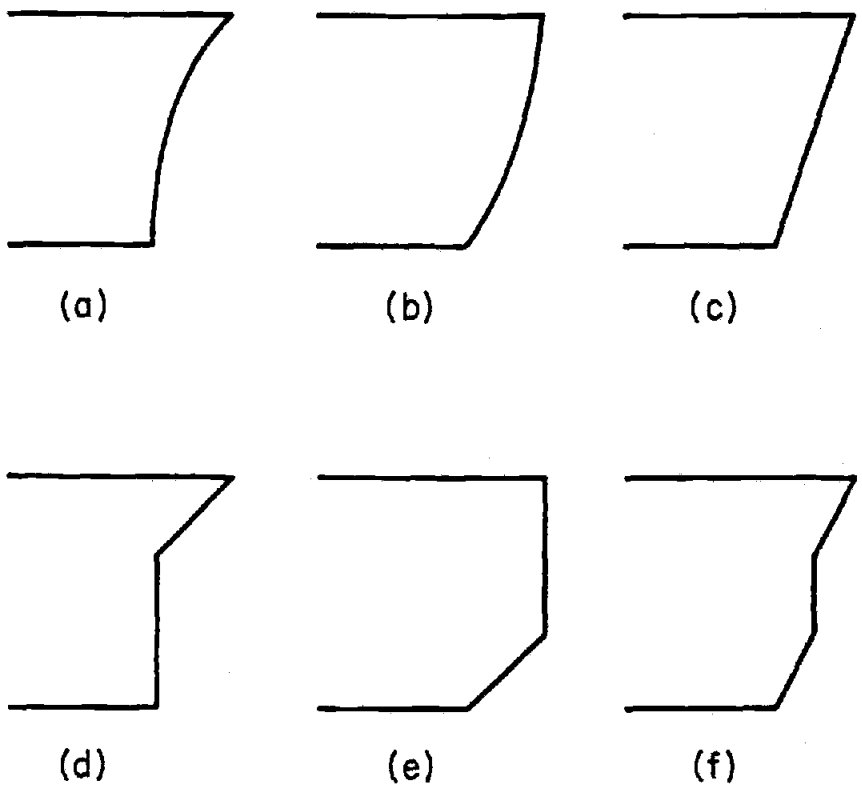

Figure IV-4

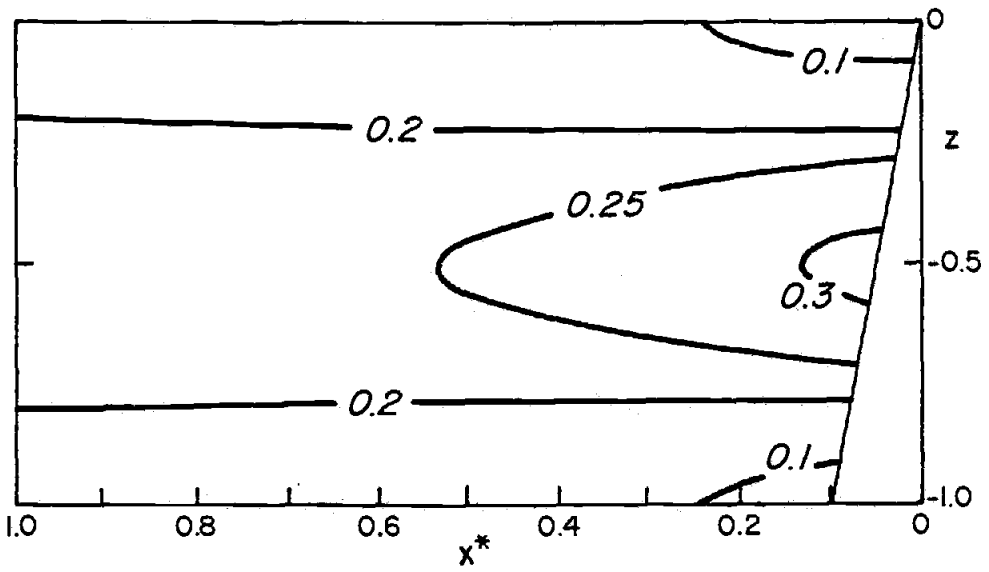

Figure IV-5

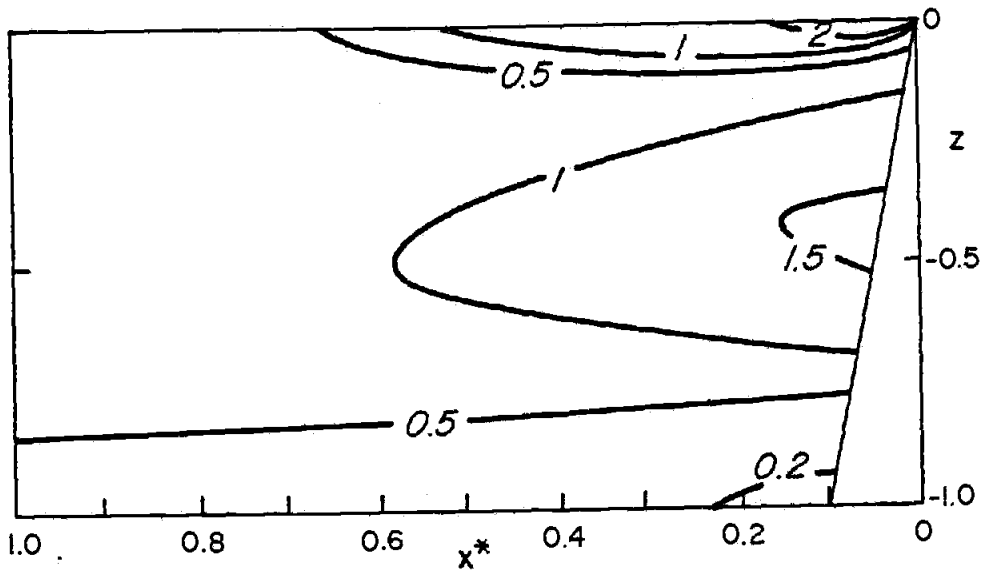

Figure IV-6

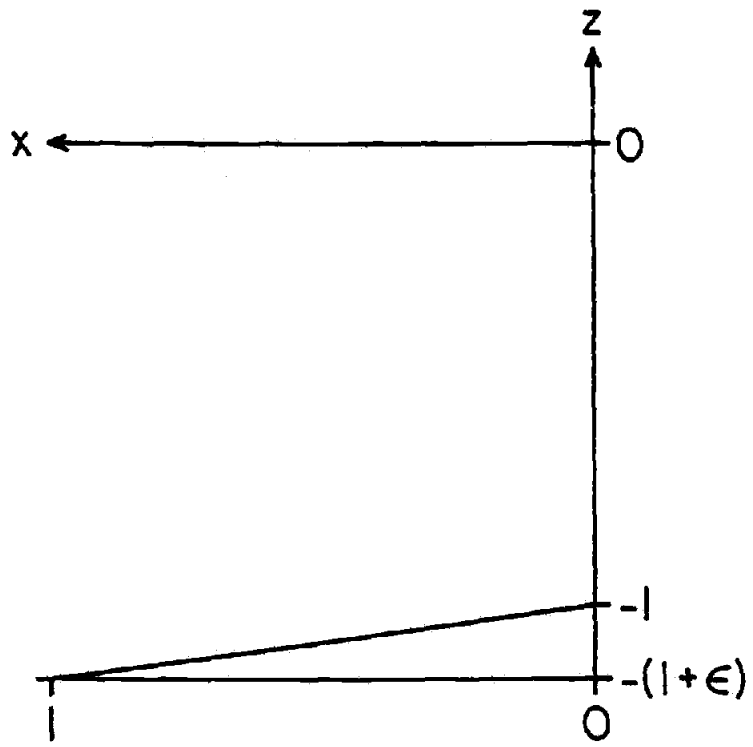

Figure IV-7

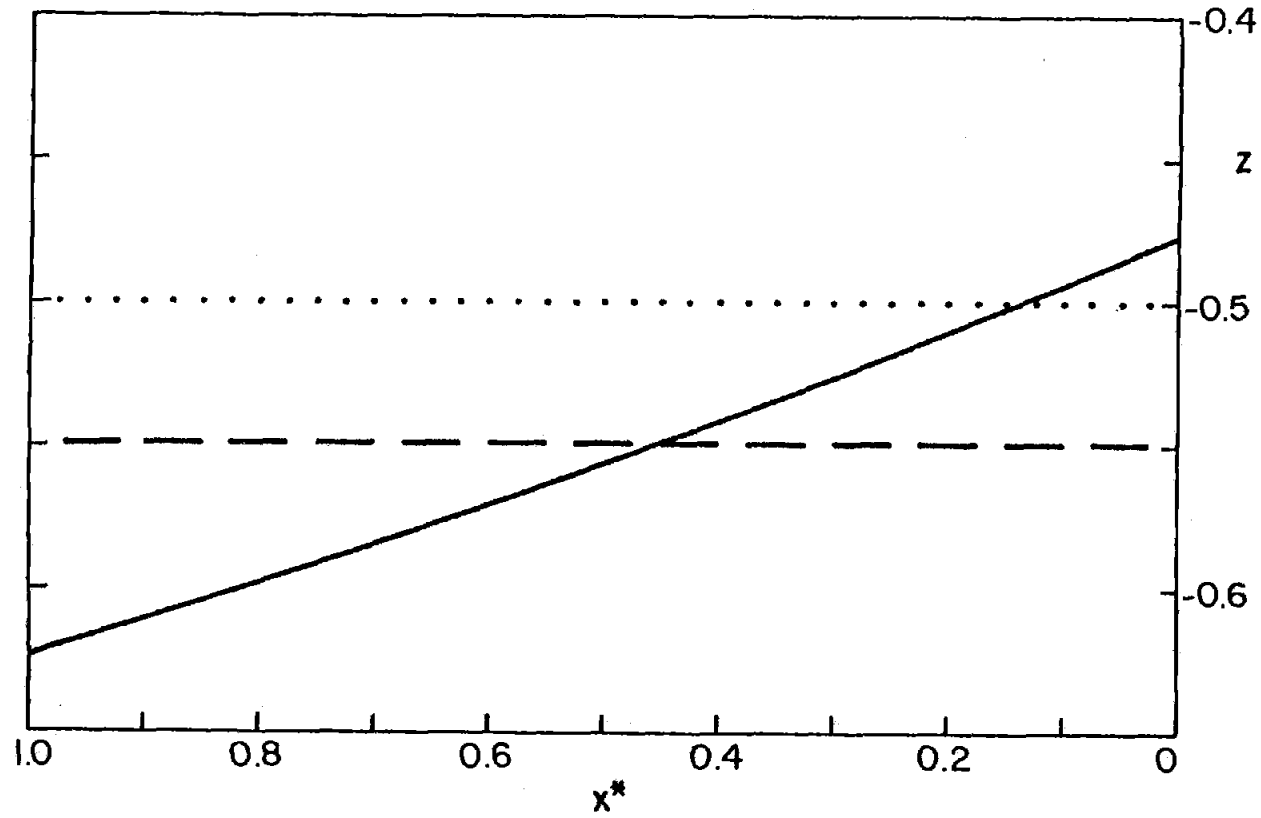

Figure IV-8

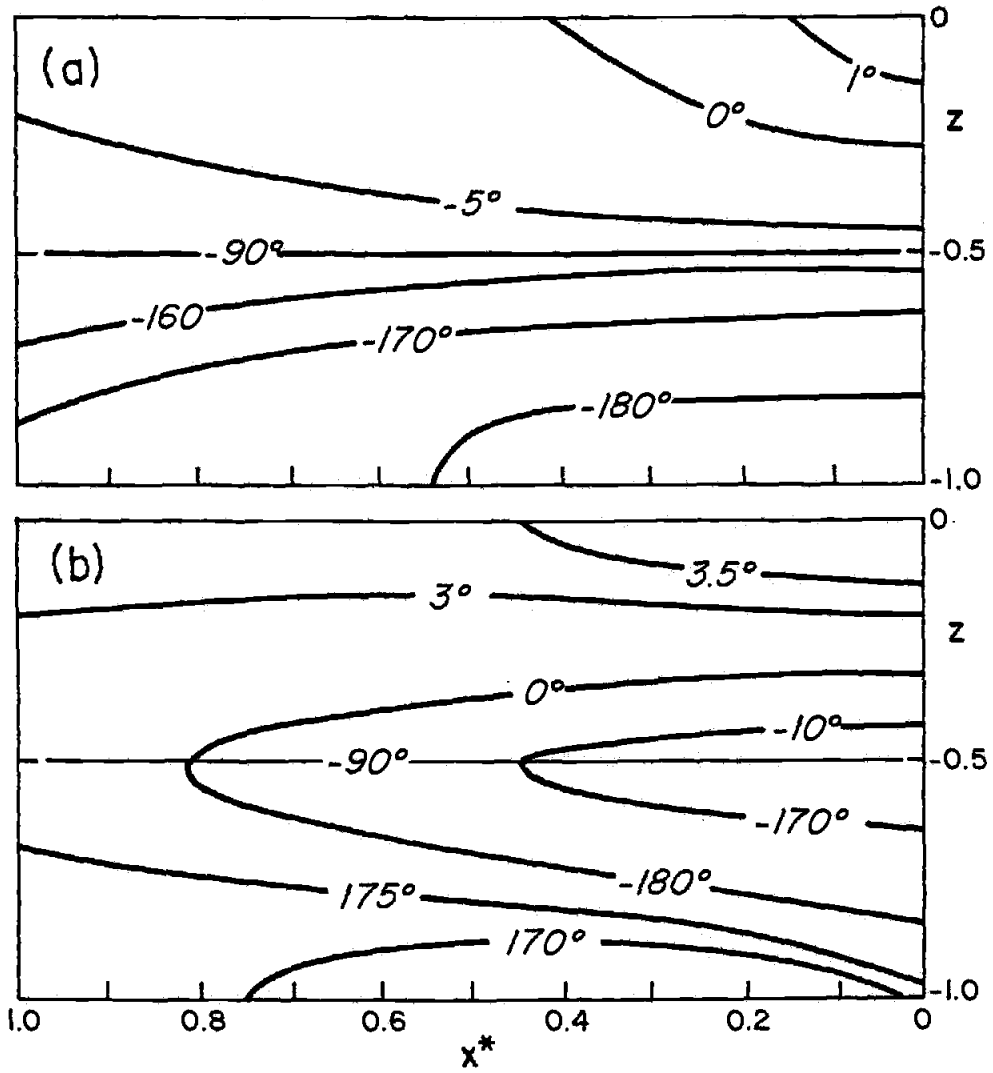
(a)
1°
0°
-5°
-90°
-160
-170°
-180°
0
z
-0.5
-1.0
(b)
3.5°
3°
0°
-10°
-90°
-170°
-180°
175°
170°
0
z
-0.5
-1.0
1.0
0.8
0.6
0.4
0.2
0
x*

Figure IV-9

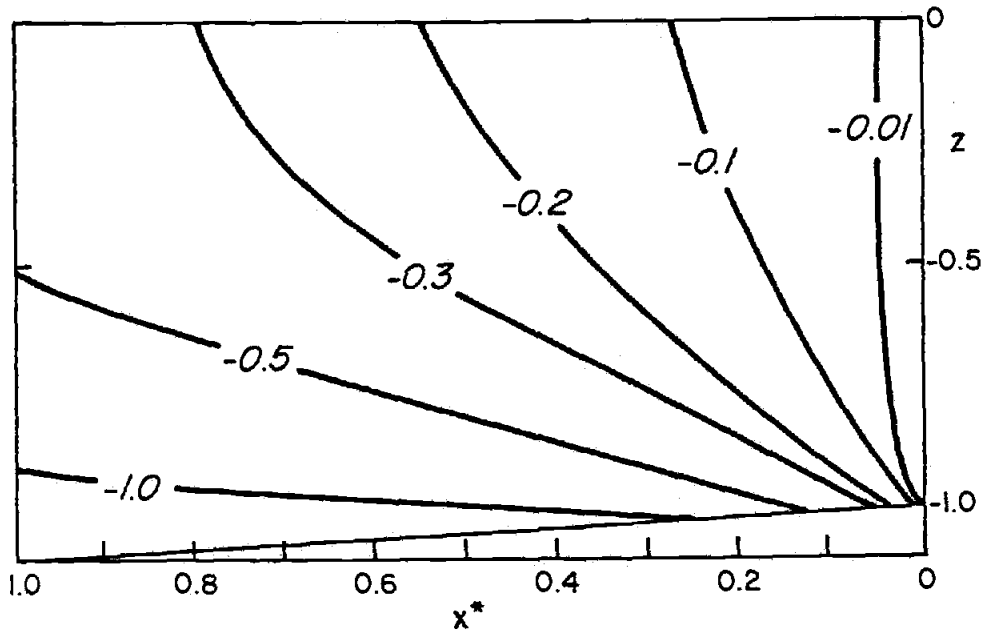

Figure IV-10

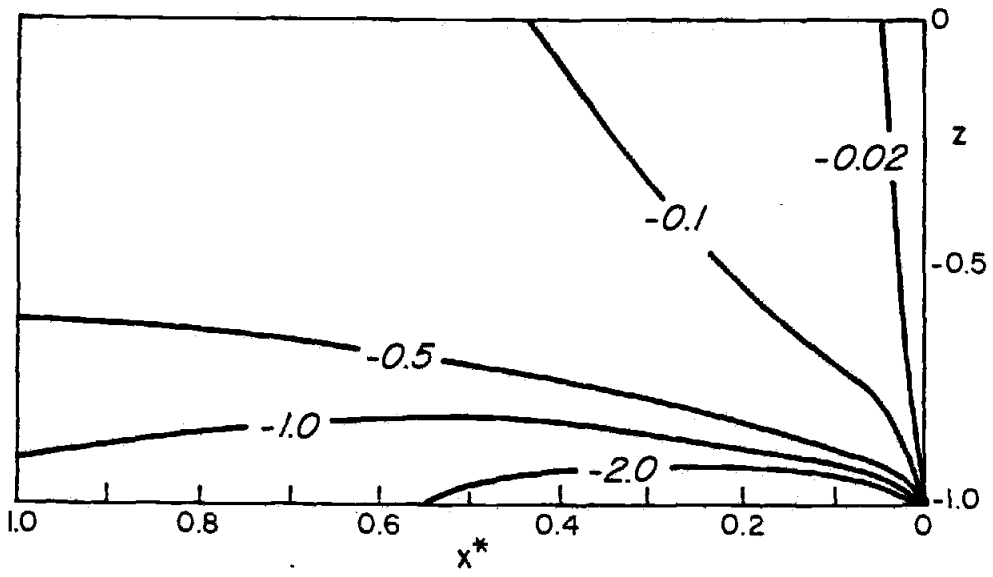

Figure IV-11

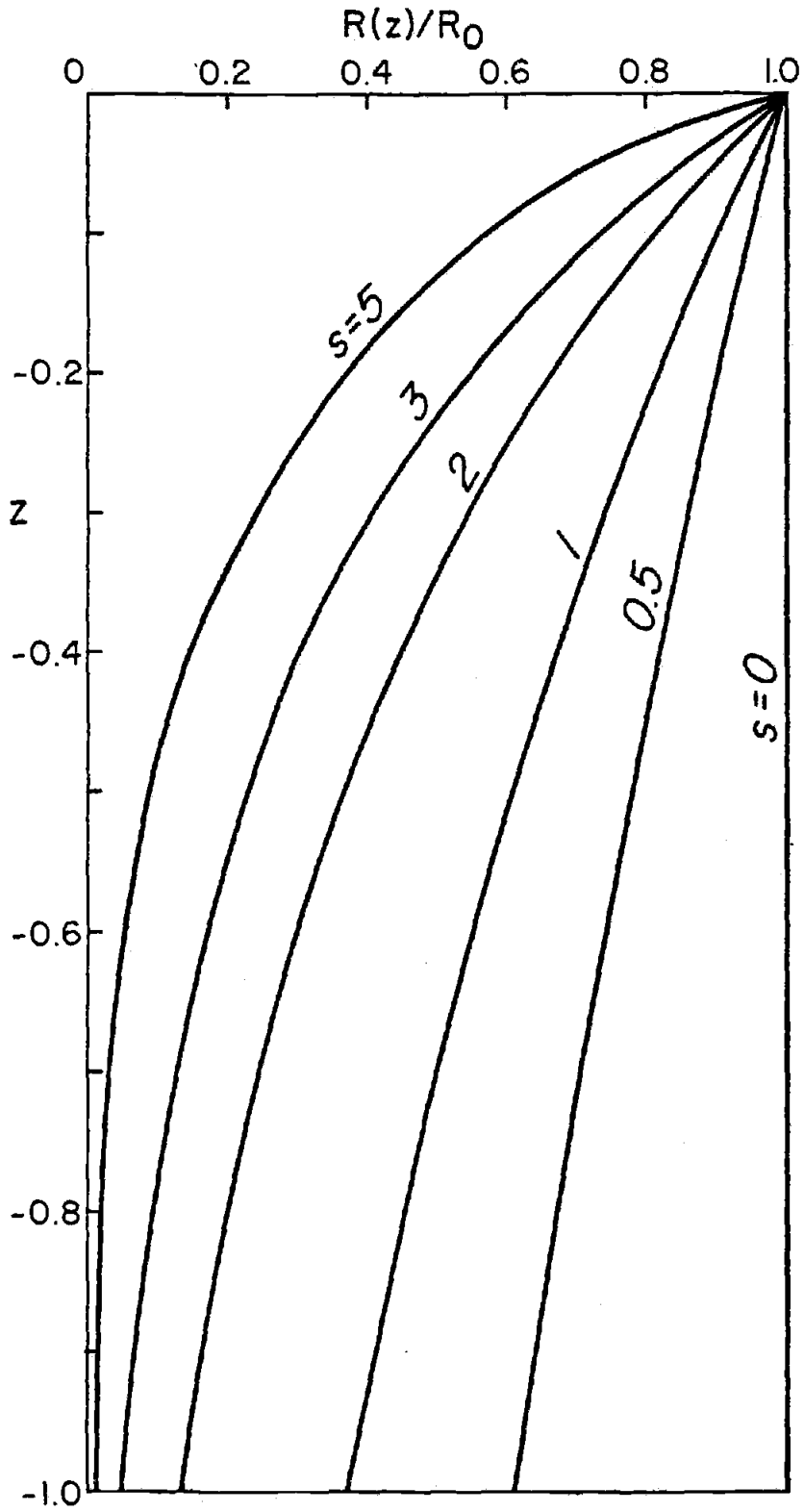

Figure IV-12

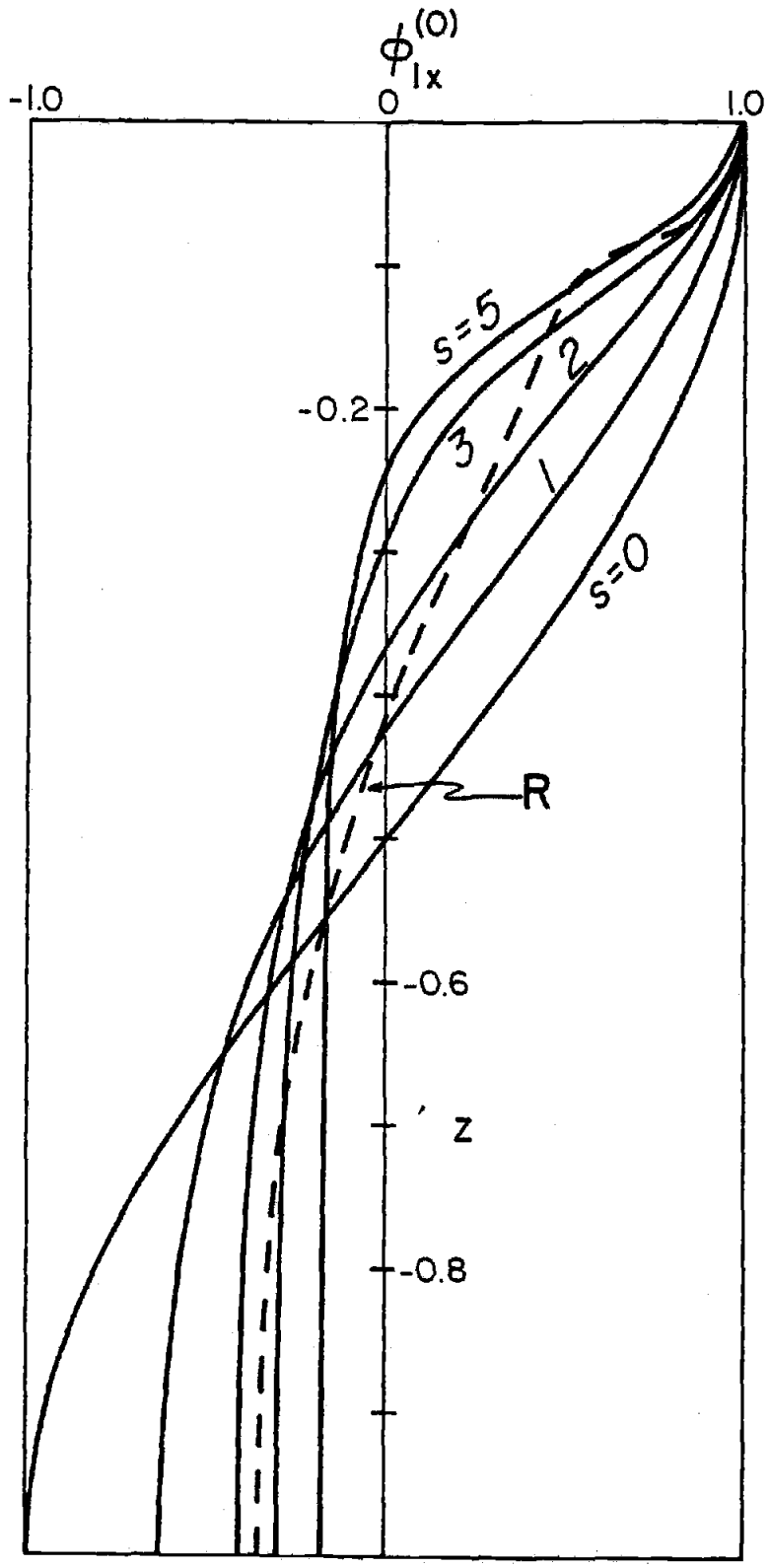

Figure IV-13

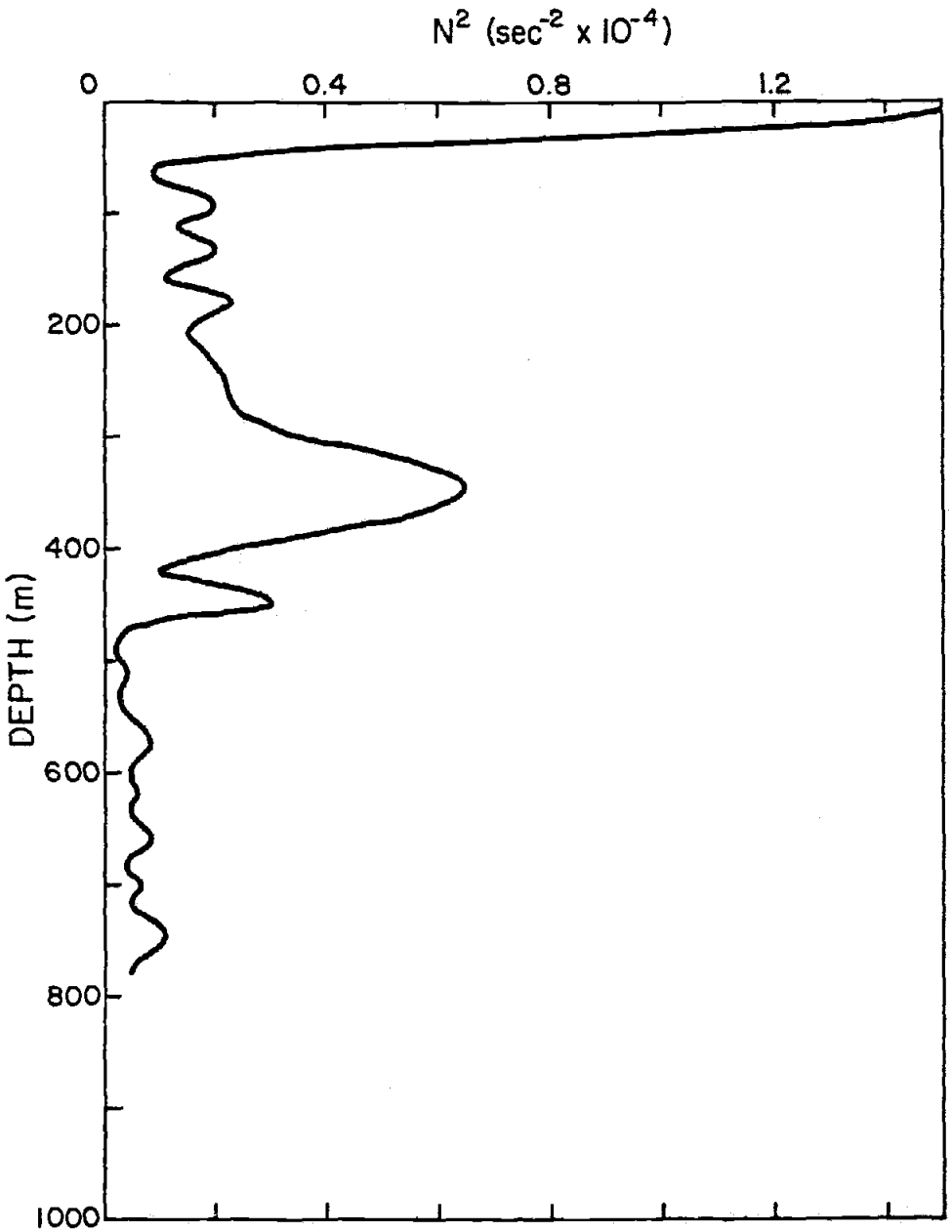

Figure IV-14

REFERENCES

Allen, J. S., 1973. Upwelling and coastal jets in a continuously stratified ocean. J. Phys. Oceanogr., 3: 245-257.

Allen, J. S., 1975. Coastal trapped waves in a stratified ocean. J. Phys. Oceanogr., 5: 300-325.

Allen, J. S., and Romea, R. D., 1980. On coastal trapped waves at low latitudes. J. Fluid Mech., 98: 555-585.

Allen, J. S., and Smith, R. L., 1981. On the dynamics of wind driven currents. Phil. Trans. R. Soc. Lond. A,302: 617-634.

Brink, K. H., 1982a. A comparison of long coastal trapped wave theory with observations off Peru. J. Phys. Oceanogr., in press.

Brink, K. H., 1982b. The effect of bottom friction on low frequency coastal trapped waves. J. Phys. Oceanogr., 12: 127-133.

Brink, K. H., and Allen, J. S., 1978. On the effect of bottom friction on barotropic motion over the continental shelf. J. Phys. Oceanogr., 8: 919-922.

Brink, K. H., Allen, J. S., and Smith, R. L., 1978. A study of low frequency fluctuations near the Peru coast. J. Phys. Oceanogr., 8: 1025-1041.

Brink, K. H., Halpern, D., and Smith, R. L., 1980. Circulation in the Peruvian upwelling system near 15°S. J. Geophys. Res., 85: 4036-4048.

Clarke, A. J., 1976. Observational and numerical evidence for wind forced coastal trapped long waves. J. Phys. Oceanogr., 7: 231-247.

Greenspan, H. P., 1968. The Theory of Rotating Fluids, Cambridge University Press, Cambridge, 328 pp.

Hogg, N. G., 1980. Observations of internal Kelvin waves trapped round Bermuda, J. Phys. Oceanogr., 10: 1353-1376.

Huthnance, J. M., 1975. On trapped waves over a continental shelf. J. Fluid Mech., 69: 689-704.

Huthnance, J. M., 1978. On coastal trapped waved: analysis and numerical calculation by inverse iniration. J. Phys. Oceanogr., 8: 74-92.

Huyer, A., Gilbert, W. E., Schramm, R., and Barstow, D., 1978. CTD observations off the coast of Peru, R/V Mellville 4 March-22 May 1977, and R/V Columbus Iselin, 5 April-19 May 1977. Data report 71, Oregon State University, Reference 78-18, 409 pp.

Kundu, P. K., Allen, J. S., and Smith, R. L., 1975. Modal decomposition of the velocity field near the Oregon coast. J. Phys. Oceanogr., 5: 683-704.

Miles, J. W., 1972. Kelvin waves on oceanic boundaries. J. Fluid Mech., 55: 113-127.

Pedlosky, J., 1974. On coastal jets and upwelling in bounded basins. J. Phys. Oceanogr., 4: 3-18.

Pedlosky, J., 1979. Geophysical Fluid Dynamics. Springer-Verlag, New York, 624 pp.

Rhines, P., 1970. Edge- bottom-, and Rossby waves in a rotating stratified fluid. Geophys. Fluid Dyn., 1, 273-302.

Romea, R. D., and Smith, R. L., 1982. The compilation of evidence for coastal trapped waves along the Peru coast. In preparation.

Smith, R. L., 1978. Poleward propagating perturbations in sea level and currents along the Peru coast. J. Geophys. Res., 83: 6083-6092.

Vermersch, J. A., and Beardsley, R. C., 1976. A note on the theory of low frequency waves in a rotating stratified channel. Studies in Applied Math., 55: 281-292.

Chapter V

THE COMPILATION OF EVIDENCE FOR COASTAL TRAPPED WAVES ALONG THE PERU COAST

1. Introduction

Evidence for the existence of coastally trapped waves along the central Peru coast has been previously presented by Smith (1978). He showed that measurements made during the CUEA (Coastal Upwelling Ecosystems Analysis) JOINT-2 experiment in May-July 1976 and March-May 1977 indicated poleward propagation of fluctuations in sea level and currents between 10° and 15°S with phase speeds of about 200 km day^{-1}. The structure of the current fluctuations and the dynamical balances suggested that the waves were internal Kelvin wave-like (Smith, 1978; Brink, et. al., 1978; Brink, et. al., 1980). Although the frequency range of the propagating fluctuations (0.1 to 0.2 cpd) was similar to that of weather events, the fluctuations were not correlated with winds measured at 12°S or 15°30'S and an equatorial origin was hypothesized.

Additional, and in some cases, considerably longer time series measurements have become available for the same time period as the CUEA experiment: meteorological and tide gage data from the Ecuador and Peru coasts equatorward of 10°S, and current meter data from the ESACAN (Estudio del Sistema de Afloramiento Costero en el Area Norte) experiment conducted by the Institut fur Meersukunde an der Universitat Kiel and Instituto del Mar del Peru at 5°S off the Peru coast during March-May 1977. The ESACAN data set is of particular interest because it provides an opportunity to study the wave structure at lower latitudes and the possibility of linking equatorially generated fluctuations to those observed between 10° and 15°S during the CUEA experiment.

The combined data set includes current and temperature measurements

near 5°, 10°, 12°, and 15°S off Peru, coastal winds near 4°, 7°, 12°, and 15°S, hydrographic sections normal to the coast at those latitudes, and sea level from the tide gages on the Galapagos Islands (0°27'S) and on the South American continent between 2° and 17°S. Atmospheric pressure data were obtained near many of the tide gages. Presentation and basic analysis of the data near 15°S may be found in Brink, et. al. (1980), and a discussion of the ESACAN data near 5°S is given by Fahrbach, et. al., (1981). The statistics of the CUEA and ESACAN current meter data are given by Brockmann, et. al., (1980), in a study on the Peru undercurrent.

In this study we utilize the CUEA and ESACAN current meter and coastal wind data and the longer tide gage records to reexamine the conclusions presented by Smith (1978) and to extend his analyses farther equatorward. The locations of the observations used are shown in Figure 1. A more detailed discussion of the data set is presented in the Appendix. Unless explicitly stated otherwise, the time series data presented and analyzed in this paper have been initially subjected to a low pass filter (half power point = 1.96 days) to eliminate diurnal and higher frequency phenomena.

2. The Longer Time-Series

The longest reliable data records are those of sea level and atmospheric pressure at La Libertad (2°12'S), Callao (12°03'S), and San Juan (15°21'S), and those of current and coastal wind near San Juan. After low-pass filtering to remove diurnal phenomena, the common period for continuous data extends for 405 days from 27 March 1976. The

atmospheric pressure records were used to 'adjust' sea level to provide an equivalent to a subsurface pressure, i.e., the 'inverted barometer' effect was removed by adding the atmospheric pressure (in mb) to sea level (in cm). The adjusted sea levels, the current measured at 55 m over the shelf (120 m) at 15°S and the coastal wind at San Juan are shown in Figure 2.

The dominant fluctuations in sea level are clearly similar at the three tide gage stations, and the tendency for the extrema at a southern station to lag the equivalent extrema at a northern station may be seen in Figure 2 (cf., Figure 2 in Smith, 1978). The relation of the shelf current fluctuations to those of sea level is clearly apparent, e.g., equatorward (northwestward along the coast) flow occurs only in connection with sea level minima. The coastal wind is remarkably uniform in direction and is apparently not the cause of the fluctuations in the coastal current.

Figure 3 shows the autospectra of Callao and San Juan sea levels and the coherence and phase between them for the 405 day long records. The sea level records have been adjusted for atmospheric pressure effects. The high coherence and the linear dependence of phase on frequency, for frequency less than 0.13 cpd and in the 0.15-0.2 cpd band, indicates non-dispersive poleward propagation at about 240 km day^{-1}.

Although the cross spectrum suggests that the non-dispersive wave-like propagation extends to lowest frequency, there is a theoretical lower bound on frequency for transmission along the coastal waveguide. This frequency cutoff corresponds to the approximate condition for coastal trapping, given by $\sigma^2 > (\beta/\ell)^2/4$, where σ is radian frequency,

ℓ is the alongshore wavenumber, and β is a measure of the variation of the Coriolis parameter with latitude (see Allen and Romea, 1980, for an additional discussion of this point). For example, the condition is satisfied for $\sigma > 4 \times 10^{-6}$ s^{-1} (period T < 18 days) for an alongshore phase speed $c = \sigma/\ell = 240$ km day^{-1}.

Auto and cross spectra are shown in Figure 4 for La Libertad and Callao sea level. The distance between these stations is much greater (1200 km) than between Callao and San Juan (450 km), and the coherence is generally lower. However, there is again a peak in the coherence near 0.17 cpd and the 0.16-0.19 cpd band is coherent at or above the 95% confidence level. A linear dependence of phase on frequency for frequencies less than 0.2 cpd is again suggested, with the phase consistent with poleward propagation at about 240 km day^{-1}.

In contrast to the sea level, the atmospheric pressures at La Libertad, Callao, and San Juan are in phase and highly coherent for frequency ω < 0.2 cpd. Figure 5 shows the spectral computations for atmospheric pressures at La Libertad and San Juan, which are the pair with the greatest alongshore separation (>1500 km). The figure indicates that the wave-like propagation observed in sea level is not a forced response to large scale atmospheric pressure systems.

If the fluctuations represent baroclinic coastally trapped waves with the alongshore velocity in geostrophic balance, sea level and currents should be highly coherent. We shall use both sea level and currents to demonstrate propagation from 2° to 17°S and therefore we examine their relationship. The phase relation should be 180° for inviscid motion, i.e., southward flow near the coast should be

associated with higher sea level near the coast.

Figure 6 shows the cross-spectra between sea level at San Juan and alongshore current at M (55 m). The alongshore direction has been defined as the principal axis direction from the current record. This is close to the orientation of the local isobaths (Smith, 1978). Alongshore current and sea level are highly coherent for $\omega < 0.2$ and nearly 180° out of phase, consistent with a geostrophic balance. Friction may account for the lack of an exact 180° phase relationship, or it may simply result from the fact that the current meter location is 50 km equatorward of the tide gage. This latter fact would account for the observed phase difference near 0.17 cpd, assuming a propagation speed of 240 km day^{-1}.

Finally, we examine the relationship between local winds at San Juan and the alongshore current at M (55 m). The cross-spectrum (Figure 7) shows relatively high coherence for 0.06-0.09 cpd but low coherence for 0.1-0.2 cpd. Although this suggests that very low frequency motions may be locally wind driven, it supports the hypothesis that propagating disturbances in the 0.1-0.2 cpd band, which are observed in the long sea level records, are not locally wind driven.

The analysis of the long records is consistent with the findings of Smith (1978), based on considerably shorter records. The long records have provided greater confidence and resolution in the cross-spectral computations. The frequency band centered at 0.17 ± 0.02 cpd is especially suggestive of free propagating coastally trapped waves (the puzzling 'drop out' of coherence near 0.13 cpd seems real, and is also suggested in the analysis by Smith (1978) of the 72 day records).

In the analysis of the shorter current meter data from March-May 1977, we shall focus on the frequency band centered at 0.17 cpd.

3. Observations during March-May 1977

The most extensive and complete data set exists for the period of March-May 1977. Data from all sites shown in Figure 1 were obtained during that period. Brink, et. al., (1980), using the data near 15°S, showed that the local subtidal momemtum balances (v_t, p_x; v_z, T_x; v, p_y) and the empirical modes were consistent with those expected of free internal Kelvin waves. Using the spatially extensive data set from the array of measurements indicated in Figure 1, can we demonstrate that consistent poleward propagation of the fluctuations in current and sea level extends from the equatorial zone? Can we eliminate the coastal winds as the dominant driving force for the fluctuations? Are the empirical modes at 5°S and 15°S (the latitudinal extrema of the current measurements) similar? The latter is of interest because of the theoretical findings of Allen and Romea (1980) that coastally trapped baroclinic fluctuations propagating poleward from the equatorial region may take the form of barotropic shelf waves at mid-latitudes.

(a) Sea Level

The additional sea level data series available during March-May 1977 are not especially useful because the overall common period with good quality data is too short for meaningful spectral analysis; the Talara and Matarani tide gages malfunctioned at different times during the period. However, evidence for consistent poleward propagation in

sea level perturbations can be easily seen and summarized by the lagged cross-correlation between pairs of stations. Since the cross-spectral analysis of the long sea level records suggests non-dispersive propagation, the time lag for which the maximum correlation occurs between sea level stations should depend linearly on the alongshore separation of the stations.

For each pair of sea level records, we have used the longest common record length that extends into the March-May 1977 period to compute lagged cross-correlations. In Figure 8, the time lag for which maximum correlation is obtained is plotted as a function of alongshore separation for 1) each adjacent pair of sea level records, 2) each record vs. Callao sea level, and 3) San Martin vs. Matarani sea level, which we show because it has the same spatial separation, but displaced latitudinally, as the subsurface pressure gages at P and near M. With the exception of the open circle, which corresponds to the Talara-Callao pair, the correlations at the lag indicated in Figure 8 are all the highest correlations obtained for the pair and are significant at the 99% level, i.e., the probability that the correlation coefficient would result from uncorrelated data is less than 0.01. The maximum correlation between Talara and Callao occurs near 0 lag; the open circle represents the highest lagged correlation, and is significant at the 98% level. The conclusion from the lagged correlations of this suite of data, which extends from nearly 2°S to 17°S, is the same as that from the cross-spectral analysis of the three longer sea level records: perturbations in sea level propagate poleward at about 240 km day^{-1}.

The time lag for maximum correlation between the atmospheric pressure at Callao and that at La Libertad, Talara, San Juan, and Matarani is also shown in Figure 8. A well defined maximum correlation (correlation coefficient greater than 0.9 with significance level greater than 99.9%) at lags less than or equal to 0.5 days exists. Moreover, the pressure data are not significantly correlated (95% confidence level) at lags commensurate with the observed propagation of fluctuations in sea level. This corroborates the findings from the cross spectral analysis of atmospheric pressure that the pressure systems do not move in such a way as to force the observed propagation of sea level.

(b) Current Velocity

The combined ESACAN-CUEA current meter data set from March-May 1977 provides a useful alongshore array of current observations that elucidates the structure and behavior of the propagating fluctuations better than sea level. The current meter data used here have been rotated into a coordinate system in which the alongshore direction is defined by the principal axis of the vector time series.

We first look at the 5°S and 12°S data since the currents from 10°S and 15°S have been analyzed by Smith (1978) and have been shown to be coherent with those at 12°S, with phase differences consistent with free propagating coastal trapped waves. At 5°S, we use only the C2 mooring, which is located over the slope about 50 km from the coast in 1360 m water depth, and which had current measurements from 86, 126, 197, 560, and 860 m. Two other moorings were deployed at 5°S, one on the shelf nearly within the bight of the Bay of Paita

and the other 25 km farther offshore from C2. The current meters from the shelf mooring are 'contaminated' by motions in the Bay of Paita (Fahrbach, et. al., 1981) and the current measurements at the mooring farthest offshore were too deep (the shallowest current meter was at 195 m) to clearly reveal the baroclinic waves.

In Figures 9 and 10 we show the spectra and cross-spectral computations based on the hourly alongshore velocity data from the 86 m current meter at C2 and the 97 m current meter at Y. In the subtidal frequencies high coherence is found in the 0.00625-0.00804 cph (0.15-0.19 cpd) band with a maximum at 0.00714 cph (0.17 cpd). There is a shoulder or relative maximum in both the C2 and Y variance spectra in the frequency band with high coherence. This is also found in the Peyote (10°S) current and Callao sea level spectra for this period (cf., Figure 8 in Smith, 1978). Figure 10 indicates the phase by which Y leads C2 (or, equivalently, C2 lags Y). A phase plot is ambiguous in showing whether a signal actually leads or lags: Figure 10 may be interpreted as C2 lagging Y by 115° or C2 leading by 360° - 115° = 245°. The ambiguity is resolved by considering the phase between other pairs: C2-P, P-Y, P-M, Y-M and by considering the lagged correlation; C2 leading Y by 245° is the quantitatively consistent interpretation. The C2 and Y moorings are 900 km apart along the coast. The phase difference between them leads to an estimated alongshore propagation speed of 225 km day^{-1} poleward.

A geostrophic balance for the alongshore velocity is evident from the shorter current measurements obtained during March-May 1977. The cross-spectrum between alongshore current at C2 (86 m) and sea level

at Talara shows high coherence (greater than the 95% confidence level) in the 0.15-0.19 cpd frequency band with a maximum (coh^2 = 0.72) at 0.17 cpd. Talara sea level lags by 154°, which is within error of 180° and is displaced in the direction expected since Talara is equatorward of C2. At 12°S, Callao sea level and the alongshore current at Y (97 m) are coherent above the 95% confidence level in the band 0.10-0.19 cpd with a maximum coherence at 0.16 cpd (coh^2 = 0.79) and with a phase difference of 180°. These spectral calculations support our hypothesis that the sea level and current fluctuations are manifestations of the same phenomena, and that the fluctuations represent coastally trapped baroclinic waves.

The most efficient way to examine the array of alongshore current meter data is to compute empirical orthogonal functions (EOFs), utilizing the method of EOF analysis in the frequency domain (see Wallace and Dickinson, 1972, for details of the method). This technique has been successfully used by Wang and Mooers (1977) for analyzing low frequency fluctuations off the west coast of the United States. The analysis expresses the time series as a linear combination of the eigenvectors of the cross-spectrum matrix for the frequency interval of interest, and has the advantage over individual cross-spectra of including many records simultaneously. The method is closely related to the use of EOFs in the time domain applied to band-pass filtered data, however by using the cross-spectral matrix we obtain the phase as well as the magnitude of the correlation between the series, i.e., we obtain complex eigenvectors.

For each of the EOFs calculated in this and the following sections, we utilize the longest time series possible, defined by the common record length of the measurements involved. In order to isolate the wave band, and guided by the result of the individual cross-spectral computations, we choose an upper bound on the frequency interval near 0.21 cpd and band average 5 spectral estimates to obtain 10 degrees of freedom.

To give approximately equal weight to each latitude we have chosen two current meter records at each of the four latitudes (C2, P, Y, and M); to include the baroclinicity we choose the uppermost current meter and the current meter nearest 100 m. At C2, the 86 m and 126 m records had to suffice but at P, Y, and M the current meter records were from 37 m and 96 m, 37 m and 97 m, and 39 m and 100 m, respectively. The common record length for the four locations is 45.25 days beginning 0000 UT 2 April 1977, and we choose a frequency interval of 0.118-0.213 cpd. Figure 11 shows amplitude and phase (relative to Y) as a function of alongshore separation for the first EOF, which accounts for 72% of the total variance in the frequency interval. Also shown on Figure 11 is the fraction of the variance each record contributes to the first EOF, which corresponds to the coherence squared between each record and the first EOF. This is useful in order to decide whether the EOFs represent a physical entity or are a fabrication of the computational statistics.

At each location alongshore the velocity pairs are approximately in phase and a linear regression using the 8 points gives an alongshore phase speed of 204 km day^{-1} for frequency = 0.17 cpd (the line on the

phase plot indicates the behavior for a phase speed of 240 km day^{-1} for frequency = 0.17 cpd). With the exception of the deeper record at C2, each velocity record is highly coherent with the first EOF. The variance in the deeper record at C2 is predominantly in the second EOF. This calculation indicates that fluctuations in alongshore velocity propagate coherently between 5°S and 15°S, consistent with conclusions from individual cross-spectra.

The EOF amplitude is in the range 1-3 cm sec^{-1} for C2 and P and 3-6 cm sec^{-1} for Y and M, suggesting a doubling of the amplitude between 5° and 15°S. This may be rationalized as a consequence of the conservation of wave energy flux. Assuming the alongshore group speed is constant, which is the case since the waves are non-dispersive, the total energy density of the waves remains the same as it travels along the coast (neglecting frictional and other dissipative effects). Since the offshore scale of the wave decreases as it travels poleward, its amplitude must increase. An estimate of this increase is given by (see, e.g., Miles, 1972; Allen and Romea, 1980)

$$(A_{15}/A_5) = (f_{15}/f_5)^{1/2}, \qquad (3.1)$$

or

$$(A_{15}/A_5) = 1.72, \qquad (3.2)$$

where A and f are local values of amplitude and Coriolis parameter and the subscripts refer to latitude.

The predicted amplification with latitude relative to Y from (3.1) is shown in Figure 11 for the velocities near 100 m. This agreement between observations and theory is consistent with Brink's (1982a) conclusion that frictional decay scales for the Peru coast are very long, and also helps explain why waves are so persistent over long distances.

(c) Wind Forcing

We can use the same EOF technique to analyze the coastal wind data. Figure 12 shows the statistics for the first two EOFs formed from the alongshore components (rotated into their principal axis frames) of the coastal winds at Talara, Chiclayo, Callao, and San Juan. The record length and frequency interval are identical to those for the velocity EOFs of Figure 11. The first EOF contains 63% of the total variance while the second EOF contains 28%. We show both EOFs because the winds at Talara and Chiclayo fall primarily into the second EOF while the winds at Callao and San Juan fall primarily into the first EOF. This may be seen from the coherence plot in Figure 12. In addition, the modal amplitude of the first EOF is largest for Callao and San Juan while the amplitude of the second EOF is largest for Talara. The phase of the first EOF suggests that the Callao wind leads the wind at San Juan with a phase consistent with poleward propagation at 200 km day^{-1}. There is a hint that the phase behavior of the first EOF extends equatorward to Chiclayo, however the coherence of the Chiclayo wind with the first EOF is extremely low. The phase structure of the second EOF indicates that the winds at Talara and Chiclayo are approximately in phase, with a suggestion that Chiclayo leads Talara.

Using the long records, we have shown (Figure 7) that the local winds at San Juan and the alongshore current at M are not coherent in the 0.1-0.2 cpd frequency band. Table 1 shows the coherence squared and phase from cross-spectral calculations using coastal winds at Talara, Chiclayo, Callao, and San Juan, and alongshore currents at C2, P, Y, and M. The record length and frequency interval are identical to the velocity EOFs of Figure 11. The coherence is low (less than 95% significance level), particularly for local winds and currents. However, there is a suggestion that the coherence is higher for current and wind records which are spatially separated where the wind is equatorward of the current (e.g., Chiclayo wind and M 39 m).

Figure 13 shows the statistics for the first EOF for winds and currents nearest 100 m for the same record length and frequency interval as for igures 11 and 12. The current velocities are normalized to unity total variance, as are the winds, to give the two a priori equal weights. This procedure was applied by Wang and Walsh (1976) and Brink, et. al., (1978) in different problems involving modes of mixed quantities. The phase behavior of both the current fluctuations and the wind is consistent with poleward propagation at about 200 km day^{-1}, suggesting the possibility of resonance forcing. However, the phase relation between currents and wind shows the currents leading by approximately 90°. In addition, the coherence plot indicates that all the currents are highly coherent with the first EOF while all the winds are not.

This calculation supports Brink's (1982b) conclusion, based on a forced wave hindcast model using observed winds and currents as input,

that the wind driving along the Peru coast between 5°S and 15°S accounts for no more than 25% of the amplitude of the predicted current time series.

4. Vertical Modal Structure

In order to examine the vertical structure of the fluctuations in the currents we compute vertical EOFs, using the alongshore velocities from C2 at 5°S and L at 15°S. These two locations provide the greatest depth range and the highest vertical resolution and they are both located over the continental slope at about an equivalent distance offshore (when scaled by the baroclinic radius of deformation) (Figure 14). The estimated Rossby radius scale δ_R is larger at 5°S than at 15°S due to a factor of f in the calculation of δ_R, i.e., $\delta_R = c/f$, where c is alongshore phase speed. In Figure 14, where we have scaled the offshore coordinate of each profile with the local f, δ_R spans the entire shelf-slope region at 5°S while at 15°S δ_R extends out from the coast to about 2000 m depth over the slope.

At C2 a common record length of 47.5 days was available while for L we use a record length of 53.75 days. With the convention described above, the frequency intervals to maintain 10 degrees of freedom are 0.126-0.211 cpd at C2 and 0.131-0.206 cpd at L.

Figures 15 a,b show amplitude, phase and coherence as a function of depth for the first EOF at C2 and L, respectively. In each case the first EOF contains most of the total variance in the frequency interval (82%at C2 and 87% at L) and the higher EOFs all contain less than 12% of the total variance.

Both EOFs are concentrated near the surface; the EOF at C2 has a zero crossing at about 700 m depth, while the indication is that the EOF at L has a shallower zero crossing. The coherence of each record with the EOF is high near the surface and very low near the zero crossing of the EOFs, as would be expected. With the exception of the points near the zero crossing, where the phase information may be regarded as noise, both EOFs are within ± 20° of being in phase over their whole depth.

In order to establish the physical significance of the eigenvectors, it is necessary to show consistency with dynamical constraints. Accordingly, we have used the smoothed $N^2(z)$ profiles shown in Figure 16 to calculate the 'flat bottom' dynamical vertical modes at 5° and 15°S, obtaining estimates of vertical structure, Rossby radius, and alongshore phase speed for each mode. Comparison with other N^2 profiles obtained from other CTD observations which were made during the course of the experiments in 1977 shows that the profiles are typical. Figure 12 in Smith (1978) also shows the secondary maximum an N^2 between 300 and 400 m depth for a CTD station near 16° in August, 1976, 55 km from the coast, suggesting that this structure is persistent in both space and time.

The mode shapes were computed by integrating the governing equations by means of a fourth order Runge-Kutta scheme, with a trial and error procedure for determining the proper eigenvalue so that the boundary conditions are satisfied (see Kundu, et. al., 1975 Section 5 for a discussion of the equations and methods). Since the density profiles extend only to 780 m depth at 5°S and 980 m depth

at 15°S, the N^2 profile has been extrapolated in both cases to 0.1×10^{-5} s^{-2} at 4000 m depth by an exponential profile below 600 m. The starting value for the exponential profile is chosen to be an average of the measurements between 600 and 780 m depth. Parameter studies indicate that the mode is insensitive to the choice of exponential structure, e.g., doubling the value of N^2 at the bottom increases the calculated phase speed of the deep ocean mode by less than 10%.

The dynamical modes are computed assuming a flat bottom, and Figures 17 and 18 show the first dynamical modes corresponding to various mean depths. The alongshore phase speeds, zero crossing depths, and Rossby radii of the first dynamical modes are listed in Table 2. Also plotted on Figures 17 and 18 are the vertical structures of the first EOF at each location. At 5°S the first dynamical mode calculated with the actual mooring depth (1360 m) gives a zero crossing around 440 m which is shallower than that estimated by the first EOF. For a bottom depth H_0 of 4000 m (an estimate of the deep ocean depth) the zero crossing is 1675 m, which is too deep. A similar behavior is observed at 15°S, where the actual mooring depth is 650 m.

An averaged bottom depth over the scale $\delta_R \simeq 180$ km at 5°S is approximately 2000 m, while the averaged bottom depth at 15°S over the Rossby radius scale $\delta_R \simeq 60$ km is approximately 1400 km. The structures (particularly the zero crossing) of the first EOFs at 5°S and 15°S are approximated by the first dynamical modes calculated with $H_0 = 2000$ m and $H_0 = 1400$ m, respectively, suggesting that in both cases the wave structures are consistent with a constant bottom depth which is deeper than the local mooring depth but shallower than the

the deep ocean depth, and which is approximately equal to the averaged shelf-slope topography over the local Rossby radius scale.

5. Inertial Motions

The local inertial frequency at the C2 mooring is 0.175 cpd, which is almost exactly (to within the resolution of the spectral computations) the frequency at which the maximum alongshore coherence between the currents from 5°S to 15°S and between the sea level from 2°S to 15°S is observed. In other words, the 0.16-0.19 cpd frequency band is dominated by free baroclinic coastally trapped waves which propagate poleward through latitudes where their frequency is equal to the local inertial frequency. This is not surprising- Kelvin waves are well behaved when their frequency is equal to f (see Pedlosky, 1979, p.81)- but it is of interest to examine the relative strength of the inertial signal and coastally trapped waves at 5°S. Evidence from other latitudes suggest the inertial signal is relatively weak (see Figure 2 in Brink, et. al., 1980, and Figure 9 above).

We use the rotary spectrum (Mooers, 1973) to examine the velocity records, with the expectation that the inertial signal will be evident due to its preferred rotary sense. The method decomposes a two dimensional vector time series into clockwise and counterclockwise rotating parts. The sum of the two components of the rotary spectrum yields the conventional kinetic energy spectrum at a given frequency.

Figure 19 shows R, the ratio of the variance of the counter-clockwise to clockwise rotating parts for the velocity time series at C2 and L, centered around three frequencies, calculated with the

rotary spectrum. The frequencies chosen are 0.094 cpd, 0.187 cpd (the nearest spectral estimate to the local inertial frequency at 5°S) and 0.516 cpd (the nearest spectral estimate to the local inertial frequency at 15°S). A record length of 42.75 days was used for both C2 and L, starting 0000 UT 2 April 1977. For 0.094 cpd, well below the local inertial frequency at either 5° or 15°S, R is centered around 1 for both C2 and L for all depths, reflecting the lack of preferred rotary sense for frequencies much less than f. For 0.187 cpd, there is significantly more energy in the counterclockwise direction at C2 near the surface while $R \approx 1$ for L, i.e., in the wave band the signal which shows a preferred rotary sense at 5°S is nearly rectilinear at 15°S. Near the local inertial frequency at 15°S the signal at L shows significantly more energy in the counterclockwise direction near the surface with a decay in R with depth. At C2, the frequency 0.516 cpd is superinertial, i.e., greater than f, and $R \approx 1$ with the exception of one point near 200 m depth. This point perhaps reflects the presence of superinertial waves with a preferred rotary sense.

We next form EOFs using u-v pairs from five depths at C2. As for the vertical mode of alongshore velocity at C2, we choose a maximum common record length of 47.5 days and a frequency interval of 0.126-0.211 cpd, which includes the inertial frequency. The result for the first four EOFs, which contain 97% of the total variance in the band, are shown in Table 3. The first EOF contains 56% of the total variance, and $v >> u$ (the ratio v/u is 3.6, 4.3, and 8 at 86, 126, and 197 m, respectively). These ratios $v/u >> 1$ are consistent with predictions for internal Kelvin waves. The signals at 560 and 860 m both have a

low coherence with the first EOF and the v/u ratios are low, reflecting the low amplitude of the first mode internal Kelvin wave near its zero crossing. The phase relations for the first EOF are such that the alongshore currents at all depths are in phase to within ± 30° and the top three u-v pairs rotate counterclockwise (u leading implies counterclockwise rotation) while the bottom two u-v pairs rotate clockwise. This agrees qualitatively with predictions that perturbation effects on free internal Kelvin waves due to topography give u-v pairs which are 90° out of phase with counterclockwise rotation in the upper layer and clockwise rotation in the lower layer (Allen and Romea, 1980). The error in the phase relation for the u-v pairs is perhaps related to the fact that the coherence of u with the first EOF is low.

The remaining three EOFs which contain a non-negligible amount of the total variance in the band show vertically averaged values of v/u of 1.94, 1.6, and 1.14 for the second, third and fourth EOF, respectively. These values indicate a much higher level of horizontal isotropy in the velocities than that calculated for the first EOF. Since we do not expect inertial oscillations to be coherent in the vertical over depths greater than a few tens of meters (Fomin and Savin, 1973), it is difficult to interpret these EOFs. Indeed, they might represent only noise. However, the EOF decomposition implies that first mode internal Kelvin waves contain greater than 50% of the total variance in the 0.126-0.211 cpd band and that inertial oscillations account for less than 50% of the total variance.

6. Discussion

Sea level data from 2°12'S to 17°S on the west coast of South America show that low frequency (0.1-0.2 cpd) fluctuations propagate poleward along the coast with phase speeds similar to those predicted for first mode baroclinic coastally trapped waves. 405 day long sea level records of excellent quality at La Libertad, Callao, and San Juan provide the basic evidence for the process, while shorter sea level records from other locations provide supporting evidence.

Current velocities measured at 5°, 12°, and 15°S along the Peru coast show that the sea level and currents are coherent and approximately 180° out of phase, as expected for baroclinic coastally trapped waves. The empirical orthogonal function of alongshore velocity along the Peru coast shows the amplification of the waves as they travel poleward and the Rossby radius scale decreases. The phase speeds estimated from the EOF agrees with the results from the long sea level records.

The fluctuations do not seem to be the result of coastal wind forcing near the equator and the current fluctuations are of sufficient magnitude to mask the effects of local winds to at least 15°S. This conclusion is consistent with results from Brink's (1982b) forced wave calculation, where he used observed winds and currents along the Peru coast as input to hindcast alongshore currents and sea level in the 0.1-0.2 cpd frequency band. The results from the model suggest that most of the observed sea level and current fluctuations in the band are due to free waves originating equatorward of 5°S, while between 5° and 15°S winds contribute little to the observed variance.

Empirical orthogonal function decomposition of the alongshore

velocity fields at 5° and 15°S indicate that about 75% of the signal in the 0.1-0.2 cpd frequency band is due to a mode whose vertical structure and alongshore phase speed are consistent with a first mode internal Kelvin wave. The vertical structure of the mode at both locations is reasonably well approximated by the structure of the first vertical dynamical mode, calculated using realistic stratification assuming a flat bottom equal to the shelf slope depth averaged over the local Rossby radius scale. This behavior has been reported by Hogg (1981) in connection with internal waves near Bermuda. We note, however, that alongshore phase speeds obtained with a deep ocean bottom depth are in better agreement with observations than speeds obtained with the averaged slope topography.

Allen and Romea (1980) have shown theoretically that coastally trapped baroclinic fluctuations propagating poleward from the equatorial region may take the form of barotropic continental shelf waves at mid-latitudes. The EOFs calculated for vertical structure suggest that the transformation of modal structure has not taken place between 5° and 15°S.

Brink (1982a) has calculated wave properties using a numerical model with realistic stratification and shelf-slope topography. He finds that the first mode internal Kelvin-like wave near 15°S has a zero crossing over the slope at 1200 m depth, less than the zero crossing depth predicted with a flat bottom corresponding to the deep ocean depth. In addition, he finds first mode phase speeds which are less than those predicted with a deep ocean depth. These results support the observational results that the structure of internal

Kelvin waves depends on an averaged bottom topography.

The interesting question remains: Where and how are the fluctuations first energized? Luther (1980) suggests that a basin wide barotropic oceanic response to large scale atmospheric forcing exists in the 4-6 day period band at all longitudes from 60°N to 60°S latitude. We have shown that the fluctuations along the Peru coast are not a response to atmospheric pressure effects, which are connected with large scale atmospheric weather systems. Moore (1968) (see Moore and Philander, 1977) has shown that equatorially trapped free waves incident on an eastern boundary may be partially transmitted north and south along the coast as boundary trapped internal Kelvin waves (see also Anderson and Rowlands, 1976, and Cane and Sarachik, 1977). Wunsch and Gill (1976) show evidence that peaks in equatorial sea level are manifestations of first baroclinic mode inertial-gravity waves. Luther (1980) reports peaks in spectra of observed sea level in the equatorial Pacific which correspond to the first baroclinic first meridional inertial-gravity wave with frequency 0.17-0.20 cpd and the second baroclinic first meridional mode with frequency 0.13-0.15 cpd. These modes are equatorially trapped with most of their energy equatorward of 4°. Ripa and Hayes (1981) have presented spectra of bottom pressure and temperature in shallow water from the western side of the Galapagos Islands at latitudes between 1°24'N and 0°59'S, which show relatively energetic baroclinic motions in the 0.18-0.2 cpd frequency band. Luther (1980) also reports 35-80 day oscillations in equatorial sea level which he interprets as atmospherically forced equatorial Kelvin waves with phase speeds of 230 km day^{-1}. These lower

frequency waves could also be transmitted south along the Peru coast.

Measurements of sea level (e.g., Figure 3) indicate high coherence for $\omega < 0.1$ cpd and in the 0.15-0.2 cpd band. Smith (1978) shows the cross spectral analysis of current meter observations at 12° and 15°S for May-July 1976 and March-May in Figures 5, 6, 8, and 9 of that paper. During the 1976 period there was coherent propagation for $\omega \leq 0.1$ cpd and near 0.2 cpd but not near 0.14 cpd. The spectra show relatively little energy near that frequency. For the current meter data taken in the 1977 period, the spectral peaks are near 0.17 (Figure 10) and the cross spectra show coherent propagation from 5° to 12°S in the band centered around 0.17 cpd. Thus the observed frequency band for forced first baroclinic first meridional equatorial inertial-gravity waves coincides with the observed frequency band for poleward propagating fluctuations along the Peru coast. The gap in coherence between motion in the 0.1-0.2 cpd band and lower ($\omega < 0.1$ cpd) frequency motions may reflect the separation in frequency space of equatorial Kelvin and inertial-gravity waves.

A sea level record from Baltra (0°27'S, 90°17'W) at the Galapagos Islands is the only data available that enables us to directly extend our analysis and trace the fluctuations in sea level to the equator. The Baltra record has several gaps which prevents us from using one long record. The auto-spectrum of six-hourly sea level at Baltra was calculated with three-448 point segments which were ensemble averaged. The cross-spectrum between sea level at Baltra and La Libertad and La Libertad and Callao was computed for the same segments. The auto-spectra of sea level at Baltra and La Libertad for this time period

show peaks at 0.205 and 0.188 cpd, respectively, with the coherence above the 90% significance level in the 0.187-0.214 cpd band. The peak coherence, which is significant at 95%, is at 0.205 cpd, with Baltra leading by 398°. Baltra and La Libertad are separated by about 1050 km, which gives a phase speed of about 200 km day^{-1}. For the same record periods, Callao has a spectral peak at 0.170 cpd and leads La Libertad by 300°, which implies a phase speed of 240 km day^{-1}. For the cross-spectrum between sea level at La Libertad and Callao for the same record periods, the 0.161-0.187 cpd band is coherent above the 90% significance level, with a maximum at 0.17 cpd. The phase relation between Baltra and La Libertad is ambiguous since we have no intermediate points to add confidence to our interpretation of the sense of phase propagation. In addition, the coherence between Baltra and La Libertad is not as good as for the longer time series of sea level along the Peru coast. Nevertheless, the evidence suggests an equatorial origin for the fluctuations along the Peru coast, although more detailed observations are necessary.

NO PAGE

	WIND			
Current	Talara	Chiclayo	Callao	San Juan
C2 86 m	.03/-120°	.16/-171°	.36/-5°	.04/-132°
P 37m	.09/16°	.31/-28°	.16/143°	.05/-109°
P 96m	.14/68°	.27/7°	.26/155°	.04/-29°
Y 37m	.14/129°	.33/99°	.35/-121°	.04/75°
Y 97m	.16/91°	.44/94°	.23/-90°	.01/-47°
M 39m	.35/-128°	.44/-124°	.03/70°	.10/114°
M 100m	.15/93°	.06/-133°	.03/59°	.07/68°

CHAPTER V
TABLE 1: Coherence Squared/ Phase (in degrees) between winds and currents for the 0.118-0.213 cpd frequency band . Record length: 45.25 days. Phase positive for top leads side. 10 degrees of freedom; 95% confidence level for coherence squared is 0.53.

TOTAL DEPTH (m)	ZERO CROSSING (m)	c_1 (cm s^{-1})	δ_R (km)
(a) 5°S (1977)			
1360	440	157	124
2000	760	177	139
4000	1675	239	188
(b) 15°S (1977)			
650	320	98	26
1400	510	146	39
4000	1610	247	66
(c) 15°S (1976)			
650	320	106	28
1400	500	158	42
4000	1550	259	69

CHAPTER V

TABLE 2: Depth of zero crossing, alongshore phase speed c_1 and Rossby radius scale δ_R for the forst vertical dynamical mode for alongshore velocity, calculated with various bottom depths, using realistic stratification from 1977 (Figure 16) from over the slope near (a) 5°S and (b) 15°S. Also shown are the results with stratification from 1976 (see Appendix). At 5°S, 1360 m corresponds to the C2 mooring depth, while at 15°S the mooring depth is 650 m for L (Figure 14).

		EOF 1			EOF 2			EOF 3			EOF 4		
C2		A	θ	γ^2	A	θ	γ^2	A	θ	γ^2	A	θ	γ^2
86 m	u	0.14	-90	0.16	0.16	1	0.08	0.37	37	0.31	0.61	66	0.41
	v	0.50	12	0.83	0.05	6	0.01	0.24	86	0.05	0.36	-114	0.06
126 m	u	0.14	-150	0.39	0.15	-73	0.18	0.15	-79	0.13	0.21	114	0.11
	v	0.60	- 3	0.84	0.36	-82	0.11	0.12	-60	0.01	0.25	-20	0.02
197 m	u	0.06	-57	0.09	0.05	93	0.03	0.14	-88	0.14	0.46	9	0.73
	v	0.48	7	0.82	0.25	-113	0.08	0.22	-152	0.04	0.32	93	0.05
560 m	u	0.26	20	0.21	0.59	111	0.41	0.66	-6	0.36	0.10	-90	0.01
	v	0.21	-23	0.17	0.63	71	0.55	0.52	156	0.26	0.22	22	0.02
860 m	u	0.03	59	0.20	0.06	-80	0.37	0.02	146	0.07	0.07	113	0.21
	v	-0.05	-3	0.34	0.06	148	0.19	0.08	89	0.28	0.07	-2	0.09

TABLE 3: Amplitude (A), phase (θ) and coherence squared (γ^2) for the first 4 EOFs of u-v pairs at C2, calculated from 6-hourly data with a common record length of 47.5 days, beginning 0000 UT 2 April 1977, and a frequency interval of 0.126-0.211 cpd. The amplitudes are normalized such that the sum of the squares of each EOF equals 1. EOFs 1, 2, 3 and 4 contain 56%, 20%, 14% and 7% of the total variance in the band, respectively. $\theta_1 > \theta_2$ implies 2 leads 1.

NO PAGE

Figure Captions

Figure 1. Location of observations used in this paper. Dots indicate current meter moorings, crosses (+) indicate tide gages with nearby meteorological stations, and the open square indicates an airport meteorological station. The 200 m isobath is also shown.

Figure 2. Sea level, corrected for atmospheric pressure effects, at La Libertad, Callao, and San Juan, and vector plots of wind at San Juan and current velocity at M (55 m).

Figure 3. Auto spectra of sea level from the Callao (solid line) and the San Juan (dashed line) tide gages, based on 405 days of hourly data, beginning 0000 UT 27 March 1976, and the coherence and phase between Callao and San Juan sea level. Phase is positive for Callao leading. The 99% confidence level is indicated on the coherence plot. The line on the phase versus frequency diagram represents 240 km day^{-1} phase speed for poleward propagating nondispersive waves.

Figure 4. Auto spectra of sea level from the La Libertad (solid line) and the Callao (dashed line) tide gages, for the same period as in Figure 3, and the coherence and phase between La Libertad and Callao sea level. Phase is positive for La Libertad leading. The 95% confidence level is indicated on the coherence plot. The line on the phase versus frequency diagram represents 240 km day^{-1} for poleward propagating nondispersive waves.

Figure 5. Auto-spectra of La Libertad (solid line) and San Juan (dashed line) atmospheric pressure, and the coherence and phase between them, with the same period and analysis as in Figure 3. Phase positive for La Libertad leading. The 99% confidence level is indicated on the coherence plot.

Figure 6. Auto-spectra of alongshore current at M (55 m) (solid line) and sea level at San Juan (dashed line) and the coherence and phase between them, with the same period and analysis as in Figure 3. Phase positive for current leading. The 99% confidence level is indicated on the coherence plot.

Figure 7. Auto-spectra of alongshore wind (solid line) at San Juan and alongshore current (dashed line) at M (55 m), and the coherence and phase between them, with the same period and analysis as in Figure 3. Phase positive for wind leading. The 95% confidence level is indicated on the coherence plot. Scale on left of auto-spectral plot applies to wind while scale on right applies to current.

Figure 8. The lag (equatorward series leading) at maximum correlation between: 1) adjacent pairs of sea level records (see Figure 1), each sea level record vs. Callao sea level, and San Martin sea level vs. Materani sea level (circles); 2) tide gages at Agave (15°S) and P (+); 3) each atmospheric pressure record vs. Callao atmospheric pressure (triangles) All points represent a correlation

significant at the 98% confidence level, and all but the Talara-Callao (open circle) correlation represent the absolute maximum of the cross-correlation function. The Talara-Callao pair also has a maximum at 0 lag.

Figure 9. Auto spectra based on 49.7 days of hourly data of alongshore currents at C2 (86 m) (solid line) and Y (97 m) (dotted line) beginning 2100 UT 31 March 1977. The 95% confidence interval is shown.

Figure 10. Coherence and phase between alongshore currents at C2 (86 m) and Y (97 m), for the same time period as in Figure 9. Phase is positive for Y leads C2. The 95% confidence level is shown on the coherence plot.

Figure 11. The alongshore structure of the first EOF for the 0.118-0.213 cpd frequency band for the alongshore currents at C2 (86 m, 126 m), P (36 m, 96 m), Y (36 m, 97m) and M (39 m, 100 m), based on 6 hourly data. A common record length of 45.25 days is utilized, beginning 0000 UT 2 April 1977. Open circles represent shallow records at each location while dark circles represent deeper records. The first EOF contains 72% of the total variance in the frequency band. (a) Amplitude; (b) phase, relative to Y (the line indicates the behavior for a phase speed of 240 km day^{-1} with ω = 0.17 cpd); a linear regression gives an alongshore phase speed of 204 km day^{-1} with ω = 0.17 cpd; $\theta_1 > \theta_2$ implies 2 leads 1; (c) coherence squared (the 95% confidence level is shown).

Figure 12. The alongshore structure of the first and second EOFs for the same record length and frequency interval as in Figure 11 for alongshore winds at Talara (T), Chiclayo (CH), Callao (CA) and San Juan (SJ). The first EOF contains 63% of the total variance in the frequency band while the second EOF contains 28%. (a) amplitude; (b) phase, relative to Callao; (c) coherence squared (the 95% significance level is shown).

Figure 13. The alongshore structure of the first EOF for the same record length and frequency interval as in Figure 11 for alongshore winds (triangles) at Talara (T), Chiclayo (CH), Callao (CA), and San Juan (SJ) and alongshore currents at C2 (86 m) (open circle), P (96 m), Y (97 m) and M (100 m) (dark circles). The first EOF contains 55% of the total variance in the frequency interval. (a) normalized amplitude (the current velocities are normalized to unity variance as are the winds); (b) phase relative to Callao (the line represents the behavior for a phase speed of 240 km day^{-1} with ω = 0.17 cpd; (c) coherence squared (the 95% level is shown).

Figure 14. Shelf-slope topography at 5°S and 15°S latitude as a function of depth, where the offshore coordinate is scaled with the local f in each case. The locations of the C2 current meters at 5°S are indicated by open circles while the locations of the current meters at M and L are indicated by dark circles.

Figure 15. The vertical structure of amplitude, phase (relative to the shallowest record) and coherence squared (the 95% significance level is shown) for (a) the C2 mooring and (b) the L mooring for the first EOF of alongshore velocity, based on 6 hourly data. For the C2 mooring, a recore length of 47.5 days is used, beginning 0000 UT 2 April 1977, with a frequency interval of 0.126-0.211 cpd and the First EOF contains 82% of the total variance in the frequency band. For the L mooring a record length of 53.75 days beginning 0600 UT 17 April 1977 is used, with a frequency interval of 0.131-0.206 cpd and the first EOF contains 87% of the total variance in the frequency band.

Figure 16. $N(z)^2$ profile, smoothed with a three point mooving average, based on measurements every 10 m, near the Peru continental slope, at 4°58.9'S, 81°33'W , 1922 m water depth, May 22 1977 (dashed line); 15°15.5'S, 75°40.0 W, 1353 m water depth May 9 1977 (solid line)

Figure 17. First vertical dynamical mode for alongshore velocity calculated for a flat bottom depth of 2000 m and 4000 m (figure truncated at 2200 m), using the dashed N^2 profile shown in Figure 16. Also plotted is the vertical structure (open circles) of the first EOF of alongshore velocity at C2 (normalized by the maximum value) from Figure 15 a.

Figure 18. First vertical dynamical mode for alongshore velocity calculated for a flat bottom of 1400 m and 4000 m (figure truncated at 2200 m) using the solid N^2 profile shown in

Figure 16. Also plotted is the vertical structure (dark circles) of the first EOF of alongshore velocity at L (normalized by the maximum value) from Figure 15b.

Figure 19. The ratio of the variance of the counterclockwise to the clockwise rotating parts as a function of depth for the velocity time series at C2 (open circles) and L (dark circles) calculated using the rotary spectrum with hourly data. A record length of 42.75 days was used for both C2 and L, starting 0000 UT 2 April 1977. The ratio is computed centered around 3 frequencies: 0.094 cpd, 0.187 cpd (the local inertial frequency at 5°S), and 0.516 cpd (the local inertial frequency at 15°S). Hourly data was used. Bandwith = $\pm$ 0.06 cpd.

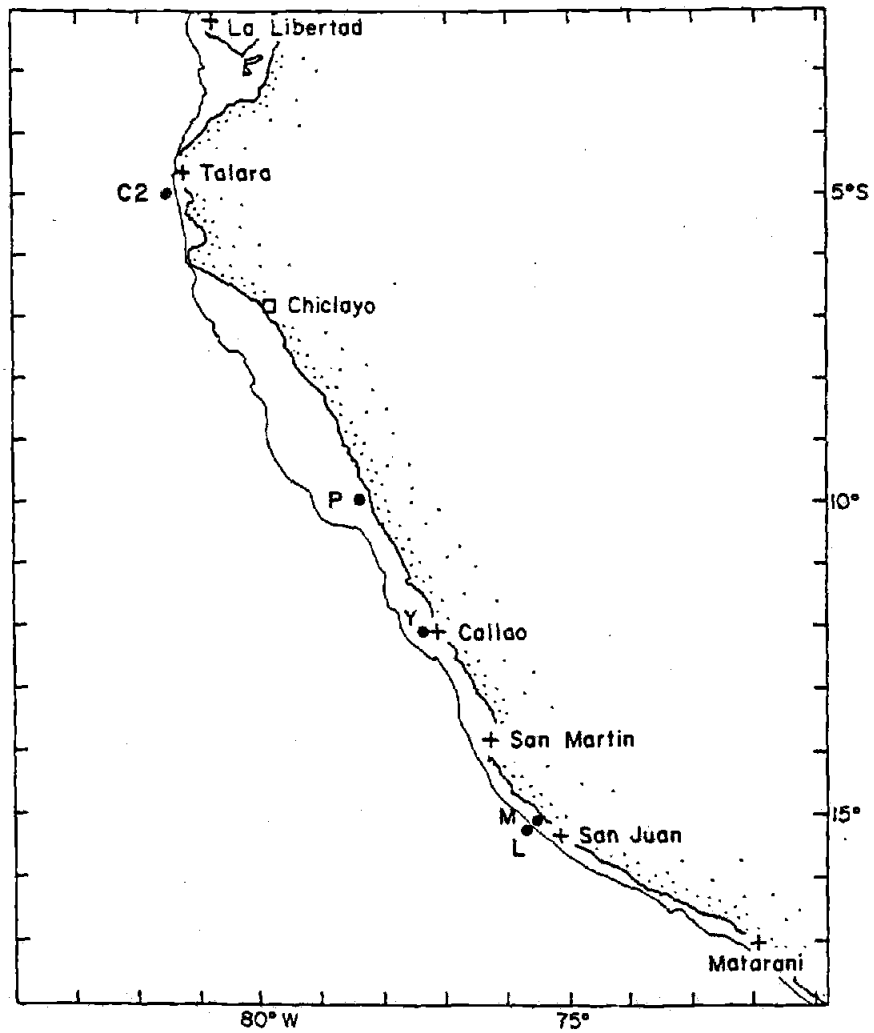
La Libertad
Talara
C2
Chiclayo
P
Y
Callao
San Martin
M
L
San Juan
Matarani
5°S
10°
15°
80° W
75°

Figure V-1

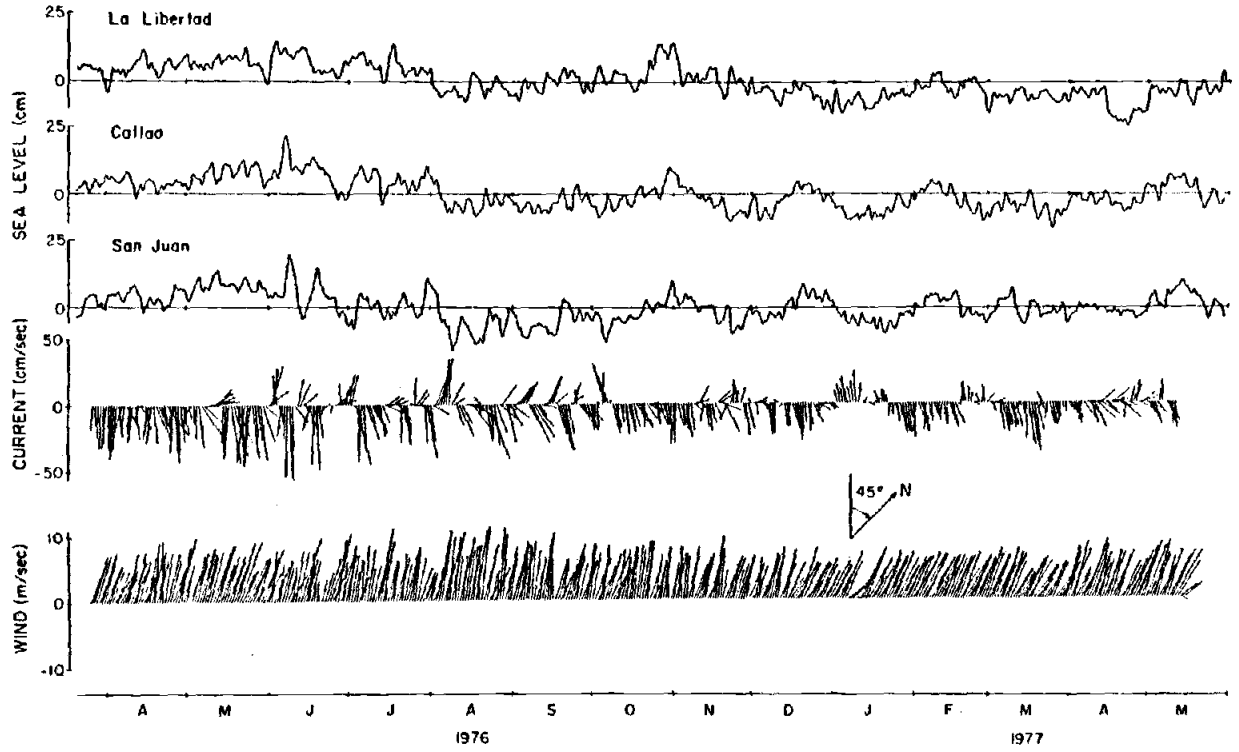
La Libertad
Callao
San Juan
SEA LEVEL (cm)
25
0
CURRENT (cm/sec)
50
-50
45°
N
WIND (m/sec)
10
-10
A
M
J
J
A
S
O
N
D
J
F
M
A
M
1976
1977

Figure V-2

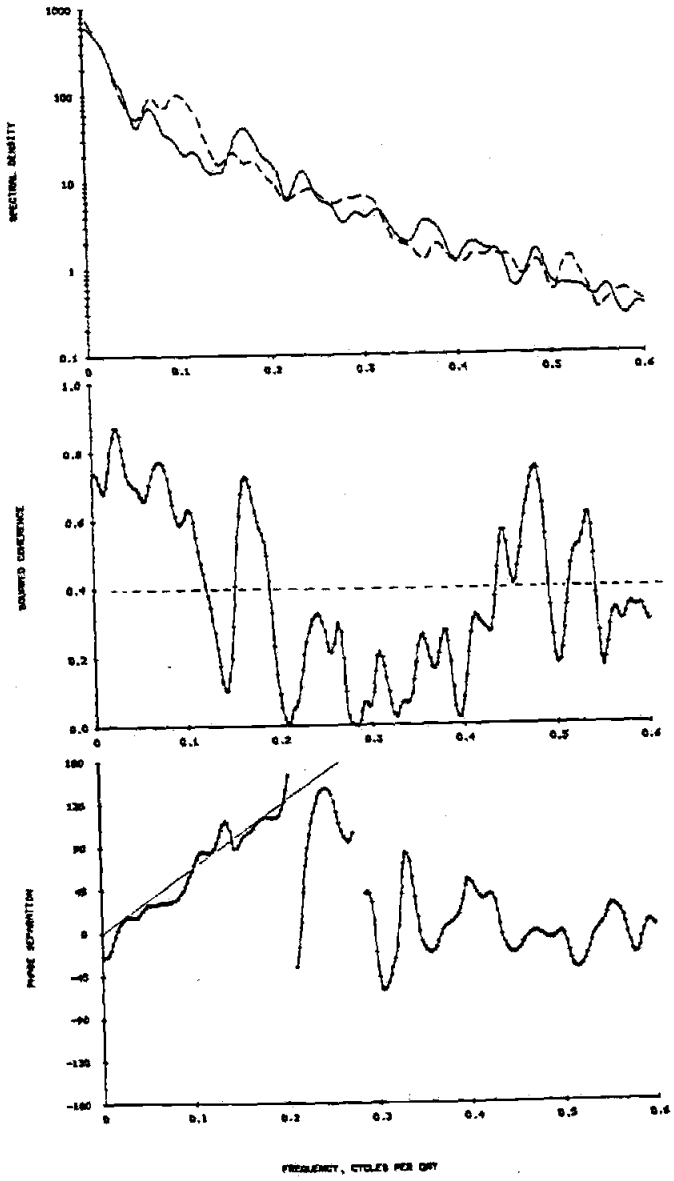
SPECTRAL DENSITY
SQUARED COHERENCE
PHASE SEPARATION
FREQUENCY, CYCLES PER DAY

Figure V-3

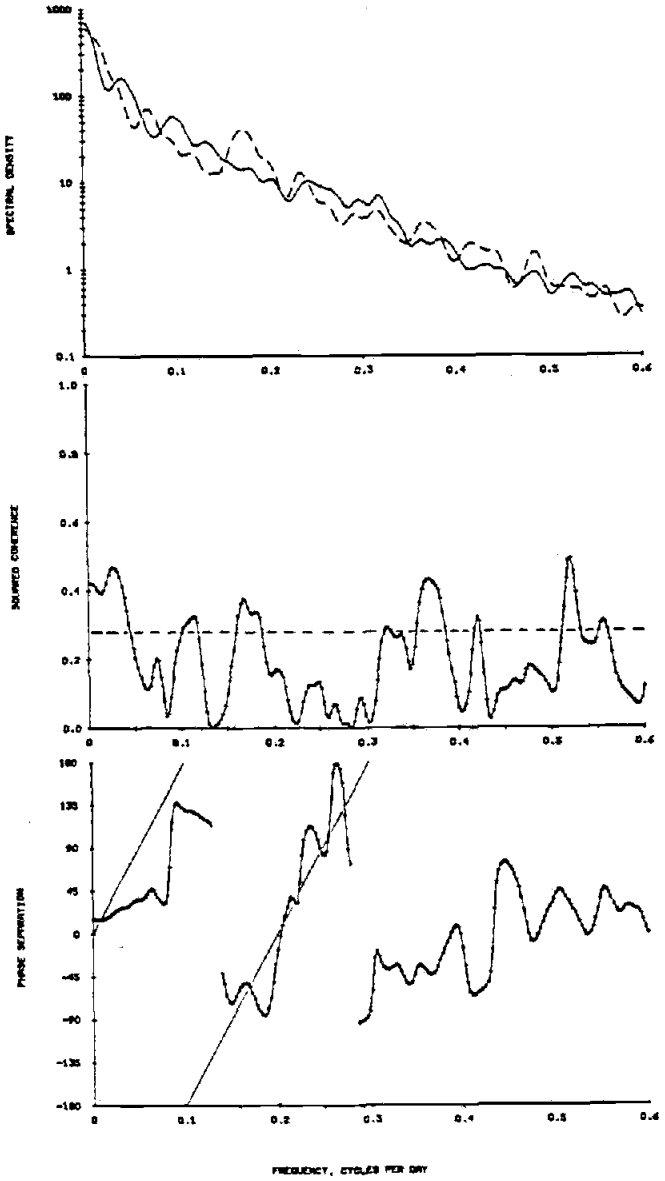
SPECTRAL DENSITY
SQUARED COHERENCE
PHASE SEPARATION
FREQUENCY, CYCLES PER DAY

Figure V-4

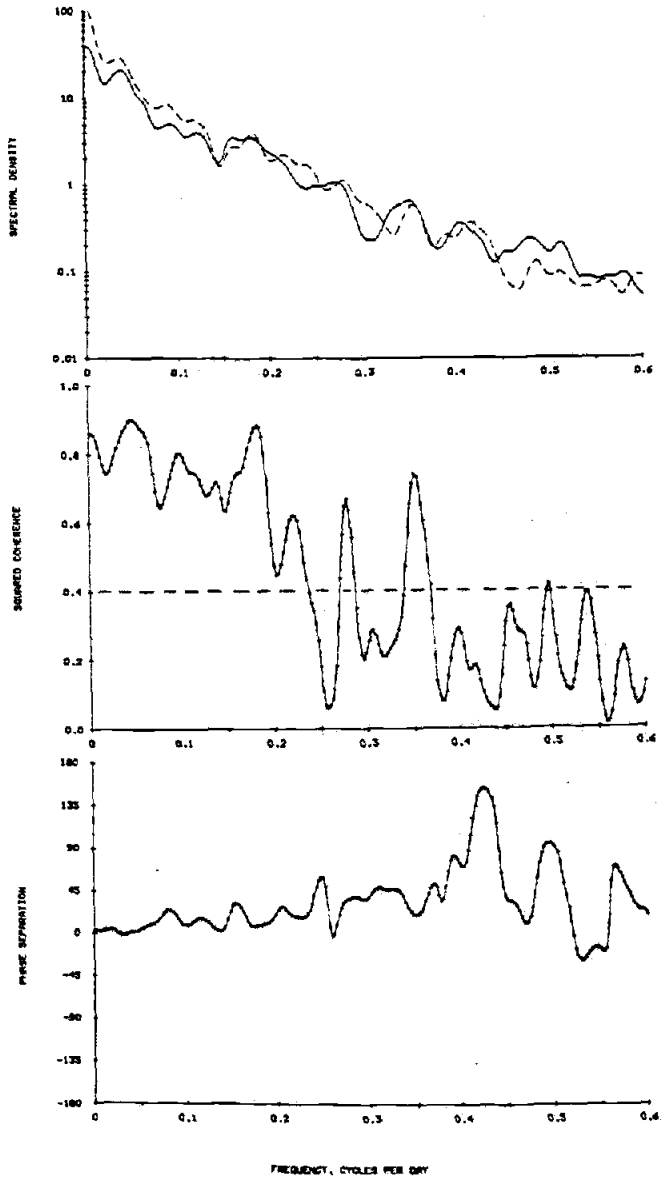
SPECTRAL DENSITY
SQUARED COHERENCE
PHASE SEPARATION
FREQUENCY, CYCLES PER DAY

Figure V-5

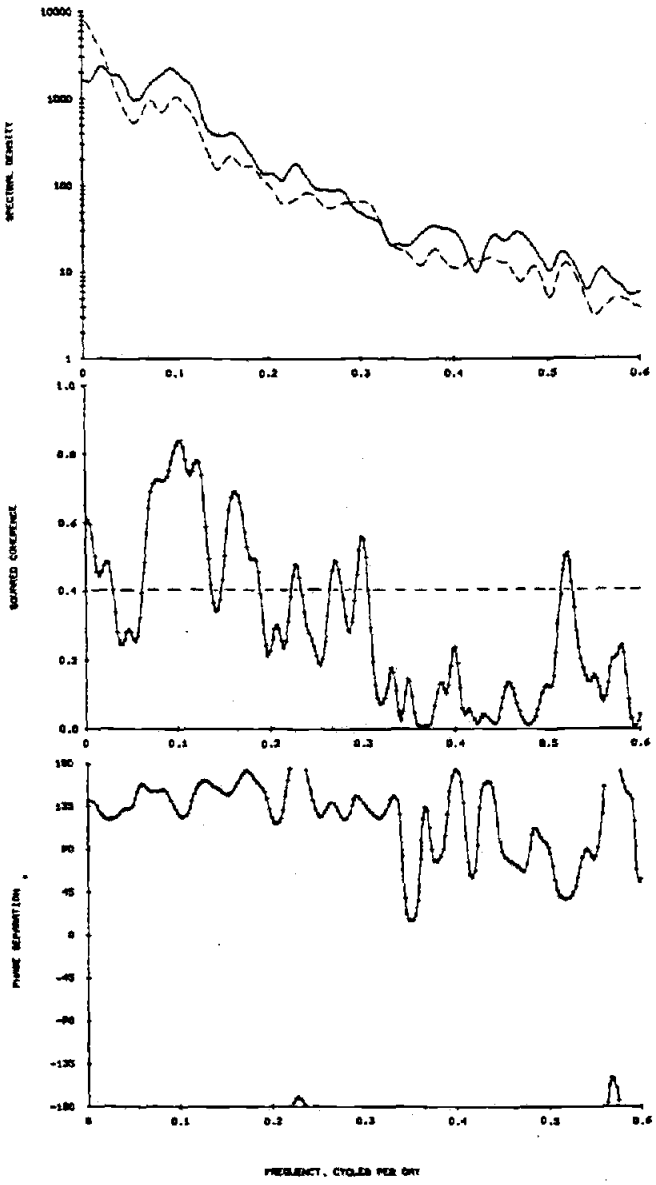
SPECTRAL DENSITY
SQUARED COHERENCE
PHASE SEPARATION
FREQUENCY, CYCLES PER DAY

Figure V-6

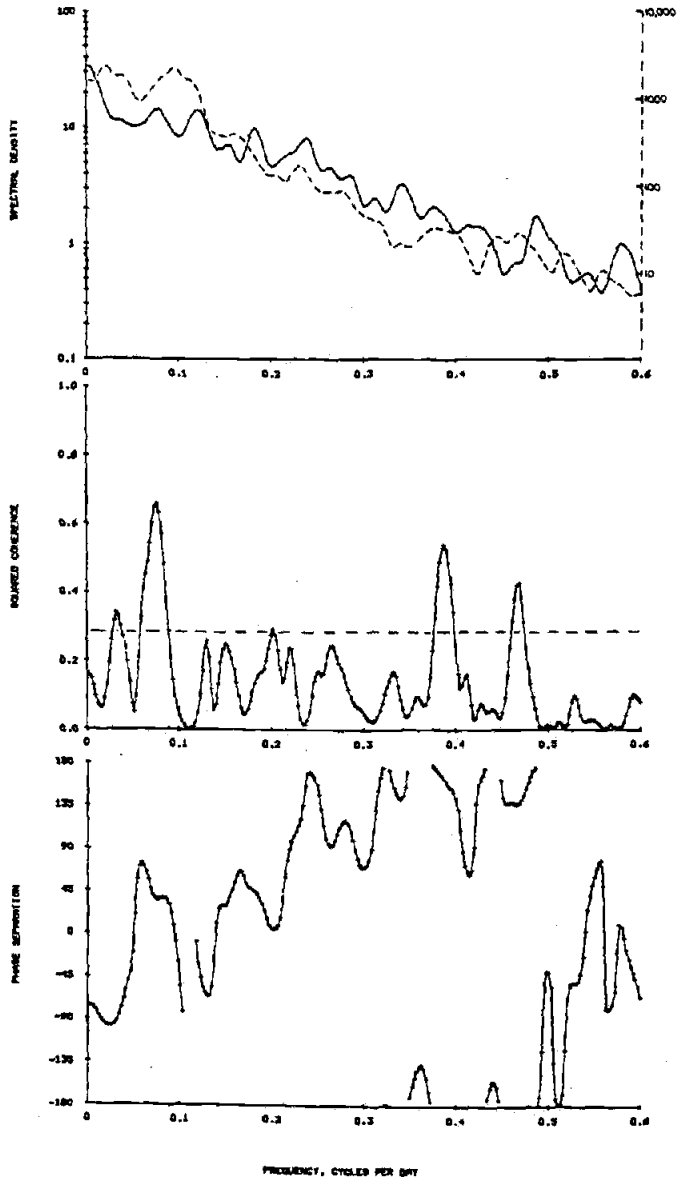
SPECTRAL DENSITY
SQUARED COHERENCE
PHASE SEPARATION
FREQUENCY, CYCLES PER DAY

Figure V-7

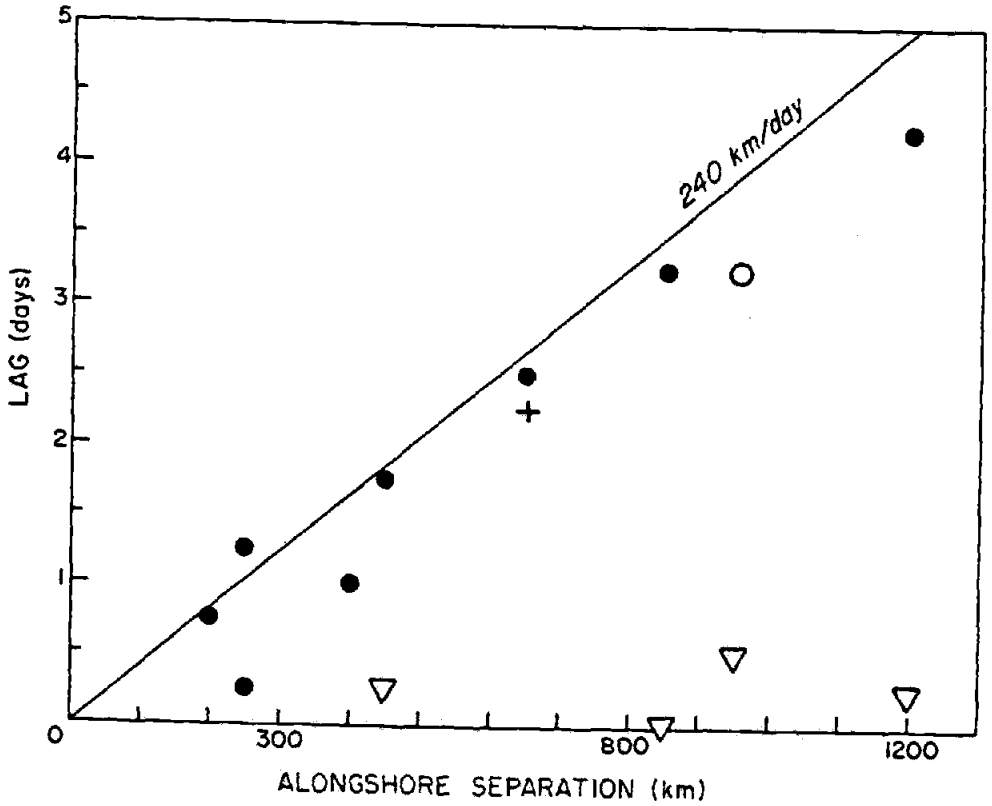
5
4
3
2
1
0
LAG (days)
240 km/day
300
800
1200
ALONGSHORE SEPARATION (km)

Figure V-8

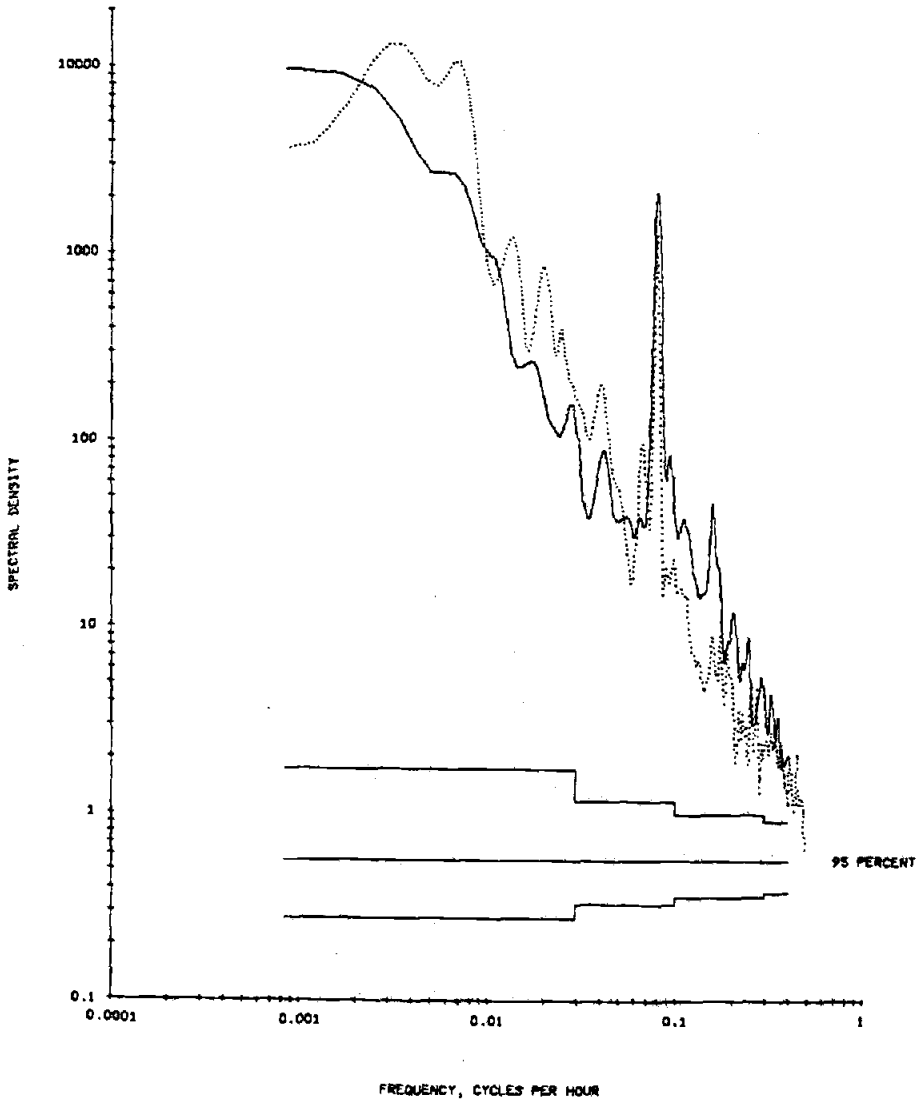
10000
1000
100
10
1
0.1
SPECTRAL DENSITY
0.0001
0.001
0.01
0.1
1
95 PERCENT
FREQUENCY, CYCLES PER HOUR

Figure V-9

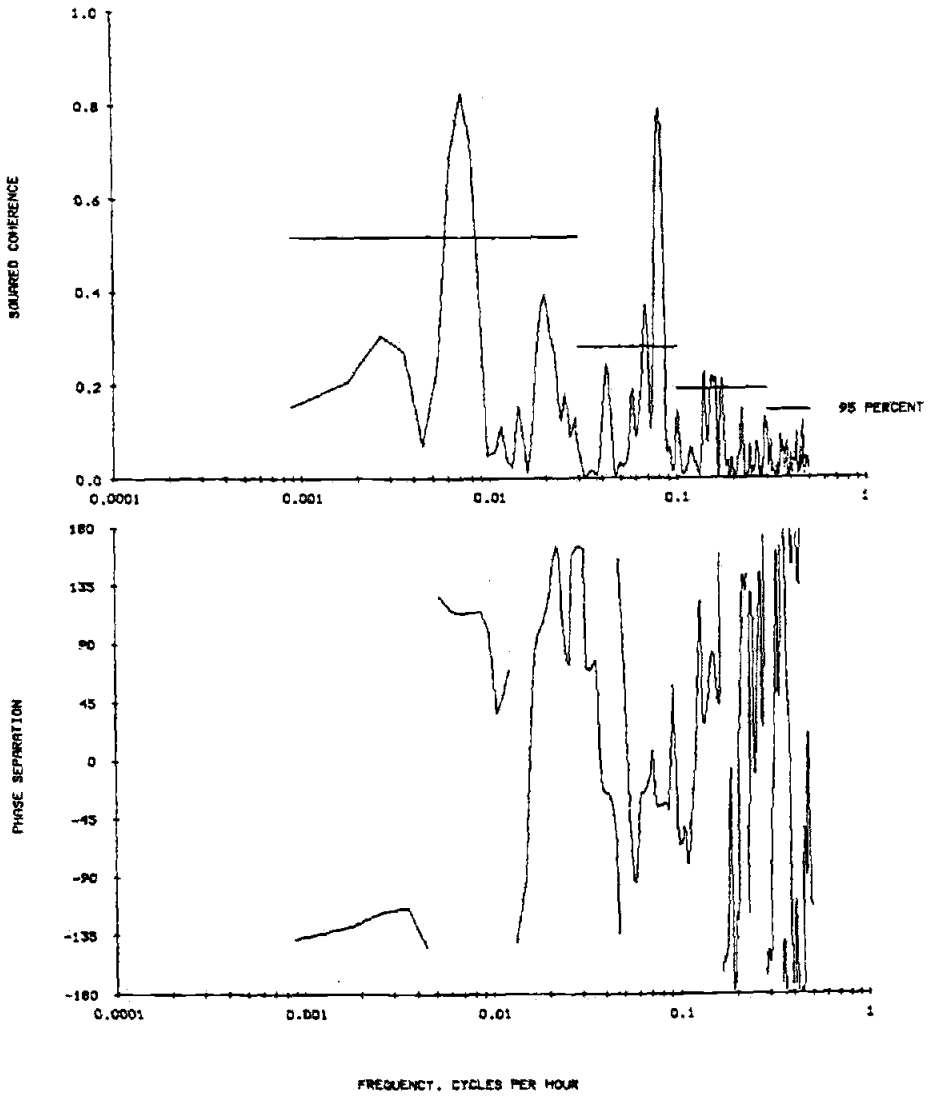
SQUARED COHERENCE
1.0
0.8
0.6
0.4
0.2
0.0
95 PERCENT
0.0001
0.001
0.01
0.1
1
PHASE SEPARATION
180
135
90
45
0
-45
-90
-135
-180
FREQUENCY, CYCLES PER HOUR

Figure V-10

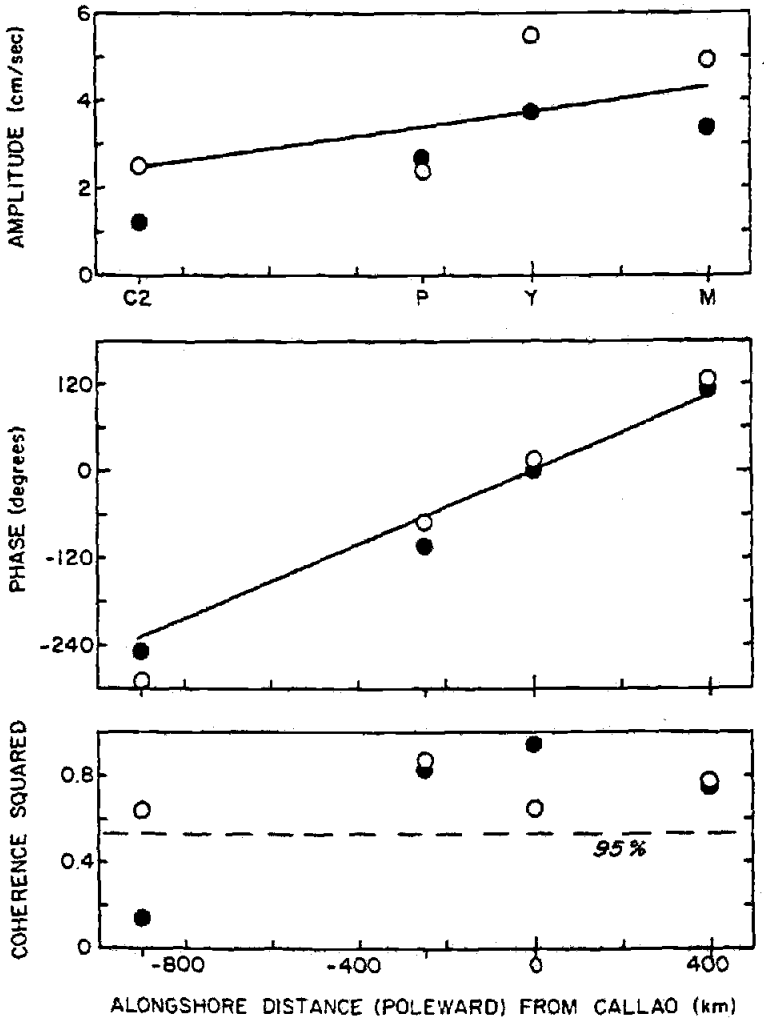
AMPLITUDE (cm/sec)
6
4
2
0
C2
P
Y
M
PHASE (degrees)
120
0
-120
-240
COHERENCE SQUARED
0.8
0.4
0
95%
-800
-400
0
400
ALONGSHORE DISTANCE (POLEWARD) FROM CALLAO (km)

Figure V-11

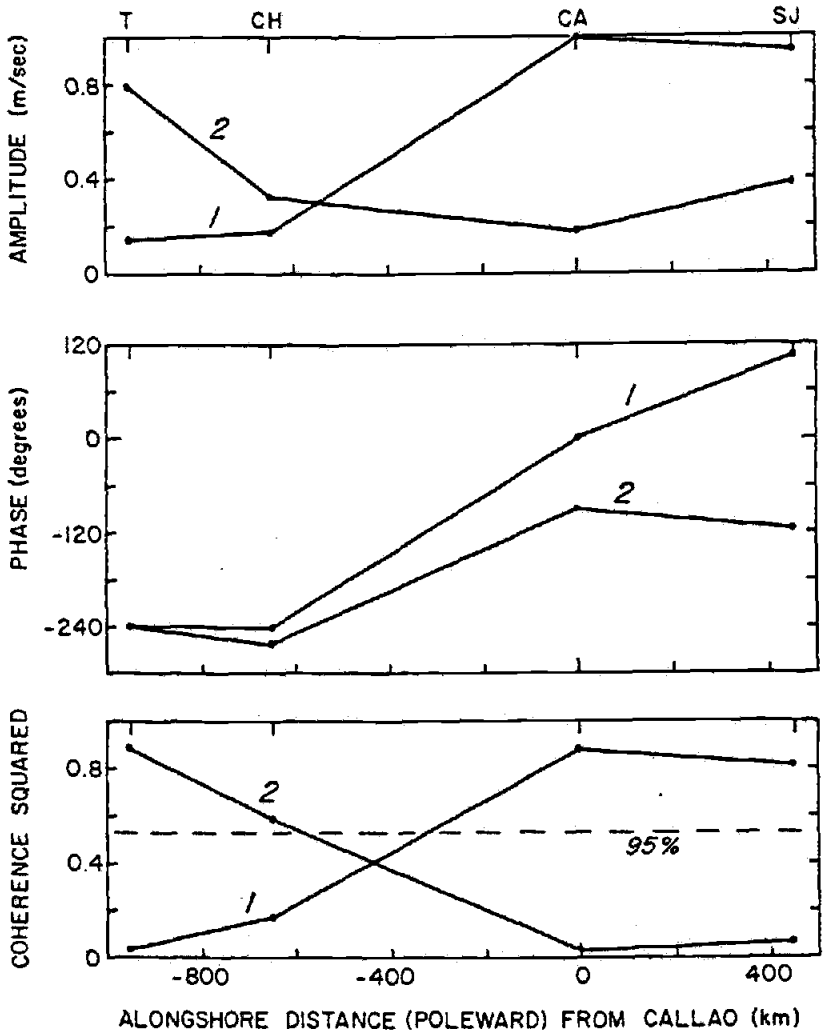
T
CH
CA
SJ
AMPLITUDE (m/sec)
0.8
0.4
0
2
1
PHASE (degrees)
120
0
-120
-240
1
2
COHERENCE SQUARED
0.8
0.4
0
2
95%
1
-800
-400
0
400
ALONGSHORE DISTANCE (POLEWARD) FROM CALLAO (km)

Figure V-12

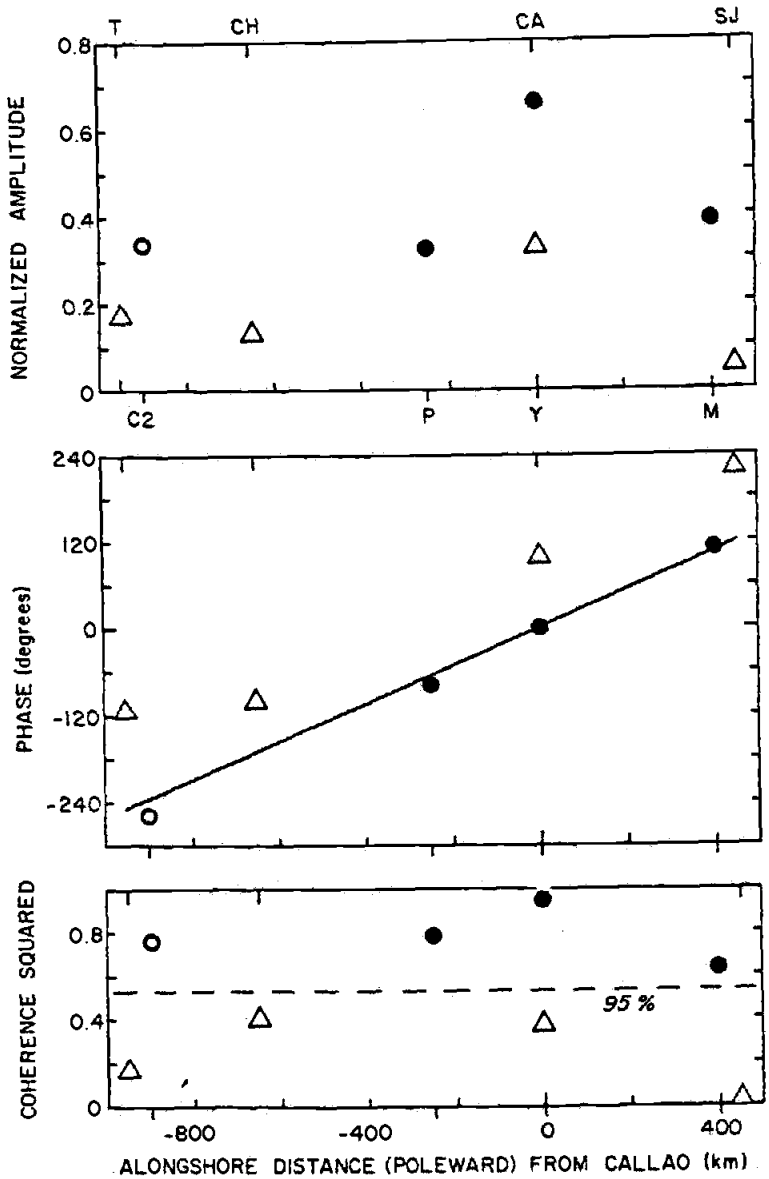
T
CH
CA
SJ
NORMALIZED AMPLITUDE
0.8
0.6
0.4
0.2
0
C2
P
Y
M
240
120
0
-120
-240
PHASE (degrees)
COHERENCE SQUARED
0.8
0.4
0
95 %
-800
-400
0
400
ALONGSHORE DISTANCE (POLEWARD) FROM CALLAO (km)

Figure V-13

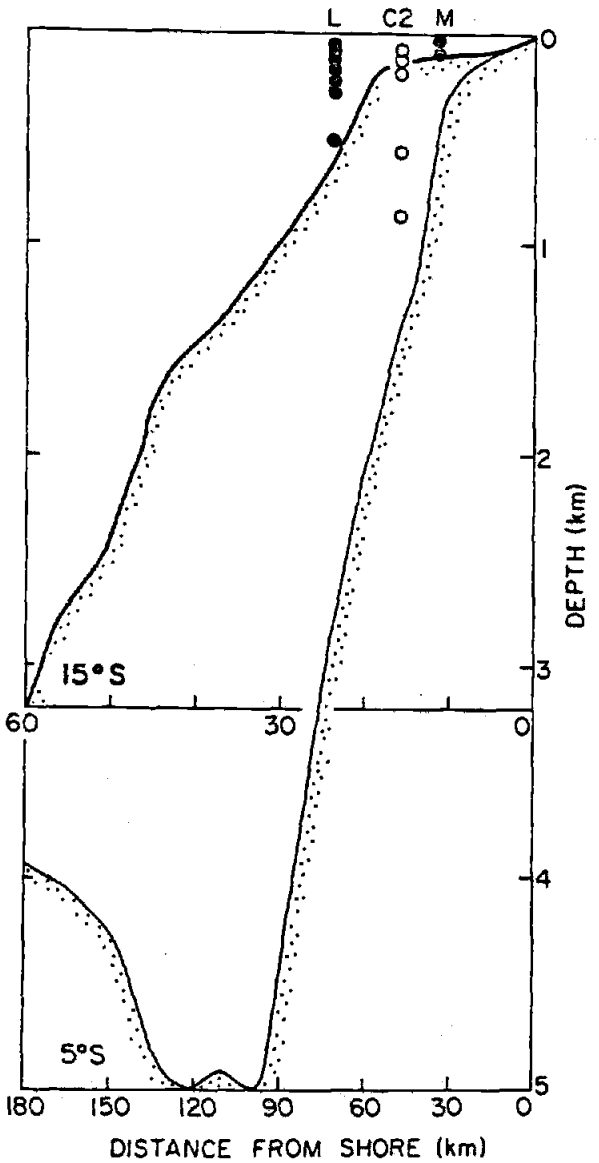
L
C2
M
0
1
2
3
4
5
DEPTH (km)
15°S
60
30
0
5°S
180
150
120
90
60
30
0
DISTANCE FROM SHORE (km)

Figure V-14

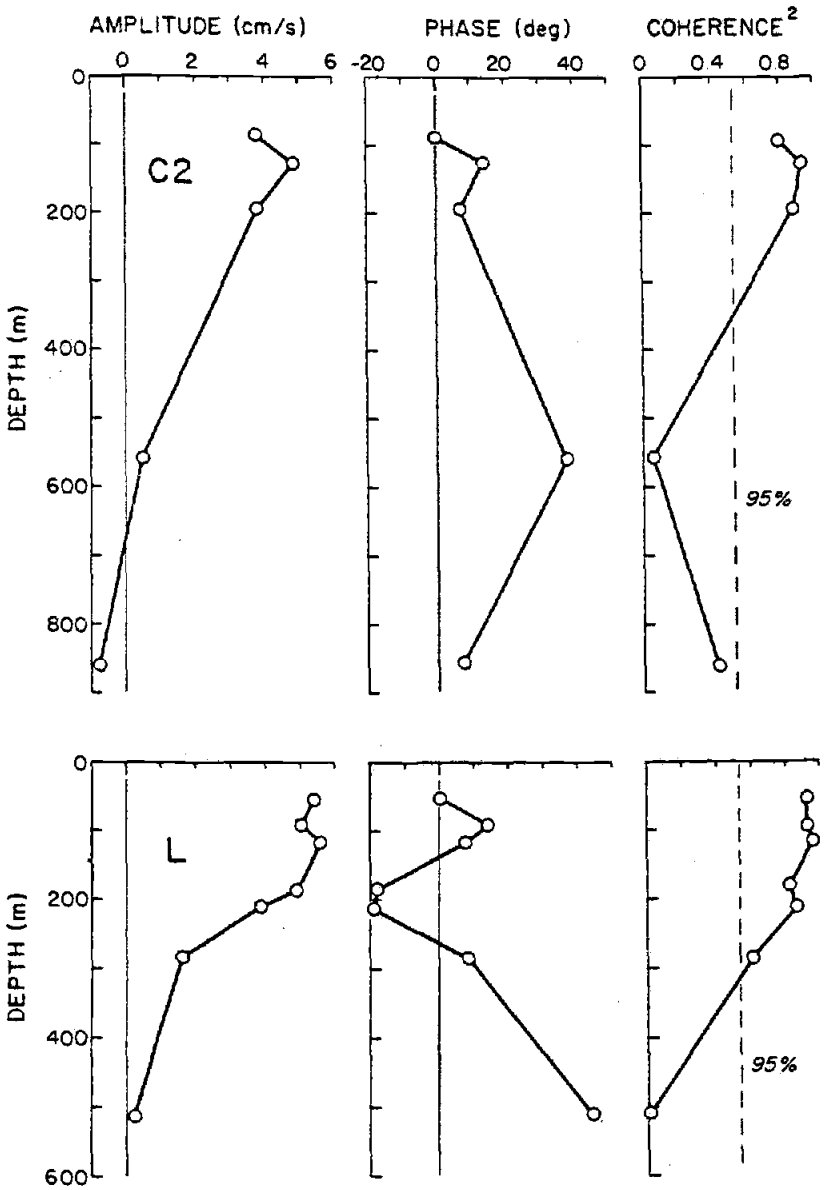
AMPLITUDE (cm/s)
PHASE (deg)
COHERENCE²
0
2
4
6
-20
0
20
40
0
0.4
0.8
C2
L
DEPTH (m)
0
200
400
600
800
95%

Figure V-15

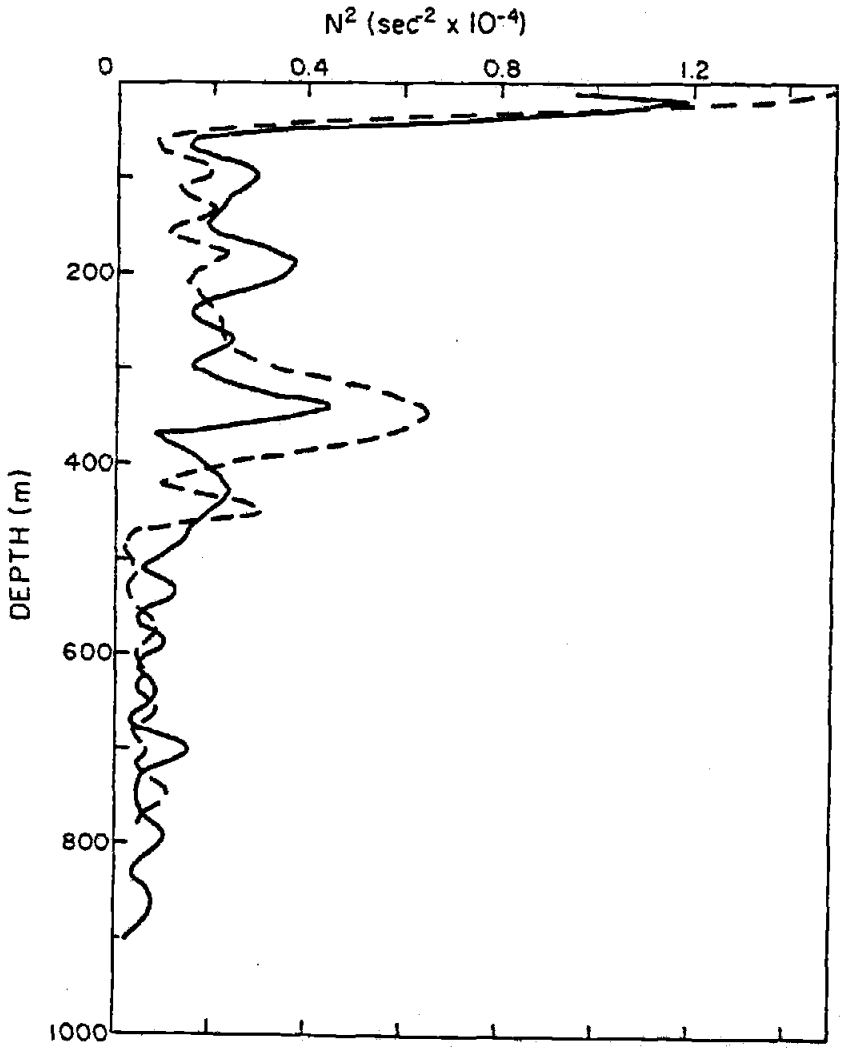

Figure V-16

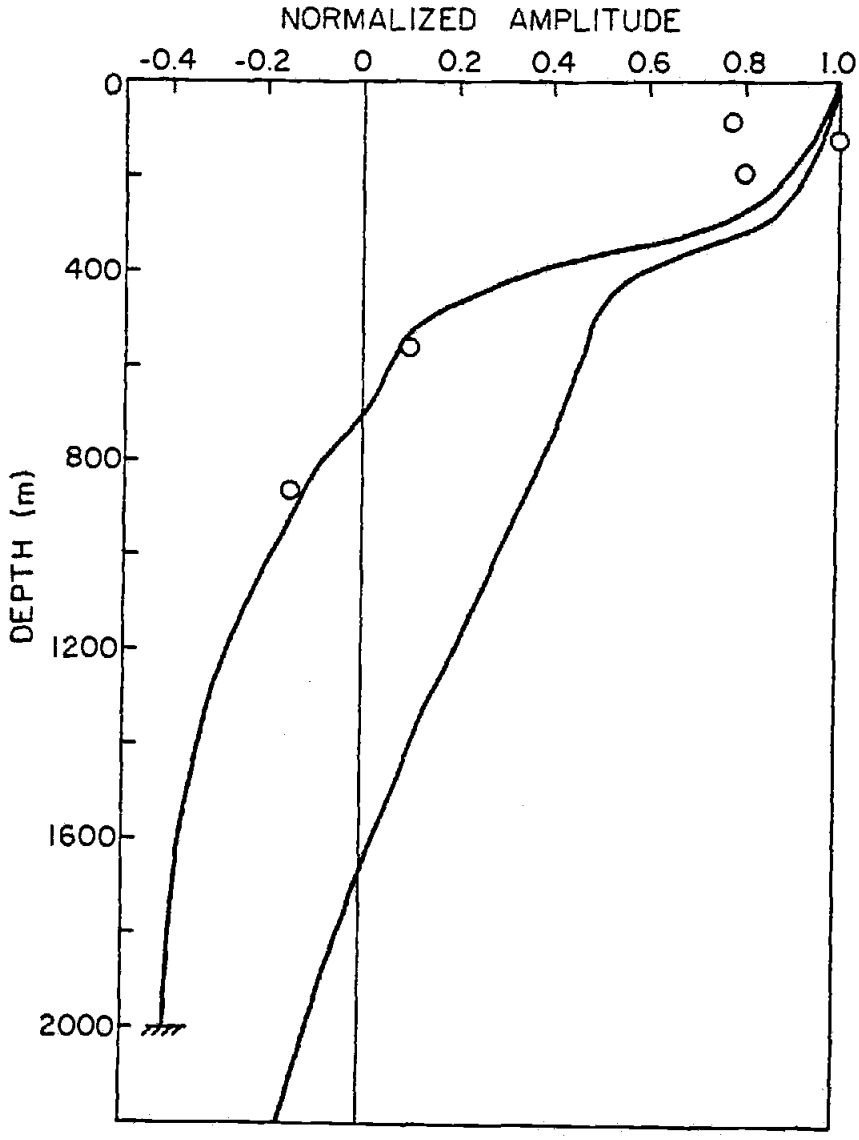
NORMALIZED AMPLITUDE
-0.4
-0.2
0
0.2
0.4
0.6
0.8
1.0
0
400
800
1200
1600
2000
DEPTH (m)

Figure V-17

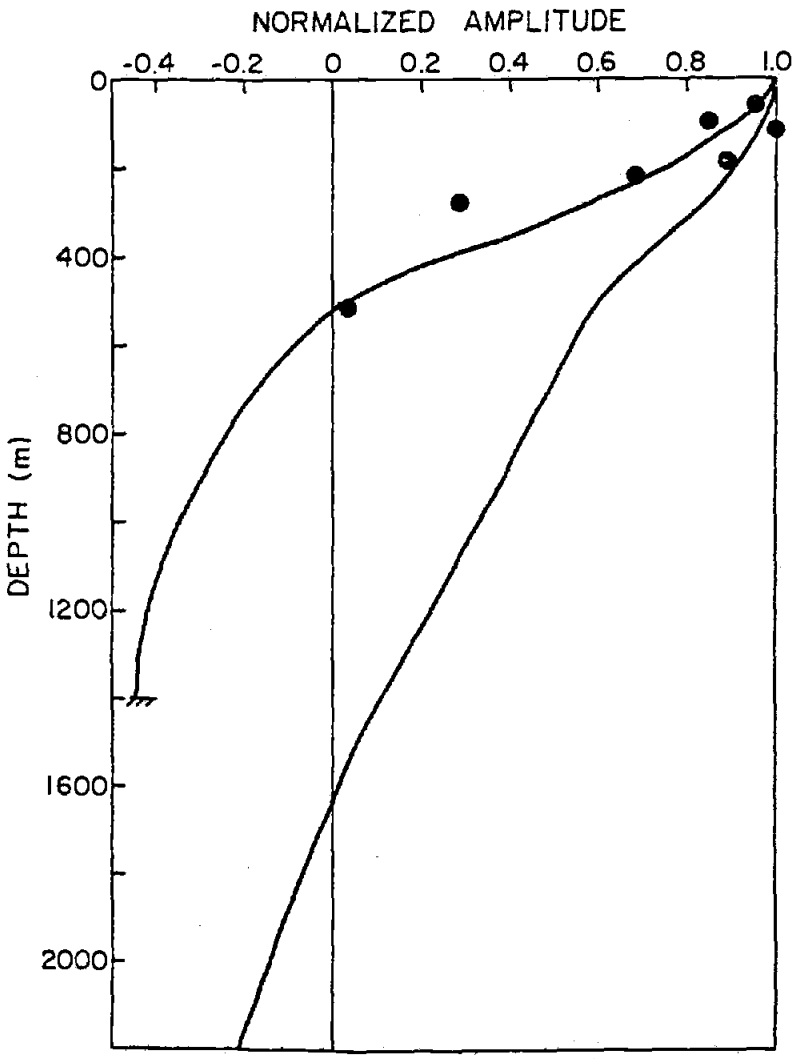
NORMALIZED AMPLITUDE
-0.4
-0.2
0
0.2
0.4
0.6
0.8
1.0
0
400
800
1200
1600
2000
DEPTH (m)

Figure V-18

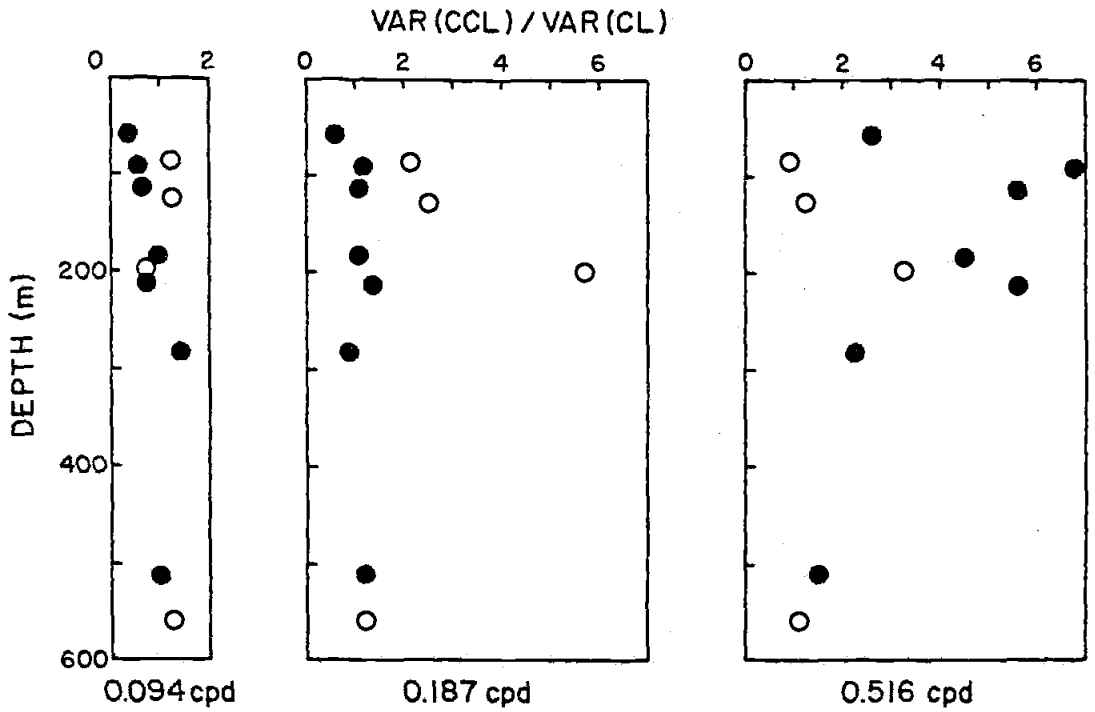
VAR (CCL) / VAR (CL)
0
2
0
2
4
6
0
2
4
6
DEPTH (m)
200
400
600
0.094 cpd
0.187 cpd
0.516 cpd

Figure V-19

REFERENCES

Allen, J. S., and Romea, R. D., 1980. On coastal trapped waves at low latitudes in a stratified ocean. J. Fluid Mech., 98: 555-585.

Anderson, D. L. T., and Rowlands, P. B., The role of inertia-gravity and planetary waves in the response of a tropical ocean to the incidence of an equatorial Kelvin wave on a meridional boundary. J. Mar. Res., 34:395-417. 1976.

Brink, K. H., Allen, J. S., and Smith, R. L., 1978. A study of low frequency fluctuations near the Peru coast. J. Phys. Oceanogr., 8: 1025-1041.

Brink, K. H., Halpern, D., and Smith, R. L., 1980. Circulation in the Peruvian upwelling system near 15°S. J. Geophys. Res., 85: 4036-4048.

Brink, K. H., Smith, R. L., and Halpern, D., 1978. A compendium of time series measurements from moored instruments during the MAM '77 phase of JOINT-II, CUEA Technical Report 45, Oregon State University, Reference 78-17, 72 pp.

Brink, K. H., 1982a. The effect of bottom friction on low frequency coastal trapped waves. In preparation.

Brink, K. H., 1982b. A comparison of long coastal trapped wave theory with observations off Peru. In preparation.

Brockmann, C., Fahrbach, E., and Urquizo, W., 1978. ESACAN data report. Istitut fur Meereskunde an der Christian-Albrechts-Universitat, Nr. 51, ISSN 0341-8561.

Brockmann, C., Fahrbach, E., Huyer, A., and Smith, R. L., 1980. The poleward undercurrent along the Peru coast: 5° to 15°S. Deep Sea Res., 27A: 847-856.

Cane, M. A., and Sarachik, E. S., 1977. Forced baroclinic ocean motions II, the linear equatorial bounded case. J. Mar. Res., 35: 395-432.

Fomin, L. M., and Savin, M. T., Vertical coherence of inertial motions in the ocean. Izv. Acad. Sci. USSR Atmos. Oceanic Phys., Engl. Transl. 9: 331-334. 1973

Hogg, N. G., 1980. Observations of internal waves trapped round Bermuda. J. Phys. Oceanogr., 10: 1353-1376.

Huyer, A., Gilbert, W. E., Scramm, R., and Barstow, D., 1978. CTD observations off the coast of Peru, Data Report 71, Oregon State University 78-18, 409 pp.

Kundu, P. K., Allen, J. S., and Smith, R. L., 1975. Modal decomposition of the velocity field near the Oregon coast. J. Phys. Oceanogr., 5: 683-704.

Kundu, P. K., 1976. An analysis of inertial oscillations observed near the Oregon coast. J. Phys. Oceanogr., 6: 879-893.

Luther, D.S., 1980. Observations of long period waves in the tropical oceans and atmosphere. Ph.D. Thesis, Woods Hole Oceanographic Institution- Massachusetts Institute of Technology, 210 pp.

Miles, J. W., 1972. Kelvin waves on oceanic boundaries. J. Fluid Mech., 55: 113-127.

Mooers, C. N. K., 1973. A technique for the cross spectrum analysis of pairs of complex valued time series with emphasis on properties of polarized components and rotational environments. Deep Sea Res., 20: 1090-1141.

Moore, D. W., Planetary-gravity waves in an equatorial ocean. PhD. Thesis, Harvard University. 1968.

Pedlosky, J., 1979. Geophysical Fluid Dynamics. Springer-Verlag, New York, 624 pp.

Ripa, P., and Hayes, S. P., 1981. Evidence for equatorial trapped waves at the Galapagos Islands. J. Geophys. Res., 86: 6509-6516.

Smith, R. L., 1978. Poleward propagating perturbations in currents and sea level along the Peru coast. J. Geophys. Res., 83: 6083-6092.

Smith, R. L., 1980. A comparison of the structure and variability of the flow field in the three coastal upwelling regions: Oregon, Northwest Africa, and Peru. Submitted to Coastal Upwelling-1980, F. A. Richards, Ed., Am. Geophys. Union.

Stevenson, M. R., and Taft, B. A., 1971. New evidence of the equatorial undercurrent east of the Galapagos Islands. J. Mar. Res., 29: 103-115.

Wallace, J. M., and Dickinson, R. E., 1972. Empirical orthogonal representation of time series in the frequency domain, Part 1: Theoretical considerations. J. Appl. Meteor., 11: 887-892.

Wang, D. P., and Mooers, C. N. K., 1977. Long coastal trapped waves off the west coast of the United States, summer 1973. J. Phys. Oceanogr., 7: 856-864.

Wang, D. P., and Walsh, J. J., 1976. Objective analysis of the upwelling ecosystem off Baja California. J. Mar. Res., 34: 43-60.

Wunsch, C., and Gill, A. E., 1976. Observations of equatorially trapped waves in Pacific sea level variations. Deep Sea Res., 23: 371-390.

BIBLIOGRAPHY

Adams, J. K., and V. T. Buchwald, 1969: The generation of continental shelf waves. J. Fluid Mech., 35, 815-826.

Allen, J. S., 1973: Upwelling and coastal jets in a continuously stratified ocean. J. Phys. Oceanogr., 3, 245-257.

Allen, J. S., 1975: Coastal trapped waves in a stratified ocean. J. Phys. Oceanogr., 5, 300-325.

Allen, J. S., 1976a: Some aspects of the forced wave response of stratified coastal regions. J. Phys. Oceanogr., 6, 113-119.

Allen, J. S., 1976b: On forced, long continental shelf waves on an f-plane. J. Phys. Oceanogr., 6, 426-431.

Allen, J. S., and R. D. Romea, 1980: On coastal trapped waves at low latitudes in a stratified ocean. J. Fluid Mech., 98, 555-585.

Allen, J. S., and R. L. Smith, 1981: On the dynamics of wind-driven shelf currents. Phil. Trans. R. Soc. Lond. A, 302, 617-634.

Anderson, D. L. T., and A. E. Gill, 1975: Spin up of a stratified ocean, with applications to upwelling. Deep Sea Res., 22, 583-596.

Anderson, D. L. T. and P. B. Rowlands, 1976: The role of inertia-gravity and planetary waves in the response of a tropical ocean to the incidence of an equatorial Kelvin wave on a meridional boundary. J. Mar. Res., 34, 395-417.

Bretherton, F. P., 1970: The general linearized theory of wave propagation. Mathematical Problems in the Geophysical Sciences, Am. Math. Soc., Providence, R.I., W. H. Reid, ed., 13, 61-102.

Brink, K. H., 1982a. A comparison of long coastal trapped wave theory with observations off Peru. J. Phys. Oceanogr., in press.

Brink, K. H., 1982b. The effect of bottom friction on low frequency coastal trapped waves. J. Phys. Oceanogr., 12, 127-133.

Brink, K. H., and J. S. Allen, 1978. On the effect of bottom friction on barotropic motion over the continental shelf. J. Phys. Oceanogr., 8, 919-922.

Brink, K. H., J. S. Allen, and R. L. Smith, 1978. A study of low frequency fluctuations near the Peru coast. J. Phys.Oceanogr., 8, 1025-1041.

Brink, K. H., Halpern, D., and R. L. Smith, 1980. Circulation in the Peruvian upwelling system near 15°S. J. Geophys. Res., 85, 4036-4048.

Brockmann, C., E. Fahrbach, and W. Urquizo, 1978. ESACAN data report. Institut fur Meereskunde an der Christian-Albrechts-Universitat, Nr. 51, ISSN 0341-8561.

Brockmann, C., E. Fahrbach, A. Huyer, and R. L. Smith, 1980. The poleward undercurrent along the Peru coast: 5° to 15°S. Deep Sea Res., 27A, 847-856.

Brooks, D. A., and C. N. K. Mooers, 1977. Wind-forced continental shelf waves in the Florida current. J. Geophys. Res, 82, 2569-2576.

Buchwald, V. T., 1976. The diffraction of shelf waves by small coastal irregularities. Proc. IUTAM Symposium on Waves on Water of Variable Depth.(in press).

Buchwald, V. T., and J. K. Adams, 1968. The propagation of continental shelf waves. Proc. Roy. Soc. London, A305, 235-250.

Cane, M. A., and E. S. Sarachik, 1977. Forced baroclinic ocean motions: II.The linear equatorial bounded case. J. Mar. Res., 35, 395-432.

Clarke, A. J., 1976. Coastal upwelling and coastally trapped long waves. Ph.D. Thesis, Cambridge University, 178 pp.

Clarke, A. J., 1977. Observational and numerical evidence for wind-forced coastal trapped long waves. J. Phys. Oceanogr., 7, 231-247.

Cutchin, D. L., and R. L. Smith, 1973. Continental shelf waves: low frequency variation in sea level and currents over the Oregon continental shelf. J. Phys. Oceanogr., 3, 73-82.

Fomin, L. M., and M. T. Savin, 1973. Vertical coherence of inertial motions in the ocean. Izv. Acad. Sci. USSR Atmos. Oceanic Phys., Engl. Transl., 9, 331-334.

Gill, A. E., and A. J. Clarke, 1974. Wind induced upwelling, coastal currents, and sea level changes. Deep Sea Res., 21, 325-245.

Gill, A. E., and E. H. Schumann, 1974. The generation of long shelf waves by the wind. J. Phys. Oceanogr., 4, 83-90.

Gradshteyn, I. S., and I. M. Ryzhik, 1980. Tables of Integrals, Series, and Products, Academic Press, New York, 1160 pp.

Greenspan, H. P., 1968. The Theory of Rotating Fluids, Cambridge University Press, Cambridge, 328 pp.

Grimshaw, R., 1977. The effects of a variable Coriolis parameter, coastline curvature, and variable bottom topography on continental shelf waves. J. Phys. Oceanogr., 7, 547-554.

Hogg, N. G., 1980. Observations of internal Kelvin waves trapped round Bermuda. J. Phys. Oceanogr., 10, 1353-1376.

Huppert, H. E., and Stern, M. E., 1974. Ageostrophic effects in rotating stratified flows. J.Fluid Mech., 62,369-385.

Huthnance, J. M., 1975. On trapped waves over a continental shelf. J. Fluid Mech., 69,689-704.

Huthnance, J. M., 1978. On coastal trapped waves: analysis and numerical calculation by inverse itiration. J. Phys. Oceanogr., 8, 74-92.

Huyer, A., W. E. Gilbert, R. Shramm, and D. Barstow, 1978. CTD observations off the coast of Peru. Data Report 71, Oregon State University, 78-18, 409 pp.

Kundu, P. K., 1976. An analysis of inertial oscillations observed near the Oregon coast. J. Phys. Oceanogr., 6, 879-893.

Kundu, P. K., and J. S. Allen, 1976. Some three dimensional characteristics of low-frequency current fluctuations near the Oregon coast. J. Phys. Oceanogr., 6, 181-199.

Kundu, P. K., J. S. Allen, and R. L. Smith, 1975. Modal decomposition of the velocity field near the Oregon coast. J. Phys. Oceanogr., 5, 683-704.

Luther, D. S., 1980. Observations of long period waves in the tropical ocean and atmosphere. Ph. D. Thesis, Woods Hole Oceanographic Institution-Massachusetts Institute of Technology, 210 pp.

Mcreary, J. P., 1981. A linear stratified model of the coastal undercurrent. Philos. Trans. R. Soc. London, Ser. A, 298, 603-635.

Miles, J. W., 1972. Kelvin waves on ocean boundaries. J. Fluid Mech., 55, 113-127.

Mooers, C. N. K., 1973. A technique for the cross spectrum analysis of pairs of complex valued time series with emphasis on properties of polarized components and rotational environments. Deep Sea Res., 20, 1090-1141.

Moore, D. W., 1968. Planetary-gravity waves in an equatorial ocean. Ph.D. Thesis, Harvard University.

Mysak, L. A., 1967. On the theory of continental shelf waves. J. Mar. Res., 25, 205-227.

Pedlosky, J., 1969. Linear theory of the circulation of a stratified ocean. J.Fluid Mech., 35, 185-205.

Pedlosky, J., 1974. On coastal jets and upwelling in bounded basins. J. Phys. Oceanogr., 4, 3-18.

Pedlosky, J.,1979. Geophysical Fluid Dynamics. Springer-Verlag, New York, 624 pp.

Philander, S. G. H., 1978. Forced oceanic waves. Rev. Geophys. and Space Phys., 16, 15-46.

Picaut, J., 1981. Seasonal upwelling in the eastern Atlantic. Unpublished Manuscript. Tropical Ocean-Atmosphere Newsletter, 5, 2-3.

Reid, R.O., 1958. Effect of Coriolis force on edge waves (1) investigation of the normal modes. J. Mar. Res., 16, 109-144.

Rhines, P., 1970. Edge-bottom-and Rossby waves in a rotating stratified fluid. Geophys. Fluid Dyn., 1, 273-302.

Ripa, P., and S. P. Hayes, 1981. Evidence for equatorial trapped waves at the Galapagos Islands. J. Geophys. Res., 86, 6509-6516.

Robinson, A. R., 1964. Continental shelf waves and the response of sea level to weather systems. J. Geophys. Res., 69, 367-386.

Smith, R. L., 1978. Poleward propagating perturbations in currents and sea level along the Peru coast. J. Geophys. Res., 83, 6083-6092.

Smith, R. L., 1980. A comparison of the structure and variability of the flow field in the three coastal upwelling regions: Oregon, Northwest Africa, and Peru. Submitted to Coastal Upwelling-1980, F. A. Richards, Ed., Am. Geophys. Union.

Stevenson, M. R.,and B. A. Taft, 1971. New evidence of the equatorial undercurrent east of the Galapagos Islands. J. Mar. Res., 29, 103-115.

Vermersch, J. A., and R. C. Beardsley, 1976. A note on the theory of low frequency waves in a rotating stratified channel. Studies in Applied Math., 55, 281-292.

Wallace, J. M., and R. E. Dickinson, 1972. Empirical orthogonal representation of time series in the frequency domain, Part 1: Theoretical considerations. J. Appl. Meteor., 11, 887-892.

Wang, D. P., and J. J. Walsh, 1976. Objective analysis of the upwelling ecosystem off Baja California. J. Mar. Res., 34, 43-60.

Wang, D. P., and Mooers, C. N. K., 1977. Long coastal trapped waves off the west coast of the United States, summer 1973. J. Phys. Oceanogr., 7, 856-864.

Weisberg, R. H., A. Horigan, and C. Colin, 1978. Equatorially trapped Rossby-gravity wave propagation in the Gulf of Guinea. J. Mar. Res.,37, 66-86.

Wunsch, C., 1977. Response of an equatorial ocean to a periodic monsoon. J. Phys. Oceanogr., 7, 497-511.

Wunsch, C., 1978. Observations of equatorially trapped waves in the ocean: A review prepared for equatorial workshop, July 1977. Review Papers of Equatorial Oceanography, FINE Workshop Proccedings.

Wunsch, C., and A. E. Gill, 1976. Observations of equatorially trapped waves in Pacific sea level variations. Deep Sea Res., 23, 371-390.

APPENDICES

Chapter II

Appendix A Sinusoidal Forcing

a) Interior Solutions

With a wind stress given by (5.1), we seek interior solutions given by (5.4), and, in a manner similar to the representation for $\tilde{h}$ in (2.12), we define

$$\tilde{g}(x) = \tilde{g}_I + \tilde{g}_B. \tag{A1}$$

The solutions to (2.11), (2.13), and (2.14) for $\tilde{\phi}$, $\tilde{g}_I$ and $\tilde{g}_B$, subject to (2.20a) and (2.21b) and appropriate for an eastern boundary, are

$$\tilde{\phi} = -mT_0[\omega(k^2 + \ell^2) - (k\beta/\delta)]^{-1} [\exp(ikx) - \exp(Q_- x)], \tag{A2a}$$

$$Q_{\pm} = (i\beta/2\omega\delta) \pm [\ell^2 - (\beta/2\omega\delta)^2]^{1/2}, \tag{A2b}$$

$$\tilde{g}_I = fmT_0[k\beta - \omega\delta\delta_{R(1)}^{-2}]^{-1} \exp(ikx), \tag{A3}$$

$$\tilde{g}_B = C_0 \exp(Rx), \tag{A4a}$$

$$R = (i\beta/2\omega\delta) - [\delta_{R(1)}^{-2} - (\beta/2\omega\delta)^2]^{1/2}, \tag{A4b}$$

where assumption (2.5a) has been used in (5.7) and where the constant C_0 in (A4a) may be determined from (2.21a) after a solution for $\hat{h}$ on the shelf is obtained.

For

$$\omega >> k\beta\delta_{R(1)}^2/\delta, \quad \omega >> \tfrac{1}{2}(\delta_{R(1)}\beta/\delta), \tag{A5a,b}$$

applied to (A3) and (A4) respectively, we obtain

$$\tilde{g}_I \sim - fmT_0(\delta_{R(1)}^2/\omega\delta) \exp(ikx), \quad \tilde{g}_B \sim C_0\exp(-x/\delta_{R(1)}). \tag{A5c,d}$$

Eq. (A5d) is the interior extension of a coastal trapped internal Kelvin wave. This case is investigated in Section 5a. Note that in

general (A5b) implies (A5a) since $\delta_{R(1)}k << 1$. Condition (A5a) corresponds to forcing at wavenumbers and frequencies above the cutoff for long internal Rossby waves.

For very low frequency forcing, i.e., for

$$\omega << k\beta\delta^2_{R(1)}/\delta, \quad \omega << \tfrac{1}{2}(\delta_{R(1)}\beta/\delta), \tag{A6a,b}$$

we obtain

$$\tilde{g}_I \sim fm(T_0/k\beta)\exp(ikx), \; \tilde{g}_B \sim C_0\exp(i\omega\delta x/\beta\delta_{R(1)}{}^2), \tag{A6c,d}$$

and the interior solution takes the form of an interior Sverdrup flow (A6c) and a westward propagating internal Rossby wave (A6d). This case is briefly discussed in Section 5b.

The relevant expression (2.20b) for the forcing at $\xi = 1$ by the interior barotropic motion is

$$\tilde{\phi}_{x(0)} = im(T_0/\omega)(k + iQ_+)^{-1}. \tag{A7}$$

In general $\tilde{\phi}_{x(0)}$ is complex and the forced shelf circulation will have components both in phase and out of phase with the wind stress driving. For the purposes of calculating specific solutions in Section 5a for the shelf velocities, we employ the approximate expression

$$\tilde{\phi}_{x(0)} \simeq T_0/\omega, \tag{A8a}$$

obtained with the conditions

$$\ell^2 >> (\beta/2\omega\delta)^2, \; |k| \to 0. \tag{A8b,c}$$

The condition (A8b) is restrictive, implying the period $T' < 20$ days. However, for $\ell^2 \geq (\beta/2\omega\delta)^2$, with $|k| \to 0$,

$$|\tilde{\phi}_{x(0)}|^2 \sim (T_0/\omega)^2, \tag{A8d}$$

i.e., $\tilde{\phi}_{x(0)}$ has the same magnitude for the more general case (see Fig. 7 with $k/\ell = 0$).

The limit

$$\ell^2 \geq (\beta/2\omega\delta)^2, \quad k >> \ell, \tag{A9a,b}$$

yields

$$\tilde{\phi}_{x(0)} \sim -i(T_0/\omega), \tag{A9c}$$

and the response, while of the same magnitude as $\tilde{\phi}_{x(0)}$ obtained in the limit (A8b,c), is out of phase with the wind stress by a factor of $\pi/2$. This behavior is evident in Figs. 7 and 8 with $(k/\ell) = 15.0$.

Condition (A8c) corresponds to a wind stress with x wavenumber $k = 0$, traveling along the coast. For $\ell < 0$ (equatorward traveling disturbance), $\tilde{\phi}_{x(0)} < 0$. For $\ell > 0$, $\tilde{\phi}_{x(0)} > 0$. Condition (A9b) corresponds to a wind stress traveling in the onshore-offshore direction. For both $k > 0$ and $k < 0$, $\tilde{\phi}_{x(0)} < 0$.

We also note that $\tilde{\phi}_{x(0)}$ is independent of ω for small ω, i.e., the condition

$$(|\ell|, |k|) << \beta/2\omega\delta \tag{A10a}$$

yields

$$\tilde{\phi}_{x(0)} \sim im(T_0\delta/\beta), \tag{A11b}$$

corresponding to a Sverdrup balance in the interior.

b) Shelf Equations

We restrict our attention to cases where (A5a,b) are satisfied and use (A5c,d) for $\tilde{g}_I$ and $\tilde{g}_B$. For oceanic parameters at 6° latitude off the west coast of South America (e.g., $\delta_R' \approx 100$ km, $\beta' \approx 2.3 \times 10^{-13}$ cm^{-1} sec^{-1}), (A5a,b) are satisfied for periods $T' < 60$ days.

We seek a forced response on the shelf of the form (5.4). The equations for the shelf variables, obtained by utilizing (5.4) in (2.17a,b) are

$$\phi_{\xi\xi} - \delta_B^{-1}\phi_\xi - \ell(\omega\delta_B)^{-1}\,(f\phi - \hat{g}) = i\hat{T}_0(\omega\delta_B)^{-1}, \tag{A12a}$$

$$\hat{g}_{\xi\xi} + a\delta_B^{-1}\hat{g}_\xi - (\delta/\delta_R)^2\hat{g} + af\ell(\omega\delta_B)^{-1}\,(f\phi - \hat{g}) = -iaf\hat{T}_0(\omega\delta_B)^{-1}, \tag{A12b}$$

where

$$\hat{T}_0 = T_0 + i\ell\tilde{g}_{I(0)}. \tag{A12c}$$

As in Section 4, the shelf equations are forced by the alongshore component of the wind stress at the coast and by the interior baroclinic motion.

With (5.4), the boundary conditions (2.19a,b), (2.20b), and (2.21a,b) are

$$\phi = 0, \quad f(\ell/\omega)\hat{g} - \hat{g}_\xi = if(\hat{T}_0/\omega), \quad \text{at } \xi = 0, \tag{A13a,b}$$

$$\phi_\xi = \tilde{\phi}_{x(0)}, \quad \text{at } \xi = 1, \tag{A13c}$$

$$\hat{g} = \tilde{g}_B(\delta), \quad \tilde{g}_{Ix(0)} + \tilde{g}_{Bx(\delta)} = \delta^{-1}\hat{g}_\xi, \quad \text{at } \xi = 1. \tag{A14a,b}$$

With (A5a,b), except very near the equator, the interior baroclinic forced response is relatively small. This is reflected in the ratio of the interior forcing term $i\ell\tilde{g}_{I(0)}$ and the coastal wind stress term T_0, which appear in the forcing $\hat{T}$; i.e.,

$$i\ell\tilde{g}_{I(0)}/T_0 \sim (m\ell/\omega)(f\delta)(\delta_R/\delta)^2 i, \tag{A15}$$

which is $O(\delta)$ and therefore small. Accordingly, with (A5a,b) we employ the approximation

$$\hat{T} \simeq T_0. \tag{A16}$$

Note that with (A6),

$$i\ell\tilde{g}_{I(0)}/T_0 \sim m\ell f(k\beta)^{-1} i, \tag{A17}$$

which is $O(1)$ in general, indicating that for forcing at very low frequencies baroclinic interior motions may be as important as the alongshore coastal wind stress.

Chapter II

Appendix B Exponential Slope

Analytical results to (A12a,b) are obtainable if an exponential slope (Buchwald and Adams, 1968) is assumed:

$$H = \exp[(\xi - 1)/\delta_B]. \tag{B1}$$

In this case, $H_\xi/H = \delta_B^{-1}$ is a constant. This depth profile, while still highly idealized, is not an unreasonable approximation to actual shelf-slope topography.

We obtain approximate solutions under the assumption

$$a_{(0)} = H_1/H_{2(0)} << 1. \tag{B2a}$$

We utilize the expansion

$$a = a_{(0)} \exp(-\xi/\delta_B) + O(a_{(0)}^2), \tag{B2b}$$

so that (A12a,b) may be written to $O(a_{(0)}^2)$ in the form

$$\hat{\phi}_{\xi\xi} - \delta_B^{-1}\hat{\phi}_\xi - (\ell/\omega\delta_B)(f\hat{\phi} - \hat{g}) = 0, \tag{B3a}$$

$$\hat{g}_{\xi\xi} - (\delta/\delta_R)^2\hat{g} = [a_{(0)}\exp(-\xi/\delta_B)][-(f\ell/\omega\delta_B)(f\hat{\phi} - \hat{g}) - \delta_B^{-1}\hat{g}_\xi + (\delta/\delta_R)^2\hat{g}], \tag{B3b}$$

where we define

$$\hat{\phi} = \phi + iT_0/\ell. \tag{B3c}$$

For simplicity, we adopt an f-plane analysis (f = 1) here, and assumptions (A5a,b).

The boundary conditions are

$$\hat{\phi} = iT_0/\ell, \quad \hat{g} - (\omega/\ell)\hat{g}_\xi = iT_0/\ell, \quad \text{at } \xi = 0, \tag{B4a,b}$$

$$\hat{\phi}_\xi = \tilde{\phi}_{x(0)}, \quad \hat{g} = C_0, \quad \hat{g}_\xi + (\delta/\delta_{R(1)})\hat{g} = 0, \quad \text{at } \xi = 1, \tag{B4c,d,e}$$

where $\tilde{\phi}_{x(0)}$ is given by (A8a) and C_0 is the coefficient from (A5d).

With (B2a), (B3a,b) are weakly coupled and may be solved, subject to (B4a-e), by perturbation methods. We solve (B3a) for $\hat{\phi}$ only, subject to (B4a,c), to obtain a first order approximation, $\hat{\phi}_0$. Similarly, we solve (B3b) for $\hat{g}$ only, subject to (B4b,e) to obtain a first order approximation, $\hat{g}_0$.

These are

$$\hat{g}_0 = K_o \exp[-\xi(\delta/\delta_R)], \tag{B5a}$$

$$\hat{\phi}_0 = \exp(\xi/2\delta_B)(D_0 \sinh\gamma\xi + iT_0\ell^{-1} \cosh\gamma\xi), \tag{B5b}$$

where

$$K_0 = i(T_0/\ell)[1 + (\omega/\ell)(\delta/\delta_R)]^{-1}, \tag{B5c}$$

$$D_0 = [-i(T_0/\ell)(\tfrac{1}{2}\delta_B^{-1}\cosh\gamma + \gamma\sinh\gamma) + \tilde{\phi}_{x(0)} \exp(-\tfrac{1}{2}\delta_B)]/$$

$$(\tfrac{1}{2}\delta_B^{-1} \sinh\gamma + \gamma\cosh\gamma), \tag{B5d}$$

$$\gamma^2 = (\ell/\omega)\delta_B^{-1} + (2\delta_B)^{-2}. \tag{B5e}$$

These solutions are written for $\ell > 0$.

We substitute $\hat{g}_0$ into (B3a) to obtain an O(1) correction $\hat{\phi}_1$. The $O(a_{(0)})$ correction to $\hat{g}$, $a_{(0)}\hat{g}_1$, is obtained by substituting $\hat{\phi}_0$, $\hat{g}_0$, and $\hat{\phi}_1$ into (B3b). Finally, we utilize $a_{(0)}\hat{g}_1$ in (B3a) to obtain the O(a) correction $a_{(0)}\hat{\phi}_2$ to $\hat{\phi}$. The corrections satisfy homogeneous boundary conditions at $\xi = 0$ and $\xi = 1$. Additional corrections are $O(a_{(0)}^2)$ so that the approximate solutions are

$$\hat{\phi} = \hat{\phi}_0 + \hat{\phi}_1 + a_{(0)}\hat{\phi}_2 + O(a_{(0)}{}^2), \tag{B6a}$$

$$\hat{g} = \hat{g}_0 + a_{(0)}\hat{g}_1 + O(a_{(0)}{}^2). \tag{B6b}$$

The corrections may be obtained in a straightforward manner but their algebraic form is complicated and they are omitted here.

This perturbation procedure was verified by comparison with expansions for $a_{(0)} << 1$ of exact solutions which may be obtained in the weak slope limit $\delta_B >> 1$.

The coefficient K_0 possesses a singularity for $(\omega/\ell)(\delta/\delta_R) = -1$ (see B6a), while D_0 is unbounded for

$$\tanh\gamma = -2\delta_B\gamma. \tag{B7}$$

The first singularity corresponds to wind forcing at the resonant frequency for free internal Kelvin waves, and (B7) corresponds to the excitation of the free shelf wave modes. These resonances occur only for $\ell < 0$.

Substitution of (5.5) into (2.18c,d) yields the shelf velocities:

$$v_1 = -(\delta H)H_1^{-1}\,\hat{v}_1(\xi) \quad \exp[-i(\omega\bar{t} - \ell y)], \tag{B8a}$$

$$v_2 = -(\delta H)H_1^{-1}\,\hat{v}_2(\xi) \quad \exp[-i(\omega\bar{t} - \ell y)], \tag{B8b}$$

where

$$\hat{v}_1(\xi) = \hat{\phi}_\xi + a^{-1}\hat{g}_\xi, \tag{B9a}$$

$$\hat{v}_2(\xi) = \hat{\phi}_\xi - \hat{g}_\xi. \tag{B9b}$$

The solutions (B6a,b) simplify considerably if the limits $(\delta_R/\delta) << 1$ and $(\delta_R/\delta) >> 1$ are examined. These approximate solutions may be utilized in (B9a,b) to obtain approximate shelf velocities. For $(\delta_R/\delta) << 1$,

$$\hat{v}_1(\xi) \simeq -iT_0(a\omega)^{-1} \exp(-\delta\xi/\delta_R)$$

$$+ \exp(\xi/2\delta_B) \{D_0[(2\delta_B)^{-1} \sinh\gamma\xi + \gamma\cosh\gamma\xi]$$

$$+ iT_0\ell^{-1} [(2\delta_B)^{-1} \cosh\gamma\xi + \gamma\sinh\gamma\xi]\}, \quad \text{(B10a)}$$

$$\hat{v}_2(\xi) \simeq iT_0\omega^{-1} \exp(-\delta\xi/\delta_R)$$

$$+ \exp(\xi/2\delta_B) \{D_0[(2\delta_B)^{-1} \sinh\gamma\xi + \gamma\cos\delta\xi]$$

$$+ iT_0\ell^{-1} [(2\delta_B)^{-1} \cosh\gamma\xi + \gamma\sinh\gamma\xi]\}. \quad \text{(B10b)}$$

For $(\delta_R/\delta) >> 1$,

$$\hat{v}_1(\xi) \simeq -iT_0(a\ell)^{-1} (\delta/\delta_R) \exp(-\delta\xi/\delta_R), \quad \text{(B11a)}$$

$$\hat{v}_2(\xi) \simeq [\tilde{\phi}_{x(0)} + iT_0\ell^{-1} (\delta/\delta_R)] \exp[(\xi - 1)/2\delta_B]$$

$$\times [(2\delta_B)^{-1}\sinh\gamma\xi + \gamma\cosh\gamma\xi]/[(2\delta_B)^{-1}\sinh\gamma + \gamma\cosh\gamma]. \quad \text{(B11b)}$$

We may also examine the behavior of the solutions for low frequency, keeping in mind the conditions (A5a,b) required to preserve their validity. In particular, for $\gamma^2 \simeq \ell(\omega\delta_B)^{-1} >> 1$, $\gamma >> \delta/\delta_R$,

$$\hat{v}_1(\xi) \simeq -iT_0(a\ell)^{-1} (\delta/\delta_R) \exp(-\xi\delta/\delta_R), \quad \text{(B12a)}$$

$$\hat{v}_2(\xi) \simeq iT_0\ell^{-1} L_0 \exp(-\gamma\xi) + \tilde{\phi}_{x(0)}\gamma^{-1} \exp[\gamma(\xi - 1)], \quad \text{(B12b)}$$

where

$$L_0 = \omega\ell^{-1}(\delta/\delta_R) + \gamma^{-2} [(\delta/\delta_R)^2 + \delta(\delta_R\delta_B)^{-1}]. \quad \text{(B12c)}$$

Chapter III

APPENDIX A: SOLUTIONS FOR SLOWLY VARYING f

In this section we treat f as a slowly varying function of y, so that $f = f(\eta)$, $\eta = \beta y$, and $\beta \ll 1$. The equations that describe the problem and that may be derived from (2.1) with the above definition for f are (2.6), (2.8), (2.9) and

$$[p_{xx} + (f/N)^2 p_{zz}]_t + f_y p_x = 0. \qquad (A1)$$

(a) Free wave problem

An understanding of the free wave problem is useful. Therefore we consider a vertically unbounded ocean governed by a homogeneous version of (2.6) with the rigid lid condition (2.8) removed. A free wave solution is sought of the form

$$p(x,y,z,t) = \mathrm{Re}\{\phi(x;\eta) \exp[-i(\omega t + mz + \int_{y_0}^{y} \ell dy)]\}, \qquad (A2)$$

where here $\ell = \ell(\eta)$ and ϕ depends parametrically on η.

If (A2) is substituted in (A1) and a homogeneous version of (2.6), the result is

$$\phi_{xx} - (fm/N)^2\phi + i(\beta/\omega) f_\eta \phi_x = 0, \qquad (A3)$$

$$\phi_x + (f\ell/\omega)\phi + if(\beta/\omega)\phi_\eta = 0, \quad \text{at } x = 0. \qquad (A4)$$

The variable ϕ is expanded in the form

$$\phi = A(\phi_0 + i\beta\phi_1 + \ldots), \qquad (A5)$$

where A is a complex constant with $|A| = 1$ and ϕ_0, ϕ_1 are real variables. Substituting (A5) in (A3) and (A4) we find that the lowest order solution ϕ_0 satisfies the same equations and boundary conditions as the constant f solutions (2.3)-(2.9) (with no forcing) but with $f = f(\eta)$. This solution is

$$\phi_0 = C(\eta) \exp(-f\ell x/\omega), \qquad m/N = \ell/\omega. \tag{A6}$$

The equation for ϕ_1 is

$$\phi_{1xx} - (fm/N)^2\phi_1 = -(f_\eta/\omega)\phi_{0x}, \tag{A7}$$

with boundary conditions

$$\phi_{1x} + (f\ell/\omega)\phi_1 = -(f/\omega)\phi_{0\eta}, \qquad \text{at } x = 0, \tag{A8}$$

$$\phi_1, \ \phi_{1x} < \infty, \qquad \text{as } x \to \infty. \tag{A9}$$

A compatibility condition for ϕ_1 may be determined by multiplying (A7) by ϕ_0 and integrating over x from 0 to ∞:

$$\int_0^\infty [\phi_0\phi_{1xx} - (fm/N)^2\phi_0\phi_1]dx = -(f_\eta/\omega) \int_0^\infty \phi_0\phi_{0x}dx. \tag{A10}$$

Utilizing the boundary conditions on ϕ_0 and ϕ_1, we obtain

$$C(\eta) = (f/f_0)^{\frac{1}{2}}, \tag{A11}$$

where f_0 is a reference value of the Coriolis parameter.

This implies an $f^{\frac{1}{2}}$ growth in amplitude of an internal Kelvin wave as it propagates poleward and vertically and corresponds to the

conservation of wave energy flux. The amplification agrees with results obtained by Miles (1972) for external Kelvin waves and by Allen and Romea (1980).

(b) Forced Problem

In a manner similar to the method used in Section 2, we seek a solution to (A1) in terms of the Fourier cosine transform. The transformed problem is (2.18b,c) and

$$[\hat{p}_{xx} - (fm/N)^2 \hat{p}]_t + f_y \hat{p}_x = 0. \tag{A12}$$

where the transform is defined by (2.17).

The solution to (A12) may be written

$$\hat{p} = \hat{p}_0 + \hat{p}_1, \tag{A13}$$

where $\hat{p}_1$ is assumed to be a small perturbation ($\hat{p}_1 << \hat{p}_0$), and where

$$\hat{p}_0 = \hat{Y}_0 \exp(-fmx/N). \tag{A14}$$

The problem for $\hat{p}_1$ is

$$[\hat{p}_{1xx} - (fm/N)^2 \hat{p}_1]_t = f_y \hat{Y}_0 (fm/N) \exp(-fmx/N). \tag{A15}$$

The solution to (A15) subject to (2.18c) is

$$\hat{p}_1 = \hat{Y}_1 \exp(-fmx/N) - \tfrac{1}{2}\hat{Y}_{1p} x\exp(-fmx/N), \tag{A16}$$

where

$$\hat{Y}_{1pt} = \hat{Y}_0 f_y. \tag{A17}$$

Therefore the total solution for $\hat{p}$ is (absorbing Y_1 in Y_0)

$$\hat{p} = (\hat{Y}_0 - \tfrac{1}{2}\hat{Y}_{1p}x)\exp(-fmx/N). \qquad (A18)$$

We now use (A17) and (A18) in the remaining boundary condition (2.18b) to obtain

$$-(m/N)\hat{Y}_{0t} + \hat{Y}_{0y} - \tfrac{1}{2}\hat{Y}_0(f_y/f) = \tau(y,t). \qquad (A19)$$

Eq. (A19) is a forced first order wave equation which includes a slowly varying Coriolis parameter. The transformation $\hat{Y}_0 = f^{\frac{1}{2}}\hat{Y}_0'$ yields

$$-(m/N)\hat{Y}'_{0t} + \hat{Y}'_{0y} = f^{-\frac{1}{2}}(\eta)\,\tau(y,t). \qquad (A20)$$

Eq. (A20) for the scaled variable Y_0' is similar to (2.20), the forced wave equation obtained for constant f, but with a factor of $f^{-\frac{1}{2}}(\eta)$ multiplying the forcing function.

With an initial condition given by (2.22), the solution for a general wind stress $\tau = \tilde{F}(y)\,\tilde{T}(t)$ is (2.25), where

$$p_D = -(2N/\pi)\int_0^\infty f^{-\frac{1}{2}}[\beta(y + Nt/m)]\,\tilde{F}(y + Nt/m)$$
$$\exp(-fmx/N)\,m^{-1}\cos mz\,dm. \qquad (A21)$$

For forcing given by (3.1) (Example A) or (3.11) (Example B), the f-plane results are similar to the solutions obtained with (A21), with the rescaling p (slowly varying f) = $f^{-\frac{1}{2}}$ p (f-plane).

Chapter III
APPENDIX B: GENERALIZED INTEGRAL TRANSFORM IN x

The solution to (2.3) is derived here in an alternate manner with a generalized integral transform in x. In this case, boundary conditions (2.6) and (2.8) are replaced by the equivalent conditions

$$p_{zt} = -(N^2/f)\, \tau(y,t)\, \delta(x), \qquad z = 0, \tag{B1}$$

$$p_{xt} + f p_y = 0, \qquad x = 0 \tag{B2}$$

where here the Ekman suction in the upper coastal corner is represented by a delta function at x = 0 (B1).

We express p and τ as Fourier integrals in time and in y, i.e.,

$$[\tilde{\tau}(\ell,\omega),\ \tilde{p}(x,\ell,z,\omega)]$$

$$= \int_{-\infty}^{\infty} \int_{-\infty}^{\infty} [\tau(y,t),\ p(x,y,z,t)] \exp(-i\omega t) \exp(-i\ell y)\, dt\, dy, \tag{B3}$$

$$[\tau(y,t),\ p(x,y,z,t)]$$

$$= (2\pi)^{-1} \int_{-\infty}^{\infty} \int_{-\infty}^{\infty} [\tau(\ell,\omega),\ p(x,\ell,z,\omega)] \exp(i\omega t) \exp(i\ell y)\, d\omega\, d\ell. \tag{B4}$$

Utilization of (B3) in (2.3), (2.9), (B1) and (B2) gives

$$\tilde{p}_{xx} + (f/N)^2\, \tilde{p}_{zz} = 0, \tag{B5}$$

$$\tilde{p},\ \tilde{p}_x,\ \tilde{p}_z < \infty, \qquad \text{as } x \to \infty,\ z \to -\infty, \tag{B6}$$

$$\tilde{p}_z = iN^2(f\omega)^{-1}\, \tilde{\tau}\, \delta(x), \qquad \text{at } z = 0, \tag{B7}$$

$$\tilde{p}_x + f(\ell/\omega)\, \tilde{p} = 0, \qquad \text{at } x = 0, \tag{B8}$$

plus appropriate radiation conditions for $x \to \infty$, $z \to -\infty$.

Eq. (B8) is satisfied by the transform

$$\tilde{p}(x,\ell,z,\omega) = \int_0^\infty \Phi(\alpha,\ell,z,\omega)[\sin\alpha x - \omega(f\ell)^{-1}\,\alpha\cos dx]d\alpha$$

$$+ W(z,\ell,\omega)\, H(\omega/\ell)\, \exp(-f\ell x/\omega), \qquad \text{(B9)}$$

where the last term is present only for $(\ell/\omega) > 0$. The transform variable Φ may be obtained my multiplying both sides of (B9) by $\sin\alpha x - \omega(f\ell)^{-1}\,\alpha\cos\alpha x$ and integrating over x from 0 to ∞, i.e.,

$$\Phi(\alpha,\ell,z,\omega) = (2/\pi)[1 + (\omega\alpha)^2(f\ell)^{-2}]^{-1} \int_0^\infty \tilde{p}(\sin\alpha x - \omega\alpha(f\ell)^{-1}\cos\alpha x]dx. \qquad \text{(B10)}$$

Similarly, W is obtained by multiplying (B9) by $\exp(-f\ell x/\omega)$ and integrating with respect to x from 0 to ∞, i.e.,

$$W(z,\ell,\omega) = 2f(\ell/\omega) \int_0^\infty \tilde{p}\, \exp(-f\ell x/\omega)dx. \qquad \text{(B11)}$$

We obtain the transformed problem for Φ by multiplying (B5) and (B6a) by $\sin\alpha x - \omega\alpha(f\ell)^{-1}\cos\alpha x$, integrating over x from 0 to ∞, and integrating by parts where appropriate. The result is

$$\Phi_{zz} - (N\alpha/f)^2\, \Phi = 0, \qquad \text{(B12)}$$

$$\Phi_z < \infty, \qquad \text{as } z \to -\infty, \qquad \text{(B13)}$$

with solution

$$\Phi = A(\alpha,\ell,\omega)\, \exp(N\alpha z/f). \qquad \text{(B14)}$$

$W(z)$ is obtained by multiplying (B5) and (B6a) by $\exp(-f\ell x/\omega)$ and integrating over x from 0 to ∞. This yields

$$W = W_0(\ell,\omega)\ \exp(iN\ell z/\omega), \tag{B15}$$

where the positive root is chosen in (B15) to satisfy the radiation condition, giving a downward flux of wave energy for $\ell/\omega > 0$. The total solution is

$$p(x,\ell,z,\omega) = \int_0^\infty A(\alpha,\ell,\omega)[\sin\alpha x - \omega\alpha(f\ell)^{-1}\cos\alpha x]\ \exp(Nz\alpha/f)\ d\alpha$$

$$+ H(\omega/\ell)W_0(\ell,\omega)\exp(-f\ell x/\omega)\exp(iN\ell z/\omega). \tag{B16}$$

We find A and W_0 by substituting (B16) in the remaining condition (B7):

$$(N/f) \int_0^\infty \alpha A[\sin\alpha x - \omega\alpha(f\ell)^{-1}\cos\alpha x]d\alpha$$

$$+ i\ H(\omega/\ell)\ W_0 N(\ell/\omega)\exp(-f\ell x/\omega) = i\ N^2(f\omega)^{-1}\ \tilde{\tau}\ \delta(x). \tag{B17}$$

To find W_0, when $\omega/\ell > 0$, multiply both sides of (B17) by $\exp(-f\ell x/\omega)$ and integrate with respect to x from 0 to ∞, and to find A, multiply both sides by $\sin\alpha x - \omega\alpha(f\ell)^{-1}\cos\alpha x$ and integrate over x from 0 to ∞. This gives

$$W_0 = (2N/\omega)\ \tilde{\tau}, \qquad (\omega/\ell) > 0, \tag{B18}$$

$$A = -\ i(2/\pi)\ N(f\ell)^{-1}[1 + (\omega\alpha)^2(f\ell)^{-2}]^{-1}\ \tilde{\tau}. \tag{B19}$$

With a particular forcing τ the pressure may now be calculated from (B4), (B16), (B18), and (B19) and the velocities computed using (2.1a) and (2.4a,b).

As a simple example, consider a traveling plane wave coastal wind stress where

$$\tau(y,t) = \tau_0 \exp(-i\omega_0 t - i\ell_0 y). \tag{B20}$$

The solution for p is

$$p = 2N\tau_0(\pi\omega_0)^{-1} \exp[-i(\omega_0 t + \ell_0 y)]$$
$$\times\{-i\omega_0(f\ell_0)^{-1}\int_0^\infty [\sin\alpha x - \omega_0\alpha(f\ell_0)^{-1}\cos\alpha x][1 + (\omega_0\alpha)^2(f\ell_0)^{-2}]^{-1} \exp(N\alpha Z/f)d\alpha$$
$$+ H(\omega_0/\ell_0)\, \pi \exp(-f\ell_0 x/\omega_0) \exp(iN\ell_0 z/\omega_0)\} \tag{B21}$$

Evaluation of the integral in (B21) yields (3.23), where σ and ℓ in (3.23) are equal to ω_0 and $-\ell_0$ in (B21).

Chapter IV

APPENDIX A: EXPONENTIAL N^2 PROFILE

We have obtained results for both steep and weak slope topographies with general stratification. We now examine a particular more realistic stratification, but one which still allows analytical solutions, i.e., an exponential N^2 profile given by

$$R(z) = R_0 \exp(sz), \tag{A1}$$

where R_0 = constant. Profiles of R(z) are plotted for various s in Figure 12.

The x-z structure of the O(1) solution is given by (3.14), where $P_n(z)$, the vertical modal structure, is obtained by solving (3.15), (3.16) and (3.17) with the appropriate R. With (A1), the eigenvalue problem yields

$$\phi_n^{(0)} = \zeta^{1/2} \exp(-\ell x/\omega_n^{(0)}) \left[J_1(\ell\zeta^{1/2}/\omega_n^{(0)}s) + G_n Y_1(\ell\zeta^{1/2}/\omega_n^{(0)}s)\right], \tag{A2}$$

where

$$G_n = -J_0(\ell R_0/\omega_n^{(0)}s)/Y_0(\ell R_0/\omega_n^{(0)}s), \tag{A3}$$

and where the dispersion relation for the O(1) egienvalue $\omega_n^{(0)}$ is

$$J_0[\ell R_0 \exp(-s)/\omega_n^{(0)}s] + G_n Y_0[\ell R_0 \exp(-s)/\omega_n^{(0)}s] = 0. \tag{A4}$$

J_0, J_1, Y_0 and Y_1 are Bessel functions of the first and second kind of order 0 and 1 and

$$\zeta(z) = R^2(z) = R_0 \exp(2sz). \tag{A5}$$

The vertical structure of $\phi_{1x}^{(0)}$, which corresponds to alongshore velocity, is plotted in Figure 13 for various s, where the

modes are rescaled so that $P_{1(0)} = 1$. This is the O(1) modal solution, which is unaffected to first order by friction or topography and is the same for both the steep and weak slope problems. As s increases, the zero crossing of the mode becomes shallower and the bottom velocity decreases in accordance with the constraint of zero depth integrated mass flux in each mode, which follows from the integration over z of $P_n^{(0)}$ and the use of (3.13a). The ratio $|v(z = 0)/v(z = -1)|$ is shown in Table 2 as a function of s.

Figure 14 shows a smoothed N^2 profile calculated from measurements taken near 5°S latitude over the slope. The vertical structure of v associated with the first dynamical mode (the dashed curve labelled R in Figure 13), obtained numerically with the stratification shown in Figure 14, indicates that the bottom velocity is a fraction of that predicted by the solution for constant stratification (the curve labelled s = 0 in Figure 13). The mode shape was computed by integrating the governing equations by means of a fourth order Runge-Kutta technique, with a trial and error procedure for obtaining the proper eigenvalue so that the boundary conditions are satisfied (see Kundu et al., 1975, Section 5, for a discussion of the method). The profile was extrapolated to $N^2 = 0.1 \times 10^{-5} s^{-2}$ at the bottom at 4 km depth by an exponential profile below 780 m depth (parameter studies indicate that the modal structure is relatively insensitive to the exact choice of exponential structure). Although the N^2 profile is different from the exponential profiles, the mode shape for s between 2 and 3, particularly near z = -1, is a reasonable approximation to the vertical structure calculated with the N^2

profile shown in Figure 14, therefore we expect estimates of frictional effects to be more realistic with s between 2 and 3 than with s = 0.

Corrections to ω may be obtained using (A2), (A3) and (A4) in (3.20) for the steep slope and (4.11) for the weak slope. The $O(\lambda_1^{(0)})$ frictional corrections to ω for both cases are shown in Table 2 for various s. Table 2 is discussed in Section 5.

Chapter IV

APPENDIX B: WEAK SLOPE; MATCHING TO THE OUTER SHELF

In Section 4, the coastal weak slope solution becomes invalid for large x, when baroclinic motions decay with a Rossby radius scale from the coast leaving a barotropic onshore flow, which crosses constant depth contours. We show here that the barotropic component represents the first term in an expansion that matches to an outer shelf solution which represents a topographic Rossby wave. For simplicity, we set $R = R_0$ = constant and consider the frictionless case $\lambda = 0$. The qualitative results presented here are unchanged for general R and with bottom friction, but the analysis is more complicated.

The outer shelf equations are obtained for offshore scale $L \gg \delta_R$, i.e., for $R = O(\varepsilon) \ll 1$. The lowest order equations are

$$\tilde{\phi}_{xx} + R^{-2}\tilde{\phi}_{\eta\eta} = 0, \tag{B1}$$

$$\tilde{\phi}_{\eta} = 0, \text{ at } \eta = 0, \tag{B2a}$$

$$\tilde{\phi} = 0, \text{ at } x = 0, \tag{B2b}$$

$$\tilde{\phi} < \infty, \text{ as } x \to \infty, \tag{B2c}$$

$$(\ell/\omega)\tilde{\phi} = -\varepsilon^{-1} R^{-2}\tilde{\phi}_{\eta}, \text{ at } \eta = -1, \tag{B2d}$$

where the tilda superscript denotes an outer shelf variable. The solution is

$$\tilde{\phi}_n = C_n \sin(k_n s) \cosh(Rk_n \eta), \; n = 1, 2, \ldots, \tag{B3}$$

where C_n is an arbitrary constant. This topographic wave, where the motions arise from the sloping bottom, was studied by Rhines (1970)

and was also obtained by Vermersch and Beardsley (1976). The wave is bottom trapped for $Rk_n \geq 1$ and is approximately barotropic for $Rk_n \ll 1$.

The relation between k_n and ω_n is obtained from the bottom boundary condition (B2d) and is

$$\ell/\omega_n = \varepsilon^{-1} R^{-1} \tanh(Rk_n)k_n. \tag{B4}$$

In the limit of small Rk_n, (B3) and (B4) may be written, to $O(Rk_n)$, as

$$\tilde{\phi}_n \simeq C_n \sin(k_n x)(1 + \tfrac{1}{2}R^2 k_n{}^2\eta^2), \tag{B5}$$

$$k_n{}^2 \simeq (\ell/\omega_n)\varepsilon. \tag{B6}$$

The weak slope solution, with a vertical wall at $x = 0$, is derived to $O(\varepsilon)$ in Section 4. For $x \to \infty$, this solution is

$$\phi_{n\infty}{}^{(1)} \sim A_0, \tag{B7}$$

where A_0 is given by (4.15a) with $m = 0$. For R = constant and $\lambda = 0$,

$$\phi_{n\infty}{}^{(1)} \sim \varepsilon(n\pi/R)(-1)^n. \tag{B8}$$

For the purpose of matching to the outer shelf solution (B5), we must evaluate $\phi_{n\infty}$ at the next order. The procedure is identical to that used for the $O(\varepsilon)$ problem, but with more complicated algebra, and the result is

$$\phi_{n\infty}{}^{(2)} \sim (1/2)\eta^2 Rn\pi\varepsilon^2 \phi_{n\infty}{}^{(1)}. \tag{B9}$$

Since $\phi_n{}^{(0)} \to 0$ as $x \to \infty$, the asymptotic solution for ϕ_n as $x \to \infty$ to $O(\varepsilon^2)$ is

$$\phi_{n\infty} \sim \varepsilon\phi_{n\infty}^{(1)} \left[1 + 1/2\eta^2 \, Rn\pi\varepsilon\right]. \qquad (B10)$$

Eq. (B10) for $\phi_{n\infty}$ represents the first two terms in the expansion of $\cosh[\eta(n\pi\varepsilon R)^{1/2}]$. With $\ell/\omega_n = n\pi/R$ from (3.26b), (B5) for $x \to \varepsilon$ matches ϕ_n for $x \to \infty$ with

$$C_n = (n\pi\varepsilon/R)^{-1/2} \, \phi_{n\infty}^{(1)}. \qquad (B11)$$

Chapter V
Appendix

A summary of the observations obtained during the ESACAN experiment is given by Brockmann, et. al., (1978). The complete set of data from moored instruments and hydrographic stations from the CUEA program has appeared in a series of data reports published by Oregon State University (e.g., Enfield, et. al., 1978). In both experiments the currents were measured by Aanderaa current meters on taut subsurface moorings. The sampling interval was 10 min. for the ESACAN array and 15 or 20 min for the CUEA arrays, and the instruments recorded temperature as well as current speed and direction. These data were averaged to provide hourly data sets. The data from the CUEA anemometer at Callao and the subsurface pressure gages at P and near M were processed in the same manner as the current meter data. For the spectral computations (except Figures 9 and 10), and the EOFs, the hourly data were filtered with a low-pass filter with a one half power point of 1.96 days to remove diurnal and shorter period variations and decimated to six-hourly values. Currents at each mooring were rotated into a coordinate system in which the alongshore direction is defined by the averaged principal axis direction of the vector time series at the mooring as follows: C2 (15°) (counterclockwise from north), P (10°), Y (25°), M and L (45°). The winds were rotated as follows: Talara (15°), Chiclayo (0°), Callao (36°) and San Juan (45°). Hourly tide gage and three-hourly atmospheric pressure data at Baltra and La Libertad were obtained from Instituto Oceanografico de la Armada (Ecuador). Hourly tide gage data at Talara, Callao, San Juan, and Materani were obtained from Direccion de Hidrografia y Navigacion de la Marina (Peru).

Hourly atmospheric pressure data and wind data at Talara, Chiclayo, Callao, San Juan, and Materani were obtained from Corporacion Peruana de Aerolineas Commerciales. The coastel tide gage at San Martin and additional coastal anamometers at Callao and San Juan, maintained by the Cuea program, provided hourly data.

Two representative stations during 1977 where conductivity, temperature, and depth (CTD) observations of temperature and salinity were made are used in this paper, both obtained durind Leg IV of the Mellville cruise, at 15°15.5'S, 75°40.0'W on May 9, 1977, and 4°58.9'S, 81°33.0'W, on May 22, 1977, in the approximate locations of the L moorings at 15°S and the C2 mooring at 5°S, respectively. A profile from 1976 is also used, taken on 30 July at 15°19'S, 75°41.5'W with 1350 m water depth. The procedure used to obtain and process the CTD data is discussed in Data Report 71 from Oregon State University (Huyer, et. al., 1977).